METHOD-OF-CHARACTERISTICS MODELS FOR FLOWFIELD EVALUATION OF HYPERVELOCITY TEST FACILITIES

by

ANANTHKUMAR JAYAMANI

Presented to the Faculty of the Graduate School of
The University of Texas at Arlington in Partial Fulfillment
of the Requirements
for the Degree of

DOCTOR OF PHILOSOPHY

THE UNIVERSITY OF TEXAS AT ARLINGTON
December 2023

எனது பேரன்பிற்குரிய தாய் தந்தைக்கு...

In memory,

$$\int_1^u \frac{1}{x}\,dx$$

ACKNOWLEDGEMENTS

A lot of people have helped me get to the finish line in this marathon and so, it is impossible to express my gratitude within a page or even two. Thus the short list here is just the tip of an enormous iceberg.

Prof. Frank Lu, my advisor has encouraged, inspired and guided me professionally and at times personally through thick and thin for the last six years. His profound wisdom (both technical and worldly) along with his steadfast mentoring has laid the foundation for my professional research career and am indebted to him for that. I am grateful to Prof. Luca Maddalena for numerous things — selecting me as a GTA for the coveted AeroLab, sharing his vast knowledge during various meetings, his graduate courses and his invaluable constructive criticism. Prof. Souvik Roy's PDE and ODE courses are amongst the best classes I've ever taken, which have also been instrumental in my nonequilibrium work. I am grateful for his encouragement and guidance on approaching higher level math, especially as an uninitiated layman.

Prof. Liwei Zhang and the late Prof. Donald Wilson have kindly provided valuable feedback and guidance on nonequilibrium models and numerical methods used here. I am grateful for their advice and am honored to have them on my committee. I am indebted to Prof. Vijay Gopal for all the technical discussions on gasdynamics — experimental & analytical. He kindly accepted to evaluate my dissertation towards the end of my PhD and still diligently provided valuable feedback on various chapters in this work. I also thank him for all his kind help during my time at the ARC.

I thank Prof. Daejong Kim for patiently working with me on the helium turbomachinery project and for being very understanding of my doctoral research schedule.

Likewise, I thank Dr. Daniel Palmquist (and Hy-SET LLC.) for the opportunity to work on the research project, for being very understanding of my doctoral defense schedule and showing me a glimpse of the enthralling professional world here.

Mr. David Carter, ARC's Lab Manager, has literally been available for advice day and night, lunch-time, or otherwise. His crucial help and advice in setting up and running experiments is gratefully acknowledged. Friends at the ARC have been a great source of support, technically and personally. I am especially grateful to Drs. James Peace, Rohit Pulimidi, Umang Dighe, Sandeep James and Ian Raybon for our time at the ARC. Sandeep James and Jahanavi Sugganaboyina relentlessly helped me setup and run experimental campaigns, for which I am eternally grateful.

I have also had the fortune to make great friends outside the ARC at UTA. Some of them mentioned here have paid my tuition, rent and expenses during the past few years - the unofficial PhD sponsors. I thank Achuth Venkat, Muthu Subramanian, Ganesh Thavasimuthu, Roshan Sudhakaran, Shreya Dutta and Kyle Respondek for their much valued friendship during odd-times. The "Arlington Lake" conjecture is now etched in my memory forever.

Finally, I am extremely lucky to have such wonderful and supportive parents. They have encouraged my dreams and stood by my decisions at all times. Words cannot describe the sacrifices they've made for me. Needless to say, anything worthwhile I've done (and will do) has only been made possible because of their unconditional love, in addition to the emotional, intellectual and financial support they have showered on me throughout my life. No matter what I do, theirs' is one debt I cannot repay.

I gratefully acknowledge and thank the US Department of Energy/General Atomics and Hy-SET LLC. for partly funding my doctoral degree.

12 December 2023

ABSTRACT

METHOD-OF-CHARACTERISTICS MODELS FOR FLOWFIELD EVALUATION OF HYPERVELOCITY TEST FACILITIES

Ananthkumar Jayamani, Ph.D.

The University of Texas at Arlington, 2023

Supervising Professor: Frank K. Lu, Ph.D., P.E.

Ground test facilities are an imperative part of the design and development of flying vehicles. In the case of high-enthalpy facilities, evaluating the gasdynamic and thermochemical state of the test gas poses challenges due to high temperature effects. This study aims to contribute to the development impulse facilities by developing reduced-order models resolving the flowfields of such facilities. Developed as a part of this study are various method-of-characteristics (MoC) algorithms which consider gases under varying levels of thermochemical complexity. The algorithms span from simple calorically perfect gases to full thermochemical nonequilibrium.

The first set of algorithms was limited to unsteady flow of calorically perfect gases with no area variation. The effects of momentum and heat losses were included as appropriate sink terms in the governing equations. Based on ordinary differential equations from MoC, numerical algorithms were developed to solve various gasdynamic phenomena such as weak compressions, rarefactions, shocks and contact surfaces. The momentum losses in the governing equations were estimated using established friction factors. Various empirical methods were explored to determine an

appropriate heat-transfer model. In an effort to limit the scope of model development, a detonation-driven shock tube was first modeled based on the expected ideal wave processes utilizing various MoC algorithms.

Subsequently, experiments were carried out in a small-scale detonation-driven shock tube to validate the results from the reduced-order model. The experiments used nitrogen as the high-pressure driver gas, stoichiometric oxyhydrogen as the detonation driver gas and nitrogen or helium as the driven gas. Comparison with experiments showed that the MoC model reasonably replicated detonation tube operation for all the experimental cases. Specifically, the decaying incident shock trajectory in the driven section was replicated well, and so was the peak pressure at the driven endwall. The quasi-steady plateau pressure in the detonation driver was replicated reasonably, with experimental pressure traces showing early decay than MoC pressure traces. The wave system produced by the reflected shock wave–contact surface interaction in the driven section was also predicted accurately by the MoC model.

The second set of algorithms pertained to unsteady, inviscid, quasi-one-dimensional flow of a chemically reacting mixture of gases. Gaseous mixtures were assumed to be in thermal equilibrium but finite-rate chemical reactions were permitted. Initially, the variables associated with chemical composition were evaluated using the open-source toolkit, Cantera. The final results reported here use a stand-alone chemistry solver developed during this study, which evaluates rate constants using Arrhenius equation. A new integration procedure was formulated for flows with finite-rate chemistry. Simple gasdynamic models representing supersonic combustion, normal shock wave and a quasi-one-dimensional flow were developed and validated.

The third set of algorithms deal with thermally perfect gases. These were primarily selected to investigate vectorization of the existing MoC algorithms for

nonequilibrium flows. Vectorization was carried out for the interior point solver, which yields the maximum computational impact through parallelization. Thermally perfect algorithms were also developed for other MoC subroutines, but did not have the need to be vectorized. The variation of specific heats (and their ratio) was captured using curvefits constructed within the algorithm utilizing NASA polynomials and Cantera. A thermally perfect expansion tube solver was developed based on these algorithms and validated against analytical solution. Also developed along the thermally perfect algorithms were equilibrium algorithms. These use the same vectorized approach as thermally perfect algorithm, but the thermodynamic curvefits are, or course three-dimensional. Equilibrium MoC subroutines were used to develop expansion tube and detonation-driven shock tube algorithms. The results due to these models were validated against theory and experimental data available in the literature.

The final set of algorithms simulate unsteady, inviscid, quasi-one-dimensional flow gases in thermochemical nonequilibrium. These algorithms are based on the vectorized IMoC approach developed earlier in this work. Previously developed in-house chemistry solver was modified to use Park's two-temperature model for evaluating finite-rate chemistry. While there is no (such) restriction on the chemistry solver, vibrational relaxation is limited to diatomic gases currently. Vibrational relaxation considers both vibration-translation and vibration-vibration exchanges. Validation studies carried out with these subroutines include steady-state nozzle flowfield with vibrational, thermochemical relaxation and an expansion tube flowfield. Comparison of thermochemical nonequilibrium MoC results with state-to-state and computational fluid dynamics results in the literature show that the MoC models can reliably estimate the relevant nonequilibrium phenomena.

TABLE OF CONTENTS

LIST OF ILLUSTRATIONS

LIST OF TABLES

NOMENCLATURE

A	cross-sectional area
$\mathbb{A}$	species indicator
a	speed of sound
c	mass fraction
c_p	specific heat at constant pressure
C	characteristic curve
C_f	coefficient of friction
C_h	coefficient of heat transfer
D	diameter
E_a	activation energy
e	specific internal energy
e^*	equilibrium specific internal energy
δF_f	friction
h	specific enthalpy
IMoC	inverse method of characteristics
k_f	forward reaction rate
k_b	backward reaction rate
K_p	equilibrium constant
M	Mach number
$\mathbb{M}$	molecular weight
MoC	method of characteristics
$\mathcal{N}$	mole fraction

p	static pressure
$\delta\dot{q}$	heat flux
Pr	Prandtl number
r	recovery factor
$\mathcal{R}$	universal gas constant
R	specific gas constant, $\mathcal{R}/\mathbb{M}$
Re	Reynolds number
s	specific entropy
$\mathcal{S}$	Reynolds analogy factor
t	time
T	temperature
u	one-dimensional velocity
V	volume
x	axial location
ϵ	equivalent sand grain roughness
γ	ratio of specific heats
μ	specific Gibbs free energy
ν'	reactant stoichiometric coefficient
ν''	product stoichiometric coefficient
Θ_v	characteristic vibrational temperature
ζ	thermal source function
ρ	density
σ	species source function
θ	wall corner angle
τ	relaxation time

Subscripts

0	stagnation property
$+$	right running characteristic
$-$	left running characteristic
CJ	Chapman–Jouguet property
e	thermochemical equilibrium property
f	frozen property
i	mixture species index
j	chemical reaction index
o	pathline
rt	rotational-translational mode
s	shock property
v	vibrational mode
VT	vibration–translation
VV	vibration–vibration
w	wall property
∞	freestream property

Superscripts

$\bar{}$	molar property

CHAPTER 1

INTRODUCTION [1]

Wind-tunnel testing has played a crucial role in the development of aircraft since the days of the Wright brothers. Even with the advent of high-speed computing and advanced methods for computational fluid dynamics, wind tunnel testing is yet to be supplanted, as it provides invaluable data and insights into aircraft aerodynamics. With a history even longer than powered flight itself, these test facilities have seen their fair share of designs and iterations stemming from the requirements for duplication (or simulation) of flight from incompressible to supersonic to hypersonic. In the case of wind tunnels associated with low-flight velocities, the low power requirements allow for long duration, or "continuous" facilities. However, wind tunnels simulating high-speed flight are so often hampered by the enormous power requirements [1, 2] that a majority of the so-called hypervelocity test facilities have extremely short duration, operating by impulsively accelerating the test gas, see Fig. 1.1.

The simplest design of these short-duration facilities called a shock tube is shown schematically in Fig. 1.1a. This device traces its origins to the 1890s [3, 4], when Vieille constructed a cylindrical tube with two sections separated by a breakable partition. One of the sections was increasingly pressurized until the partition ruptured, leading to the formation of a shock wave (SW) in the low-pressure section which was the object of Vielle's study. As the high-pressure section drives a shock

[1] Contains excerpts from the paper entitled 'Method-of-Characteristics Model for a Low-Enthalpy, Detonation-Driven Shock Tube' by Jayamani, A., and Lu, F. K., Physics of Fluids, Vol. 34, No. 6, 2022. doi: 10.1063/5.0093888, reproduced with the permission of AIP Publishing

wave in the low pressure section, the former is called the driver section, while the latter is called the driven section. The ideal interface separating these two gases is called a contact surface (CS). An idealized operation of the shock tube is shown in Fig. 1.1b through the trajectories of the pertinent waves described above, known in the literature as a wave diagram. Also shown in Fig. 1.1b are different regions of interest from a gasdynamic perspective. Regions ④ and ① represent the initial gas states in the driver and driven sections respectively. Region ③ represents the quasi-steady state achieved by the driver gas after expansion into the driven section. Correspondingly, Region ② represents the quasi-steady state achieved by the driven gas behind the shock wave (SW) in the driven section.

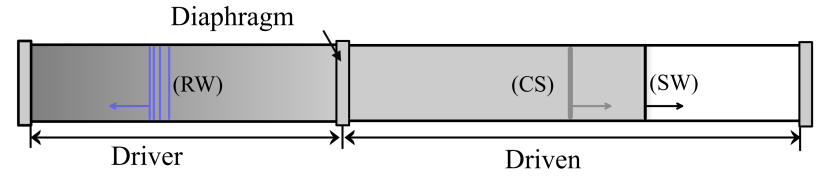

(a) Schematic.

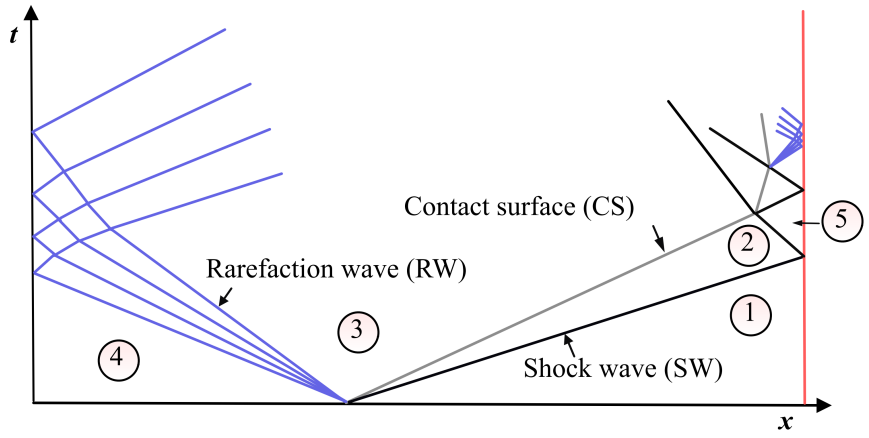

(b) Wave diagram.

Figure 1.1: Shock tube.

Based on classical gasdynamics and the wave diagram shown in Fig. 1.1b, the quasi-steady regions in a shock tube operation can be related [5]. Originally introduced by Bernhard Riemann and primarily known in the current literature as the shock tube equation, this relation is given by

$$\frac{p_4}{p_1} = \frac{p_2}{p_1}\left\{1 - \frac{(\gamma_4 - 1)(a_1/a_4)(p_2/p_1 - 1)}{\sqrt{2\gamma_1}\sqrt{2\gamma_1 + (\gamma_1 + 1)(p_2/p_1 - 1)}}\right\}^{-2\gamma_4/(\gamma_4 - 1)} \tag{1.1}$$

From Eq. 1.1, it can be inferred that a higher compression of the test gas can be obtained by either using a light driver gas with high ratio of specific heats γ, or by increasing the sonic velocity of the driver gas, or both. Trivially, this effect could also be produced by increasing the initial fill pressure ratio across the diaphragm. From gasdynamics, the test gas pressure ratio p_2/p_1 also represents the shock strength in the driven section. As shock strength in turn determines the enthalpy of the test gas, achieving a stronger shock wave results in a higher enthalpy test gas.

It took almost half a century after Vielle's experiment for the role of shock tubes in gasdynamic research to be recognized. This recognition spawned a widespread use of shock tubes in studying shock waves and the uniform flow behind them [6, 7, 8, 4, 9]. Along with this research came the realization that the Mach number of the test gas is practically limited to about 1.8 for an entirely air-filled shock tube [7, 10, 8]. As the flight velocity simulation requirements surpassed the capabilities of shock tubes, new design philosophies were implemented which extended the range of flight velocities that short-duration facilities can simulate. Some of these design philosophies include employing a low molecular weight driver gas such as helium or hydrogen and/or heating them using conventional methods [8, 11, 12], or by an electric arc discharge [13], compressing the driver gas using pistons [14, 15, 16], or combusting the driver

gas either through deflagration [8, 17, 18, 19] or detonation [18, 4, 20]. While the above philosophies improve the driver performance in a classical shock tube, another method pertains to the driven section. An expansion tube [21], as it is known, adds a lower pressure section after the driven section which serves as the nozzle equivalent for transient facilities. The lower pressure section is generally known as the acceleration section, as it serves to further accelerate the test gas in teh driven section. For this case, the state of the driven gas after expansion can be obtained by modifying the shock tube equation (1.1) to account for non-zero driven gas velocity as follows,

$$\frac{p_4}{p_1} = \frac{p_2}{p_1}\left\{1 + \frac{\gamma_4 - 1}{2a_4}u_4 - \frac{(\gamma_4 - 1)(a_1/a_4)(p_2/p_1 - 1)}{\sqrt{2\gamma_1}\sqrt{2\gamma_1 + (\gamma_1 + 1)(p_2/p_1 - 1)}}\right\}^{-2\gamma_4/(\gamma_4 - 1)} \tag{1.2}$$

In the above equation, the driven gas properties are denoted by the subscript 4 and the accelerant gas properties are denoted byt the subscript 1. Apart from the non-zero initial velocity, it can be seen that the general observations discussed above for a shock tube also hold for an expansion tube. A detailed discussion of expansion tube operation is posponed to Chapter 2.

Given all the myriad options for hypervelocity facilities, this work focuses only on two designs of impulse facilities, that is, detonation-driven shock tubes and expansion tubes. These designs can also be used as a combination leading to a detonation-expansion tube, which is not considered here. To provide a perspective of the contributions due to this work, a preliminary historical background on these facilities, with current literature are provided individually below.

1.1 Historical perspective—detonation tunnels

A detonation-driven shock tube, or a detonation tube for short, is a modification to the classical shock tube, where the driver section is filled with a detonable gaseous mixture instead of an inert gas. This mixture which is initially raised to a high

pressure and temperature by a detonation wave, is subsequently expanded unsteadily to drive a shock wave in the driven section. As the strength of the shock wave in the driven section depends on the pressure ratio and sonic velocity ratio between the driver and driven sections, this modification outperforms the classical shock tube in terms of the driven shock velocities achievable. In addition to its high performance, the detonation tube also offers several other advantages as a hypervelocity test facility.

The construction and assembly of the core facility is quite simple compared to a free-piston tunnel or facilities employing a statically heated driver gas. The assembly is also versatile enough to be converted between different modes of detonation tube operation or to be operated as an expansion/shock tube [22, 12]. A wide variety of test gas conditions from low to high enthalpies can be easily achieved by varying the detonable driver gas composition [23, 24, 12]. Since the pressure ratios between the detonation driver and driven sections can be low, mylar diaphragms which are easy to fabricate and install compared to thick metal diaphragms can be used, thereby significantly reducing shock formation losses associated with the latter diaphragms. Additionally, the use of a mylar diaphragm circumvents the potential damage to instrumentation in case of inadvertent impact by high-velocity fragments from diaphragm rupture. More important, since the gas state achieved behind a detonation wave exhibits excellent repeatability, the test gas state simulated is subsequently well repeatable [4, 12, 25]. The primary disadvantage of a detonation tube is the high safety requirements for handling combustible gaseous mixtures. However, careful planning and remote operation can ensure facility and personnel safety.

Despite the overall advantages, historical use of detonation tubes as a hypervelocity test facility seems sporadic. The concept of a simple detonation tube was theoretically studied in detail as early as 1957 by Bird [18]. Subsequent analytical and experimental studies were performed throughout the 1960s in North America

focusing mostly on what will be called here as the downstream-mode detonation tube [4, 26, 20, 27]. Around the same time, Yu conducted experiments on another design of detonation tubes, termed here as the upstream-mode detonation tube, at the Institute of Mechanics, Chinese Academy of Sciences [28]. Yu's experiments were discontinued due to high mechanical loading on the facility produced by detonation wave reflection on the driver endwall [29] .

The studies mentioned so far were primarily exploratory in nature. The establishment of detonation tubes as a viable means for hypervelocity testing in modern days started in the 1990s with extensive contributions from the Chinese Academy of Sciences, RWTH Aachen University and NASA's HYPULSE Facility at GASL.[2] Yu with Grönig and co-workers from RWTH Aachen University modified his original setup by adding a damping section to the detonation driver endwall to reduce loads on the facility [29, 30]. The studies at the HYPULSE Facility on the other hand concentrated on the downstream-mode of operation which exhibits superior performance compared to upstream mode due to the added momentum of the downstream flowing gas. This work resulted in modifications to HYPULSE, paving way for the development of detonation–expansion tunnels [31, 24]. Further, collaboration with GASL led to the development of a downstream-mode detonation tunnel at the University of Texas at Arlington's Aerodynamics Research Center (ARC) [32, 33].

1.2 Historical perspective—expansion tubes

The expansion tube, as mentioned earlier, is similar in construction to a shock tube, but consists of an additional section trailing the driven section. As the additional section is filled to lower pressures than the driven section and helps accelerate the test gas, it is termed the acceleration section. An expansion tube contrasts other

[2]The HYPULSE facility is being installed at Purdue University as of date.

high–enthalpy impulse facilities in the way energy is added to the test gas. While other designs employ high–performance drivers and add energy to the test gas primarily by a shock wave, an expansion tube adds energy in two stages, initially by a shock wave and thereafter by an unsteady expansion wave. Such an approach was developed to circumvent the undesirable high temperature effects on the test gas brought forth by adding a predominant share of energy through shock waves.

The expansion tube was introduced theoretically by Trimpi in the 1960s [21], which was followed by extensive experimental studies by NASA [34, 35]. Coincidentally, the HYPULSE facility discussed above was employed as an expansion tube in NASA Langley, which was subsequently modified by GASL into a detonation tunnel and expansion tube. The studies at NASA revealed that the theoretical performance map of the expansion tube was not always achievable due to viscous effects and high-frequency disturbances in the test gas. However, use of expansion tubes at NASA still continued based on experimental determination of useable test gas conditions. In the early 1990s, Paull and Stalker theoretically resolved the reason behind the large disturbances in the expansion tube test gas [36]. They showed mathematically that some disturbances present in the compressed test gas can be amplified during unsteady expansion and suggested attenuation criteria based on sound speed ratios across the expanded driver and test gas. This led to an increased use of expansion tube as a hypervelocity facility subsequently. Some of the expansion tube facilities currently in operation in the USA includes LENS facilities at CUBRC [37], HEX at Texas A&M University [38], HET at CalTech [39], and MHExT at The University of Michigan [40].

1.3 Current research scope and plan

The recent revival of interest in hypersonic flight has spawned a wide range of efforts to repurpose and/or construct new hypervelocity facilities for ground testing. Due to the relative ease of construction and tractable power requirements, a majority of these facilities are short duration, also known as impulse facilities. Despite these advantages, the short duration, unsteady operation invites problems during the design phase in terms of reliably estimating the facility performance/simulation envelope. With maximum possible facility flow timescales $\tau_f \sim \mathcal{O}(10^{-3})$s, errors in estimating an impulse facility flowfield may result in severe performance penalties and test-time reduction. For instance, an improperly designed shock tunnel nozzle may have an unacceptably long starting time, which in turn may result in no useful test time at all! Perhaps a sub-optimal length selection for various sections in a shock/expansion tube may result in early disruption of quasi-steady state available for testing. Moreover, hypervelocity facilities are generally susceptible to high temperature effects, as a significant amount of energy is deposited into the test gas in an effort to meet various simulation enthalpy requirements. This energy deposition results in marked changes to the test gas composition and internal energy distribution, which in turn affects the facility gasdynamics.

An illustrative scenario for the occurrence of thermochemical non-equilibrium in an impulse facility is the gasdynamic expansion through a reflected shock tunnel nozzle. Consider the quasi-steady state operation of a nozzle post shock reflection at the driven section endwall. Due to the high pressure and temperature caused by the reflected shock, the reservoir test gas (that is, air) will generally be in thermochemical equilibrium at the endwall. But a significant portion of its internal energy will be locked in higher energy modes, in addition to a significant fraction of dissociated oxygen. As the gas expands through the nozzle, the internal energy is redistributed

to the lower energy modes and recombination of atomic species occurs. Simultaneously, the expansion process also accelerates the test gas and its static pressure drops throughout the nozzle. Thus, the thermochemical time scales outpace the flow time scale near the nozzle inlet, but the former pair starts to slow down as the gas expands. Given the qualitative thermodynamic information about the expansion process, this trend is clearly evident from the Millikan–White correlation and from the standard form of the Arrhenius rate law for chemical rate constants. The opposite trend occurs for the gasdynamic time scales where the flow rates are slow at the reservoir and increase throughout the expansion process. So, in a hypervelocity nozzle, the entire range of conditions from thermochemical equilibrium to non-equilibrium to frozen state is present. Thus, to appropriately model hypervelocity flows in test facilities, the underlying thermochemical non-equilibrium processes should be accounted for.

From a gasdynamic perspective, a detonation-driven shock tube presents a complex problem. The facility relies on the establishment of a detonation wave in the combustible driver gas to provide a high performance driver. But, the presence of a detonation wave in the driver is practically tied to a trailing rarefaction wave in the driver (see Taylor rarefaction in Chapter 2 for more discussion on this aspect). Thus, when the detonation wave reaches the end of the driver section, it transmits as a shock wave into the adjacent inert section and subsequently decays in strength due to the transmitted trailing rarefaction wave. If the transmitted rarefaction wave is strong, then the shock wave decay occurs even as it reaches the facility endwall. These scenarios in a detonation tube often involve interaction of complex gasdynamic wave systems, the resolution of which is laborious at best and inaccurate at worst. Still, these unsteady phenomena determine the test gas state, available test time and structural loads on the facility. Even for an inviscid flow, these phenomena result in laborious calculations, which make simple parametric analyses at the design stage

almost impossible for a detonation tube. Further, the typical facility lengths are such that the effects of frictional and heat losses on the gasdynamics is non-negligible, thus inviscid calculations can be rendered inaccurate [23, 22, 25]. Recognizing these difficulties early, RWTH Aachen University developed an inviscid Riemann solver with the working gases assumed to be in thermochemical equilibrium [41]. This code, called KASIMIR, was used predominantly around the world for detonation tube development [23, 22, 42].

With the rapid advancements in computational fluid dynamics (CFD), later developments in the Chinese Academy of Sciences and GASL utilized CFD to aid in the development of new detonation driver techniques [43, 12]. Nowadays, quasi-one-dimensional CFD analyses seem to be the norm in aiding new facility development [43, 44, 45]. At the most, these analyses incorporate a one-dimensional thermochemical equilibrium solver accounting for heat and frictional losses, or use simplified chemical reactions with no heat or frictional losses. For a detonation tube, the former is expected to give reasonable results, as the only way energy is added to the test gas is through a shock wave and, oxyhydrogen detonation can be well approximated through equilibrium analyses. However, the latter model can be seen to overestimate driven shock speed in Li et al. [45], underscoring the need to account for heat and frictional losses. Further, if the simulations need to be extended to detonation–expansion tubes or, if the detonation tubes additionally incorporate a nozzle where gasdynamic expansion takes place, the effect of thermochemical non-equilibrium can become important. Under such circumstances, thermochemical equilibrium analysis will no longer be appropriate, while thermochemical non-equilibrium CFD analyses would be expensive to conduct parametric studies at the design stage, even for shock tubes [46]. Thus, it is necessary to explore alternative techniques to CFD which are more efficient and still reliable for high-enthalpy simulations.

Historically, unsteady quasi-one-dimensional flows have been resolved theoretically using the method of characteristics (MoC) due to the hyperbolic nature of the problem. This method reduces the governing partial differential equations to ordinary differential equations (ODEs), thereby providing an easier route to the solutions of relevant physical phenomena. Barring the trivial case of a simple region where self-similarity holds [47], non-simple regions have generally been solved using MoC. Such early efforts applicable to perfect gas flows were assisted either by hand calculations or a hand-drawn graphical approach [48, 18]. These methods involve projecting the simplified ODEs from known initial value locations to a later point in time to obtain their location of intersection, followed by calculation of the required flowfield properties. Applied over an extensive initial value line, this method results in a mesh of points at which the integral curves of the ODEs intersect and where the flowfield solution is also calculated. Alternatively, the solution procedure can utilize a pre-defined grid of points in the space–time domain where the intersecting ODEs and thereby the flowfield properties are determined, provided that the grid points are within the domain of influence of the initial value line [47]. The former approach is now known as direct MoC and the latter as inverse MoC [49].

In the case of expansion tubes, direct MoC based methods have been commonly used to design and supplant the operation of various facilities [39, 40, 50]. These methods only resolve simple regions in the flowfield and neglected frictional and heat losses. (LENS-X facilities have also shown to be supplanted by non-equilibrium CFD analyses [50, 51].) For detonation-driven shock tubes, apart from Bird's work [18], the author is unaware of an MoC-based model in the literature. An interesting parallel to the detonation-driven shock tube can be found in a propulsive device called a pulse detonation engine. One of the designs, called a partially-filled pulse detonation engine, provides the closest match to a detonation-driven shock tube described above.

A review of pulse detonation engine literature shows extensive use of MoC models. Skinner [52] modeled a partially-filled pulse detonation engine using the direct MoC method and considered the effects of frictional and heat losses. Skinner's method was later adapted by other authors to model fully-filled pulse detonation engines with heat losses alone [53] or both heat and frictional losses [54]. Morris [55] used an inverse MoC-based model to study pulse detonation engine without considering the influence of losses. Peace and Lu used a similar approach and extended the analysis to partially-filled detonation tubes incorporating a nozzle [56]. Though all of these models were limited to perfect gas MoC, the method itself is not limited to perfect gases.

A literature survey showed that direct MoC methods have been used to resolve both unsteady one-dimensional and steady two-dimensional nonequilibrium flows. For instance, chemical nonequilibrium in steady nozzle flows was resolved by Quan et al.[57], thermal nonequilibrium in steady expanding jets was resolved by Palmer and Hanson[58], thermochemical nonequilibrium in unsteady centered expansion fan was resolved by Connor [59]. Direct MoC has been favored over inverse MoC for chemical nonequilibrium flows as it specifically tracks pathlines. Early on, Quan et al. [57] reported that using the inverse MoC for chemically reacting flows leads to large errors in massfractions (discussed further in Chapter 4) and algorithm stability problems. However, for steady two-dimensional flows under thermal non-equilibrium, inverse MoC has been successfully applied by Palmer and Hanson [58]. For an excellent treatise on nonequilibirum MoC, refer to Sedney [60]. Thus, MoC algorithms can be an excellent option to model hypervelocity flowfields, both for efficient parametric analyses at the design phase and also for identifying new operational points in an existing facility. However, the literature listed above either simulate thermal, or chemical nonequilibrium, but not both. Also, a survey of the recent literature surprisingly

shows no MoC based models for simulating nonequilibrium flows in impulse facilities. Thus, this work sets out to develop MoC algorithms for thermochemical nonequilibrium flows, to model high enthalpy flowfields in hypervelocity facilities. But before embarking on a full nonequilibrium MoC model, it is advantageous to verify that perfect gas MoC can still capture the complex gasdynamics of a detonation-driven shock tube, for instance. Therefore, a multi-step approach has been taken in developing increasingly complex MoC algorithms by isolating various perceived bottlenecks, as detailed below.

1.3.1 Phase 1

In this phase, the reliability of MoC models in resolving complex flow phenomena in a detonation tube consisting of multiple gas slugs suffering heat and frictional losses is studied. As a first step to simplify the problem, high-temperature effects were neglected, thus the MoC algorithms developed were for a calorically perfect gas. Also, only one mode of detonation tube operation, namely, the downstream mode (see §2.2.1) was investigated. This was deemed acceptable, as the generic algorithm used to resolve a detonation tube is very similar to that required for an expansion tube. Thus, validating the detonation tube algorithm, with significantly more complex gasdynamics than an expansion tube was also expected to mean that an MoC expansion tube algorithm was reliable.

In the initial detonation tube studies, of particular interest was the deceleration of shock waves in the driven section. This occurs due to the inherent nature of a detonation wave propagation outlined earlier, combined with the effect of frictional losses in the test gas behind the shock wave [61, 62]. Studies have also shown that heat and frictional losses in a single-shot, fully-filled pulse detonation engine influence its gasdynamics significantly [53, 54, 56] and, thus, the effect of these driver gas losses on

the driven gas state in detonation tunnels also need to be captured. Moreover, for a detonation tube operating in the reflected shock tunnel mode, the reservoir condition which is the state of the driven gas at the endwall is of primary importance, as this determines the flow expansion through the nozzle and subsequently the test gas properties at the test section. The reservoir state itself is governed by the driven shock dynamics as it moves towards the endwall and after its reflection from the endwall. As the reflected shock moves away from the endwall, it also interacts with the contact surface in the driven section. The outcome of this interaction as detailed in §2.2.3, influences the reservoir state and the test time available for reflected shock tunnel operation. All these phenomena were considered in the numerical and experimental facets of the first phase of this work, to ensure that the MoC model is reliable as a simulation tool. This initial model which is based on inverse MoC, incorporates heat and frictional losses through various empirical approaches available in the literature. A simpler version of the model which used a constant friction factor approach was reported by the author previously [63]. To validate the results from the MoC model, a small-scale detonation tube was constructed and experiments were carried out using stoichiometric oxyhydrogen driver and different driven gases. The work carried out during this phase is detailed in Chapter 3.

1.3.2 Phase 2

As Phase 1 proved that MoC models can resolve low-enthalpy detonation tube flowfields, Phase 2 was aimed at extending the IMoC algorithms to nonequilibrium flows. Therefore, Phase 2 investigated the feasibility of using IMoC models for flows under chemical nonequilibrium. To simplify the problem again, the flow was assumed to be always in thermal equilibrium. While the effect of area variation was added to the governing equations, frictional and heat losses to the walls were neglected for

simplicity. Due to the exploratory nature of this phase, only two continuous wave algorithms (discussed further in Chapters 3 and 4) were developed. For aiding the MoC algorithms in direct evaluation of finite-rate chemical kinetics and for computational efficiency, stand-alone chemistry subroutines were developed. Using the MoC algorithms, three validation cases were modeled and simulated. The first two cases were simplified to be chemically reacting steady flows in a one-dimensional duct. These include supersonic combustion in a duct and chemical relaxation behind a normal shock wave. These results were compared against direct ODE based solvers available in the literature. As these studies showed that inverse MoC was both reliable and stable, a steady nozzle flow with chemical nonequilibrium was then simulated using MoC. To validate the MoC nozzle results, an ODE solver representing chemical nonequilibrium occurring in a quasi-one-dimensional nozzle was also developed. Chapter 4 summarizes the work carried out in Phase 2.

1.3.3 Phase 3

Experience from Phase 2 showed that existing IMoC algorithms applied to nonequilibrium flows may not be highly accurate, as the subroutines rely on linear interpolation of all dependent variables along the initial value line. Additionally, the original inverse MoC algorithms were developed about half a century ago primarily for perfect gas flows and do not effectively utilize the existing computational power and architecture. Thus, in Phase 3 the existing IMoC algorithm was optimized through vectorization. Also, improved interpolation procedure was introduced to increase the solver accuracy. Considering easier extension to nonequilibrium algorithms, this phase developed thermally perfect and thermochemical equilibrium MoC subroutines. Thus, all the improvements to the original IMoC algorithms were carried out in thermally perfect and thermochemical equilibrium algorithms. These subroutines were used to

develop reduced-order models for expansion tubes and upstream detonation drivers. The thermally perfect expansion tube model ignored losses, so that the MoC results could be validated against analytical solutions. The thermochemical equilibrium algorithms also considered the effect of frictional and heat losses. These results were compared to the experimental data available in the literature. These developments are discussed in Chapters 5 and 6.

1.3.4 Phase 4

Finally, in Phase 4, the IMoC algorithm was extended to flows in thermochemical nonequilibrium. MoC subroutines representing shock waves, contact surfaces and weak compression and expansion waves were developed. The integration approach in these subroutines were based on the vectorized skeleton algorithms developed in Phase 3. Stand-alone chemistry solver developed in Phase 2 was modified to account for thermochemical nonequilibrium. The MoC subroutines so developed were used to simulate three validation cases. The first two cases represented thermal and thermochemical nonequilibrium occurring in a steady state quasi-one-dimensional nozzle flow. The final model resolved an expansion tube flowfield under thermochemical nonequilibrium. The validation data for these cases were obtained from state-to-state and CFD results existing in the literature. These efforts are detailed in Chapter 7.

1.4 Contributions

The scientific contributions from this work at various phases are outlined below,

- Phase 1 of this work which extended the work of Peace and Lu [56] showed that inverse MoC models can be used to estimate the operation of a low enthalpy detonation-driven shock tube with momentum and heat losses. It also showed that the MoC model can be used to estimate the endwall conditions even for a downstream detonation tube operating in an under-driven mode.
- Phase 2 showed that IMoC algorithms can be used to resolve flows in chemical nonequilibrium, which was earlier deemed impractical [57].
- Phase 3 introduced thermally perfect and equilibrium IMoC algorithms incorporating simplified losses models. Notably, the original IMoC approach was vectorized, which significantly increased the computational efficiency of the IMoC algorithm.
- Phase 4 introduced IMoC algorithms for flows under thermochemical nonequilibirum. An expansion tube model developed through this algorithm resolves a large scale expansion tube flowfield in approximately 1.5 hours, on a personal laptop.

As of writing, the findings from this work have been published as four AIAA conference papers and one ISSW conference paper. The information about these papers are below,

1. Jayamani, A., Lu, F.K., "*A Study of Detonation Driven Shock Tube Using the Method of Characteristics*", 23$^{\text{rd}}$ AIAA International Space Planes and Hypersonic Systems and Technologies Conference, AIAA 2020 -2454, March 24 -26, 2020, Montréal, Québec, Canada (virtual event) (doi: 10.2514/6.2020-2454).

2. Jayamani, A., Lu, F.K., "*A Method of Characteristics Solver for Unsteady Quasi-One-Dimensional Chemically Reacting Gas Flows*", AIAA SciTech 2021 Forum (virtual event), AIAA 2021 -0315, January 11 -15, 2021, (doi: 10.2514/-6.2021-0315).
3. Jayamani, A., Lu, F.K., "*Method of Characteristics Modeling of Non-equilibrium Flow in an Impulse Facility*", AIAA SciTech 2023 Forum, AIAA 2023-2088, January 23-27, 2023, National Harbor, Maryland, USA (doi: 10.2514/6.2023-2088)
4. Jayamani, A., Lu, F.K., "*Inverse Method-of-Characteristics Algorithms for Unsteady Gas Flows with Shifting Thermochemical Equilibrium*", 25th AIAA International Space Planes and Hypersonic Systems and Technologies Conference, AIAA 2023 -3021, May 28 June 1, 2023, Bengaluru, Karnataka, India (doi: 10.2514/6.2023-3021).
5. Jayamani, A., Lu, F.K., "*Vectorization of Inverse Method-of-Characteristics Algorithms for Quasi-One-Dimensional Unsteady Flows*", The 34$^{\text{th}}$ International Symposium on Shock Waves, 16-21 July 2023, Daegu, Korea.

Additionally, one archival journal publication has been published through Physics of Fluids.

1. Jayamani, A., Lu, F.K., "*Method-of-Characteristics Model for a Low-Enthalpy, Detonation-Driven Shock Tube*", Physics of Fluids, Vol. 34, No. 6, 2022. doi: 10.1063/5.0093888.

All the remaining conference papers are to be prepared for archival journal publications in Spring-Summer 2024.

CHAPTER 2

IDEAL WAVE PROCESSES IN IMPULSE FACILITIES [1]

The first formal chapter in this work is devoted to the gasdynamics of impulse facilities. The need for this discussion will become apparent in the subsequent chapters because the MoC algorithms developed here represent various possible gasdynamic phenomena. Development of a meaningful model using these MoC algorithms relies heavily on a precise understanding of gasdynamic processes to ensure that MoC can be appropriately applied. Additionally, the governing equations considered in these algorithms are either one-dimensional or quasi-one-dimensional. Thus, the modeling approach considered here represents a simplified version of the actual facility gasdynamics, commonly known in the literature as reduced-order models.

Since this work considers several impulse facilities which are characterized by complex gasdynamics, identifying the salient gasdynamic features that must be modeled represents the first step. For unsteady facility flowfields, this task can be accomplished by the use of wave diagrams, which represent the propagation of various gasdynamic waves throughout a given facility in both spatial and temporal coordinates. To maintain focus on ideal wave systems that are to be expected in these facilities' operation, the following discussions in this chapter assume that the flow is inviscid and one-dimensional.

[1] Contains excerpts from the paper entitled 'Method-of-Characteristics Model for a Low-Enthalpy, Detonation-Driven Shock Tube' by Jayamani, A., and Lu, F. K., Physics of Fluids, Vol. 34, No. 6, 2022. doi: 10.1063/5.0093888, reproduced with the permission of AIP Publishing

2.1 Expansion Tube

The expansion tube contains the simplest wave processes amongst the facilities considered here. As mentioned earlier, an expansion tube consists of three sections namely, a driver, a driven and an acceleration section, see Fig. 2.1a. The nomenclature of regions resembling the sections in a classical shock tube remains the same. Thus, the initial driver gas state is denoted ④ and the corresponding driven gas state is denoted ①. The initial gas state in the additional section, i.e., the acceleration section is denoted ⑤. During filling and prior to facility operation, all these initial gas states are separated by partitions called diaphragms. The diaphragm which separates the driver and driven gas is termed the primary diaphragm, as it is the first partition to rupture. A secondary diaphragm separates the driven and acceleration sections. Similar to the classical shock tube, the driven gas in an expansion tube serves as the test gas.

The ideal wave processes related to the operation of an expansion tube are shown in the x–t diagram in Fig. 2.1b, albeit, at a later time than the waves shown in the schematic, Fig. 2.1a. The facility operation begins when the primary diaphragm is ruptured. Similar to the classical shock tube, the diaphragm rupture triggers the driver gas to expand into the lower pressure driver section. In the ideal situation considered here, the primary diaphragm is assumed to vanish and the subsequent driver expansion wave is idealized to be centered, which is marked as primary rarefaction (PR) in the x–t diagram. The expanded driver gas state is denoted ③. As the driver gas expands into the driven section, the originally quiescent driven gas is set into motion through a shock wave, due to the supersonic velocities achieved by the expanding driver gas. The shock compressed driven gas state is denoted ②. Associated with the primary diaphragm, the contact surface between the driver and driven

gas is called the primary contact surface (CS_1). Following a similar nomenclature, the shock wave in the driven section is called the primary shock wave (SW_1).

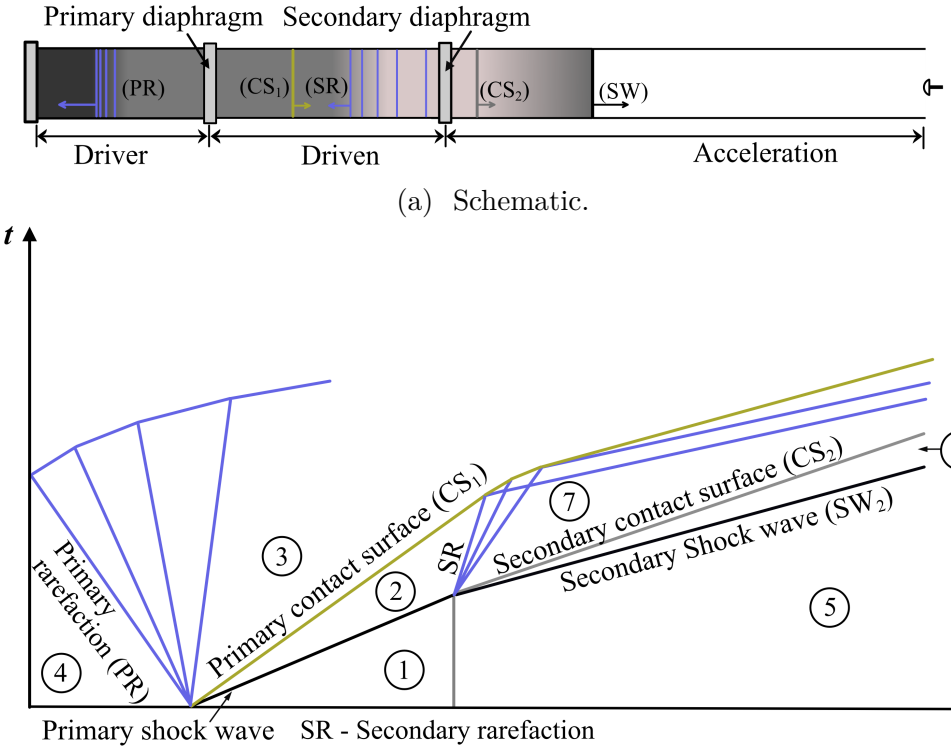

(a) Schematic.

(b) Wave diagram.

Figure 2.1: Expansion tube.

When the primary shock wave reaches the end of the driven section, the secondary diaphragm is similarly assumed to vanish instantaneously. Thus, the primary shock wave transmits across the contact surface between driven and acceleration sections. The resulting transmitted shock wave in the acceleration section is the secondary shock wave (SW_2) shown in Fig. 2.1b. The interface between the test gas and the accelerant gas becomes the secondary contact surface (CS_2). Generally, the acceleration section is pressurized to substantially lower pressures than the driven section. Thus, the reflected wave from the primary shock wave–secondary contact

surface interaction is always an expansion wave, which is depicted in Fig. 2.1b as secondary rarefaction (SR). Since the test gas in region ② travels at supersonic velocities, the leading characteristic of the secondary rarefaction is of positive slope. The secondary rarefaction accelerates the test gas to state ⑦, which represents the simulated freestream conditions. In the simplest expansion tube design, a model is placed at the end of the acceleration section. Thus, test time ideally begins when the secondary contact surface arrives at the end of the acceleration section and is terminated by the arrival of the reflected secondary rarefaction (as shown in Fig. 2.1b). In off-design scenarios or when the secondary rarefaction is strong, the test time might also be terminated by the arrival of the trailing characteristic of the secondary rarefaction wave.

2.2 Detonation Tube

Detonation tube (or tunnel) facilities are found under two general designs, the upstream and the downstream modes [64]. Prior to the discussion of the upstream or downstream modes, preliminary terminologies for a detonation driver are briefly reviewed. Consider the assembly shown in Fig. 2.2a, which is similar to the classical shock tube in construction, with the only difference being the presence of an igniter at the driver endwall. The driver section is now filled with a detonable gaseous mixture and is separated from the inert gas-filled driven section by a diaphragm. To further simplify the discussion, assume that the driven gas has a lower acoustic impedance than the driver gas, for reasons to be explained later.

The operation of this simple detonation tube begins when the igniter ignites the detonable mixture. Usually, a deflagration-to-detonation transition follows the ignition but this is ignored in the current analysis. Once a stable detonation wave forms, it propagates into the driver section solely propelled by the chemical energy

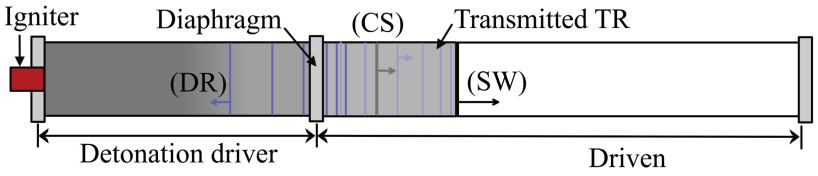

(a) Schematic.

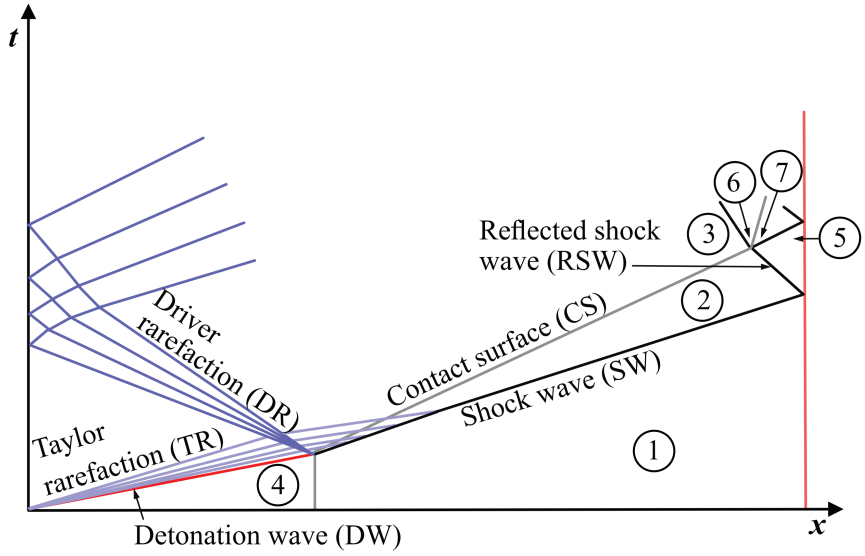

(b) Wave diagram.

Figure 2.2: Simple detonation tube.

released by the processed gaseous mixture. For a given initial gas state, such a detonation wave, called the freely propagating detonation wave, has a unique velocity based on the Chapman–Jouguet (CJ) condition, that is, chemical reactions behind the detonation wave reach completion when the expanding gas velocity reaches the local sonic velocity [65]. Naturally, this final state of the chemically reacting gas is called the Chapman–Jouguet state. The gas at the CJ state possesses a finite velocity and is at a higher pressure than the gas at the driver endwall which forms the leftmost boundary condition. Thus, the burnt gas expands unsteadily to zero velocity preserving the endwall velocity and pressure. This unsteady expansion which can be seen trailing the detonation wave in Fig. 2.2b is called the Taylor rarefaction. Eventually, as the

detonation wave reaches the diaphragm, assume that the diaphragm instantaneously disappears, leaving only an immiscible gaseous interface, the contact surface. Since the driven gas is inert, the impacting detonation wave will transform into a shock wave across the contact surface resulting in a reflected wave at the interface, which travels back into the driver gas. This reflected wave will always be an expansion wave if the acoustic impedance of the driven gas is less than that of the driver gas, which is the already assumed initial condition. Now, as the reflected expansion wave, denoted driver rarefaction in Fig. 2.2b, travels into the driver gas, it interacts with the Taylor rarefaction and a non-simple region ensues behind the contact surface. The Taylor rarefaction, which emerges after this interaction reaches and transmits across the contact surface only to reach and decelerate the transmitted shock wave in the driven section. This adverse effect prevents the attainment of a constant region of test gas behind the transmitted shock wave in impulse facilities of reasonable length. To circumvent this problem, two different detonation tube operations were developed historically, the downstream mode and the upstream mode.

2.2.1 Downstream mode

A detonation tube operating in the downstream mode is similar in design and operation to the simple detonation tube discussed above. The primary problem in the simple detonation tube is the decelerating driven shock wave caused by the Taylor rarefaction in the driver section. The downstream mode of operation tackles this problem by eliminating or attenuating the Taylor rarefaction through adding a high-pressure driver to the aft of the detonation driver. A schematic of the downstream mode is shown in Fig. 2.3a, along with a wave diagram in Fig. 2.3b to show all the relevant processes. Figure 2.3a shows the assembly of the downstream detonation tube consisting of three sections, with each isolated from the subsequent section by a

diaphragm. The first section which generally contains a light gas under high pressure is simply called the high-pressure driver. The second section which serves as the actual driver for the test gas contains a detonable gaseous mixture and is called the detonation driver. The last section called the driven section contains the test gas. For clarity, these diaphragms are respectively called primary and secondary diaphragms. Similarly, the gaseous interface between the high-pressure driver and detonation driver is called the primary contact surface (CS_1), while that between the detonation driver and the driven section is called the secondary contact surface (CS_2). The wave diagram in Fig. 2.3b corresponds to all the expected gasdynamic processes, while the schematic in Fig. 2.3a shows a particular instant in the detonation tube operation.

Figure 2.3a shows that the detonation driver in the downstream detonation tube does not contain an igniter. This aspect directly ties in with the operation of this type of facility. Previous studies [31, 66] have shown that, for high-enthalpy detonation drivers, the rupture of metallic primary diaphragm accompanied by the strength of the initial shock wave are sufficient to provoke a detonation wave in the gaseous mixture . Thus, an igniter is employed for supplementary reasons, for instance, to aid direct initiation. Regardless, only the initiation mechanism differs, with the remainder of the processes described being the same. Consider the former design, where all the sections have been filled to the required pressures and composition. This detonation tube operation begins when the primary diaphragm ruptures, rapidly creating a detonation wave (DW) in the detonation driver. As the high-pressure gas expands into the detonation driver, a gasdynamic equilibrium occurs between the expanding high-pressure driver gas and the detonated gaseous products, in turn determining the strength of the Taylor rarefaction (TR). Based on the extent of the high-pressure driver gas expansion, identified as primary rarefaction, three different

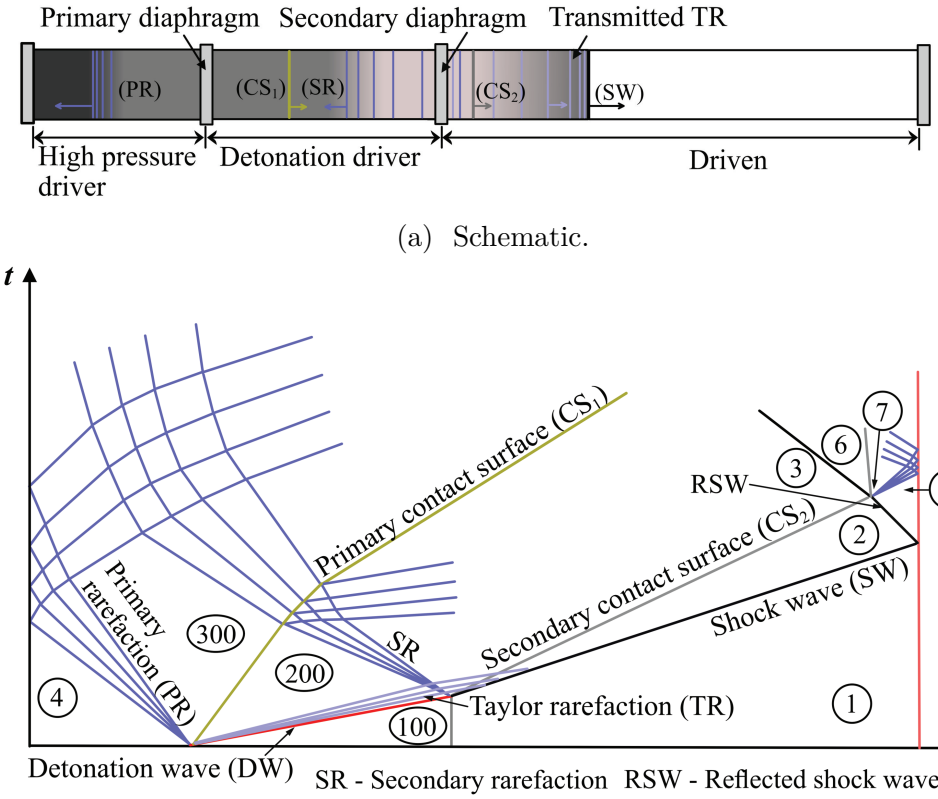

(a) Schematic.

(b) Wave diagram.

Figure 2.3: Downstream mode detonation tube.

operating scenarios are possible in a downstream detonation tube, as depicted in Fig. 2.4 in a pressure–velocity plot.

The lowest value that p_4 can assume for the downstream mode is denoted as location b in the ordinate. Below this value, the high-pressure gas behind the detonation wave will cause a shock wave in the high-pressure driver, negating its purpose. Increasing p_4 from b causes a relatively weak primary rarefaction PR to form, as shown in the x–t diagram of Fig. 2.3b. Note that the trailing characteristic in region (300) is shown to be subsonic here, which will not necessarily be the case for a strong primary rarefaction. Thus, for a weak primary rarefaction, the high pressure driver gas expands to pressures and velocities lower than the CJ state. This operating con-

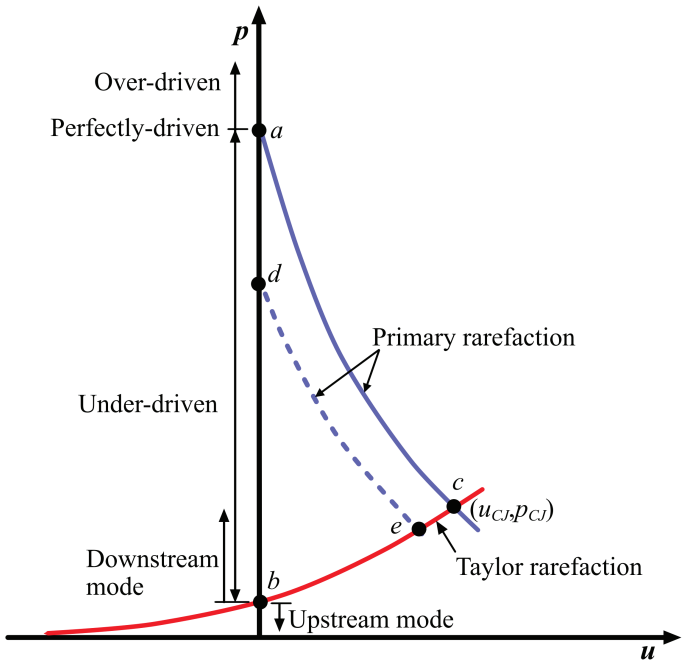

Figure 2.4: Effect of driver pressure in the downstream mode.

dition, called the under-driven mode, is represented in Fig. 2.4 by the sample curve de. As the value of p_4 increases from b to a, the strength of the primary rarefaction increases, in turn reducing the strength of Taylor rarefaction behind the detonation wave. Correspondingly, the locus of possible final states at the trailing characteristic of the Taylor rarefaction, that is, state (200) in Fig. 2.3b is given by the curve bc. The second scenario, where p_4 is such that the driver gas expands exactly to the CJ state pressure and velocity is called the perfectly-driven mode. In Fig. 2.4 the corresponding driver state is denoted as a and, obviously, the final state in driver rarefaction is given by c.

While the Taylor rarefaction is seen to be completely annihilated for the perfectly-driven mode, in Fig. 2.4, chemical reactions still proceed to reach the CJ state behind the freely propagating detonation wave. If p_4 is increased above a, the driver gas expands to pressures and velocities above the CJ state and, thus, the detonation wave

velocity will be higher than the freely propagating detonation wave for a given gaseous mixture. This mode is which is rarely realized in practice is called the over-driven mode.

When the detonation wave reaches the secondary diaphragm and ruptures it, a shock wave SW is transmitted into the driven section and a secondary rarefaction wave SR travels back into the detonation driver. Note the orientation of the leading characteristic, which is shown to be subsonic. This is typical of a detonation driver in the under-driven mode, as the flow is subsonic throughout the Taylor rarefaction. However, the trailing characteristic of the secondary rarefaction may or may not be supersonic depending upon p_{100}/p_1. In the case of a perfectly-driven mode, due to the CJ condition, the detonation driver velocity is sonic in state (200). Hence, the leading characteristic of the secondary rarefaction is perpendicular to the abscissa, and the trailing characteristic always turns supersonic. While the perfectly-driven mode exhibits no driven shock attenuation, for the under-driven mode, the strength of the Taylor rarefaction and the acoustic impedance ratio across the detonation driver and the driven section determine the driven shock wave attenuation. Nonetheless, the literature for downstream detonation tubes/tunnels shows that a carefully selected under-driven mode of operation can still provide useful test time for high-enthalpy testing [22, 66]. Finally, the terminology for this design, that is, the downstream mode is derived from the direction of the detonation wave propagation in the detonation driver. Though the terms upstream and downstream can be easier to define in a steady-state flow, a transient flow with omnidirectional waves and fluid motion can present a dilemma. In this case, as the test gas is of prime significance, the direction of initial motion of the test gas is taken to be downstream, from which the naming convention follows directly.

2.2.2 Upstream mode

A detonation tube operating in the upstream mode is similar in construction to the downstream detonation tube except that an igniter is present in the detonation driver. A schematic of the assembly is shown in Fig. 2.5a with the wave diagram shown in Fig. 2.5b corresponding to a later time than the schematic. The naming convention for this design may be obvious from Fig. 2.5b, where the detonation wave is seen traveling upstream relative to the test gas. The deceleration of the driven shock wave is eliminated in this design by utilizing the Taylor rarefaction as the driver rarefaction in a manner detailed below.

The upstream detonation tube schematic shown in Fig. 2.5a contains three sections, namely, the damping section, the detonation driver and the driven section, each separated by a diaphragm. The detonation driver and driven section are respectively filled with a detonable gaseous mixture and the test gas. The diaphragm between the detonation driver and the driven section is called the primary diaphragm, as it ruptures first. The detonation driver in this design houses an igniter near the primary diaphragm, as there is no implicit mechanism that can be used to produce a detonation wave. If the upstream-mode design were to consist only of a detonation driver and a driven section, the detonation wave on reaching the endwall of the detonation driver will reflect as a shock wave. This results in very high structural loads on the endwall and has been linked to damaged facilities [29]. To circumvent this complication, an additional section is added to the end of the detonation driver, but is now filled with a low-pressure inert gas. Thus, the detonation wave transitions into a shock wave in this inert section. Eventually the transmitted shock wave reaches and reflects off the endwall resulting in stagnation pressures significantly lower than that caused by an incident detonation wave. Since this section damps the overall structural loads

on a detonation tube, it is called the damping section. The diaphragm between the detonation driver and the damping section is called the secondary diaphragm.

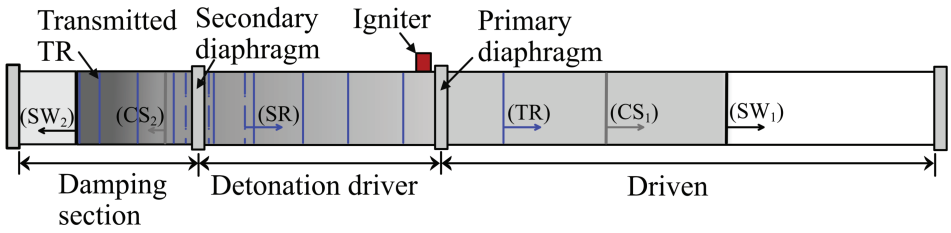

(a) Schematic.

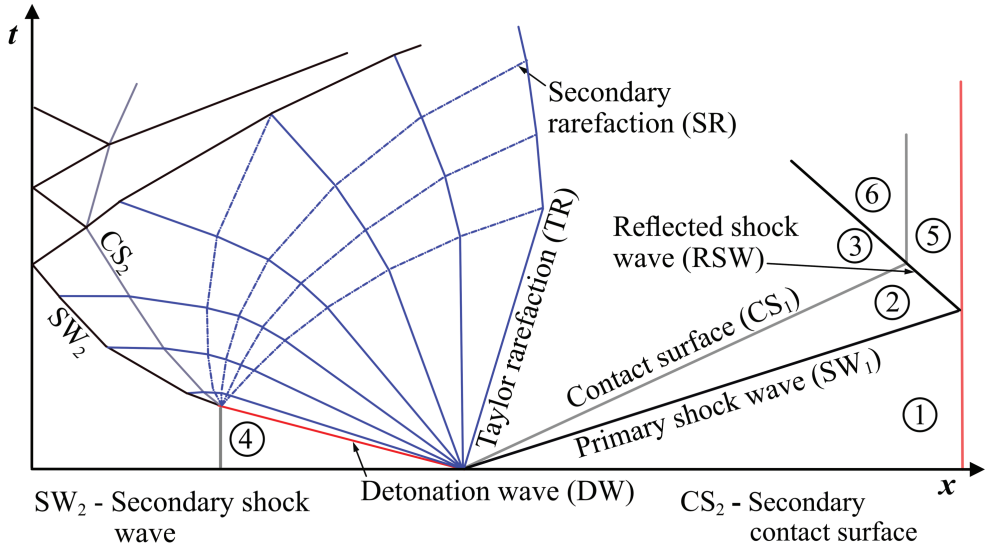

(b) Wave diagram.

Figure 2.5: Upstream mode detonation tube.

For simplicity, the process of detonation wave formation is neglected and instead the detonation wave is assumed to form instantaneously at the primary diaphragm. The detonation wave then propagates in the upstream direction to consume the detonable mixture. Now, if the primary diaphragm were a rigid wall, the burnt gas behind the detonation wave can be expected to expand through the Taylor rarefaction to zero velocity at the wall. It is assumed that the primary diaphragm disappears

at the moment the detonation wave forms in the detonation driver. Thus, the final velocity and pressure at the end of Taylor rarefaction are determined by the velocity and pressure the test gas acquires as a result of the primary shock wave in the driven section. This way, the Taylor rarefaction becomes the driver rarefaction in the upstream detonation tube. Moreover, as a freely propagating detonation wave has a unique CJ state, the driver gas is essentially excited to the same "initial condition" prior to unsteady expansion. The resulting primary shock wave that is caused by the expanding driver gas is also of a constant velocity. Eventually, the propagating detonation wave reaches the end of the detonation driver and ruptures the secondary diaphragm.

Since the damping section is of significantly lower pressure than the detonation driver, a secondary shock wave SW_2 is formed in the damping section with a reflected rarefaction wave traveling back into the detonation driver. This reflected, secondary rarefaction wave SR interacts with the incoming Taylor rarefaction, resulting in a non-simple region. At the end of this interaction, the secondary rarefaction emerges in the driven section, while the Taylor rarefaction is transmitted into the damping section. The transmitted Taylor rarefaction refracts across the secondary contact surface and then decelerates the secondary shock wave as seen in Fig. 2.5b. The facility gasdynamics discussed so far only describe the wave processes before various shock waves reach the endwalls. The reflection of shock waves at the endwalls and their subsequent interactions with the contact surfaces are described next.

2.2.3 Driven section endwall phenomena

The temporal evolution of the driven gas state at the endwall represents an important aspect of reflected-shock tunnel operation. In a reflected-shock tunnel, where a nozzle is attached to the endwall of the driven section, the stagnated driven gas at

the endwall becomes the reservoir for the nozzle. It is desirable to achieve a constant reservoir condition and sustain this gas state for as long as possible during facility operation. While this study does not account for a nozzle at the driven endwall, it is still possible to evaluate the maximum available time for nozzle operation, with a completely closed endwall. In fact, at the initial parametric study stage, it would be logical to simply base all calculations on a detonation tube with closed endwall as a nozzle design may not yet be available. However, appropriately chosen reservoir conditions from the parametric analysis can be used to design a nozzle, which in turn can be used for further simulations to understand the nozzle starting transients and, subsequently, the available test time. It is expected that the following discussion on endwall phenomena will throw light on the statements above.

Consider the wave processes in the driven section of the upstream-propagating detonation tube shown in Fig. 2.5a. When the primary diaphragm ruptures, the primary shock wave (SW_1) forms instantaneously and starts traveling down in the driven section, compressing an ever increasing volume of the test gas. The primary shock wave is trailed by the test gas slug, denoted as region ②, which ends at the contact surface (CS_1). In the upstream mode, region ② is of constant properties because the primary shock wave strength is constant. After traversing the entire driven section, the primary shock reaches the endwall. The incoming test gas in region ② must then come to rest. This occurs through the reflection of the incident primary shock wave at the endwall. The reflected shock wave (RSW) stagnates the incoming test gas which also increases its static pressure and temperature. This stagnant region behind the reflected shock wave denoted as ⑤ in Fig. 2.5b is the reservoir gas for nozzle operation. In this case, as region ② is of constant properties, so is region ⑤, which is processed by the reflected shock wave. These phenomena are shown schematically in Fig. 2.6.

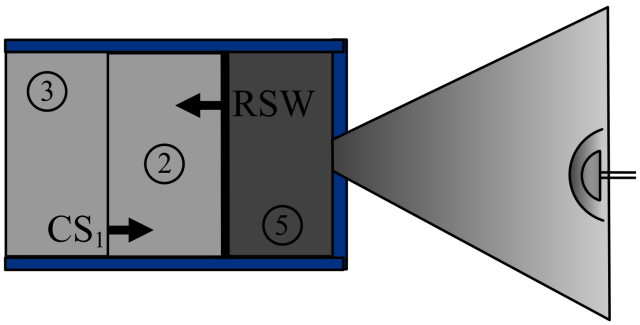

Figure 2.6: Reflected shock tunnel endwall phenomena.

On further traveling into the driven section, the reflected shock wave encounters and interacts with the oncoming contact surface, resulting in a transmitted shock wave into the driver gas. Despite this interaction, the contact surface remains intact due to the inviscid flow assumption. The static pressure and velocity must be continuous across the contact surface even after this interaction. Therefore, a reflected wave is simultaneously formed in region ⑤, with the shock wave transmitted into region ③. The nature of this reflected wave is determined by the change of acoustic impedance across the contact surface [67, 68].

In the special case when the there is no change in acoustic impedance between gases in region ② and region ③, the shock wave essentially perceives no change in medium, as the pressure rise brought about by the shock waves on either sides of the contact surface is the same. This situation results in a degenerate reflected wave at the interface, a Mach wave that does not alter the test gas in region ③. Since the acoustic impedances of the expanded driver gas and compressed driven gas are matched across the contact surface, this situation is called tailored operation, which results in the desired prolonged steady-state reservoir condition, until waves from the driver expansion reach region ⑤. This is shown schematically in Fig. 2.7a and depicted in the wave diagram in Fig. 2.5b.

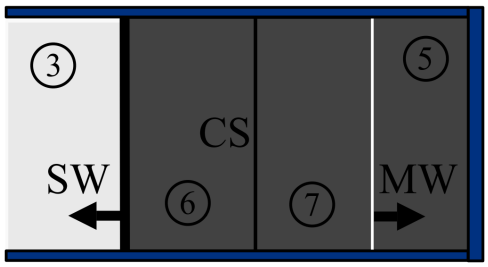

(a) Tailored operation.

(b) Overtailored operation.

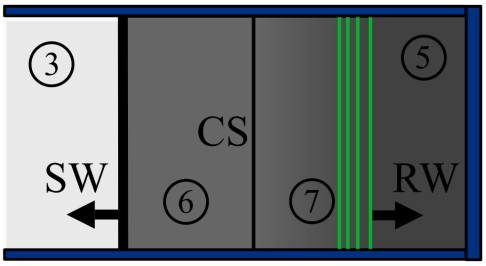

(c) Undertailored operation.

Figure 2.7: Reflected shock wave–contact surface interactions.

If the acoustic impedances of regions ② and ③ do not match, two types of reflected waves are possible during the shock wave–contact surface interaction. When the expanded driver gas in region ③ has higher acoustic impedance than the test gas in region ②, the incident shock wave perceives a heavier gas across the contact surface. Thus, a reflected shock wave propagates into region ⑤, as seen in Fig. 2.7b. A reflected shock tunnel operating under such a condition is said to be overtailored. On the other hand, if the driver gas in region ③ has lower acoustic impedance than the test gas in region ②, the incident shock wave perceives a lighter gas across the contact surface. In this case, a reflected rarefaction wave propagates into region ⑤ as seen in Fig. 2.7c and the shock tunnel is now undertailored. Schematics of these wave processes are shown in Figs. 2.2b and 2.3b respectively. Clearly, both these situations result in earlier disruption of the steady-state reservoir properties and, in turn, limit the overall time available for nozzle operation.

Though the above discussion assumed that the incident shock wave strength is constant, in the case of an under-driven downstream detonation tube, the primary shock wave will decelerate due to the transmitted Taylor rarefaction. In the worst case scenario, the Taylor rarefaction affects even the reflected shock wave as it travels back from the driven endwall. As this means that region ② is also affected by the Taylor rarefaction, neither region ② nor ⑤ possesses constant properties. Therefore, for the shock wave–contact surface interface, local values of acoustic impedances across the contact surface will determine the reflected wave type, still following the transmission criteria discussed above. These considerations may also illustrate the difficulty in estimating the wave processes for an under-driven downstream detonation tube operation, for instance. The gasdynamic processes described so far represent the dominant flow physics in all the impulse facilities. Thus, in subsequent chapters relevant features for a specific facility will be reiterated briefly to reinforce the reduced-order model development.

CHAPTER 3

DEVELOPMENT AND VALIDATION OF A CALORICALLY PERFECT DETONATION TUBE MODEL [1]

This chapter reports the preliminary feasiblity studies investigating the effectiveness of inverse MoC algorithms in resolving detonation-tube flowfields with non-negligible momentum and heat losses. Since this represents the initial phase of the overall research, the MoC subroutines utilized in the reduced-order model development here are based on existing algorithms available in the literature [49]. The modifications to these original algorithms are minimal, in that they are restricted to the investigation of simplified approaches that can capture losses in the a given flowfield. The development of a global detonation tube algorithm however, has been attempted from scratch here. As it may be obvious from the discussions so far, the development of such a detonation tube model requires more tools than just the MoC subroutines. Simplified calculations to capture the detonation wave dynamics, interactions between various discontinuities and endwall calculations are to be carried out alongside MoC subroutines. These approaches are detailed further in this chapter. Additionally, experiments were designed and carried out using a low enthalpy oxy-hydrogen detonation tube to validate the MoC model. This experimental campaign and the validation studies are also described in detail here.

[1] Includes excerpts from the paper entitled 'Method-of-Characteristics Model for a Low-Enthalpy, Detonation-Driven Shock Tube' by Jayamani, A., and Lu, F. K., Physics of Fluids, Vol. 34, No. 6, 2022. doi: 10.1063/5.0093888

3.1 Description of the theoretical model

This section details the theoretical considerations behind the MoC model for a downstream detonation tube. Briefly, the governing equations for a one-dimensional gas flow are simplified using MoC and the simplified equations are in turn used to develop various algorithms representing fundamental gasdynamic phenomena. These generic algorithms which are called unit processes, similar to the nomenclature of Zucrow and Hoffman [49] are then used to build a theoretical detonation tube model. Apart from the overall detonation tube algorithm, individual subsections are also devoted to the interactions not covered by MoC, for methods calculating sink terms associated with losses and about the applicability of the detonation tube model. Most of the underlying MoC analyses and algorithms detailed here are based on Zucrow and Hoffman [69, 49] and Gale [70].

3.1.1 Governing equations and method of characteristics formulation

The governing equations of continuity, momentum and energy for an unsteady, one-dimensional flow of a perfect gas in differential form are

$$\frac{\partial \rho}{\partial t} + u\frac{\partial \rho}{\partial x} + \rho\frac{\partial u}{\partial x} = 0 \tag{3.1a}$$

$$\rho\left(\frac{\partial u}{\partial t} + u\frac{\partial u}{\partial x}\right) + \frac{\partial p}{\partial x} = \frac{\delta F_{\mathsf{f}}}{V} \equiv \beta \tag{3.1b}$$

$$\rho\left(\frac{\partial h}{\partial t} + u\frac{\partial h}{\partial x}\right) - \left(\frac{\partial p}{\partial t} + u\frac{\partial p}{\partial x}\right) = \frac{\delta \dot{q}}{V} - u\beta \equiv \Psi \tag{3.1c}$$

In the above, the static pressure p, velocity u, density ρ and enthalpy h are functions of time t and one-dimensional space x. Since the effects of momentum and heat losses are of interest here, appropriate volumetric sink terms denoting such losses are added to the momentum and energy equations as $\delta F_{\mathsf{f}}/V$ and $\delta \dot{q}/V$ respectively. More details about these sink terms will be discussed in §3.1.3. The continuity equa-

tion, on the other hand, contains no sink term since the effect of mass addition or removal is not considered.

To make the system of equations tractable, the number of dependent variables are reduced by introducing the caloric equation of state. Assuming the fluid to be calorically perfect, the static enthalpy can be expressed as

$$dh = c_p dT \tag{3.2}$$

where c_p is the specific heat at constant pressure and T is the temperature. From the perfect gas law

$$p = \rho RT \tag{3.3}$$

where R is the gas constant, the energy equation is rewritten as

$$\frac{\partial p}{\partial t} + u\frac{\partial p}{\partial x} - a^2\left(\frac{\partial \rho}{\partial t} + u\frac{\partial \rho}{\partial x}\right) = (\gamma - 1)\Psi \equiv \psi \tag{3.4}$$

where γ is the specific heat ratio. With the above simplification, the governing equations now have three dependent variables p, ρ and u. Also, in Eq. (3.4), γ is a constant due to the calorically perfect gas assumption. However, a thermally perfect gas model can be incorporated by letting c_p vary as a function of temperature in Eq. (3.2). The only practical difference this will introduce into the energy equation and thereby the remainder of this method is that γ will not be a constant but a function of temperature. Obviously, T can be evaluated from the calculated dependent variables and perfect gas law.

Equations (5.1a), (5.1b) and (3.4) are first-order, quasi-linear partial differential equations with two independent variables x and t. The method of characteristics is applied on these equations reducing them to ODEs along certain curves called characteristic curves. However, the existence of the characteristic curves is not guaranteed. For instance, the governing equations for an irrotational, two-dimensional flow of a

compressible fluid admit real and distinct characteristics only when the flow is supersonic, whereas the characteristics are imaginary when the flow is subsonic [69]. Thus, it is first desirable to establish the existence of characteristic curves for this system. Following Zucrow and Hoffman [49], application of the MoC to the above equations results in the following characteristic curves

$$\left[\frac{dt}{dx}\right]_o = \lambda_o = \frac{1}{u} \tag{3.5a}$$

$$\left[\frac{dt}{dx}\right]_\pm = \lambda_\pm = \frac{1}{u \pm a} \tag{3.5b}$$

Therefore, unlike for the steady two-dimensional flow mentioned above, the characteristic curves for a one-dimensional unsteady flow are distinct and real for both subsonic and supersonic flows making the system hyperbolic.

From Eqs. (5.3a) and (5.3b), the physical interpretation of the characteristic curves, denoted as characteristics for short, are obtained. The first characteristic C_o, given by Eq. (5.3a), represents the motion of the gas and so is a pathline. The remaining characteristics $C_\pm$, given by Eq. (5.3b), are acoustic disturbances that propagate along and against the local fluid velocity, respectively. Analogous to the disturbances in a two-dimensional steady flow, these characteristics are called Mach lines. Further, as these three characteristics must pass through every point in a flowfield [49], it is deduced that every gas parcel adjusts to its surroundings based on the information it receives from the corresponding Mach lines reaching it at a specific time. Conversely, information about any perturbation that is caused by a gas parcel propagates in the form of Mach lines on either sides of the gas parcel. In the physical flow, these characteristics are merely two planar waves propagating in opposite directions from the source of the disturbance, namely, the gas parcel.

With the existence of the characteristic curves confirmed, the method of characteristics can further be carried out to reduce the governing equations to the form

$$\left[\frac{dp}{dx}\right]_o - a^2\left[\frac{d\rho}{dx}\right]_o = \frac{\psi}{u} \tag{3.6a}$$

$$\left[\frac{dp}{dt}\right]_\pm \pm \rho a\left[\frac{du}{dt}\right]_\pm = \psi \pm a\beta \tag{3.6b}$$

The above equations, called the compatibility equations, are valid along the characteristics noted in their subscripts. Thus, Eq. (5.2a) is valid along pathlines and Eq. (5.2b) is valid along Mach lines. Since the changes in a gas state can only happen across these characteristics, the variation of gas properties in a flowfield can be evaluated by integrating Eqs. (5.3a) and (5.2b) from a known initial condition. The only restrictions for using this method are that the dependent variables be continuous everywhere in the flowfield and that the prescribed initial value line itself is not a characteristic. While the latter condition is satisfied on the initial value line for an impulse facility, the former condition restricts this method to continuous regions. For a detonation tube where discontinuities are an inherent part of the gasdynamic processes, the above equations can still be utilized with supplementary considerations as detailed in the next section.

As a supplementary note, the compatibility equation for the pathline can be used to make an interesting observation for a downstream detonation tube flowfield. First, it is observed that the compatibility equation for the pathline, Eq. (5.2a), is the conservation of energy for every continuum parcel in the flowfield. This can be conveniently written as

$$\left[\frac{dp}{dt}\right]_o - a^2\left[\frac{d\rho}{dt}\right]_o = \psi \tag{3.7}$$

In its original form (see Eq. (3.4)), the above equation can be simplified for negligible momentum and heat losses as

$$\left[\frac{dh}{dt}\right]_o - \left[\frac{1}{\rho}\frac{dp}{dt}\right]_o = 0 \tag{3.8}$$

The above equation can again be re-interpreted based on the combined first and second laws of thermodynamics, which is given by

$$\left[\frac{dh}{dt}\right]_o = \left[T\frac{ds}{dt}\right]_o + \left[\frac{1}{\rho}\frac{dp}{dt}\right]_o \tag{3.9}$$

Comparing Eq. (3.8) and Eq. (3.9), it is seen that the compatibility equation for the pathline also represents the conservation of its entropy for this case.

Consider the case of a downstream detonation tube operating in the underdriven mode. Once the secondary diaphragm ruptures, the burnt driver gas expands into the driven section, resulting in the formation of a shock wave (SW_1) in the driven section (see Fig. 2.3b). Since the detonation driver is underdriven, the Taylor rarefaction has not been completely annihilated by the expanding high pressure driver gas. In other words, the burnt gas in the detonation driver is not of a constant gasdynamic state. Thus, shock wave (SW_1) decays as it travels in the driven section, due to the positive pressure and velocity gradient in the driver gas at a given instant. This process is shown in the wave diagrams as transmission of the Taylor rarefaction into the driven section. Since the energy acquired by the driven gas is dictated by the velocity of shock wave (SW_1), a decaying driven shock will impart lesser energy to the testgas as it travels in the driven section. Additionally, from normal shock relations [5], the change in entropy across a normal shock increases with its velocity. Thus, every testgas pathline must have a different entropy behind the decaying shock wave (SW_1). But, from Eq. (3.9) , for a flowfield with no losses, the entropy must be conserved along every pathline. Thus, in an underdriven detonation tube flowfield with no losses,

testgas pathlines behind the decaying shock wave (SW_1) will have differing entropies between themselves. But, the entropy along a given testgas pathline is conserved from the time it was compressed by the shock wave until its re-compression by the reflected shock wave. In this work, such a flowfield will be referred to as a multi-isentropic flowfield.

3.1.2 Unit processes for fundamental gasdynamic phenomena

The ODEs derived in the last section through the method of characteristics can be integrated by a time-marching scheme typical of hyperbolic equations. The scheme employed in this work is known as the inverse-marching method, named after the way the characteristic curves are projected from a later point in time to an initial value line during the integration. An alternative scheme, called the direct-marching method of characteristics, or direct MoC for short, involves projecting two characteristics forward in time, while the remaining characteristic is projected backward in time. The inverse marching method of characteristics scheme, or IMoC, utilizes a predefined x–t grid where the solution to the ODEs is obtained. On the other hand, the solution grid-space for direct MoC is determined as a part of the iteration procedure itself. Therefore, based on the sparsity of characteristics in a locality, additional grid points will have to be introduced or removed from the x–t space. Between these methods, direct MoC is expected to be more accurate than inverse MoC due to the way backward projected characteristics are resolved [49]. However, in the author's opinion, compared to direct MoC, IMoC is easier to implement for a variety of problems. Additionally, previous studies show [55, 56] that despite the theoretical claims of reduced accuracy, IMoC schemes still model experiments reliably.

Within the direct MoC scheme, specific integration procedure depends on the fundamental gasdynamic phenomena considered, as different independent algorithms

are developed by incorporating appropriate flow physics into the general ODEs. Though the current work utilizes such individual algorithms to model impulse facilities, by no means are these algorithms restricted to the application shown here. Subsequent chapters will exemplify the previous statement by utilizing IMoC algorithms to model supersonic combustion in a one-dimensional duct, chemical non-equilibrium in a hypersonic nozzle expansion and behind a steady normal shock wave or thermochemical non-equilibrium in an expansion tube. Thus, the individual algorithms reported in this section are generic flow solvers which can be called to solve a particular gasdynamic problem. These IMoC algorithms, called unit processes [49], can be grouped under two categories: continuous waves and discontinuous waves. Continuous wave unit processes discussed here can model rarefaction and weak compression waves, and continuous waves reaching an endwall. Discontinuous wave unit processes account for shock waves and contact surfaces. The selection of unit processes for algorithm development in this study reflects the expected wave processes in a detonation tube (see §2.2), with the exclusion of the detonation wave. Obviously, a calorically perfect gas model cannot be expected to capture the chemical reactions behind a shock wave, which represents the simplest interpretation of a detonation wave. The incorporation of a detonation wave into the detonation tube model is discussed in §3.1.5, while this section discusses the algorithms for various unit processes.

3.1.2.1 Continuous waves

Continuous waves which represent the largest component of waves in an impulse facility operation can be modeled through the interior point and wall point solvers. The characteristics for both these processes are shown schematically in Fig. 3.1. In all the unit processes described here, the coordinates of all the grid points are assumed to be known. Additionally, along the grid points in the initial value

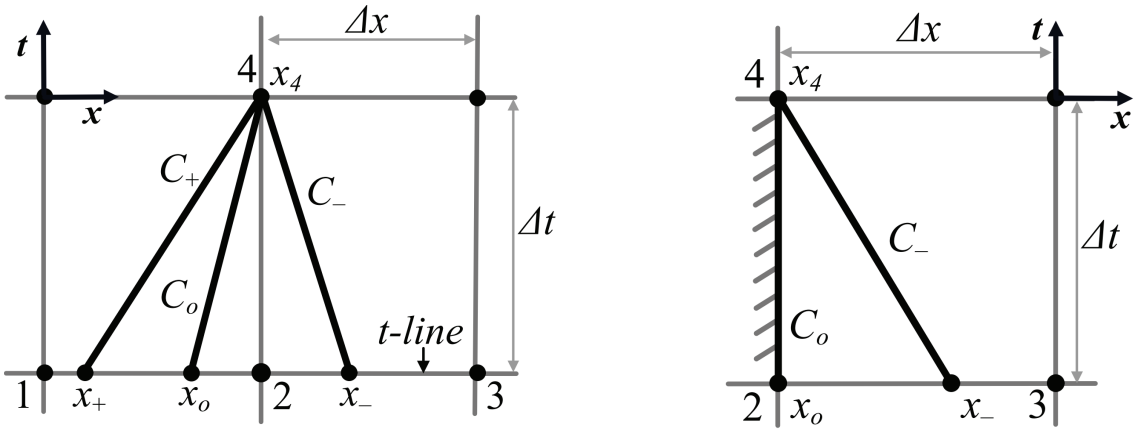

(a) Interior point (b) Wall point.

Figure 3.1: Discretization methodology for continuous waves.

line marked t-line in Fig. 3.1a, all the dependent variables are also assumed to be known. Linear interpolation is used when the initial values of the dependent variables are required at regions in between the grid points. For this linear interpolation to be meaningful, the characteristic curves projected from location 4 must intercept the t-line between grid points 1 and 3, see Fig. 3.1a. This is ensured if the spatial and temporal grid spacing are governed by the Courant–Friedrichs–Lewy criterion [49], that is, $\Delta t(u \pm a)_{max} < \Delta x$. Even though the unit process schematics depict the characteristics as straight lines, these are approximations to the actual characteristics that may not be straight, for instance, in non-simple regions. Still, for a sufficiently small grid spacing the straight line approximation should approach such curvilinear characteristics. Finally, the integration along these characteristic curves is carried out using the Euler predictor–corrector method for all the unit processes discussed hereafter.

A relatively straight forward implementation of this integration method is the interior point solver which is discussed first. Since the integration is carried out

numerically, the finite-difference formulation of the simplified ODEs is given below to aid the discussion:

$$(x_4 - x_o) = \frac{1}{\lambda_o}\,\Delta t \tag{3.10a}$$

$$(x_4 - x_\pm) = \frac{1}{\lambda_\pm}\,\Delta t \tag{3.10b}$$

$$(p_4 - p_o) - a^2(\rho_4 - \rho_o) = \frac{\psi}{u}(x_4 - x_o) \tag{3.10c}$$

$$(p_4 - p_\pm) \pm \rho a\,(u_4 - u_\pm) = (\psi \pm a\beta)\,\Delta t \tag{3.10d}$$

The subscripts for Δt in the above equations have been removed as unnecessary since $\Delta t_o = \Delta t_\pm = \Delta t$ due to the way the x–t grid is defined. The integration procedure for the above equations starts with the predictor step. Referring to Fig. 3.1a, let the initial value line span across points 1, 2 and 3, and let grid point 4 be the location at which the flow properties need to be computed. Assuming that the local region is devoid of discontinuities, all three types of characteristics can be expected to intersect at location 4 as shown in Fig. 3.1a. Thus, the first step of the integration procedure is to identify these characteristics intersecting at location 4. Once these are identified and their origin located on the initial value line, simultaneous integration of the compatibility equations yields the dependent variables at location 4.

To illustrate the procedure, consider integrating along the C_+ characteristic seen in Fig. 3.1a. This requires information about its slope λ_+, as inferred from the characteristic equation given by Eq. (5.4b). However, since this characteristic itself is unknown initially, assume that the slope of the C_+ characteristic at location 4 is the same as that at grid point 1. Now, utilizing Eq. (5.4b), the C_+ characteristic can be projected back in time from location 4 to the initial value line 1–2, intersecting it at x_+. With the new origin identified, the slope of the C_+ characteristic is updated and the characteristic is projected back to the initial value line until the location of

x_+ converges. Note again that the dependent variables are assumed to be known only at the grid points 1, 2 and 3. Thus, the values of all the dependent variables at the location x_+ are determined by linear interpolation between grid points 1 and 2 during every iteration. In Eqs. (5.4a)–(5.4d), these interpolated initial values are denoted by adding relevant subscripts to the dependent variables. Once the value of C_+ is determined, a similar procedure is undertaken for identifying relevant C_o and C_- characteristics intersecting at location 4. Of course, appropriate characteristic equations need to be used for integrating along C_o and C_- characteristics, along with the interpolating grid changing between 1–2 and 2–3 based on their origins, x_o and x_- respectively. Finally, to complete the predictor step, the information obtained about all the characteristic curves are utilized to solve the compatibility equations (5.4c) and (5.4d), producing the values of all dependent variables at location 4.

The following corrector step is similar in procedure to the predictor step. The only difference in the scheme is that the slope of the characteristic curves are evaluated based on average flow properties on the characteristic curves, as the dependent variables are known at location 4 now. Similarly, the sink terms and the coefficients of the derivatives in the compatibility equations are also evaluated using averaged properties along the characteristic curves. Subsequently, the corrector step is repeated until all the dependent variables reach a specified tolerance, upon which the algorithm returns the values at location 4.

The unit process for the interior point discussed above represents the generic algorithm for continuous regions. Likewise, other unit processes can be obtained by either simplifying or adding additional criteria to the interior point algorithm. In the case of the unit process for a wall point, simplifications as discussed further are employed. The schematic of characteristics for a left wall point is shown in Fig. 3.1b. Due to the no-flow condition, the gas parcel which was on the wall initially stays on the

wall as shown by the pathline; its velocity remains zero. Further, as the domain ends with the gas parcel that is in contact with the left wall, the C_+ characteristic vanishes. This removes the characteristic and compatibility equations corresponding to the C_+ characteristic. Also, since the velocity of the gas parcel is already known at location 4, only the C_- characteristic in Eq. (5.4b) needs to be evaluated. The remaining dependent variables p and ρ can merely be evaluated by solving the compatibility equations for C_o and C_- characteristics. Again, to integrate these reduced governing equations, the iterative Euler predictor–corrector method described for the interior point solver is followed. For a right endwall, the C_- characteristic vanishes instead of the C_+ seen above, while the remaining arguments and integration procedure remain the same as a left endwall.

3.1.2.2 Discontinuous waves

In contrast to the the continuous waves discussed so far, discontinuous wave processes cannot be directly modeled through MoC alone, as at least one of the dependent variables experiences a jump across discontinuities. However, the regions on either sides of a discontinuity can be treated through MoC separately and both the regions can be connected through supplementary criteria, described subsequently. Additionally, even though the discontinuities are again solved on a predetermined x–t grid, their motion cannot be expected to coincide with the grid points. Thus, the algorithms for discontinuities differ slightly from the continuous unit processes.

The simplest discontinuous wave process that can be modeled through MoC is the contact surface. By definition, a contact surface is an ideal interface between two different gas states across which static pressure and velocity are continuous, but other thermodynamic properties may be discontinuous. For inviscid flow, the effect of diffusion and mixing is neglected, resulting in a planar interface, across which no mass

flows. Thus, the contact surface itself becomes a pathline, as shown in the schematic for the contact surface unit process in Fig. 3.2a. At any given time in the x–t grid, the contact surface has two sides marked by subscripts l and r signifying left and right sides of the contact surface. The supplementary criteria in this case are provided by the definition $p_l = p_r = p$ and $u_l = u_r = u$. Clearly, the remaining properties on either side of the contact surface can be different and therefore retain their subscripts. It is assumed that the initial values of the gas properties are known at locations 1, 2 and 3. While locations 1 and 3 are predefined grid points, location 2 represents the initial position of the contact surface. Similar to the convention for continuous waves, the location of contact surface at the next time line (t-line) is denoted as 4. But, as opposed to continuous wave unit processes, x_4 is initially unknown here and must be determined as a part of the contact surface unit process. For convenience, the finite-difference formulation of the simplified ODEs is rewritten for a contact surface

$$(x_4 - x_2) = \frac{1}{\lambda_o}\,\Delta t \tag{3.11a}$$

$$(x_4 - x_\pm) = \frac{1}{\lambda_\pm}\,\Delta t \tag{3.11b}$$

$$(p_4 - p_2) - a_l^2(\rho_{4l} - \rho_{2l}) = \frac{\psi_l}{u}(x_4 - x_2) \tag{3.11c}$$

$$(p_4 - p_2) - a_r^2(\rho_{4r} - \rho_{2r}) = \frac{\psi_r}{u}(x_4 - x_2) \tag{3.11d}$$

$$(p_4 - p_\pm) \pm \rho a\,(u_4 - u_\pm) = (\psi \pm a\beta)\,\Delta t \tag{3.11e}$$

The compatibility equation for a pathline has been split into the left and right sides, as seen in Eqs. (3.11c) and (3.11d), which is unlike that for the continuous wave, Eq. (5.4c). With the condition that pressure and velocity be continuous across the contact surface, the other equations are essentially the same as that of the interior point unit process. For the predictor step, location 4 is first identified by projecting

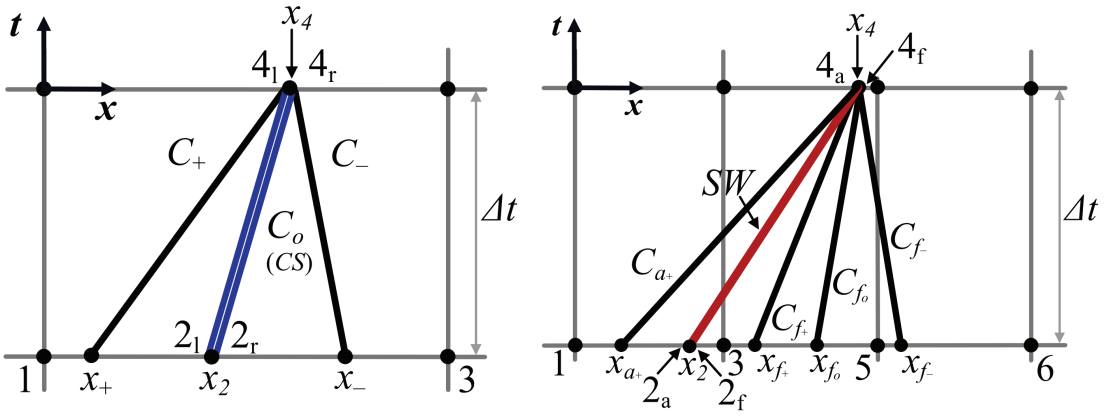

(a) Contact surface. (b) Shock wave.

Figure 3.2: Discretization methodology for discontinuous waves.

the contact surface to the next t-line using Eq. (3.11a) and assuming that $u_2 = u_4$. With location 4 identified, the algorithm for Mach lines can now follow the same procedure discussed for an interior point unit process. The only additional procedure for the Mach lines is that while determining their origin, the interpolation procedures must take into account the distinct gas properties at 2_l and 2_r.

As seen from the above, the method of identifying various characteristics in the contact surface unit process differs slightly from the interior point unit process. In this case, the pathline, that is, the contact surface is projected forward in time, but the Mach lines are projected backward in time from the new location of the contact surface. On the other hand, in the interior point algorithm, all the characteristics are projected backward in time. After identifying all the characteristics, the compatibility equations for Mach lines given by Eq. (3.11e) are used to solve for p_4 and u_4. These values in turn are used to solve for ρ_{4l} and ρ_{4r} with the aid of compatibility equations (3.11c) and (3.11d). This completes the predictor step and leads to the iterative corrector steps. Similar to the interior point unit process, the corrector algorithm here uses average properties for various terms in the finite difference equations, namely,

the slopes of the characteristics, sink terms and coefficients of the difference terms. Again, the calculations for these average properties must also appropriately consider the differing properties across the contact surface at locations 2 and 4. Since the final location of the contact surface x_4 was initially unknown, the convergence criteria in this case also include x_4, in addition to the dependent variables.

The unit process for a shock wave is similar to that of a contact surface. Figure 3.2b is a schematic of the shock wave unit process, showing the continuous waves ahead and aft of the propagating shock wave. The wave system depicted follows the general rules for a propagating shock wave, that is, the shock will overtake all continuous waves ahead of it and will be overtaken by the characteristic that travels along its direction of motion. To emphasize that the waves ahead and aft of the shock wave are treated as separate wave systems, the subscripts f and a are added to the respective characteristic systems. Ahead of the shock wave, three grid points define the required initial value line, given by points 3, 5 and 6. The shock wave itself is at location 2 on the initial t-line, but the discontinuous flow properties across the shock wave necessitate the nomenclature 2_f and 2_a to denote the appropriate fluid properties on either side. As with the previous algorithms, the new location of the shock wave is marked as x_4.

Behind the shock wave, the initial value line is extended to include another grid point, location 1, to account for the overtaking C_+ characteristic. The algorithm begins by estimating x_4 using the initial values of the shock wave velocity and position. Since the shock wave overtakes all the characteristics ahead of it at the next t-line, the state of the fluid immediately ahead of the shock wave 4_f is merely obtained by using the interior point unit process. The inputs required for the interior point unit process which are the fluid properties at grid points 3, 5 and 6, along with the location of final solution point, 4 are all known. The results from the interior point

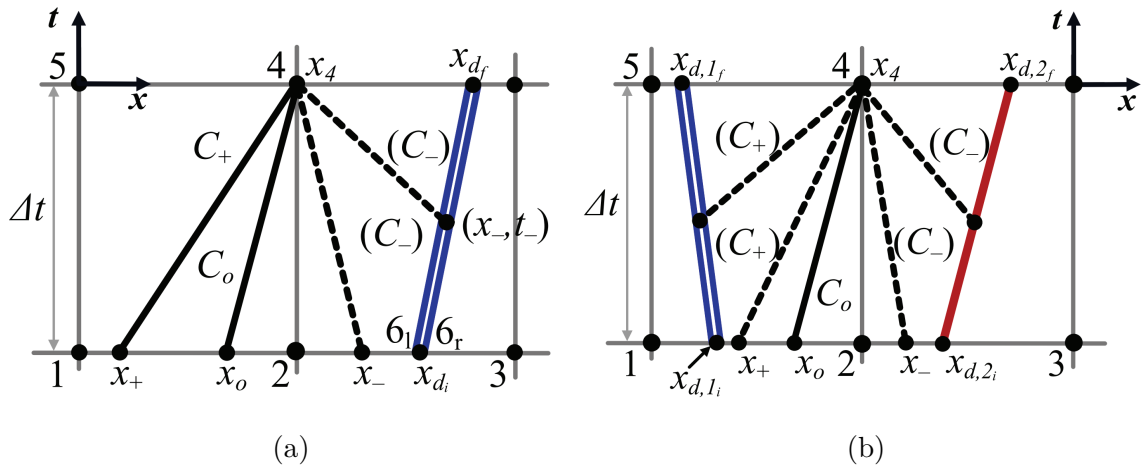

Figure 3.3: Unit process for a grid point with (a) a nearby discontinuity, (b) surrounding discontinuities.

unit process along with the shock velocity at location 4 are then used to obtain post-shock fluid properties 4_a using the Galilean transformation and the Rankine–Hugoniot conditions.

The C_{a_+} characteristic that meets the shock wave at location 4 must now be identified. As before, the initial guess for the origin of the C_{a_+} characteristic is taken to be the adjacent grid point, location 1. However, the slope of the C_{a_+} characteristic can employ average properties of fluid and sonic velocities along the characteristic from the first integration step since the fluid properties at 4_a are already known. Further, using the calculated slope, the C_{a_+} characteristic is projected from location 4_a, to the initial value line to find its updated origin. This process of inverse marching is repeated until the origin of the C_{a_+} characteristic converges. Finally, based on the flow properties at the origin of the C_{a_+} characteristic and using the post-shock fluid velocity at 4_a, the compatibility Eq. (5.4d) is solved to obtain the static pressure at location 4_a. From physical reasoning, the C_{a_+} characteristic carries information about the flowfield behind the shock wave, to which the shock wave must adapt.

Therefore, as the shock wave adapts to this information, the post-shock static pressure must match the value of static pressure computed through the C_{a_+} compatibility equation. Hence, the static pressures p_{4_a} obtained through both these methods are compared and the shock velocity is in turn adjusted, so that the next iteration may begin. For subsequent iterations, the entire process described above is repeated using updated shock velocities until the static pressures from the Rankine–Hugonoit and C_{a_+} compatibility equations converge. Obviously, the convergence of static pressures between both these methods provides the supplementary criterion bridging either side of the shock wave.

The procedure described above and the schematic in Fig. 3.2b correspond to a right-running shock wave. For a left-running shock wave, the regions ahead and aft of the shock wave in Fig. 3.2b are interchanged. While the wave system ahead of the left-running shock wave is identical to the forward region in Fig. 3.2b, the associated trailing characteristic will be C_{a_-} instead of the C_{a_+} characteristic shown in Fig. 3.2b. Hence, the unit process for a left-running shock wave follows the same algorithm as a right-running shock wave, but with the relevant characteristic and compatibility equations for the trailing C_{a_-} characteristic.

The IMoC algorithms discussed so far were developed with the intent of representing various gasdynamic processes. The implementation of these algorithms over a predefined grid, however, results in a specific scenario which cannot be solved by these algorithms. Consider the scenario in Fig. 3.3a, where a contact surface is moving through the predefined x–t grid. If there are no discontinuities in the nearby grid points, the movement of the contact surface can be modeled by the contact surface unit process described above. However, the grid point marked 4 may not be represented by the interior point solver because the C_- characteristic may not originate on the initial value line, but instead on the nearby contact surface. To account for

this possibility, a modified interior point solver has been developed, which is depicted in Fig. 3.3a. Prior to calling this algorithm, the nearby contact surface motion must be resolved for this time-step, so that the contact surface's final location x_{d_f} along with the fluid properties at this final location are known. For the scenario shown in Fig. 3.3a, the gas velocity is positive and the region to the left of the contact surface is subsonic. Thus, the calculations for the C_+ and C_o characteristics are identical to the interior point solver because their origin is expected to be on the line segment 1–2, similar to the interior point solver.

Due to the ambiguity in identifying the origin of the C_- characteristic, the interior point solver is modified as follows. Noting that the C_- characteristic may originate from either of the two line segments 2–x_{d_i} or x_{d_i}–x_{d_f}, the initial guess for λ_- is based on the gas properties at 6_l. Subsequently, using Eq. 5.4b the C_- characteristic is projected back from location 4. If the projected origin x_- lies between locations 2 and x_{d_i}, then the interpolation procedure for fluid properties is similar to the interior point solver. However, if $x_- > x_{d_i}$, then the intersection of C_- characteristic and the contact surface can be solved using rudimentary geometry, as both λ_- and u_{CS} are known. Once the coordinates of the intersection (x_-,t_-) are calculated, the gas properties at this location can be obtained through interpolation along the trajectory of the contact surface $x_{d_i} - x_{d_f}$. Finally, the compatibility Eq. (5.4d) can be populated using the characteristic origin (x_-,t_-) and the corresponding gas properties obtained during interpolation. The remaining procedure to solve the compatibility equations as well as the subsequent iterative procedure follows the predictor–corrector algorithm outlined for the interior point solver. Though Fig. 3.3a shows the discontinuity as a contact surface, the same unit process can also be applied to a shock wave. Additionally, a similar algorithm can developed to resolve a grid point which lies to the right of a discontinuity. In this case, the C_+ characteristic may be expected to originate from

the discontinuity and thus its integration procedure employs the modified method described above.

Another scenario to be considered in a detonation tube model is that a grid point may lie in between two discontinuities as shown in Fig. 3.3b. This can be expected when a contact surface interacts with a shock wave or when two shock waves interact. When such a scenario is encountered, the modified integration procedure discussed above can be used for multiple characteristics in a manner shown in Fig. 3.3b. The type of discontinuities shown and their direction of propagation in Fig. 3.3b are representative. Either of the discontinuities may be of a different type and/or they might move in a different direction. As long as the trajectory of the discontinuities have been resolved and therefore appropriate gas properties along the sides facing location 4 are known, the unit process described above can be employed to calculate the gas properties at location 4.

As a side note, it may be recognized that this algorithm violates one of the initial assumptions, that is, the initial value line must not be a characteristic. Such a restriction allowed the initial value data for any unit process to be specified arbitrarily. However, if the initial value data are specified on a characteristic, then the data cannot be arbitrary. Instead, the data must satisfy the corresponding compatibility equations on the characteristic [71]. This requirement is always satisfied here since the trajectories for the discontinuities themselves are resolved using the required compatibility equations.

3.1.3 Momentum and heat losses

The treatment of sink terms declared in the momentum and energy equations in §3.1 brings in unavoidable empiricism into the MoC model. For the detonation tube model considered here, these losses are expected to be driven by wall friction

and convective heat transfer at the tube walls. Given that the current model is one-dimensional, the physical mechanisms that cause these losses cannot be modeled physically. Moreover, some of the mechanisms such as the unsteady growth of the boundary layer and its interaction with the detonation cells are still subjects of current research [72]. Thus, the effect of these loss mechanisms are included in the model through empirical methods as described below.

In the order of the governing equations, consider the sink term in the momentum Eq. (5.1b). From the definition of the coefficient of friction C_f, the tangential force that retards the local fluid motion is given by

$$\delta F_\mathsf{f} = -\frac{C_\mathsf{f}}{2}\rho u|u|A_p dx \tag{3.12}$$

where A_p is the wetted perimeter. Thus, the volumetric momentum sink term in Eq. (5.1b) becomes

$$\beta = -\frac{1}{2}\rho u|u|\frac{4C_\mathsf{f}}{D} \tag{3.13}$$

where D is the diameter of the tube.

Noting that Eq. (3.12) is also the standard Fanning equation used in hydraulic engineering [69], experimental friction factor curvefits can be used to account for this sink term. Though the literature shows that similar impulse facility models use different curves to calculate the friction factor for different flow regimes [73, 74, 75, 76, 44], this work uses an integrated friction factor equation for concise programming. The equation below is due to Cheng [77], whose work uses Nikuradse's experimental data [78]:

$$\frac{1}{4C_\mathsf{f}} = \left(\frac{Re}{64}\right)^{\alpha}\left(1.8\log\frac{Re}{6.8}\right)^{2(1-\alpha)\beta}\left(2\log\frac{3.7D}{\epsilon}\right)^{2(1-\alpha)(1-\beta)} \tag{3.14}$$

where Re is the Reynolds number based on pipe diameter, ϵ is the equivalent sand grain roughness and

$$\alpha = \frac{1}{1 + (Re/2720)^9} \quad \text{and} \quad \beta = \frac{1}{1 + [Re/(160D/\epsilon)]^2}$$

Cheng's [77] original equation, which was written for the Darcy friction factor, has been adjusted for the Fanning friction factor considered in Eq. (3.12). Additionally, as Nikuradse's [78] experiments were performed with water, to account for compressibility effects, C_f obtained through the above equation is multiplied by a correction factor utilized by Liepmann and Goddard [79] and Goddard [80] expressed as

$$\Gamma = \left[1 + r\frac{(\gamma - 1)}{2}M^2\right]^{-1} \tag{3.15}$$

The recovery factor r in the above equation is approximated based on the solutions for compressible boundary layer on a flate plate [81, 82].

$$r = \begin{cases} \sqrt{Pr_L} & Re < 2000 \\ \sqrt[3]{Pr_L} & Re \geq 2000 \end{cases} \tag{3.16}$$

where $Pr_L = \mu c_p/k$ is the laminar Prandtl number. Despite the use of the laminar Prandtl number, the above approximation for the turbulent recovery factor represents experimental data to a reasonable accuracy [82] and is accepted practice [83, 74, 75, 76].

Consider next the heat loss term in the energy Eq. (5.1c). Using Reynolds analogy and the modified Newton's law of cooling, the local heat loss rate from the hot gas to the cold tube wall can be written as

$$\delta\dot{q} = C_h \rho u c_p (T_w - T_0) \tag{3.17}$$

where the heat transfer coefficient is given by

$$C_h = \frac{C_\mathsf{f}}{2\mathcal{S}} \tag{3.18}$$

and where $\mathcal{S}$ is the Reynolds analogy factor. The subscripts w and 0 represent wall and stagnation conditions respectively. The heat transfer coefficient can be approximated in two different ways which lead to two different heat loss models. If the original Reynolds analogy is to be followed, then, $\mathcal{S} = 1$. However, if the modified Reynolds analogy proposed by Colburn is considered, then $\mathcal{S} = Pr_L^{2/3}$ [81, 82]. The heat loss term in the energy equation can be written as

$$\frac{\delta \dot{q}}{V} = \frac{4C_h}{D} \rho u c_p (T_w - T_0) \tag{3.19}$$

The stagnation temperature in the above equation also takes into account the recovery factor r. Thus,

$$T_0 = T \left(1 + r \frac{\gamma - 1}{2} M^2 \right) \tag{3.20}$$

As an additional option, Eckert's reference temperature method can be incorporated into the frictional and heat losses calculations described above [83]. To do so, the local gas density and transport properties for the loss calculations are evaluated at a reference temperature

$$T^* = T + 0.5(T_w - T) + 0.22(T_0 - T) \tag{3.21}$$

Note that these updated values are only applicable specifically to the losses calculation, whereas the origins of the characteristic and compatibility equations employ appropriate local properties obtained through the interpolation procedure described previously.

The empirical methods discussed above for approximating heat losses were initially derived for laminar boundary layers on a flat plate, under zero pressure gradient. Still, these have been reliably used to model losses suffered by unsteady gas flows. Wilson et al. successfully modeled several operational conditions of a magnetohydrodynamic generator using a hybrid Lax-Wendroff/MoC model [73]. In their model, friction factor, and thereby frictional losses, was evaluated through Hagen–Poiseuille and

Colebrook–White equations, while heat losses were approximated through Reynolds analogy. Groth et al. modeled frictional losses in a piston tunnel based on friction factors from the Hagen–Poiseuille relation and an explicit approximation to the Colebrook–White equation [74]. Heat losses were modeled using modified Reynolds analogy. To account for the losses due to obstructions in the flow path, pressure head losses were also included. Jacobs used a similar losses model to that of Groth et al. in the L1d code to model shock tubes and free piston tunnels [75, 76]. As opposed to Groth et al., L1d assumes a smooth wall in the friction factor equations for turbulent flow regime. Additionally, L1d also incorporates Eckert's reference temperature method into the calculations for heat losses. Luo et al. modeled heat losses in an upstream-mode detonation tube using an approach similar to L1d [44]. They reported that the frictional losses model, when approximated through a smooth wall friction factor, did not replicate the shock velocities observed in their experiments. Thus, they corrected the sink term in the momentum equation using an arbitrary factor, adjusting which produced shock velocities closer to experiments. In this work, instead of utilizing an additional correction factor to the momentum sink term, the pipe wall roughness ϵ has been used as the free parameter to aid replication of experimental shock velocities. Moreover, as the literature points to a variety of heat losses models providing reasonable results, any of the above described models can be selected independently in this code (See §3.3).

3.1.4 Non-MoC analyses

Though a majority of the detonation tube gasdynamics can be accounted for through the MoC unit processes, certain isolated situations exist which require supplementary analyses. The first of these exceptions is to determine the properties of a freely propagating detonation wave. As the MoC unit processes are limited to a

calorically perfect gas, the Shock and Detonation Toolbox (SDT) [84] (which itself requires the Cantera package [85]) is used to calculate the detonation wave velocity and the associated CJ state properties. Subsequently, Cantera is used to generate curvefits of the dynamic viscosity of the burnt gas, with the composition held fixed at the CJ state. A previous version [63] of this model utilized the NASA CEA [86, 87] for calculating CJ detonation wave properties; however, this was replaced by the SDT due to the relative ease of Cantera's MATLAB integration and also for obtaining thermochemically frozen gas properties at the CJ state.

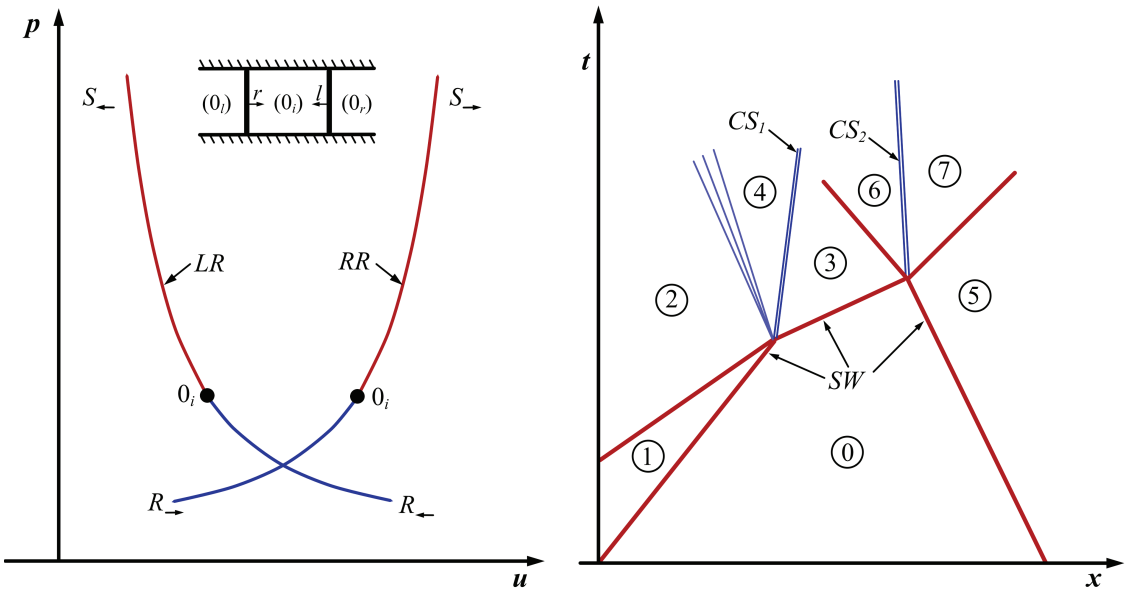

Figure 3.4: Representation of interacting discontinuities – (a) Wave polar, (b) Space-time.

Further analyses described here are in regard to the interaction between discontinuities. These situations may be the interaction between two shock waves or that between a shock wave and a contact surface. All these interactions can be solved graphically in the pressure–velocity diagram shown previously in Fig. 2.4. In view

of its similarity to the shock polar diagram, the pressure–velocity diagram will be subsequently called the wave polar diagram, as it depicts the loci pertaining to the gasdynamics of normal shocks as well as rarefaction waves.

For numerical implementation of the wave polar diagram, algebraic equations representing the loci for shock waves or rarefaction waves are utilized to resolve the outcome of a typical interaction. The approach presented here closely follows Courant and Friedrichs [47]. As a prequisite, consider the schematic of wave propagation in a duct shown in Fig. 3.4a. The waves marked by l and r represent generic left and right traveling waves respectively, which can be either shock or rarefaction waves. For a left traveling wave, the locus curves of all possible states achievable from an initial state i are represented by the curve LR. To differentiate between the wave types, the shock wave locus is shown in red, while the locus for a rarefaction wave is shown in blue. The locus curves LR are written as

$$u = u_i - \xi_i(p),\ p > p_i \quad (S_{\leftarrow}) \tag{3.22a}$$

$$u = u_i - \zeta_i(p),\ p < p_i \quad (R_{\leftarrow}) \tag{3.22b}$$

where

$$\xi_i(p) = (p - p_i)\sqrt{\frac{2}{\rho_i[(\gamma+1)p + (\gamma-1)p_i]}} \tag{3.22c}$$

and

$$\zeta_i(p) = \frac{2a_i}{\gamma - 1}\left[\left(\frac{p}{p_i}\right)^{(\gamma-1)/2\gamma} - 1\right] \tag{3.22d}$$

Similarly, the locus RR, which represents the possible states achievable behind a right traveling wave, is written as

$$u = u_i + \xi_i(p), p > p_i \quad (S_{\rightarrow}) \tag{3.23a}$$

$$u = u_i + \zeta_i(p), p < p_i \quad (R_{\rightarrow}) \tag{3.23b}$$

Obviously, post-shock pressures are always higher than the initial pressures, while post-expansion pressures are lower, as seen in the different branches of the curves LR and RR. Additionally, if the initial gas velocity is zero, a gas processed by a shock wave travels in the same direction as the shock wave. On the other hand, a gas processed by a rarefaction wave travels in the opposite direction to that of the rarefaction wave.

As a first example, consider the rupture of the primary diaphragm discussed in §2.2.1 and shown in Fig. 2.3b. As the diaphragm ruptures, the primary rarefaction which is a left running wave processes the driver gas, while the Taylor rarefaction which is a right running wave, processes the burnt gas from the CJ state. When the gases on either side of the primary contact surface reach gasdynamic equilibrium, $u_{CS_1} = u_{300} = u_{200}$. Thus, the wave polar analysis results in the following condition at the primary contact surface

$$u_{CS_1} = u_4 - \zeta_4(p_{CS_1}) = u_{CJ} + \zeta_{CJ}(p_{CS_1}) \tag{3.24}$$

The above condition can be solved using a root finding algorithm to obtain p_{CS_1}, which in turn can be used to find all the other gasdynamic properties using isentropic relations.

Consider the interaction between the reflected shock wave and the secondary contact surface in the driven section, shown in Fig. 2.3b. In the vicinity of the interaction, let the gas behind the reflected shock wave be represented by state 5, while the gas on either side of the contact surface be represented by states 2 and 3, as shown in Fig. 2.3b. The outcome of this interaction as discussed before causes a transmitted shock wave into the detonation driver and a reflected rarefaction wave into the driven gas. Thus, the burnt gas in state 3 is processed by a left-moving shock wave, while the driven gas in state 5 is processed by a right-moving rarefaction wave,

finally achieving local gasdynamic equilibrium across the secondary contact surface $u_{CS_2} = u_6 = u_7$. In the wave polar analysis, this outcome is expressed as

$$u_{CS_2} = u_3 - \xi_3(p_{CS_2}) = u_5 + \zeta_5(p_{CS_2}) \tag{3.25}$$

Once the above equation is solved for the local values of static pressure and gas velocity, state 6 can be calculated using normal shock relations on state 3. Properties for state 7, on the other hand, are obtained from state 5 using isentropic relations. It was discussed before (see Fig. 2.2b and §2.2.3) that the shock wave–contact surface interaction can also result in a situation where both the transmitted and reflected waves are shock waves. Such an outcome is governed by the following condition

$$u_{CS_2} = u_3 - \xi_3(p_{CS_2}) = u_5 + \xi_5(p_{CS_2}) \tag{3.26}$$

The above shock wave–contact surface analysis can also be applied to the transmission of a detonation wave into a shock wave in the driven section. Since the detonation wave is treated as a planar discontinuity in this study, the CJ condition is used to set up the function $\zeta_i(p)$ representing the initial state from which the burnt gas expands and drives the initial shock wave into the driven section.

Finally, consider the interaction between shock waves as shown Fig. 3.4b. First, when two colliding shock waves are of opposing directions, transmitted shock waves emerge on either side and a contact surface originates at the location of collision, emphasizing the discontinuous entropy change due to differing shock strengths. This interaction marked by regions 0–3–6–7–5 in Fig. 3.4b is again given by Eq. (3.26). Note that the wave polar for the shock wave–contact surface interaction might have differing specific heat ratios across the contact surface, while the wave polar for the case of interacting shock waves in the same medium will have the same specific heat ratio. In the second case where the colliding shock waves are of the same direction,

with $\gamma \leq 5/3$, a transmitted shock and a reflected weak rarefaction occurs [47]. Again, to separate regions of differing entropies, a contact surface originates at the location of interaction. From the appropriate wave polar analysis, this interaction is described by

$$u_{CS_1} = u_2 - \zeta_2(p_{CS_1}) = u_0 + \xi_0(p_{CS_1}) \tag{3.27}$$

3.1.5 Detonation tube model

The MoC unit processes and the supplementary analyses described in the previous sections are now used to develop a detonation-tube model, Fig. 3.5a. The algorithm used for the MoC model is shown diagrammatically in Fig. 3.5b, with each line representing an MoC unit process, while the numbered locations indicate wave polar analysis. Additionally, the regions displayed as white space, which may contain continuous waves, employ the interior point algorithm. The detonation tube algorithm begins by reading the input file from the user, which contains the initial conditions for the high-pressure driver, detonation driver and driven sections along with the geometry of the facility. First, the ZND subroutine in Shock and Detonation Toolbox [85] is called to obtain the CJ state where chemical reactions reach completion behind the detonation wave. For subsequent MoC calculations of the burnt gas, its chemical composition and vibrational excitation levels are frozen at their corresponding CJ state properties. Thus, the burnt gas γ and specific gas constant also remain fixed at their respective CJ state values for calorically perfect MoC unit processes. Further, the evaluated CJ state along with the high-pressure driver initial conditions are utilized in the wave polar analysis to obtain gas properties on either side of the primary contact surface. This serves as the starting solution to the overall MoC procedure, as represented by the wave polar analysis marked 1 in Fig. 3.5b. At

this point, the entire flowfield contains two discontinuities, the detonation wave and the primary contact surface, which are dealt with first for a given t-line.

Based on the ideal wave processes described in §2.2.1, the detonation wave is assumed to instantaneously originate from the primary diaphragm and propagate with constant velocity. Thus, for every new t-line, it is convected through the x–t grid with constant velocity and the burnt gas immediately behind the detonation wave is assumed to be at the CJ state. Meanwhile, the primary contact surface is advanced through the MoC unit process for a contact surface. For grid points immediately surrounding these discontinuities, the modified interior point solver is employed, as represented by the blue lines in Fig. 3.5b. Now the remaining continuous regions in the flowfield are solved. The gas properties at the high-pressure driver endwall is calculated using the wall point unit process. Finally, flow properties in the remaining white space at that t-line are solved using the interior point solver. This process is repeated until the detonation wave reaches the end of the detonation-driver section.

Once the detonation wave reaches the end of the detonation driver, the secondary diaphragm vanishes and the detonation wave transmits into the driven section as a shock wave. This phenomenon is resolved by the wave polar analysis, marked as location 2 in Fig. 3.5b, with the CJ state and the driven section as initial conditions on either side of the secondary contact surface. Thus, the post-transmission state of the gases on either side of secondary contact surface is now known, essentially providing the initial velocity of the transmitted shock wave in the driven section.

At this stage in the algorithm, three discontinuities are present in the flowfield, namely, the shock wave, and the primary and secondary contact surfaces. For a given t-line, the solution procedure is similar to the method described above. The discontinuities are resolved first by using the contact surface and shock wave unit processes. As opposed to the constant velocity detonation wave, the strength of

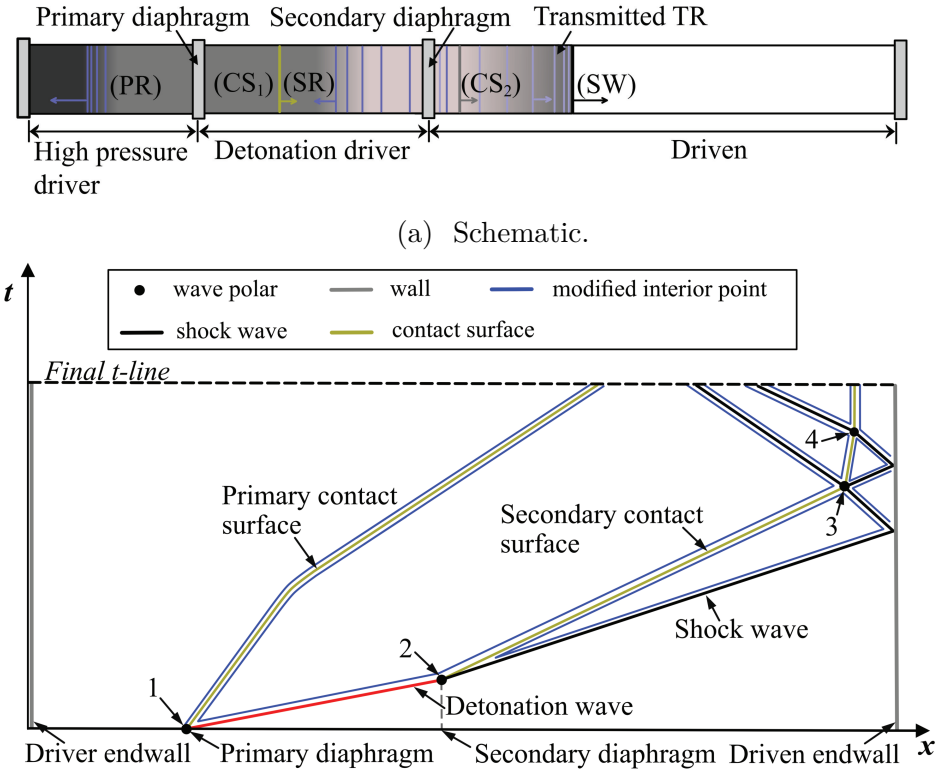

(a) Schematic.

(b) Diagrammatic algorithm.

Figure 3.5: Model for a downstream detonation tube.

the transmitted shock wave in the driven section will decay due to the transmitted Taylor rarefaction and losses in the driven gas due to heat and friction. Clearly, these effects are accounted for in the shock wave unit process, which resolves the shock wave dynamics in the driven section. The grid points behind the shock wave and on either side of the contact surfaces are resolved using the modified interior point solver as shown in Fig. 3.5b. Subsequently, the wall point solver is invoked to resolve the driver end wall condition, while the interior point solver computes the fluid states at all the other grid points. This procedure is repeated until the shock wave reaches and reflects off the driven endwall.

Generally, shock wave reflection at an endwall occurs in between the predefined t-lines, which can be determined based on the local incident shock wave velocity. Subsequently, the reflected shock properties are calculated using standard shock reflection relations and the location of the reflected shock wave is updated for the current t-line. For every t-line after this event, the solution algorithm scans for intersection between different discontinuities. If no interactions are found, then the calculation procedure for every t-line is essentially as described before, but with the added calculation of driven endwall conditions.

If two discontinuities indeed interact, for instance, the reflected shock wave and the secondary contact surface, marked by location 3 in Fig. 3.5b, wave polar analysis is used to determine the outcome. At location 3 specifically, a reflected shock wave is depicted to form. Therefore, the algorithm creates a new shock wave for the current t-line. In the event of a shock wave overtaking another shock wave, a new contact surface is created based on the results from the wave polar analysis and the slower shock wave is removed from the flowfield, representing its disappearance. In this situation and likewise in that marked as location 4, the modified interior point unit process is used to capture the effect of a reflected rarefaction wave. Based on the new state of the discontinuities obtained from the wave polar analysis, grid points that lie in between the transmitted discontinuities are populated. This procedure is repeated as necessary for a given t-line, when multiple interacting discontinuities are found. Once all such interactions are resolved, the remaining discontinuities are advanced using the appropriate discontinuous wave unit process. Finally, the continuous regions for the current t-line are resolved using interior point, modified interior point (if necessary) and wall point unit processes. The abovementioned steps for resolving continuous regions and interacting discontinuities are then repeated for every subsequent t-line to calculate the complete flowfield of a downstream detonation

tube. It is noted that the primary complexity of an MoC-based flowfield algorithm lies in the treatment of interacting discontinuities. For the detonation tube algorithm, identifying interacting discontinuities and populating grid points adjacent to these interactions takes up more than 50 percent of the overall algorithm.

3.1.6 Remarks on actual detonation tube gasdynamics and thermochemistry

The wave processes discussed in §2.2 are idealized and invite further comments regarding the validity of the detonation tube model. The first idealization one may note is the diaphragm rupture process. The model considered here assumes that the diaphragms disappear instantaneously in the detonation tube operation. In reality, the rupture of the diaphragm is a complex, almost unpredictable, three-dimensional phenomenon. As the diaphragm deforms and ruptures, the driver gas which accelerates through the partially ruptured diaphragm drives a curved shock wave of increasing strength near the diaphragm. After multiple shock reflections from the wall, the curved shock transforms into a planar shock wave some distance from the diaphragm [88, 89]. It is known that the "formation distance" can be reduced to a length of few diameters (2–8) by either loading the diaphragm near its limits [88] or using a thin diaphragm [90]. Note that the former method when used for diaphragms separating sections with a large pressure difference also results in a very high acceleration of the contact surface, thus mimicking the infinite acceleration assumed in the numerical model.

For the primary diaphragm, the experiments reported here ensured that the diaphragm was loaded to at least 90 percent of the rupture pressure to minimize the rupture time. However, the ruptured diaphragm fragments remain in the flowpath, the effect of which has been neglected. The secondary diaphragm, on the other hand, utilized a thin mylar film which was completely incinerated by the detonation wave

on incidence, a better representation of the model idealization. Hence, the actual wave system in a detonation tube does not have a single "origin" as shown in Figs. 2.2b, 2.3b and 2.5b.

Following diaphragm rupture, a planar contact surface is assumed to form instantaneously at the origin and remain as a planar discontinuity throughout the detonation tube operation. In experiments, following a diaphragm rupture, the interface quickly transitions into a contact region, which in turn thickens with the square root of time due to viscous effects [91]. Therefore, the reflected shock wave from the driven endwall does not interact with a contact surface but with a wide contact region. Due to this phenomenon, the validation experiments also serve to verify the ability of the detonation tube model to resolve the reflected shock wave–contact surface interaction. As will be seen in the subsequent section, the maximum L/D of the driven section employed in the experiments was around 66, which is less than typical impulse facility driven section lengths ($L/D \approx 100$) [12]. In the latter, the impact of an ever-growing contact region is more pronounced, in the form of a marked reduction in the useful test gas slug length. In the experiments carried out in this study, this effect can be expected to be significantly reduced due to the driven section L/D. Therefore, the validity of this model is limited to detonation tubes with relatively low driven section L/Ds, similar to the validation experiments reported here.

The detonation tube model does not physically account for the unsteady boundary layers that develop in various gas slugs. Therefore, the model cannot provide direct information on some of the design aspects that are tied-in with boundary layer growth. For instance, an optimal length of the driven section will correspond to that where the driven gas boundary layer does not grow so large as to merge onto itself from opposite walls. When such boundary layer closure occurs, the remaining gas slug resembles a turbulent pipe flow and therefore the useful test gas slug length is short-

ened or nonexistent [8]. However, the detonation tube model will always consider the useful gas slug to span from the secondary contact surface to the incident shock wave in the driven section, which may be untrue. Similarly, the model cannot account for the interaction of the reflected shock wave with the incoming boundary layer system in different gas slugs. In light of this latter uncertainty, the endwall phenomena are given importance in the model validation experiments. In these experiments, the endwall transducer was mounted along the axis of the tube and therefore would be immersed in the core inviscid gas behind the reflected shock wave. Thus, the endwall static pressure measurements will not be affected significantly by the reflected shock wave-boundary layer interaction. However, the reflected shock wave-contact surface interaction in the experiments also leads to a contamination of the test gas by the detonation driver gas, which can change the test gas composition at the endwall [12, 2]. But, since the detonation tube model and the experiments are limited to low enthalpy operation, the resulting weakly compressed test gas slug is relatively longer and therefore, the effect of endwall contamination can also be expected to be weak.

In the detonation driver, the model assumes that the detonation wave instantaneously reaches CJ velocity upon primary diaphragm rupture. In practice, rapid detonation wave formation in a combustible mixture bypassing typical flame acceleration mechanisms is referred to as direct initiation [92]. While flame acceleration is bypassed, a freely propagating CJ detonation wave might still be attained far away from the initiation source due to an initially unstable, stronger detonation wave.

There are different practical methods with strong ignition sources to cause direct or nearly-direct initiation [92]. For upstream detonation tubes, direct initiation by a pre-detonator tube has been reliably carried out in TH2-D [12] and the JF tunnels [25]. For downstream detonation tubes, shock-induced detonation has been demonstrated in GASL [93] and UTA/ARC [33]. GASL reported that direct initiation occurs in

a 150 mm diameter tube, even for highly diluted oxyhydrogen mixtures (up to 65 percent Ar or He), as long as $p_4/p_{100} > 20$. Experience with downstream detonation tubes at the UTA/ARC also confirms GASL's observation that in a similar diameter tube, a fully-formed detonation wave is attained at a length-to-diameter ratio of $L/D \approx 2.6$ from the diaphragm. Thus, in carefully designed facilities, the effect of run-up distance for CJ detonation wave formation can be neglected in the detonation driver, regardless of the mode of operation. The measures taken in this study to reduce detonation wave run-up distance are detailed in the experimental setup section.

Further comments about the detonation driver deal with modeling of the detonation wave itself. Despite the use of the ZND theory to calculate the final CJ state behind the detonation wave, the model assumes that the detonation wave is a planar discontinuity. Given that the ZND reaction zone thickness for typical oxyhydrogen detonation is orders of magnitude lesser than the grid size considered here, the treatment of a detonation wave as a planar discontinuity is justified. While the detonation tube model considers losses in all the working gases, the effect of losses on the detonation wave itself is generally neglected. It can be noted that the steady-state detonation wave velocity, even for ZND theory, is typically obtained using the CJ condition which assumes thermochemical equilibrium and neglects heat transfer and frictional losses. Thus, if the effect of losses are included in the detonation wave front propagation, the leading shock wave velocity can be expected to be slower. But, accounting for the effect of gasdynamic losses, even at the simplest level, requires consideration of the structure of the detonation wave.

For instance, if the ZND view is adopted, then, the effect of losses on the chemically reacting gases trailing the leading shock wave must be considered. Clearly, this will require an unsteady finite-rate-chemistry solver, which is beyond the scope of this phase of work. However, for the L/D ratios of interest for impulse facilities,

the effect of losses on detonation wave propagation can be neglected following the arguments of Zeldovich. For the oxyhydrogen mixture and the tube diameters used here, the reaction zone thickness is sufficiently small that the information about wall losses is communicated to a negligible cross section within the reaction zone. Since the detonation wave is inferred to be propelled by the chemical energy released in the reaction zone, negligible losses suffered by the latter also holds for the former. It may now be reconciled that the shock wave module similarly discards the effect of losses on the shock wave front by using inviscid Rankine–Hugoniot relations. This does not restrict the model applicability, as the shock wave, being a few mean free paths thick, is a true discontinuity from the continuum perspective. However, any pathline that traverses the shock wave, by the continuum postulate, possesses dimensions orders of magnitude higher than the shock wave thickness. Therefore, the losses on the particle paths immediately behind the shock wave are accounted for by using appropriate compatibility relations, as discussed earlier.

The working gases in turn are restricted to a calorically perfect assumption based on the governing equations considered in §3.1. Since the predominant gas-dynamic phenomenon differs across different gas slugs, the appropriateness of the perfect gas assumption on different gas slugs can be evaluated separately. First, the high-pressure driver gas primarily undergoes expansion to lower pressures throughout the detonation tube operation. Consequently, the temperature of the driver gas drops as it expands to lower pressures, initially through the primary rarefaction and later by a transmitted secondary rarefaction wave. At sufficiently long duration into the detonation tube operation, the reflected shock wave from the driven endwall will be transmitted into the high-pressure driver gas. For the low-enthalpy operation considered here, the transmitted shock wave reaching an expanded high-pressure driver

gas is expected to be of lower strength to induce high-temperature effects. Thus, the perfect gas assumption should hold for the high-pressure driver gas.

In contrast to the high-pressure driver, the 2-γ model used for the burnt gas behind the detonation wave needs clarification. Since the burnt gas state behind the detonation wave is calculated from the ZND model, subsequent gasdynamics of the burnt gas during detonation tube operation is the focus of this analysis. As the burnt gas expands through the Taylor rarefaction, its temperature drops and the gas may undergo recombination, at least immediately near the CJ state. A quantitative evaluation of this phenomenon will require a full unsteady finite-rate chemistry solution of the Taylor rarefaction. However, a qualitative understanding of the associated thermochemistry can still be obtained by investigating its limiting solutions neglecting gasdynamic losses. One of the limits, a thermochemically frozen primary and Taylor rarefaction can be obtained easily using the methods described in §3.1.4. The other limit, a thermochemically equilibrated rarefaction utilizes (thermochemical) equilibrium Riemann invariants given by

$$dp \pm \rho_e a_e du = 0 \tag{3.28}$$

where the positive sign represents the C_+ characteristic traveling through a simple expansion and the negative sign corresponds to the C_- characteristic. The subscript e is appended to emphasize that the gas state is calculated under a thermochemical equilibrium assumption.

Equation (3.28) is derived by simplifying the lossless finite-rate chemistry MoC under infinite rate processes and thus vanishing source terms [94]. The solution to the above Riemann invariants can be obtained through direct numerical integration, aided by equilibrium gas state calculations from CEA or Cantera. The final state of the Taylor rarefaction is determined by the attainment of gasdynamic equilibrium across

the primary contact surface, that is, continuity of pressure and velocity. Knowing the initial state of the driver gas and the CJ state behind the detonation wave, numerical integration of appropriate C_+ and C_- characteristics can be carried out repetitively until the matching solution is found. Additionally, the effect of secondary rarefaction on the burnt gas needs to be considered. This is rendered difficult, even for the frozen limit, due to the non-simple interaction between the secondary rarefaction and the incoming Taylor rarefaction, as was discussed in §2.2. Nevertheless, an estimate of the limiting effect of thermochemistry can be obtained by assuming that the final state of the Taylor rarefaction drives a shock wave into the driven section. Thus, the equilibrium Riemann invariant can be used again, in conjunction with governing equations for a shock wave in the driven section, to obtain the matching solution across the secondary contact surface. The frozen solution for this scenario is again based on §3.1.4.

The MoC model was validated by experiment, which will be described later in §3.2. For now, it suffices that Case 2 (see Table 3.1) with a nitrogen driver and a helium driven gas is selected for the analysis, as it represents the strongest rarefaction waves the burnt gas will experience in the series of experiments that was performed. Moreover, as both helium and nitrogen are calorically perfect, the effect of thermochemistry in the expanding burnt gas can be isolated. The results of these calculations are plotted in a wave polar diagram in Fig. 3.6a and the gaseous mixture state throughout the rarefaction waves is plotted in Fig. 3.6b.

In Fig. 3.6a, the Taylor rarefaction is marked as 'Taylor RW' and the matching high pressure driver rarefaction is marked as 'HP RW'. The limiting estimate of secondary rarefaction is marked as 'DD RW_2'. Clearly, this will originate from the final state of appropriate Taylor rarefaction. The matching condition in this case depends upon the transmitted shock wave in the driven section, which is marked as 'Driven

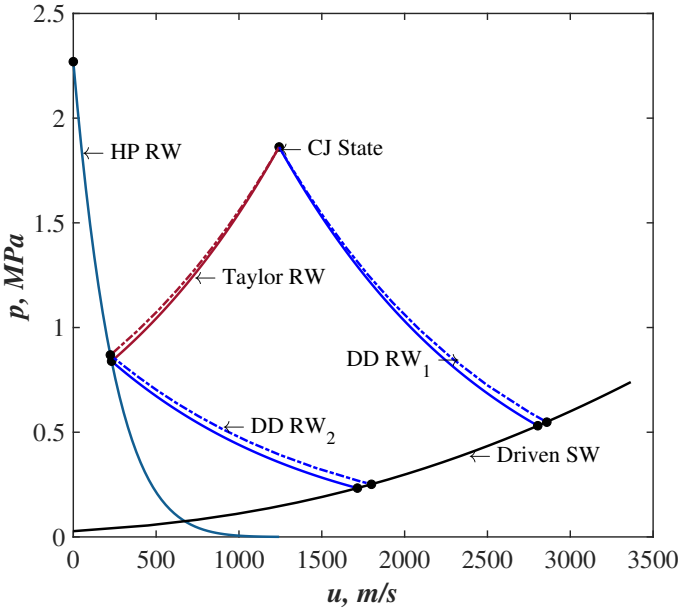

(a) Wave polar representation.

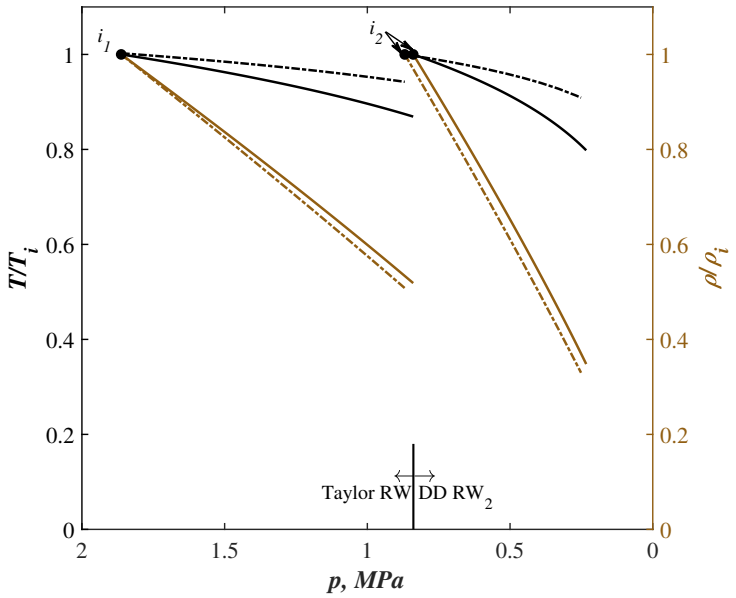

(b) Burnt gas state variation.

Figure 3.6: Effect of thermochemistry on burnt gas dynamics (continuous line: frozen solution, chained line: equilibrium solution).

SW'. Besides, the typical initial solution used for shock transmission into the driven section is also plotted in Fig. 3.6a and marked as 'DD RW_1'. In Fig. 3.6b, the ordinate is nondimensionalized against the initial conditions for a given rarefaction wave with the CJ state marked as i_1 and the final state of Taylor rarefaction marked as i_2. The abscissa utilizes absolute values so that Taylor and secondary rarefaction waves can be observed individually. In Fig. 3.6, the equilibrium solutions are shown as chained curves, while the continuous curves represent frozen solutions.

The remarks about perfect gas behavior of driver and driven gases are further validated in Fig. 3.6a, where the equilibrium wave polars of driver (HP RW) and driven (Driven SW) gases are coincident with their frozen counterparts. For the Taylor rarefaction, the wave polar shows that even between the limiting solutions, the final state varies little, namely, both pressure and velocity differ only by about three percent. This is attributed to the weak recombination that occurs throughout the Taylor rarefaction, which causes mass fractions to change weakly as the gas expands. The net effect is that the final state density, static pressure and γ and subsequently the sonic velocity differ by about three percent at most, between equilibrium and frozen solutions.

Note that the temperature calculated by the frozen gas expansion differs by about eight percent from the equilibrium solution, as the former does not account for the energy released due to recombining molecules. The same trend is seen in the representative secondary rarefaction but the difference between the frozen and equilibrium solutions worsens. This may be expected, as the differing initial conditions between the frozen and equilibrium expansions compound the effect of thermochemistry. Quantitatively, the density, static pressure and sonic velocity at the end of secondary rarefaction differ by about eight percent between the full equilibrium and frozen solutions, while the gas velocity differs by about five percent. Though these

differences seem non-negligible, it is expected that the non-simple interaction of the secondary rarefaction with the Taylor rarefaction will result in a weaker expansion than these calculations. Thus, the effect of thermochemistry on the final gas state is expected to be lesser than the differences the values quoted above. Note that the observations on thermochemistry are specific to the experiments carried out here. In the case of gaseous mixtures which undergo considerable recombination throughout the rarefaction waves, the effect of thermochemistry will cause even larger differences between the frozen and equilibrium solutions; this MoC model may not be adequate.

Instead of helium which has been used in the discussion above, the typical driven gas employed in an impulse facility is air. Even for a detonation tube operating in the underdriven mode, this will inevitably cause deviation from the calorically perfect gas assumption. Estimates for the effect of thermochemistry on the driven gas were calculated based on the initial conditions for Case 1 shown in Table 3.1. Preliminary estimates show that the reflected shock wave at the endwall could induce about a ten percent reduction of molecular oxygen mass fraction, while nitrogen shows negligible dissociation. Thus, to avoid the effect of dissociation, pure nitrogen was used as the driven gas in the experimental studies. Still, the incident shock velocities will induce vibrational excitation in the compressed driven gas, with the value of γ expected to vary by at most six percent, as obtained via an equilibrium normal shock solution. Even under thermochemical equilibrium, it is known that the static pressure and fluid velocities behind a strong normal shock wave are roughly independent of the gas state behind the shock [95]. Thus, where thermally perfect behavior is expected, the experimental data from static pressure transducers can still provide meaningful comparison against the static pressure and shock velocities estimated by the MoC model. The most significant deviation to the calorically perfect gas assumption occurs at the endwall, where the reflected shock wave is estimated to cause a reduction in γ

of about eight percent. Given the higher uncertainty in the capability of the simple MoC model to capture complex endwall gasdynamics, this deviation is a necessary sacrifice in the present study.

3.2 Experimental campaign

For validating the MoC model, experiments were designed and carried out in a small detonation tube. The final test matrix of the experiments, which reflects some of the model validation goals, is shown in Table 3.1. In addition to the information in Table 3.1, the initial fill pressure ratios were the same for all three cases. While the detonation driver was filled to atmospheric pressure, the high pressure driver and driven sections respectively had initial fill pressure ratios of 22.4 ± 0.2 and 3.7 ± 0.03 relative to the detonation driver. Since the experiments were performed in an environment-controlled facility, the detonable mixture was assumed to be at the facility's room temperature of 293 K.

Table 3.1: Test matrix (all sections have an ID of ¾ in).

Case	**High-Pressure Driver**		**Detonation Driver**		**Driven**		**Objective**
	Length (m)	**Gas**	**Length (m)**	**Gas**	**Length (m)**	**Gas**	
1	0.24	N_2	1.092	$H_2 + \frac{1}{2}O_2$	0.742	N_2	Reflected rarefaction wave
2	0.24	N_2	1.092	$H_2 + \frac{1}{2}O_2$	0.742	He	Reflected shock wave
3	0.24	N_2	0.584	$H_2 + \frac{1}{2}O_2$	1.25	N_2	Long driven

Table 3.1 shows that the overall $L/D \approx 100$ as is in the typical range of impulse facilities [96]. As discussed above, facilities with such a length-to-diameter ratio can be expected to incur non-negligible heat and frictional losses on their gasdynamics. The use of an oxyhydrogen mixture in the detonation driver is typical, due to hydro-

gen's high enthalpy of formation, which results in excellent driver performance. The detonable mixture tends to be maintained at stoichiometric proportions for optimum chemical energy release and effective detonation initiation. Despite the possibility of shock-induced detonation, an igniter was added to the detonation driver to cause rapid initiation or, at least, reduce the run-up distance associated with the detonation wave formation. Besides, the igniter would also serve to weaken and rupture the polyethylene diaphragms separating the high pressure driver and detonation driver. Finally, the driven gases used in all the cases were inert. Nitrogen was used instead of air, to avoid dissociation of oxygen and thereby remain closer to the calorically perfect gas assumption.

It is impossible to avoid vibrational excitation, as the required acoustic impedance ratio (see §2.2.1) across the detonation driver and driven sections will always result in shock velocities inducing vibrational excitation in nitrogen. Though argon as a driven gas would have been a better option for a heavy gas without vibrational excitation under similar initial pressure ratios, nitrogen was chosen to retain closer similarity to air, the typical test gas. Preliminary calculations for Case 1 showed that the interaction between the driven shock wave and secondary contact surface resulted in a reflected rarefaction wave, as the shock-processed nitrogen is a heavy gas compared to the expanding driver gas. Thus, a set of experiments with a light driven gas, helium, was performed, which was expected to result in a reflected shock wave as the driven shock wave crossed the secondary contact surface. These expected outcomes are identified for each case in the objective column in Table 3.1.

3.2.1 Experimental setup

A schematic of the setup assembly is shown in Fig. 3.7 along with the piping and instrumentation used for the experiments. The detonation tube setup consisted of

multiple steel tubes with a constant internal diameter of 3/4 in and a cumulative facility length of 83.5 in. The high-pressure driver section, denoted as HP in the schematic and shown as a single section, comprised of two carbon steel tubes of lengths 5 and 4 in. The detonation driver which was of different lengths is shown in the schematic by the sections identified as DD. The first section marked DD comprised of three carbon steel tubes of lengths 6 in, 11 in and 5 in. The following section, which is marked DD/DR was a single stainless steel tube of length 20 in. This section was either an extension of the detonation driver or a part of the driven section, as specified in Table 3.1. The final section marked DR was a single stainless steel tube of length 28 in, used as the driven section in all experiments.

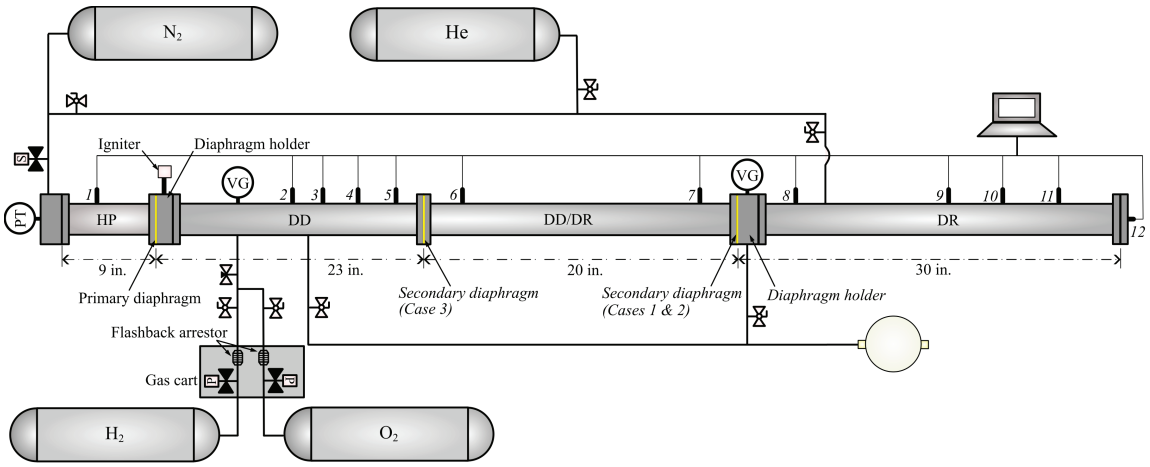

Figure 3.7: Schematic of the detonation tube setup. VG: vacuum gauge, PT: pressure transducer, $1, \ldots, 12$: PCB dynamic pressure transducers

The high-pressure driver, detonation driver and driven sections were separated from each other by primary and secondary diaphragms. The primary diaphragm was always sandwiched between the high pressure driver and the following diaphragm holder marked in Fig. 3.7. The primary diaphragm consisted of three polyethylene sheets of thicknesses 76.2, 25.4 and 12.7 µm stacked together. The secondary di-

aphragm was a single 6 µm thick polyethylene film. The location of this diaphragm varied between the experiments as marked in Fig. 3.7. Though the diaphragm holders and tube flanges contained O-ring seals, the diaphragms were enclosed between rubber gaskets spanning the entire flange diameter. These gaskets were either in turn sandwiched between the tube flanges or in between a tube flange and a diaphragm holder. The working gases used in the setup were all supplied by high-pressure bottles. The inert gases were routed directly to the setup, while the hydrogen and oxygen supply lines were routed through a gas supply cart. This cart controlled the gas supply through pneumatic valves actuated by solenoid valves and contained flashback arrestors for safety. Due to the low gaseous volume and fill pressures, the detonation driver and driven sections were filled and vented using ball valves. The high-pressure driver, on the other hand, employed solenoid valves for remote filling and venting.

A detailed view of the igniter assembly used for direct initiation is shown schematically in Fig. 3.8. The aluminum housing for an automobile spark plug had a dimension of 3 in $\times$ 1.5 in $\times$ 1.5 in. The spark plug was connected to an ignition coil which in turn was connected to the data acquisition system but powered independently by a 12 VDC battery. The aluminum housing was connected to the diaphragm holder through two stainless steel tubes, each having an $L/D \approx 70$. Further, the tubes also housed an Omega PX313-200G5V static pressure transducer which was used to record and aid in filling the detonation section to stoichiometric proportions. Before a run, a pin valve was closed to protect the transducer from the detonation wave.

The high-pressure driver endwall was equipped with an Omega PX313-500G5V static pressure transducer, (marked as PT), to monitor the filling process. Since the reflected shocks from the endwall were expected to be weak when they reached the driver endwall, this transducer remained connected to the high pressure driver and unprotected throughout the detonation tube operation. In addition to the static

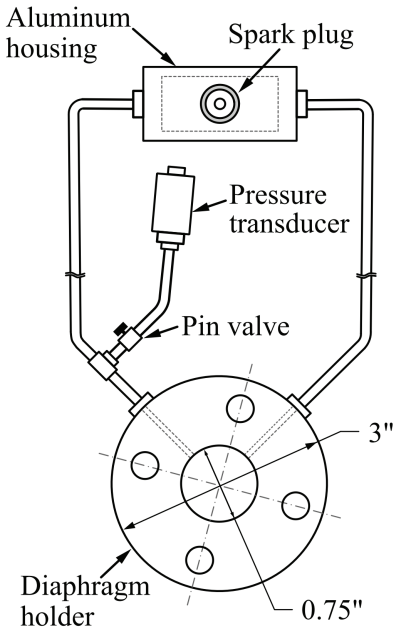

Figure 3.8: Close-up view of igniter assembly (not to scale)

pressure transducer, the detonation driver also housed an analog, industrial vacuum gauge (US Gauge), with a range of 0–0.3 MPa and minimum resolution of 3.4 kPa. This was used in tandem with the static pressure transducer to monitor the filling and venting of the detonable gaseous mixture. The driven section was fitted with a Dwyer DPGA-00 digital vacuum gauge to independently monitor its filling. Both the vacuum gauges were protected from the sharp pressure jumps during the detonation tube operation by isolating them using ball valves. Since all the vacuum gauges and pressure transducers measured gauge pressures, a mercury barometer located in the same work environment was used to track the room's atmospheric pressure during each run. Additionally, twelve PCB 111A24 high-frequency dynamic pressure transducers were installed across the setup to capture the wave processes during detonation-tube operation.

Table 3.2: Locations of dynamic pressure transducers from primary diaphragm, refer to Fig. 3.7.

1	2	3	4	5	6	7	8	9	10	11	12
−3.5	10.25	14.25	16.25	20.5	27	39	48.5	60.5	64.5	68.5	72.5

The transducer positions in inches with respect to the primary diaphragm are shown in Table 3.2. It can be noted that transducers labeled 1, 5 and 12 were flush-mounted, whereas transducers 2, 3 and 4 had a recess of approximately 2 mm. Transducers labeled 6–11 were mounted in recess ports designed with an aperture and a cavity. The opening aperture at the detonation tube inner wall was of $\sim \phi 3$ mm and depth of 3 mm, and the cavity was of $\approx \phi 6$ mm and depth of 8 mm.

Data from the dynamic pressure transducers were routed through a National Instruments PCB Model 483A ICP signal conditioner, which in turn was connected to a National Instruments PXI-6133 S series multifunction DAQ using a TB-2709 terminal base. The static pressure transducers, however, were connected to the terminal base directly, and excited independently by a 10 VDC power supply. The data from the PCB transducers were collected at a rate of 2.5 MHz, which was initiated by a LabVIEW program immediately following the trigger signal sent to the spark plug in the igniter via the host computer.

The experimental procedure for all three cases can be outlined as follows. As a preliminary step to every run, the entire tube was purged. Since all the diaphragms would have been ruptured, one of the vacuum ports was used to evacuate the entire setup to < 0.69 kPa, followed by filling the setup with the appropriate driven gas to the atmospheric pressure. All pressures were absolute unless noted otherwise. The setup was then disassembled to install the primary diaphragm stack and the secondary diaphragm. Before the working gases were filled in the detonation driver, the power

supply to the spark plug was disconnected to prevent accidental spark discharge. Since the secondary diaphragm was very delicate and prone to easy rupture under a large pressure difference, the detonation driver and driven sections were purged and filled in tandem. First, the detonation driver and driven sections were evacuated simultaneously to ≈ 48 kPa. Then, the driven section was further evacuated to < 0.39 kPa and filled with the appropriate driven gas to a pressure of 48 kPa.

Next, the detonation driver was evacuated to < 0.69 kPa and the detonation driver section was filled with hydrogen up to half of its calculated stoichiometric partial pressure. This was followed by filling the detonation driver with oxygen to its stoichiometric partial pressure. Finally, the remaining volume of hydrogen was injected into the detonation driver. This procedure was expected to promote mixing between the hydrogen and oxygen gases.

The driven section was next topped up to atmospheric pressure and evacuated to the required static pressure. The detonable mixture was then allowed to mix inside the setup for approximately 10 minutes and the power supply to the spark plug was reconnected. All the valves to the vacuum gauges and the igniter pressure transducer were closed and, at last, the high-pressure driver gas was remotely filled to the required static pressure. Once the supply to the high-pressure driver was cut-off, the LabVIEW program was executed which triggered the signal to the spark plug. This resulted in the rupture of the primary diaphragm stack and thereby began the detonation tube operation, the data of which were acquired by the LabVIEW program. Following this procedure, every case was performed thrice to demonstrate repeatability.

3.3 Results and discussion

Data obtained from the detonation-tube experiments were used for validating the MoC model. This validation effort was prefaced with a grid independence study for the MoC model, so that the numerical accuracy of the finite-difference formulation was first ascertained. An appropriate model to account for heat and momentum losses was identified for a sample experimental case. Further, the identified model was used to analyze the remaining experimental cases. Based on these analyses, experimental results were further scrutinized to reconcile any differences between MoC and experiments, detailed discussions of which follow.

3.3.1 Grid study and roughness estimation

The first step of the model validation effort, the grid independence study, determined the spatial grid sizing to be used for MoC model calculations. Since the experimental studies to be reproduced by MoC consist of three different cases, to minimize computational effort and still retain relevance to all cases, one limiting case is utilized for the grid study. Determination of this limiting case itself depended on the parameters of interest for a specific problem. For the detonation-tube operation considered here, the incident shock trajectory in the driven section predominantly determined the gas state at the endwall and was naturally the parameter of interest. Thus, the limiting case of the validation experiments trivially became that with the largest shock velocity which is Case 2 in Table 3.1. Further, for Case 2, the maximum shock velocity attainable in the MoC model occurred when the effect of losses was neglected, which was advantageous since the yet unknown parameter, the pipe roughness, was not required for this grid study.

For a preliminary coarse mesh, the entire detonation tube was divided into 200 'cells' and the fill conditions for Case 2 were set as the initial condition. The resulting

MoC solution of the shock trajectory in the driven section is plotted in Fig. 3.9a. As denoted in the plot, the initial constant velocity region represented the detonation driver and the decaying velocity region represented the driven section.

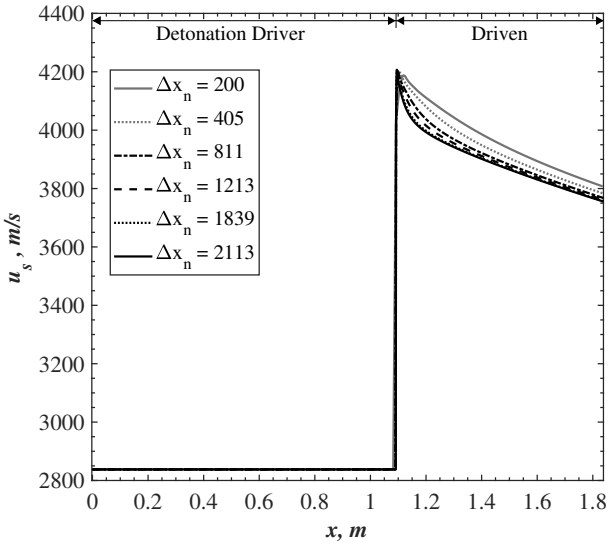

(a) Incident shock velocity.

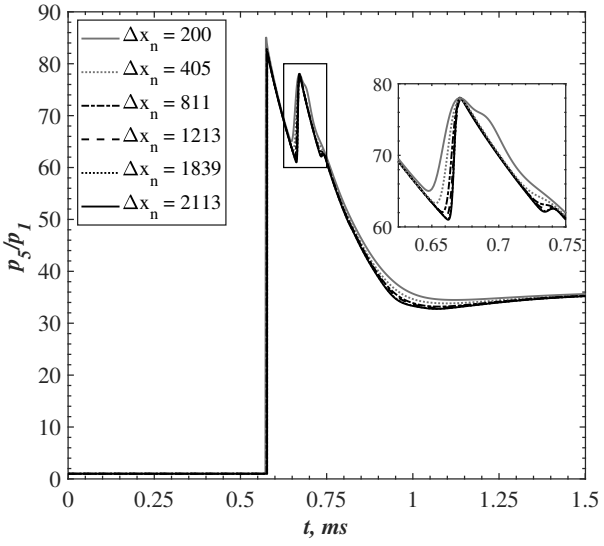

(b) Endwall pressure ratio.

Figure 3.9: Grid independence study.

The corresponding endwall pressure ratio variation throughout the detonation tube operation is shown in Fig. 3.9b. Initially, the number of cells was increased by a factor of about two. As the incident shock trajectory seemed to converge, this factor was reduced to about 1.5 and finally to 1.15. The resulting shock velocities for all these simulations are plotted in Fig. 3.9a and the corresponding endwall pressure ratios in Fig. 3.9b. The maximum difference in incident shock velocity between two successive grid sizes reduced from about 1.5 to 0.3 percent with increasing mesh sizes. Additionally, the corresponding maximum difference between the coarsest and finest grids was about 3.5 percent. Since the finest grid required a computational time of about 20 minutes on a single CPU personal tablet, a grid size of 1 213 was chosen for the validation studies, which reduced the computational time to about 10 minutes. The maximum difference in incident shock velocities between this chosen grid size and the finest grid size was about one percent, while that corresponding to endwall pressure ratios was about 1.5 percent. Note that the ideal cases simulated here are only for theoretical consideration and the actual validation cases are expected to have significant reduction in shock velocity from the values shown in Fig. 3.9a. Thus, similar to the results of a previous study [63], the grid size chosen here was expected to be conservative and of sufficient numerical accuracy.

The grid size selected in the previous step was used to identify the best momentum and heat loss model to replicate experimental results. From §3.1.3, it may be obvious that the only unknown parameter in the MoC model is the absolute roughness of the tube walls ϵ in the experimental setup. The absolute roughness in Eq. (3.14) represents equivalent sand grain roughness as defined by Nikuradse's experiments, where finely sorted sand grains were affixed to various pipes using lacquer [78]. Considering this fact and the non-availability of surface roughness data for the tubes in the experimental setup, the value of ϵ was determined as a part of this study.

This effort merely amounted to varying the absolute roughness values in the MoC model and comparing the resulting incident driven shock velocities to the experimental time-of-flight (ToF) velocities at all locations. The best loss model, it was surmised, should display minimal deviation from experimental ToF velocites for an appropriate wall roughness. As an initial guess, all the tubes were assumed to be smooth with $\epsilon = 0$, followed by increasing sand grain roughness values until a reasonable match was obtained for the incident shock velocities in the driven section. The final roughness values for the calibrated model consisted of two different values for the tubes, 0.15 mm for the sections detailed HP and DD in Fig. 3.7 and 0.01 mm for the remaining sections. This was qualitatively based on the assembly of the experimental setup, which utilized a combination of carbon and stainless steel tubes. The carbon steel tubes used for the HP and DD sections had rough walls, while the remainder of the setup assembled of stainless tubes had smoother walls. Interestingly, these estimated roughness values are of the same order of equivalent sand roughness values recommended for poor and good steel tubes in hydraulic engineering [97]. Finally, it is noted that the above process was only carried out for Case 1, in an effort to gauge the versatility and universal effectiveness of roughness values obtained from a representative case in a given setup.

Using the final estimated roughness values from Case 1, all three cases were simulated. Figure 3.10 shows the results of these simulations through plots of driven shock velocities due to all the models and for all the cases. The regions of detonation driver and driven sections are marked in each plot and the experimental shock velocities based on ToF calculations are shown as triangular and circular markers for comparison. Note that the axial locations corresponding to the experimental ToF calculations are assumed to be the midpoints between the relevant transducers. The results for the model with no momentum or heat losses are depicted by the curves

marked MI. This aligns with the observation that the flow in a continuous region is multi-isentropic, that is, the entropy along a pathline remains constant, but it may differ between different pathlines. The curves with markers RA signify that the losses have been calculated through Reynolds analogy approach discussed in §3.1.3. The curves marked MRA signify a model incorporating losses based on the modified Reynolds analogy. For any model, when the reference temperature method is additionally employed, the appropriate legend conveys this by the addition of +RT to the already noted model nomenclature. Figure 3.10 shows that a multi-isentropic model will overestimate the incident shock velocities in the detonation tube driven section.

Also plotted for every case are the estimated reflected shock velocities for different models, even though the reflected shock was not used as a benchmarking reference during calibration. From Fig. 3.10, it is seen that the Reynolds analogy adds the least amount of losses to the fluid flow for a given roughness value. The modified Reynolds analogy accounts for higher losses due to the inclusion of the effect of a non-unity Prandtl number. Further, for a given method, the addition of reference temperature based calculations increase the losses suffered by the gas. The plots for cases 1 and 2 indicate that the Reynolds analogy incorporating the reference temperature method provides the best match for the incident shock trajectories. However, it is suspected that the curves that lie above this case, that is, the Reynolds and modified Reynolds analogies should also be able to provide better matches than shown in Fig. 3.10 with higher roughness values, for instance, refer to the previous version of this work based on modified Reynolds analogy [63]. But, this has not been attempted here since a reasonable match was already obtained through one of the losses models. Figure 3.10b shows that the shock velocities from the final estimated roughness values differs appreciably from that observed in the experiments for Case 2. A detailed discussion of this mismatch is postponed to a subsequent section.

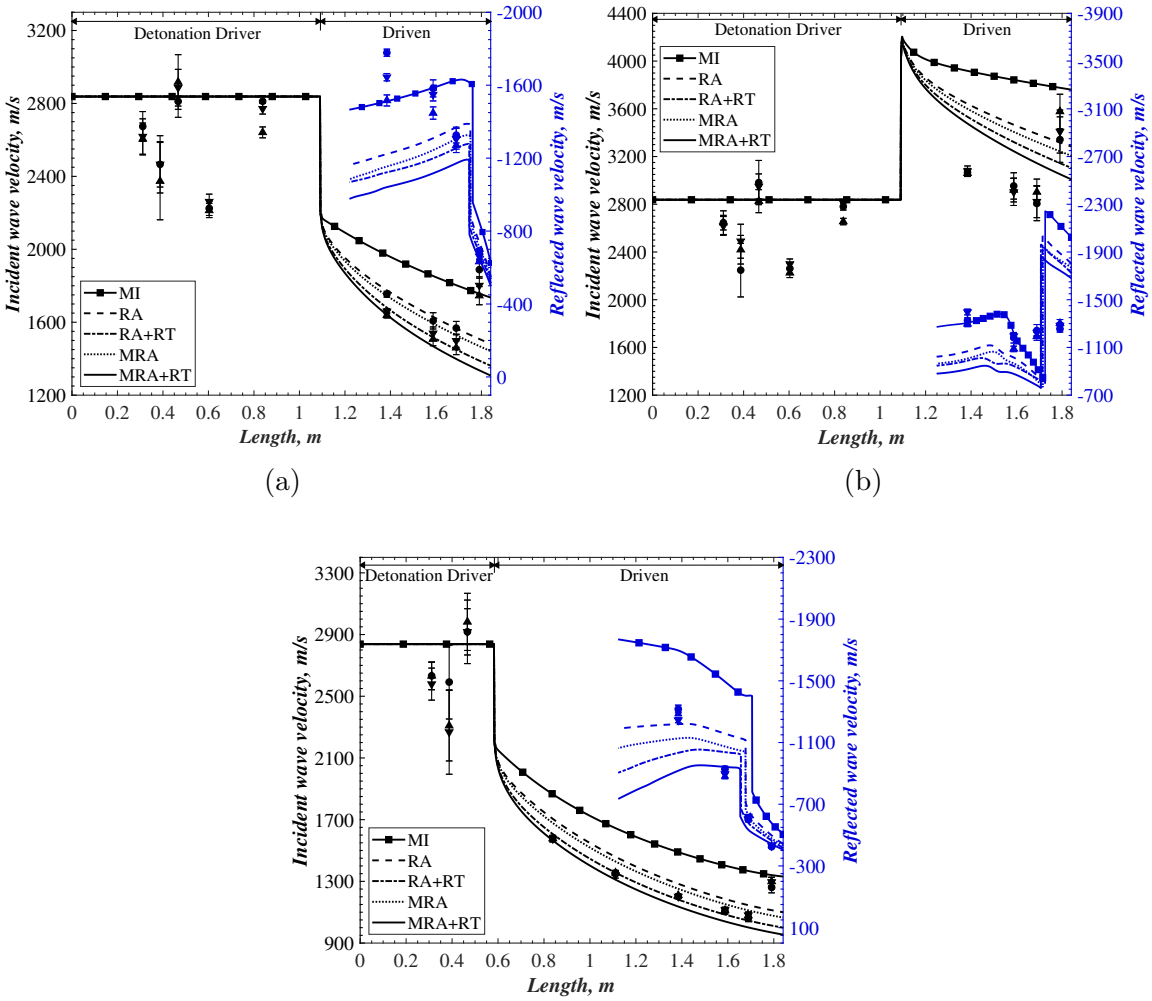

Figure 3.10: Estimation of equivalent sand roughness (Experimental velocities shown as triangular and circular markers, MI: Multi-isentropic, RA: Reynolds analogy, MRA: Modified Reynolds analogy, RT: Reference temperature). Comparison of shock velocities for (a) Case 1, (b) Case 2, (c) Case 3.

3.3.2 Typical features of experimental results

The ToF-based detonation/shock velocities shown in Fig. 3.10 indicate a pattern of wave velocities in all experiments which is discussed first. Figure 3.10 shows that the detonation wave velocities at three locations are well below the theoretical CJ wave velocity. Refer to Table 3.3 for the average percent deviation of detonation

velocities to CJ theory at various locations. The lower detonation velocities at the first two ToF values are reasoned to be caused by a single artifact, the vacuum port between pressure transducers 2 and 3, shown in Fig. 3.7. The piping leading up to the vacuum pump consisted of a ϕ6.35 mm steel tube extending 0.33 m from the detonation driver, after which the ball valve was located. This is suspected to locally weaken the detonation wave. Given that the second ToF velocity is about nine percent lower than the first ToF velocity and the first transducer is located upstream of the vacuum port, it may be inferred that the actual detonation wave velocity near the first transducer is higher than the ToF calculated value. Note that the peak pressures behind the detonation wave at all the transducers in the detonation driver were always above CJ pressures. These observations led to the conclusion that a fully-formed detonation wave was always achieved at the first transducer location.

Moreover, the third ToF detonation velocity was on an average 2.5 percent higher the theoretical CJ velocity, further justifying the locally weakened detonation wave around transducer 2. Finally, for the longer detonation driver cases, the last ToF detonation velocity was on an average 3.2 percent below the theoretical CJ velocity. Since both these transducers were highly recessed as detailed in §3.2.1, in addition to being $\approx$ 30 mm away, it can be concluded that the detonation wave at these locations was also a CJ wave. Hence, a freely propagating detonation wave was achieved in the detonation driver in the experiments.

Figure 3.10 and Table 3.3 show that the fourth ToF detonation velocity was far below the theoretical CJ wave velocity and thus an outlier. Similarly, the ToF value between the final set of transducers in the driven section seemed to be an outlier in comparison with the trend of incident shock wave velocities. Though not obvious from the experimental data, the calculated reflected shock velocity between the last set of transducers also turned out to be an outlier when superposed on the

Table 3.3: Percentage deviation of average experimental detonation wave velocity from CJ theory.

Case	**ToF Locations**				
	1	2	3	4	5
1	−7.3	−14.2	+1.2	−21.3	−3.4
2	−7.1	−15.9	+2.9	−20.3	−3.1
3	−7.9	−15.8	+3.6	NA	NA

calculated MoC shock velocities. These three outliers could again be traced to a single experimental artifact, that is, ToF calculations carried out over a combination of flush and recessed transducer data. It may be recalled that transducers 5 and 12 in Fig. 3.7 were flush mounted, while transducers 6 and 11 were recess mounted. For the outlying detonation wave velocity, transducer 5 was flush mounted, while 6 was recessed. Thus, the actual distance traversed by the detonation wave consisted of the spacing between these transducers to which was added the recess depth of transducer 6. But, the ToF calculations only consider the transducer spacing, which combined with the true traverse time resulted in a slower perceived detonation wave velocity.

For the incident shock wave in the driven section, the opposite mounting arrangement was encountered. Transducer 11 was recessed, while the endwall transducer 12 was flushed. In this case, it was necessary to consider the propagation of the shock wave near the transducer recess in more detail. When the shock wave began to traverse the transducer port's aperture, diffraction of the shock wave front occurs near the wall corner of the aperture port. As the shock wave traveled further and reached the opposite wall of the aperture, a curved shock front ensued, which bifurcated into a transmitted shock wave into the recess and a locally weakened primary shock wave propagated further into the driven section. In this case, since the aperture diameter was considerably smaller than the detonation tube's inner diameter, the primary

shock wave can be considered to propagate further with negligible attenuation. Note that the curved shock front coupled with the bifurcation process resulted in multiple wave reflections on the recess side walls [67], which are seen as high-frequency oscillations immediately behind the transmitted shock wave in all the recessed pressure transducer traces (see Figs. 3.12, 3.15 and 3.18). When the transmitted shock wave traversed the recess depth and reached the pressure transducer, the primary shock wave had already propagated further into the driven section. But, in the ToF calculations, the arrival of the transmitted shock wave at the recessed transducer was instead considered to be the first time-stamp for primary shock wave arrival. Clearly, this is untrue, and will be perceived as the delayed arrival of the incident shock wave at transducer 11. However, as transducer 12 was flushed, its pressure trace provided an accurate representation of primary shock wave arrival at this location. Therefore, the combination of recessed and flushed transducers resulted in a perceived shorter time interval for the primary shock wave to traverse the distance between them. This in turn resulted in a perceived higher shock velocity, since the axial distance between these transducers was the true distance. For a reflected shock wave travelling between these transducers, the opposite occurred, as the shock wave travels from a flushed to a recessed transducer. The trend in such a case may be expected to follow the reasoning for the outlying detonation wave velocity discussed before.

The above reasoning for outlying wave velocities can be further substantiated through ToF calculations based on MoC shock trajectories aided by estimates of transmitted shock velocities into the recess ports. The true geometry of the recess ports can be substituted by an idealized constant area geometry. Since the recess port aperture diameter was considerably smaller than the spacing between successive transducers, the transmitted shock was assumed to form instantaneously at the aperture for the high shock velocities considered here. Further, an estimate of the

transmitted shock velocity can be obtained from Whitham's theory of shock dynamics [98].

It is reiterated that this method is a heavy simplification intended to provide a qualitative estimate of the perceived experimental ToF calculations. Nevertheless, the approximate ToF method described here can be seen to estimate the experimental shock ToF calculations remarkably well for all cases, as shown in the subsequent sections. Whitham developed a simplified theory for the evolution of shock fronts primarily driven by changes in driving streamtube area, neglecting the effects of gasdynamic flow evolution further behind the shock front. Geometric shock dynamics, as this method has come to be known, can specifically resolve the evolution of an initially planar shock front as it moves around a sharp corner in a two-dimensional flow. One of the simplifications of this theory provides an algebraic solution for the local Mach number of the diffracting shock front at the wall for high initial shock velocities and arbitrary corner angles. Experimentally, this algebraic solution has been shown to be an excellent match at lower corner angles and a fair match for higher corner angles [99]. Considering the overall gasdynamics of incident shock diffraction discussed above, the transmitted shock into the recess port can be approximated by the wall shock Mach number from Whitham's theory. For an initially planar shock wave with a Mach number M_o, diffracting around a wall with a corner angle θ_w, the transmitted wall shock Mach number M_w is given by

$$M_w = M_o \exp\left(\theta_w/\sqrt{n}\right) \tag{3.29}$$

where

$$n = 1 + \frac{2}{\gamma} + \sqrt{\frac{2\gamma}{\gamma - 1}}$$

Implicitly, this approach neglects the effect of transmitted shock curvature and reflections from the opposite corner of the aperture. Further, this result was derived

by Whitham for inert shock diffraction. More recent analyses have extended this approach to sustained and/or quenched detonation diffraction, for instance, Radulescu et al. [100]. The primary difference these methods bring is the change in the value of the exponent term n. For the current case, these changes resulted in negligible difference to the overall calculation and, thus, the value of n used for detonation diffraction was simply that for inert shocks as given above.

From Eq. (3.29), transmitted shock velocity and thereby the delay in the arrival of a shock/detonation wave at the transducer diaphragm was evaluated for a given recess depth and for a sharp right-angled corner. Finally, adjusting the traditional ToF calculations for this time delay produced the experimental ToF values. For the detonation wave velocity ToF 4 in Table 3.3, these calculations indicated a perceived reduction of about 12 percent from CJ velocity (See Figs. 3.11, 3.14 and 3.17), as opposed to about 21 percent observed experimentally. The estimated results for shock ToF calculations are discussed separately for each case in the next section. Note that this estimate was not carried out for the reflected shock wave considering the reflected shock wave-boundary layer interaction.

In addition to the above effect, it is known that a recessed transducer exposed to pressure transients will produce a damped and delayed response from the original transients [101, 102]. Methods to estimate the response of recessed transducer are either too simplified resulting in high percent errors, or, require experimental estimation of transducer response [102]. Further, the mixing of different gas slugs in the recess ports during a detonation tube operation adds considerable uncertainty to these methods derived for a homogeneous gas occupying the recess port. To limit the scope this work, these approaches have not been attempted here. Therefore, the pressure traces from recessed transducers shown in the subsequent sections cannot be reliably used for quantitative comparison. Still, it can be seen that the recessed mounts

affected the ToF shock velocities negligibly, resulting in meaningful quantitative comparison. Moreover, the driven endwall transducer, which is of prime importance in the validation study was flush-mounted thus providing the true reservoir pressure for shock tunnel operation.

3.3.3 MoC model validation

Following the general discussion above, each case is now compared in more detail to the experimental results. The shock traces for individual cases are plotted again, but the MoC curves include results only for the multi-isentropic and Reynolds analogy with reference temperature methods. Since the inclusion of losses means that the entropy varies even along a pathline, the latter model will hereafter be called nonisentropic. Added to these shock trace plots are theoretical calculations that account for the effect of recess-mounted transducers, which utilize the best calibrated MoC model result. Further, the pressure trace from each available transducer is also plotted against MoC pressure trace at the corresponding location. These plots are also supplemented by a pressure contour plot in the x–t plane to show the detonation tube wave processes and thereby flowfield evolution as resolved by the MoC.

3.3.3.1 Case 1

Figure 3.11 shows the MoC shock and detonation wave traces for Case 1 described in Table 3.1. The incident and reflected shock velocities are plotted along different ordinates for clarity and the axial locations of the experimental values correspond to the midpoints between the relevant transducers. The experimental ToF values also include the associated uncertainties calculated by simple error propagation [101]. As discussed earlier, the theoretical ToF estimates accommodating for recess mounts are only calculated and plotted for incident shock velocities. To show the

effect of incorporating recess depth into theoretical ToF calculations, the plot also contains theoretical ToF values based only on MoC shock/detonation wave trajectories. These theoretical ToF values can be seen to coincide with the detonation/shock wave trajectories throughout the detonation tube. The adjusted theoretical ToF can be seen to coincide with the theoretical ToF for the detonation wave for the first, second and fourth ToF values. For the first and second values, this occurs due to the flush-mounted transducers as approximated in the calculations. For the fourth location, this coincidence occurs as the detonation wave is assumed to travel with a constant velocity. Under this condition, Eq. (3.29) can be expected to produce identical transmitted shock velocities into the recess mounts for both the transducers in the ToF calculation and, thus, there is no net delay due to the recess mounts. Therefore, the adjusted theoretical ToF values coincide with the actual theoretical ToF values. This trend is also seen in the experimental ToF values at this location, where the calculated detonation wave velocity matches closely with theoretical CJ velocity, despite both the relevant transducers being recessed.

At the third ToF location, the adjusted theoretical ToF value qualitatively predicts the perceived reduction in detonation wave velocity, but is about 12 percent higher than the experimental ToF value. This is reasoned due to the complex gasdynamics associated with detonation wave propagation. As the detonation wave diffracts around the corner of the recess port, the reaction front which drives the initial shock could potentially decouple from the shock wave. As opposed to an unsteady shock wave, which is driven by a piston motion behind it, a detonation wave is driven by the energy released by the trailing reaction front. Thus, when the reaction front decouples from the initial shock wave, the latter could decay significantly in strength. Therefore, the transmitted shock wave calculated by Whitham's rule may be stronger than the actual decaying shock wave front. Now, if the same ToF cal-

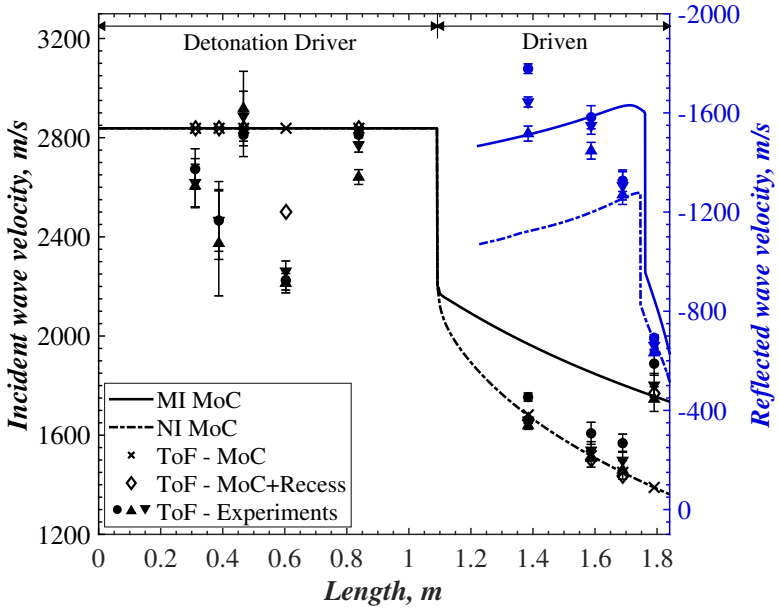

Figure 3.11: Shock/detonation wave velocity comparison: Case 1 (MI: Multi-isentropic, NI: nonisentropic)

culations as above were repeated assuming that the wave transmitted into the recess port is a Mach wave, then the perceived detonation wave velocity is about 2100 m/s. Since the experimental ToF is between the transmitted Mach wave and shock wave solutions, it is inferred that wave transmitted into the recess port is a weak shock wave. Such a scenario will also be seen at this ToF location for Cases 2 and 3.

For the incident shock velocities in the driven section, the adjusted theoretical ToF values are about one percent lower than the true theoretical ToF values, if both the transducers involved are recess mounted. Again, from Eq. (3.29), if the incident shock Mach number does not vary drastically between the two transducer locations, the corresponding transmitted shock Mach numbers vary even less, with negligible difference in the ToF calculations. Thus for mildly varying incident shock Mach numbers, identically recessed transducers can be expected to have a negligible influence

on ToF calculations. In contrast, for the last ToF value, the adjusted theoretical ToF is overestimated by about 27 percent from the true ToF due to the combination of recessed and flushed transducers used in the calculation. Also, the adjusted theoretical ToF matches well with experimental ToF values, implying that the true shock wave velocity at this location maybe better represented by the MoC curve, rather than the outlying experimental ToF values.

For the reflected shock wave, the last (location) ToF value is similarly unreliable. The subsequent experimental ToF value which is seen to match well with the MoC transmitted shock wave velocity is suspected to be an average of the local reflected and transmitted shock velocities across the secondary contact surface. This can be seen in the MoC-generated x–t plot, Fig. 3.13, where the 'inviscid' contact surface–shock wave interaction occurs around 1.74 m. Therefore, the quantitative accuracy of the MoC-estimated reflected shock wave cannot be ascertained from Fig. 3.11. However, from the reflected shock trace, it is seen that the shock wave is amplified as it is transmitted across the secondary contact surface, as exhibited by the discontinuous jump in the shock wave velocity around 1.74 m. Finally, the influence of losses on the detonation tube gasdynamics can be appreciated by observing that the multi-isentropic model overestimates the incident shock velocity at the endwall by about 27 percent.

For further comparison, experimental pressure traces at individual transducer locations are compared to their MoC counterparts. The transducer data in the detonation driver and driven sections are split respectively into two plots in Fig. 3.12. The time of arrival of the incident shock wave at the driven section endwall was chosen as the origin for both experimental and MoC results. By this method, a coincidence of the initial pressure rise at different flush transducer locations also indicates how well the MoC reproduces the detonation and shock wave velocities. For the pressure

traces, relevant transducer locations are marked on the plot individually with each trace shifted vertically by -20 units in the detonation driver and $+30$ units in the driven section. The ordinate in this case represents the local static pressure nondimensionalized by the initial static pressure at that transducer location. In Fig. 3.12a, the recessed transducers marked XDR3, XDR6 and XDR7 exhibit large oscillations in the pressure trace, due to multiple shock reflections into the recess port that are driven by the transverse oblique shock structure of a detonation wave. The initial rise of the pressure traces coincides well with MoC traces near the secondary diaphragm. But this coincidence worsens with increasing distance from the secondary diaphragm. This is expected because the experimental ToF for the detonation wave in Fig. 3.11 shows lower detonation wave velocities than the theoretical CJ velocity.

Individual pressure traces in the detonation driver show that the plateau pressures of transducers marked XDR2 and XDR5 agree with each other. While XDR5 was flush mounted, XDR2 had a slight recess of about 2 mm. Surprisingly, XDR3 and XDR4 which are also slightly recess mounted display a lesser plateau pressure compared to the surrounding transducers. A comparison of the amplitude response of XDR6 and XDR7 to the nearby flushed transducer also reveals that these responses are attenuated. While the latter attenuation is clearly due to the highly recessed transducer mounting, the former difference in the plateau pressure is attributed to the locally weakened detonation wave recorded between XDR3 and XDR4. Further examination of XDR2 shows that the experimental plateau pressure decays and deviates from the MoC estimated values after $t \approx -0.2$ ms. This can be attributed to a combination of the detonation wave run-up distance and burnt gas leakage into the extended vacuum piping discussed in previous sections. Notably, the secondary rarefaction wave from the end of detonation driver reaches XDR2 at $t \approx 0.2$ ms (see Fig. 3.13) and is unrelated to the earlier plateau pressure decay discussed here.

Driven section phenomena can be examined from the pressure traces plotted in Fig. 3.12b. Despite the initial experimental pressure rises closely trailing the MoC pressure rises, the amplitude response of the transducers can be seen to lag significantly. Such a lagging response can be attributed to the lower initial sonic velocity of the driven gas filling the recess ports and lower incident shock velocity in the driven section. Though the pressure traces in the driven section seem to match well with the MoC trace, further evaluation of the recessed transducer response is necessary to draw quantitative conclusions. Qualitatively, the MoC traces at XDR8 and XDR9 show a nearly constant plateau pressure, while the experimental traces show continuously decaying pressure. As the detonation driver pressure itself showed earlier decay in the plateau pressure compared to the MoC, the same trend observed in the driven section plateau pressure seems appropriate. From a comparison of the endwall pressure trace in Fig. 3.12b, the MoC seems to capture the peak pressure in the detonation tube. Moreover, the decay in stagnation pressure at the endwall is well replicated up to $t \approx 0.15$ ms. The immediate difference in pressure trace after this time is suspected to be due to the waves communicating early decay in the detonation driver. The higher difference in magnitude can be explained by the amplification of MoC pressure rise due to the reflected shock wave. From the endwall trace comparison, it can at least be inferred that the reflected shock velocity in the vicinity of driven endwall is well replicated by the nonisentropic model. Also, endwall peak pressure from the multi-isentropic model is about 81 percent higher than the endwall peak pressure shown in Fig. 3.12b.

More information about the overall flowfield evolution for Case 1 can be extracted from an x–t diagram, plotted in Fig. 3.13. Contours of static pressure are plotted in the x–t plane to portray the dominant wave processes. Trajectories of contact surfaces are added to this plot to aid in demarcating different gas slugs. The

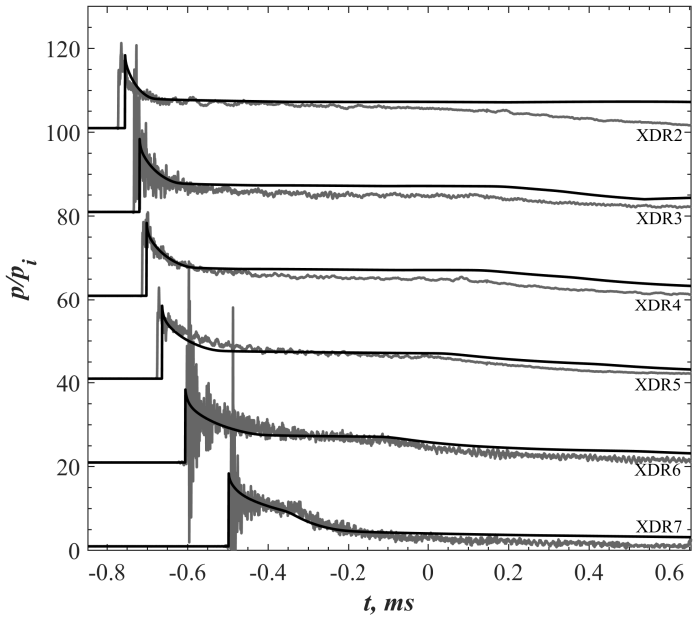

(a) Detonation driver.

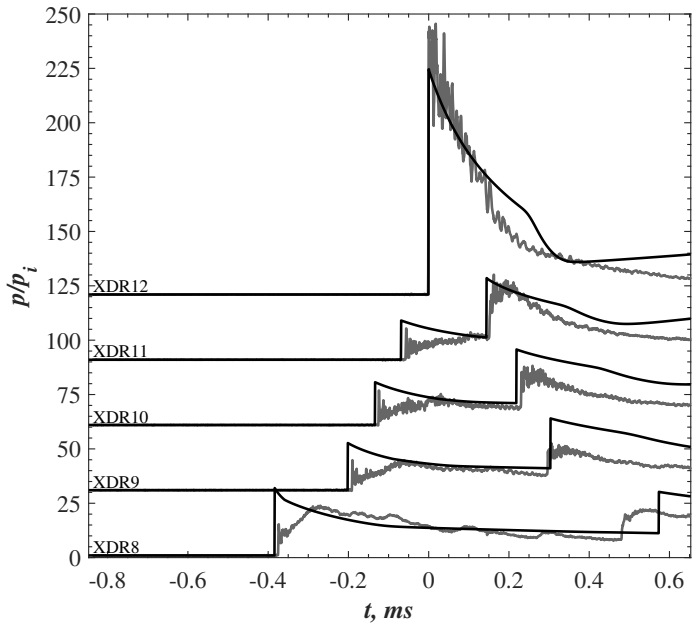

(b) Driven section.

Figure 3.12: Comparison of MoC and experimental pressure traces for Case 1

.

nomenclature used in this plot follows Fig. 2.3b. Since the MoC model also includes the effect of losses, waves in addition to the ideal wave processes described before can be seen in Fig. 3.13, communicating the effect of losses to different regions in the flowfield. The temporal origin here is also adjusted to be the time incident shock wave reaches the driven endwall, so that this plot can be used in tandem with Fig. 3.12 for validating the MoC model. As the detonation tube algorithm was based on the wave processes in Fig. 2.3b, the MoC generated x–t diagram can be seen to successfully replicate the dominant wave processes in Fig. 2.3b. Primarily, the non-simple interaction between the Taylor rarefaction and the secondary rarefaction can be seen to accelerate the Taylor rarefaction into the driven section. Clearly, the velocity of the shock wave transmitted into the driven section is lower than the detonation wave velocity, evident from its larger slope. Further, this shock wave is continuously attenuated by the transmitted Taylor rarefaction through the secondary contact surface, an effect which was also seen in Fig. 3.11. From the transmitted waves in the driven section, it can be seen that the information about the detonation driver plateau pressure reaches the secondary contact surface just prior to the reflected shock wave–contact surface interaction. This information along with the experimentally observed decay in detonation driver plateau pressure, leads to the inference that the sudden drop in experimental pressure trace in Fig. 3.12b, around $t \approx 0.15$ ms must be due to the decaying plateau pressure in the detonation driver. Thus, the ability of the MoC detonation tube algorithm to quantitatively capture the reflected shock wave–contact surface interaction is deemed inconclusive for this validation case. Still, the qualitative aspect of this phenomenon is clearly well replicated by the MoC model as marked by the local wave process surrounding this CS–SW interaction labeled Fig. 3.13.

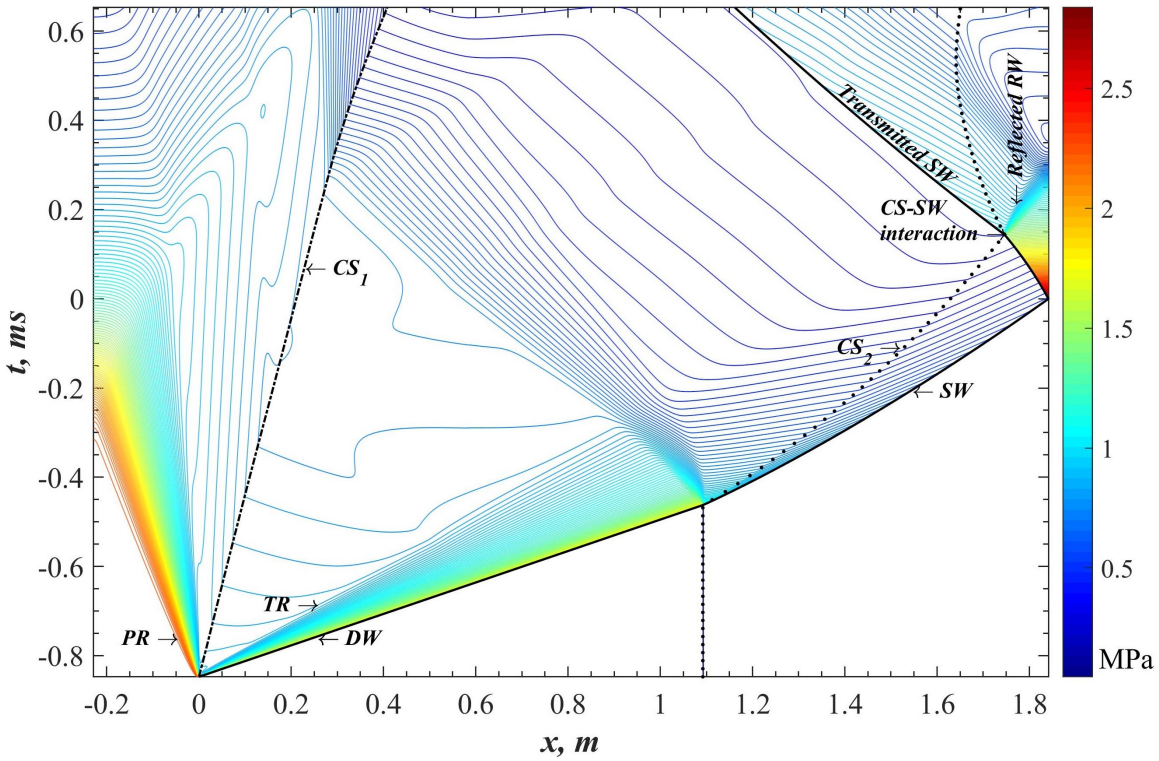

Figure 3.13: MoC generated flowfield evolution for Case 1 (also see Fig. 2.3b).

3.3.3.2 Case 2

Next, the MoC results for Case 2 are compared with experiments. Table 3.1 shows that Case 2 closely resembles Case 1 but for the use of helium as the driven gas. Apart from the objective mentioned in Table 3.1, this case may also be representative of a high-enthalpy detonation tube operation in that the transmitted shock velocity in the driven section is higher than the detonation wave velocity. This amplified transmitted shock velocity is evident from the detonation/shock wave velocities plotted in Fig. 3.14. Since the high-pressure/detonation driver assembly and initial fill conditions are the same as Case 1, the experimental and MoC detonation wave velocities in Fig. 3.14 resemble Case 1.

In contrast to Case 1, the incident shock velocity for the MoC/nonisentropic model is about 15 percent higher than the experimentally observed shock velocities. This discrepancy cannot merely be attributed to incorrectly estimated roughness values. While the setup wall roughness used in the nonisentropic model was estimated by comparing MoC and experimental results for Case 1, these values are expected to hold universally for this setup regardless of the working gases used. This may be further understood by realizing that the nonisentropic model utilizes relevant thermophysical properties for different gases and that the wall roughness is the only variable parameter. For Case 2, it turns out that the mismatch in experimental and MoC shock trace was instead due to gaseous contamination in the driven section. Detailed analysis of this experimental anomaly is performed in a following subsection. But, it will be seen that the contamination only affects the magnitude of the plots shown here, while the qualitative flowfield observed in the contaminated driven gas still matches that of a pure driven gas scenario. Therefore, the MoC flowfield obtained here for pure helium can still be used to qualitatively discuss the flowfield evolution for Case 2.

Figure 3.14 shows that the multi-isentropic model overestimates the incident shock velocity at the endwall by about 21 percent compared to the nonisentropic model. The adjusted ToF calculated for the nonisentropic model shows that the effect of recess ports is negligible when the calculations are carried out over two equally recessed transducers. For the combination of recessed and flushed transducers, the adjusted ToF severely overestimates the experimentally observed shock velocity, clearly due to the overestimated incident shock velocities from the MoC model. Figure 3.14 further shows that the reflected shock wave from the endwall accelerates into the oncoming secondary contact surface. The abrupt attenuation of this shock wave as a result of its interaction with the contact surface indicates that a reflected shock wave forms due to this interaction, as opposed to the reflected rarefaction wave that was

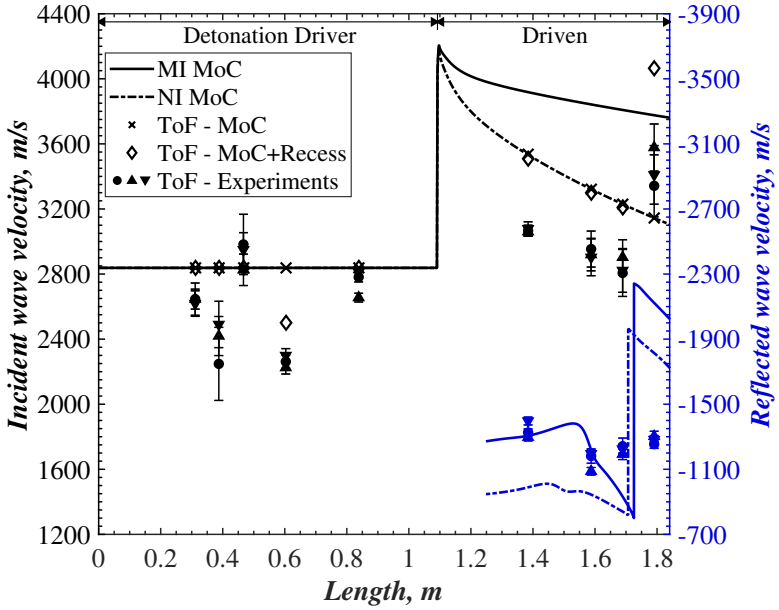

Figure 3.14: Shock/detonation wave velocity comparison: Case 2 (MI: Multi-isentropic, NI: nonisentropic).

observed in Case 1. Additionally, after this interaction, the velocity of the transmitted shock wave can be seen to increase suddenly around $x \approx 1.5$ m, due to an overtaking weak shock wave, see Fig. 3.16.

Figure 3.15 contains the experimental and MoC pressure traces at various transducer locations in the detonation driver and driven sections. Individual pressure traces in the detonation driver and driven sections are displaced vertically by the same units as Case 1. From Fig. 3.15a, the mismatch in the arrival of the detonation wave at all the transducer locations is obvious, even for XDR6 and XDR7, which display almost CJ detonation wave velocity in Fig. 3.14. Since the incident shock wave velocity in the driven section is overestimated by MoC, the time interval between the chosen origin and the arrival of detonation wave at various transducers is shortened, which is seen as the mismatch described above. However, it is seen that the initial

plateau pressure at XDR2 still matches well between experiments and MoC, as the effect of driven gas contamination will only be communicated to the detonation driver gas by the arrival of secondary rarefaction wave.

Similar to Case 1, the experimental plateau pressure at XDR2 starts to decay about 0.55 ms after the arrival of detonation wave at this location and similar attenuation of plateau pressure amplitude is seen in XDR3 and XDR4. In the pressure traces for the driven section in Fig. 3.15b, the mismatch in the location of the initial pressure rise can again be seen between MoC and experiments. Further, similar to Case 1, the experimental pressure trace for XDR8 is higher than the MoC values, despite the subsequent transducer locations showing lower pressure rise compared to MoC. This is attributed to the close proximity of XDR8 ($L/D \approx 8$) to the secondary diaphragm, which results in the recessed transducer capturing the initial stronger shock wave that is formed during diaphragm rupture. At XDR11, the experimental pressure trace can be seen to lag to an extent that the reflected shock wave reaches this location before a steady, nearly plateau pressure is attained. At the endwall, the MoC pressure trace is lower that the experimental pressure trace, despite the MoC overestimating the incident shock wave velocity in the driven section, as seen in Fig. 3.14. However, similar to the experiment, a weak reflected shock from the shock wave–contact surface interaction can be seen to reach the endwall at around 0.1 ms in the MoC pressure trace. Further, as the secondary contact surface nearly stagnates before XDR11, the MoC pressure trace for XDR11 shows the initial reflected shock wave from the endwall, followed by the right traveling weak reflected shock wave from the shock wave–contact surface interaction and finally, the return of this weak reflected shock wave from the endwall. This re-reflected weak shock wave can further be traced to the MoC pressure traces at XDR10 and XDR9.

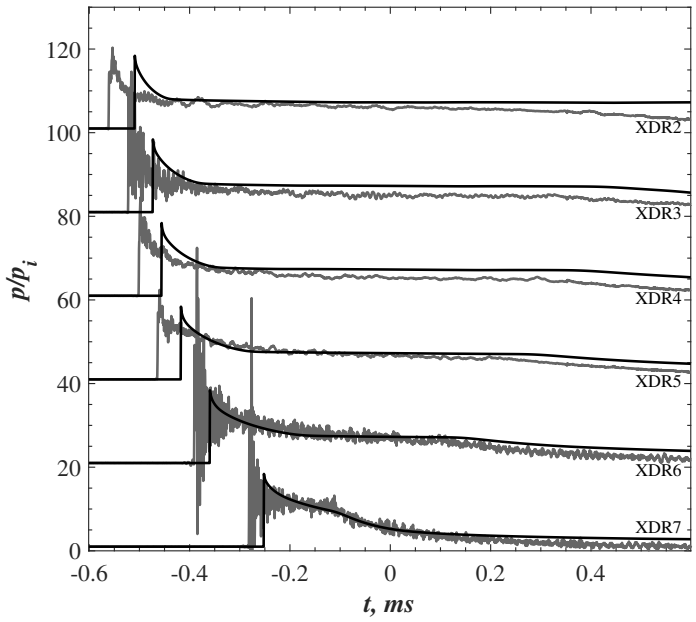

(a) Detonation driver.

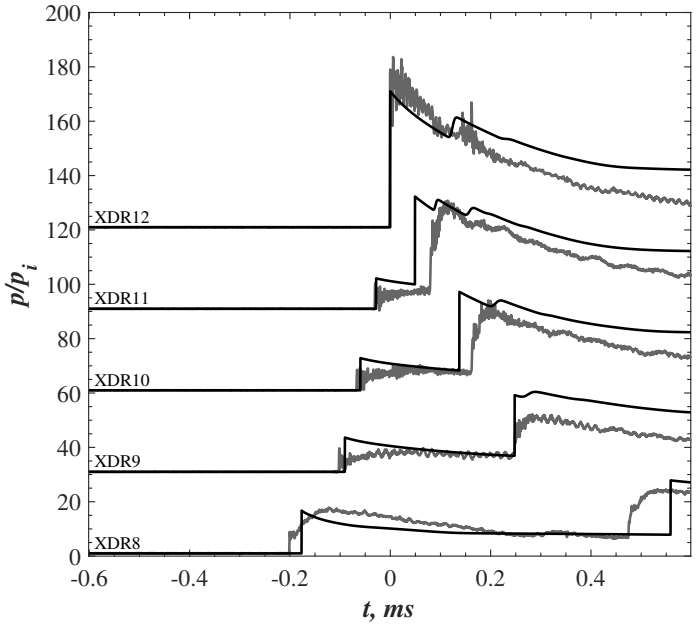

(b) Driven section.

Figure 3.15: Comparison of MoC and experimental pressure traces for Case 2.

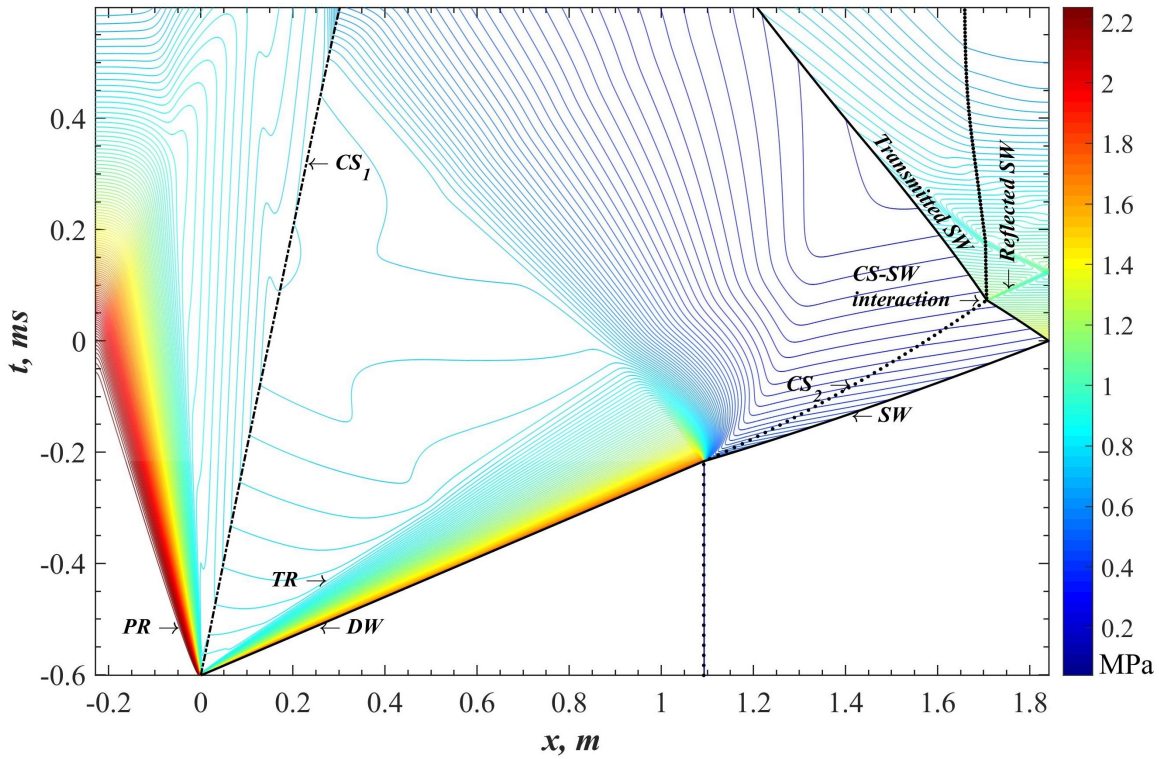

Figure 3.16: MoC generated flowfield evolution: Case 2 (also see Fig. 2.3b).

The overall flowfield for Case 2 as resolved by MoC is shown in the x–t plane in Fig. 3.16. The high-pressure driver and detonation driver flowfield can be seen to match Case 1, until the secondary rarefaction reaches the primary contact surface around $t \approx 0.5$ ms. (Note the change in ordinate scale compared to Case 1.) Since the driven gas is accelerated to high velocities, the secondary rarefaction for Case 2 is significantly stronger than Case 1, as observed in Fig. 3.16. The higher incident shock wave velocity is again obvious from its lower slope compared to the detonation wave in the detonation driver section. However, this higher shock velocity also results in a shorter time interval between the rupture of secondary diaphragm and the eventual reflected shock wave–contact surface interaction. Thus, the Taylor rarefaction can still be seen overtaking the secondary contact surface while the shock wave–contact surface interaction takes place. While this scenario is not expected for an optimally

designed detonation tube, parametric analyses to reach such a design may encounter it. Despite the overtaking trailing characteristics of the Taylor rarefaction wave, the shock wave–contact surface interaction almost stagnates the secondary contact surface resulting in a weak reflected shock wave into the driven gas. From the spatial extent of the weak reflected shock wave at a given t-line, its Mach number is inferred to be nearly unity, as such shock waves are merely resolved as compression waves by the detonation tube algorithm. This weak reflected shock wave is further reflected back from the endwall and reaches the secondary contact surface, resulting in a weak transmitted shock wave and a weak reflected rarefaction wave at the interface around $t \approx 0.16$ ms. Furthermore, this transmitted weak shock wave merges with the original transmitted shock wave around $t \approx 0.3$ ms. As has been seen already, the dynamics of this weak reflected shock can also be traced in the pressure traces at various driven transducers in Fig. 3.15b.

3.3.3.3 Case 3

Lastly, MoC results for Case 3 are compared with experimental results. The shock/detonation wave velocities are again compared initially, as shown in Fig. 3.17. Despite the shorter detonation driver than Cases 1 and 2, the detonation wave velocities in the available section resemble Cases 1 and 2 as expected. Since the initial fill condition is the same as Case 1, the initial transmitted shock wave velocity in the driven section is also the same as Case 1. However, the longer driven section results in higher attenuation of the incident shock wave compared to Case 1. Quantitatively, MoC shock velocities differ from experimental ToF values by a maximum of about three percent, except for the last ToF value. At the last ToF location, MoC underestimates the experimental shock velocity by an average of 27 percent. However, when the MoC ToF calculation accounts for the combination of recessed and flushed trans-

ducers, the accuracy improves, with the resulting shock velocity at this location being overestimated on an average by 5 percent. In this case, the multi-isentropic model overestimates the incident shock wave velocity at the endwall by about 32 percent compared to the nonisentropic model. Thus, the effect of heat and frictional losses is increasingly observed on the incident shock wave velocity as its total traveling distance increases. Naturally, this also leads to a lower velocity reflected shock wave from the endwall, as seen in Fig. 3.17.

Moreover, the location of shock wave–contact surface interaction moves further into the driven section compared to Case 1, as the attenuated contact surface trails farther behind the incident shock wave. But similar to Case 1, the shock wave–contact surface interaction amplifies the reflected shock wave from the endwall. As this transmitted shock wave moves further into the burnt gas slug, the MoC trace depicts a decelerating shock wave, while the experiments indicate that it accelerates instead. Subsequent discussions on the detonation driver gasdynamics are expected to reconcile this discrepancy, as the MoC pressure traces will be seen to deviate from experiments further into the detonation tube operation, see Figs. 3.18 and 3.19.

The pressure traces at individual transducer locations from both experiments and MoC are shown in Fig. 3.18. The magnitude of plateau pressures at XDR2 is identical between Case 3, shown in Fig. 3.18a and the previous cases, Figs. 3.15a and 3.12a. Due to the shorter detonation driver length, the secondary rarefaction wave can be seen to reach XDR2 significantly earlier as evident by the temporally shorter plateau pressure. Interestingly, here, the MoC model accurately estimates not only the arrival of the secondary rarefaction wave, but also the associated magnitude of pressure decay. At XDR2, the MoC model indicates an increase in static pressure after $t \approx -0.25$ ms, while the experimental pressure trace still shows a decay.

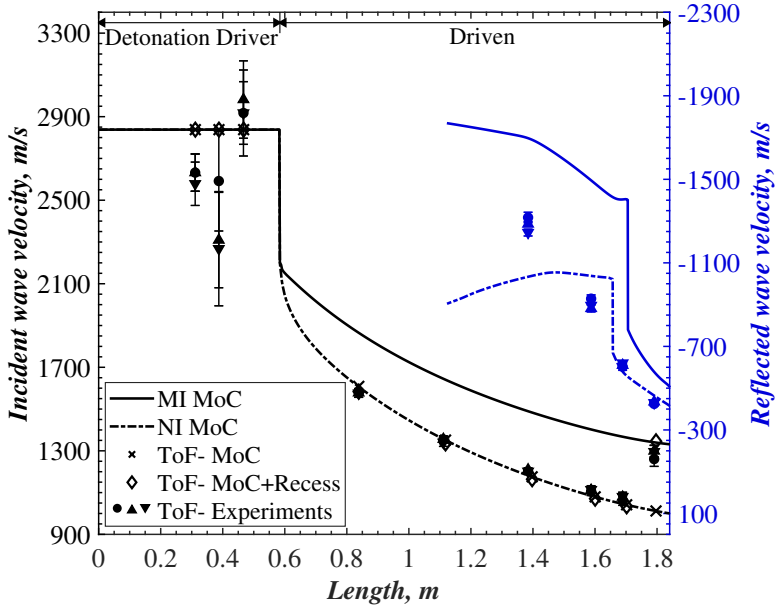

Figure 3.17: Shock/detonation wave velocity comparison: Case 3 (MI: Multi-isentropic, NI: nonisentropic).

The abovementioned traits are also observed qualitatively at XDR3. The experimental pressure trace at XDR4 shows a more rapid decay of plateau pressure than MoC, yet, the arrival of the secondary rarefaction wave at this location is coincident with that of MoC. XDR5 on the other hand shows significant difference in the magnitudes of pressure traces between experiments and MoC. Closer inspection of the experimental pressure trace at XDR5 reveals a sudden pressure spike around $t \approx -0.96$ ms, indicative of a reflected shock wave from the rupture of secondary diaphragm. This, in addition to the idealized centered secondary rarefaction wave considered in the MoC, is inferred to produce the pressure trace deviation observed at XDR5.

The corresponding pressure traces for the driven section are shown in Fig. 3.18b. In this case, the first transducer in the driven section XDR6 is even closer to the

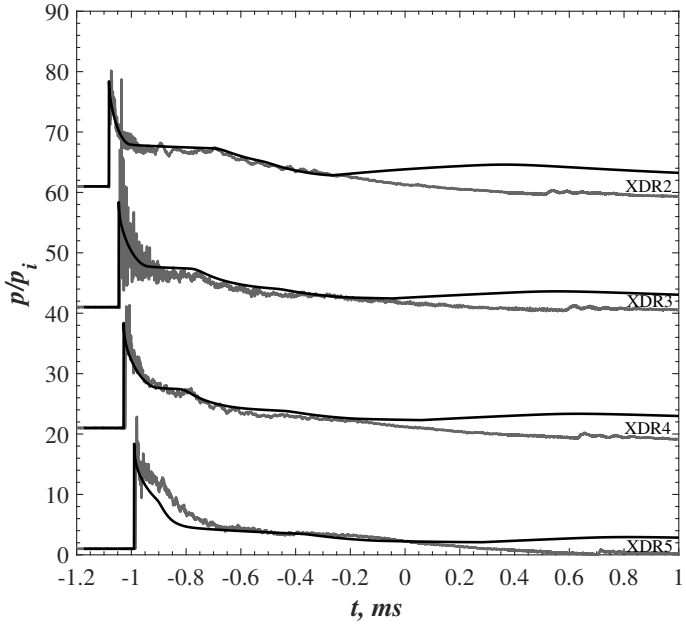

(a) Detonation driver.

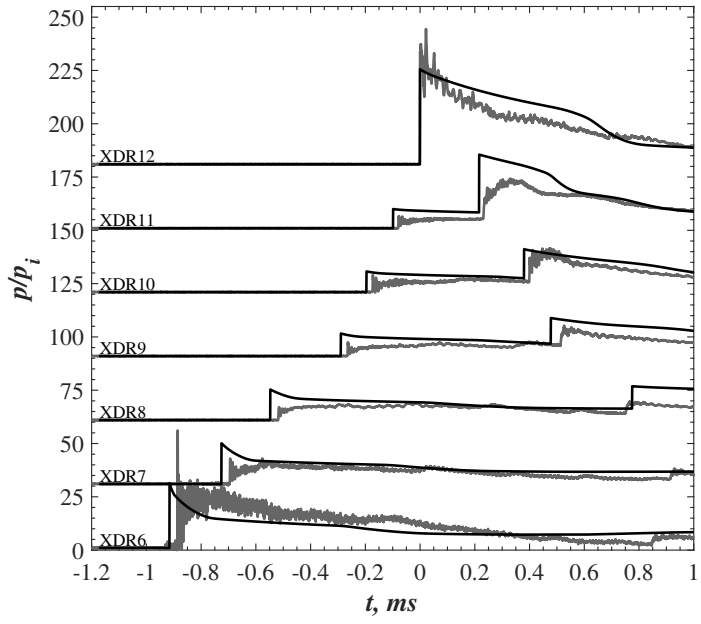

(b) Driven section.

Figure 3.18: Comparison of MoC and experimental pressure traces for Case 3.

secondary diaphragm than the previous cases (L/D $\approx$ 5). Hence, the experimental pressure trace at XDR6 is again higher than the MoC pressure trace. For transducers XDR6-XDR11, the arrival of the incident shock wave and thus the initial pressure rise in MoC pressure traces can be seen to occur earlier than the experiments, despite the close match in shock velocities seen in Fig. 3.17. This contradiction can be traced to the recessed transducers, which would clearly experience a delay in the arrival of the incident shock wave compared to a flushed transducer, which the MoC traces represent. Finally, the MoC pressure trace at the endwall, XDR12, captures the experimental peak pressure due to the reflected shock wave. But, the decay of the endwall stagnation pressure due to MoC is slower than experimentally observed.

The unsteady pressure contours for Case 3 are shown in Fig. 3.19 to elicit the dominant wave processes. Due to the heavily attenuated incident shock wave in the long driven section, the overall detonation tube operation time can be seen to increase significantly from Cases 1 and 2. In the short detonation driver, the secondary rarefaction can be seen to reach the primary contact surface at around $t \approx -0.6$ ms and accelerate it subsequently. Further, the secondary rarefaction wave is transmitted into the high-pressure driver gas, which also undergoes an expansion. Since the sonic velocity in the high-pressure driver gas is significantly lower than the burnt detonation driver gas, the transmitted secondary rarefaction can be seen to travel at much lower velocities in the former slug. Thus, the increase in static pressure in XDR2 displayed in Fig. 3.18a marks the arrival of the primary contact surface followed by the transmitted secondary rarefaction, which expands the high-pressure driver gas at slower rate than the burnt gas from where it originated. Note that the detonation tube algorithm considers instantaneous detonation wave formation and centered Taylor/primary rarefaction waves, neither of which are expected to occur in the experiments. This deviation in the initial condition for the primary contact

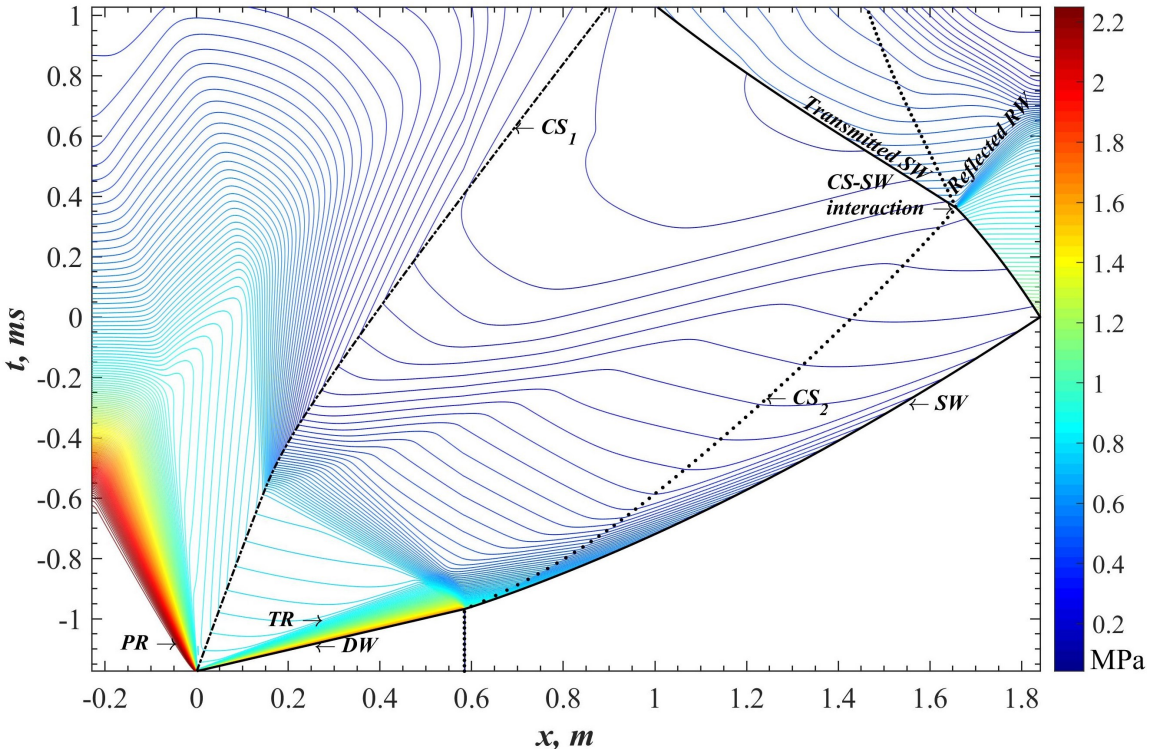

Figure 3.19: MoC generated flowfield evolution for Case 3 (also see Fig. 2.3b).

surface in addition to contact surface mixing is suspected to be the primary reason behind the mismatch surrounding the arrival of primary contact surface at XDR2 in Fig. 3.18a.

From the wave processes in the driven section, Taylor rarefaction is seen to be completely transmitted into the driven section even before the incident shock wave arrives at the endwall. Thus, the attenuation of the incident shock wave is due to a combination of the transmitted Taylor rarefaction and gasdynamic losses. The reflected secondary rarefaction wave also travels the entire driven section, is transmitted across the secondary contact surface and reaches the reflected shock wave seemingly decelerating it. The information brought in by this wave is reasoned to be the source of endwall stagnation pressure mismatch between MoC and experiments. Also, the

reflected shock wave–contact surface interaction observed in Case 3 is qualitatively similar to that of Case 1.

3.3.4 Effect of driven gas contamination

The noticeable deviation in shock velocities and pressure traces observed for Case 2 was also observed in an earlier version of this MoC model which utilized a constant C_f for all gases [63]. Such an approach was undertaken, as it had been successfully used to replicate experimental endwall pressure traces in pulse detonation engines with homogeneously filled propellant mixtures [53, 54]. Since the detonation tube considered here utilized multiple gas slugs instead of a homogeneous gaseous mixture, a variable C_f model incorporating individual gas thermophysical properties was expected to improve upon the MoC model. While this modification did improve the nonisentropic model results in terms of shock velocities and individual pressure traces, the results still overestimated the experimental incident shock velocities in the driven section by 15 percent, as seen earlier. Thus, supplemental reasons for this discrepancy were investigated to understand if the MoC model can resolve flowfields involving helium, which is an indispensable option as the driver and/or accelerator gas in impulse facilities.

Note that the detonation driver plateau pressures were estimated reasonably well by the MoC model for all cases; hence, the anomaly was restricted to helium as the driven gas. For a simple shock tube, the gasdynamic equilibrium which occurs between a driver and driven gas is also determined by the compressibility of the driven gas, which can be interpreted in terms of the pressure jump brought forth by the incident shock wave. For a given initial gas state, the Rankine–Hugoniot jump condition (see §3.1.4, for instance) shows that the pressure rise due to a normal shock wave is dependent on the gas density and γ. For a driven gas with known initial

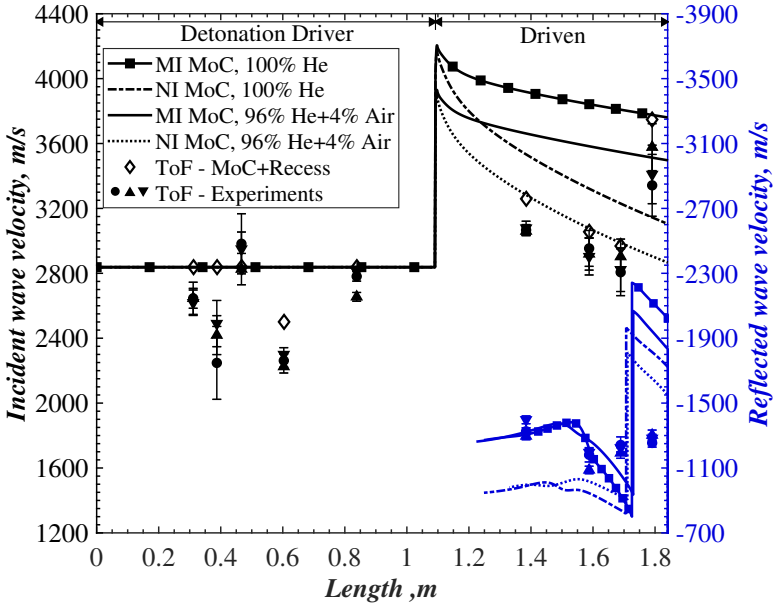

Figure 3.20: Shock/detonation wave velocity comparison: Case 2.

static pressure and temperature, both density and γ are dependent on its molecular weight which in turn depends on the mixture composition. Thus, driven gas contamination was suspected to cause the discrepancy between MoC and experimental results. Cross contamination between the detonation driver and driven sections were ruled out, since the experimental procedure ensured that the secondary diaphragm was intact immediately before each run. Thus, it was suspected that the contaminant was residual air that had entered the driven section during diaphragm replacement. As an arbitrary initial guess for air contamination, the manufacturer provided uncertainty for driven pressure gauge readings (Dwyer DPGA-00, 1 percent fullscale) was assumed, which already resulted in a good match between MoC and experimental results. Clearly, the overall results could also be tuned further by varying the amount of air contamination in the driven section. But, this has not been attempted here to restrict the scope of this phase of work.

Figure 3.20 contains the shock velocities for Case 2 with pure and contaminated helium for multi-isentropic and nonisentropic models. From the uncertainty in driven pressure gauge readings, the contaminant partial pressure can be determined, which in this case was four percent air consisting of nitrogen (78 percent), oxygen (21 percent) and argon (one percent). Note that the detonation-tube algorithm can resolve gaseous mixtures of arbitrary composition, utilizing Cantera to derive curve-fits for thermophysical properties of gaseous mixtures, which serve as the inputs for individual MoC subroutines. Here, a mere four percent air contamination causes the molecular weight of the driven gas to increase by 25 percent due to the significant difference in molecular weights between helium and air. Figure 3.20 shows that for contaminated helium, the initial incident shock velocity is lower than that for the pure helium case by about six percent. When gasdynamic losses are taken into account, the incident shock wave at the first ToF is overestimated by about 6 percent in the contaminated helium case, as opposed to 15 percent in the pure helium case. At the subsequent ToF locations, shock velocities due to contaminated helium can be seen to lie within experimental uncertainties of individual ToF values. At the last ToF location, MoC shock velocity accounting for recessed transducer again lies at one of the limits of experimental ToF uncertainty. Thus, it is seen that the adjusted ToF calculations based on geomteric shock dynamics estimate the effect of recess mounts remarkably well for different gases. Similar to previous cases, quantitative comparison cannot be drawn here for the reflected shock wave trajectory based on experimental ToF values.

Comparison of individual pressure traces between MoC accounting for contaminated helium and experimental results are shown in Fig. 3.21. From Fig. 3.21a, it is seen that the arrival of detonation wave at individual transducer is resolved more accurately by MoC compared to pure helium, Fig. 3.15a. Since the MoC model

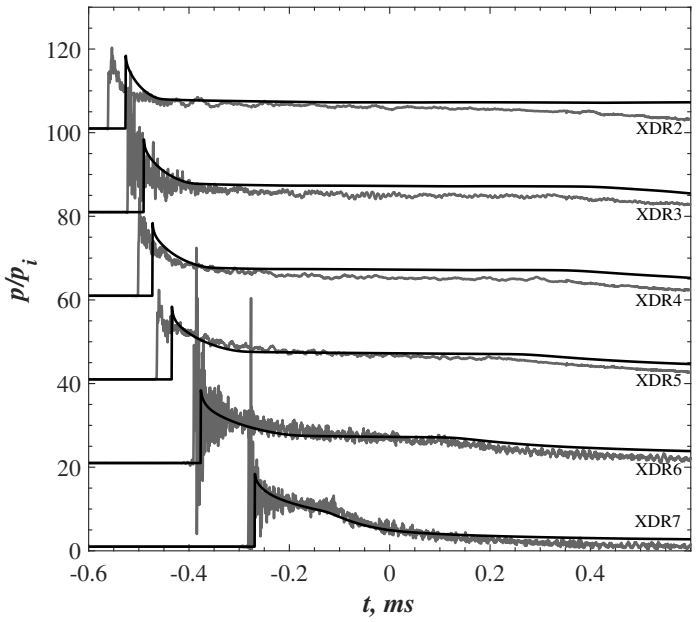

(a) Detonation driver.

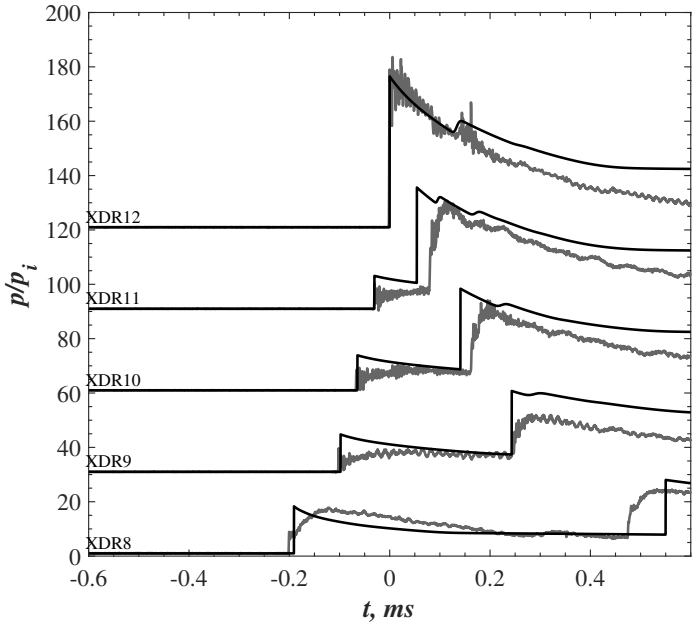

(b) Driven section.

Figure 3.21: Comparison of MoC and experimental pressure traces for Case 2.

still overestimates the incident shock wave velocity, arrival of the detonation wave at various transducers in the detonation driver still shows a mismatch, albeit, lesser than that of a pure helium case. But, as expected, the initial plateau pressures behind the detonation wave are similar to the pure helium case, as the effect of helium contamination is only communicated by the arrival of secondary rarefaction wave.

In the driven section pressure traces shown in Fig. 3.21b, the initial pressure rise for contaminated helium is always higher than the pure helium case. This is expected as the performance of a driver gas increases with the ratio of initial sonic velocities between driver and driven gases. With contaminated helium, as the gaseous mixture molecular weight increases, its sonic velocity decreases and thereby leads to higher pressure rise due to incident shock waves. Comparatively, the amplified pressure rise behind the incident shock wave decreases from about 9.5 percent at XDR8 to about eight percent at XDR11 between contaminated and pure helium. At the endwall, contaminated helium experiences about eleven percent higher pressure rise than pure helium. Clearly, the MoC stagnation pressure due to contaminated helium matches very well with experiments until the arrival of the reflected shock wave from shock wave–contact surface interaction in the driven section. Additionally, the strength of this reflected shock which reaches the endwall at $t \approx 0.12$ ms is weaker than that observed in the pure helium case, but can be seen to agree well with experiments.

As was remarked in the discussion earlier, despite the observed differences in magnitude in the gasdynamic quantities, the flowfield phenomena are qualitatively similar between contaminated and pure helium cases. However, when the driven gas is pure nitrogen, the effect of contamination will not be pronounced in the experimental data reported here, due to the similarity in molecular weights of nitrogen and air. Additionally, in the case of the detonation driver, reasonable match in plateau pressures behind the detonation wave was obtained between experiments and MoC

for all cases. Moreover, higher fill pressures and the simultaneous use of a pressure gauge and a pressure transducer are also expected to mitigate the possibility and effect of contamination in the detonation driver.

CHAPTER 4

PRELIMINARY METHOD-OF-CHARACTERISTICS MODELS FOR FLOWS IN CHEMICAL NONEQUILIBRIUM[1]

Chapter 3 showed that IMoC algorithms can reliably estimate the gasdynamic flowfield in a low enthalpy, detonation-driven shock tube. This chapter investigates the feasibility of extending the IMoC approach to flows experiencing finite-rate chemical reactions. Despite the inclusion of chemical source terms in the governing equations, the final MoC form will be shown to be similar to the calorically perfect form seen earlier. Thus, the original IMoC algorithm can be modified to account for the chemical reactions occurring in the flowfield.

Before introducing the modified governing equations for nonequilibrium flows, some aspects of high-temperature gasdynamics need to be outlined. As opposed to low-enthalpy flows, which can afford a standalone macroscopic treatment, it will be seen in Chapters 4 through 7, that high-enthalpy flows generally require a hybrid macroscopic–microscopic approach. Such a treatment is due to the fact that the laws governing the redistribution of internal energy, for instance, are built from an understanding of the underlying microscopic processes. From a molecular viewpoint, any change in the state of a gas is assumed to be purely driven by particle collisions, be it thermal or chemical. The magnitude of particle collisions required for various

[1]Contains excerpts from the paper entitled 'A Method of Characteristics Solver for Unsteady Quasi-One-Dimensional Chemically Reacting Gas Flows' by Jayamani, A., and Lu, F. K., AIAA Paper No: 2021-0315

state changes to occur vary appreciably which inevitably leads to orders of magnitude difference in time scales between these phenomena.

Based on the dominant processes of interest, two different time scales can be defined, for the ease of discussion and for solving the appropriate governing equations. First defined is the faster of the rate processes [95]—redistribution of internal energy, called thermal time scale and denoted by $\tau_{r,t}$. (In the scope of this chapter, the primary thermal state change that can occur at a finite rate is the vibrational excitation/relaxation of the molecular species.) The second time scale concerns the chemical rate processes—dissociation, or recombination and will be denoted by $\tau_{r,c}$. Finally, for any gasdynamic flow process, a unit flow time scale can be defined as τ_g.

The abovementioned time scales should be considered local and so, at various locations in a flowfield, they can assume different values. Thus, for any gasdynamic flow, the thermal and chemical rate processes can be categorized under three groups, based on the competition between these time scales. When the flow time scale vastly outpaces the relaxation time scale $\tau_g \ll \tau_r$, the gaseous molecules/atoms do not undergo enough collisions to bring about the relevant state change. Therefore, the gas can be assumed to be "frozen" in its initial state, which is called frozen flow. On the other end of the spectrum is equilibrium flow. In this case, the relaxation time scale vastly outpaces the flow time scale $\tau_r \ll \tau_g$; thus, the gas state can be assumed to adapt instantaneously to any flow change. Between these two extremes is a region where the relaxation time scale is of the same magnitude as the flow time scale $\tau_r \approx \tau_g$. Since both gasdynamic and thermochemical perturbations require time to adapt to each other, flows exhibiting this nature are known as a nonequilibrium flows.

In the discussions so far, a general notion τ_r has been maintained for the relaxation time scale. As discussed in Chapter 1, thermal and chemical nonequilibrium

can be treated separately from a theoretical standpoint. Further, flows involving finite-rate chemical reactions may at times be simplified by assuming that the rate processes for thermal relaxation occur at infinite speeds [95]. This simplification is assumed to hold in all the discussions in this chapter with further justifications provided in subsequent discussions. Therefore, it is underscored that the term chemical nonequilibrium in this chapter carries with it the assumption of thermal equilibrium. Such a simplification is also advantageous for algorithm development due to the reduction in computational complexity compared to simultaneous thermochemical nonequilibrium.

This chapter reports the initial investigation into the feasibility of extending IMoC algorithms to accommodate chemical nonequilibrium. The governing equations discussed in Chapter 3 were modified to account for finite-rate chemical reactions and were simplified again using MoC. Sample inverse marching algorithms were developed with which validation studies were carried out. To check for generality, two different reaction mechanisms available in the literature were used in the validation studies. It is stressed that the reliability of the chemical mechanism files themselves have not been studied here. Instead, assuming a sample mechanism file to be appropriate, IMoC algorithms are used to solve a representative problem. Corresponding analytic solutions are also solved using the same mechanism file to test the validity of MoC algorithms. Since the algorithms developed here can utilize an arbitrary chemical mechanism file, it is assumed that this approach is acceptable. Finally, the results from these validation studies show that IMoC algorithms can be successfully extended to chemically reacting flows.

4.1 Governing equations

In this theory section, assumptions pertaining to thermochemistry are presented initially, following which the overall governing equations for a chemically reacting gas flow are presented. Consider a gaseous mixture which contains n species. Each species is assumed to be thermally perfect, obeying its respective perfect gas law. Thus, for a gaseous mixture containing n species

$$p_i = \rho_i R_i T \qquad (i = 1, 2, \ldots, n) \quad (4.1)$$

In the above equation, the assumption of thermal equilibrium reduces the static temperature of the gaseous mixture to a single value. By definition, a perfect gas does not experience intermolecular forces. When a perfect gas is in thermal equilibrium, it may be argued on molecular kinetic grounds that every gaseous particle behaves as though the remaining particles were absent [95]. Thus, the static pressure exerted on any control surface in the system is purely based on the momentum of particles interacting with the surface. For such a gaseous mixture of perfect gases, the net static pressure exerted by the random molecular motion of the mixture on any surface is merely the addition of the individual species pressures, given in Eq. (4.1). This is generally known as Dalton's law of partial pressures, where p_i is the partial static pressure exerted by a gaseous species i.

$$p = \sum_{i=1}^{n} p_i \quad (4.2)$$

Combining Eqs. (4.1) and (4.2) and using the definition for mass fraction $c_i \triangleq \rho_i/\rho$ a global gas law can written as

$$p = \rho \sum_{i=1}^{n} c_i R_i T \quad (4.3)$$

where the subscript denotes individual species. From the above equation, the mixture's gas constant becomes

$$R_{mix} = \sum_{i=1}^{n} c_i R_i \tag{4.4}$$

Assume that the considered gaseous mixture is chemically reactive with various species denoted by $\mathbb{A}_i$. Let all the j possible elementary reactions occurring in the mixture be given by

$$\sum_{i=1}^{n} \nu'_{ij} \mathbb{A}_i \underset{k_{bj}}{\overset{k_{fj}}{\rightleftharpoons}} \sum_{i=1}^{n} \nu''_{ij} \mathbb{A}_i \qquad (j = 1, 2, \ldots, m) \tag{4.5}$$

where the number of moles of the reacting species are denoted ν' and that of the products as ν''. At any given time, the reactions shown above proceed in both the forward, that is, left-to-right, and in the backward, right-to-left directions. Associated with the progress of these reactions are forward and backward reaction rate constants denoted by k_f and k_b respectively. Based on the local thermodynamic state of the mixture, the reactions in forward or backward direction may dominate. It is also possible that the forward and backward rates balance each other, in which case thermochemical equilibrium holds. Clearly, when the mixture is in thermochemical equilibrium, no spontaneous change of state should occur, thus the state of the mixture is independent of time. However, if the reactions are not in equilibrium, then the concentration of species $[\mathbb{A}_i]$ in the mixture would vary with time. The rate of production (or depletion) of species in the mixture is given by the species source function $\sigma_{i,\mathcal{N}}$

$$\overline{\sigma}_i = \frac{d[\mathbb{A}_i]}{dt} \tag{4.6}$$

where $\overline{\sigma}_i$ denotes molar species source function for gaseous species i. This term can be evaluated based on the law of mass action, which states that "*the rate at which an elementary reaction proceeds is proportional to the product of the molar concentration*

of the reactants raised to the power of their respective stoichiometric coefficients in he reaction equation" [49]. The proportionality constant is the reaction rate constant k_f when a forward reaction is considered. Thus,

$$\text{Reaction Rate} = k_f \prod_{i=1}^{n} [\mathbb{A}_i]^{\nu_i'} \tag{4.7}$$

Hence, the change in species concentration due to the forward reaction in an elementary reaction is given as,

$$\frac{d[\mathbb{A}_i]}{dt} = (\nu_i'' - \nu_i') \times \text{Reaction Rate} \tag{4.8}$$

which then becomes

$$\frac{d[\mathbb{A}_i]}{dt} = (\nu_i'' - \nu_i') k_f \prod_{i=1}^{n} [\mathbb{A}_i]^{\nu_i'} \tag{4.9}$$

A similar equation holds for the backward reaction so the net change in the concentration of species $\mathbb{A}_i$ due to a single elementary reaction becomes

$$\frac{d[\mathbb{A}_i]}{dt} = (\nu_i'' - \nu_i') \left[k_f \prod_{i=1}^{n} [\mathbb{A}_i]^{\nu_i'} - k_b \prod_{i=1}^{n} [\mathbb{A}_i]^{\nu_i''} \right] \tag{4.10}$$

Finally, when all j possible reactions are considered, the overall change in species concentration of $\mathbb{A}_i$ becomes

$$\overline{\sigma}_i = \left. \frac{d[\mathbb{A}_i]}{dt} \right|_{net} = \sum_{j=1}^{m} (\nu_{ij}'' - \nu_{ij}') \left[k_{fj} \prod_{i=1}^{n} \left(\frac{\rho c_i}{\mathbb{M}_i} \right)^{\nu_{ij}'} - k_{bj} \prod_{i=1}^{n} \left(\frac{\rho c_i}{\mathbb{M}_i} \right)^{\nu_{ij}''} \right] \tag{4.11}$$

where the molar concentration $[\mathbb{A}_i]$ is rewritten for ease of calculations. Since the gasdynamic governing equations are generally written on a mass basis, the species source function is likewise rewritten using its molecular weight $\mathbb{M}_i$, namely,

$$\sigma_i = \mathbb{M}_i \overline{\sigma}_i \tag{4.12}$$

Equation (4.11), in its current form, requires that the rate constants for both forward and backward reactions be known. This is often impractical and/or redundant since the rate constants are generally obtained through experiments as will be

discussed shortly. Fortunately, an expression can be obtained for the relation between these rate constants when equilibrium holds. It is then assumed that the same relation also holds at nonequilibrium conditions [95, 103]. At equilibrium with the forward and backward reaction rates balancing each other, the species source function is null and Eq. (4.11) simplifies to

$$\frac{k_{fj}}{k_{bj}} = \prod_{i=1}^{n} \left(\frac{\rho c_i}{\mathbb{M}_i} \right)^{\Delta \nu_{ij}} \qquad (j = 1, 2, \ldots, m) \quad (4.13)$$

where $\Delta \nu = \nu''_{ij} - \nu'_{ij}$. At equilibrium, chemical thermodynamics stipulates that the species concentration of a gaseous mixture be related to the equilibrium constant through

$$K_{pj} = (\mathcal{R}T)^{\Delta \nu_j} \prod_{i=1}^{n} \left(\frac{\rho c_i}{\mathbb{M}_i} \right)^{\Delta \nu_{ij}} \qquad (j = 1, 2, \ldots, m) \quad (4.14)$$

From Eqs. (4.13) and (4.14), the relation between forward and backward rate constants becomes

$$\frac{k_{fj}}{k_{bj}} = K_{pj} (\mathcal{R}T)^{(\nu'_{ij} - \nu''_{ij})} \qquad (j = 1, 2, \ldots, m) \quad (4.15)$$

The equilibrium constant K_{pj} in the above equation is calculated based on the molar Gibbs free energy at thermochemical equilibrium as

$$\ln K_{pj} = -\frac{\Delta \overline{\mu}}{\mathcal{R}T} = -\frac{1}{\mathcal{R}T} \left[\sum_{i=1}^{n} \Delta \nu_i (\overline{h}_i - T \overline{s}_i) \right] \qquad (j = 1, 2, \ldots, m) \quad (4.16)$$

where the overline again indicates properties written on a molar basis. Additionally, $\overline{h}_i$ and $\overline{s}_i$ are evaluated at a reference pressure of one bar [104] and the molar enthalpy $\overline{h}_i$ in the above equation also includes the enthalpy of formation of a given species i.

The reaction rate constants utilized in Eq. (4.11) are obtained from experiments and fit into the Arrhenius form

$$k_f = A e^{(-E_a / \mathcal{R}T)} \quad (4.17)$$

where $A = BT^{\alpha}$ and is known as the frequency factor which represents the number of collisions occurring between the reacting particles. The parameter E_a is called the activation energy which is the minimum energy required for a colliding particle to enter a chemical reaction. Thus, the exponential term represents the fraction of particles with energies higher than the activation energy. As seen from Eq. (4.17), the reaction rate constants only depend on the temperature of the gaseous mixture.

Finally, the governing equations for a frictionless, quasi-one-dimensional gas flow with no heat and mass transfer are given by

$$\frac{\partial \rho}{\partial t} + u\frac{\partial \rho}{\partial x} + \rho\frac{\partial u}{\partial x} + \rho u\frac{1}{A}\frac{dA}{dx} = 0 \tag{4.18a}$$

$$\rho\frac{\partial u}{\partial t} + \rho u\frac{\partial u}{\partial x} + \frac{\partial p}{\partial x} = 0 \tag{4.18b}$$

$$\rho\frac{\partial h}{\partial t} + \rho u\frac{\partial h}{\partial x} - \frac{\partial p}{\partial t} - u\frac{\partial p}{\partial x} = 0 \tag{4.18c}$$

where Eq. (4.18c) represents the combined energy and momentum equations. To obtain an energy equation similar in form to the perfect gas modules developed in Chapter 3, where the primary dependent variables were p, ρ and u, Eq. (4.18c) is modified using Eqs. (4.4) and (4.21), and the identity for global enthalpy $h \equiv \sum_{i=1}^{n} c_i h_i$ to yield

$$\frac{\partial p}{\partial t} + u\frac{\partial p}{\partial x} - a_f^2\left(\frac{\partial \rho}{\partial t} + u\frac{\partial \rho}{\partial x}\right) = \sum_{i=1}^{n}(\gamma_f R_i T - (\gamma_f - 1)h_i)\sigma_i \tag{4.19}$$

In Eq. (4.19), h_i includes both the heat of formation and the sensible enthalpy of species i. For dimensional consistency, the specific enthalpy h_i in this case is written on a mass basis as opposed to the molar basis form $\overline{h}_i$ used in Eq. 4.16.

Similar to the global continuity equation, Eq. (4.18a), in a chemically reacting gas flow, the rate of change of mass fraction of a species i can be related to its species source function as

$$\frac{\partial \rho_i}{\partial t} + u\frac{\partial \rho_i}{\partial x} + \rho_i\frac{\partial u}{\partial x} + \rho_i u\frac{1}{A}\frac{dA}{dx} = \sigma_i \qquad (i = 1, 2, \ldots, n) \tag{4.20}$$

Utilizing the global continuity equation Eq. (4.18a) and the definition of mass fraction, Eq. (4.20) can written as

$$\rho\left(\frac{\partial c_i}{\partial t} + u\frac{\partial c_i}{\partial x}\right) = \sigma_i \qquad (i = 1, 2, \ldots, n) \quad (4.21)$$

The gasdynamic conservation equations (4.18a), (4.18b) and (4.19) along with species continuity equation (4.21) represent the governing equations for an inviscid quasi-one-dimensional chemically reacting flow. Similar to the approach used in Chapter 3, these partial differential equations can be reduced to ordinary differential equations along the paths of disturbance propagation in the flowfield. Obviously, these paths and the variation of properties along them are given by characteristic and compatibility equations respectively. The characteristic equations in this case become

$$\left(\frac{dt}{dx}\right)_o = \lambda_o = \frac{1}{u} \quad (4.22a)$$

$$\left(\frac{dt}{dx}\right)_\pm = \lambda_\pm = \frac{1}{u \pm a_f} \quad (4.22b)$$

Equation (4.22a) shows that the pathline denoted by C_o is identical to the calorically perfect MoC form. The remaining two characteristics in this case employ chemically frozen sonic speed and are denoted by C_+ and C_-. It is again iterated that the flow is implicitly assumed to be in thermal equilibrium. For a flow in the positive direction, C_+ represents the propagation of information along the flow, while C_- represents the propagation of information against the flow direction. Additionally, from Eq. (4.21), it can be seen that the species continuity equation is already in characteristic form as it represents the material derivative of a fluid parcel traveling in space and time. The characteristic curve which represents its convection is simply the pathline, which is again intuitive, as the variation in gas chemistry can only

happen along its pathline. The compatibility equations valid on a pathline are given by

$$dp_o - a_f^2 d\rho_o = \sum_{i=1}^{n} (\gamma_f R_i T - (\gamma_f - 1)h_i)\sigma_i dt_o \tag{4.23}$$

$$dc_i = \frac{\sigma_i}{\rho} dt_o \qquad (i = 1, 2, \ldots, n) \tag{4.24}$$

Equation (4.24) can alternatively be written as

$$c_i dp_o - a_f^2 d\rho_i = a_f^2 \sigma_i dt_o + c_i \sum_{i=1}^{n} (\gamma_f R_i T - (\gamma_f - 1)h_i)\sigma_i dt_o \qquad (i = 1, 2, \ldots, n) \tag{4.25}$$

Equation (4.25) can be obtained either from Eqs. (4.24) and (4.23) or by following the MoC procedure in Zucrow and Hoffman [49] for a pathline. Obviously, Eq. (4.23) represents the variation of global mixture properties while Eq. (4.25) represents the evolution of species, both on a pathline. Note that the compatibility equations for a pathline have been rewritten with temporal derivative for the ease of numerical integration. Finally, the compatibility equations valid on the C_+ and C_- characteristics are given by

$$dp_\pm \pm \rho a_f du_\pm = \sum_{i=1}^{n} (\gamma_f R_i T - (\gamma_f - 1)h_i)\sigma_i dt_\pm - \rho u \frac{1}{A}\frac{dA}{dx} a_f^2 dt_\pm \tag{4.26}$$

Though the governing equations were derived assuming finite-rate chemistry, the species continuity equation can be simplified for analysis in the case of chemically frozen or equilibrium flows. For a frozen flow, the species production term is zero as $\tau_r \to \infty$ and thus the chemical composition remains fixed. In this case, the compatibility equations simply reduce to those representing an inviscid flow case in Chapter 3 and can be solved using the modules reported there, if the gas is calorically perfect. For a flow in chemical equilibrium, $\sigma \to 0$ identically as $\tau_r \to 0$, in which case a simpler chemical equilibrium analysis would provide the gas composition at

any thermodynamic state. It can be noted that flows in chemical equilibrium can still be solved numerically using the compatibility equations derived here as $\tau_r \to 0$ is physically impossible due to the finite number of molecular/atomic collisions required for chemical reactions. Moreover, the required time steps to capture species evolution near chemical equilibrium are extremely small, which results in higher computational cost. For such a case, supplemental chemical equilibrium calculations to predict species composition change can provide improved accuracy and lesser computational cost.

4.2 Numerical implementation

The solution algorithm utilizes the characteristic and compatibility equations developed in Section 4.1 with the inverse marching method detailed in Zucrow and Hoffman [49]. Briefly, the method calculates flowfield variables at a predefined grid point based on the properties of the characteristic curves that meet at that grid point. The characteristics themselves are found by iterative projection from the predefined grid point to an initial value line. Further simplifications can be applied to these characteristic and compatibility equations depending on the phenomena being involved, thereby resulting in different solution procedures. For this preliminary study, two such procedures were developed, which can be called to solve an appropriate problem. Staying true to Zucrow and Hoffman's terminology, these modules are called the interior point module and open-end point module, the description of which follows.

4.2.1 Interior point module

The interior point module reported here is similar to the unit process developed in Chapter 3. The algorithm reported here is modified from the calorically perfect modules to account for the chemical source terms in the compatibility equations.

The overall integration algorithm is split into two steps where the gasdynamic evolution and chemical evolution are calculated separately. Integration of the gasdynamic equations is still carried out using the modified Euler predictor–corrector method, but integration of the chemical rate equations is carried out using MATLAB™'s built-in stiff ordinary differential equations solver `ode15s` [105].

To calculate the gas dynamic evolution of a fluid parcel over a time step Δt, the characteristic curves in Eqs. (4.22a) and (4.22b) are discretized as

$$\Delta t_o = \lambda_o \Delta x_o \tag{4.27a}$$

$$\Delta t_\pm = \lambda_\pm \Delta x_\pm \tag{4.27b}$$

The corresponding compatibility equations on these characteristic curves are discretized as

$$\Delta p_o - a_f^2 \Delta \rho_o = \Omega \Delta t_o \tag{4.28a}$$

$$\Delta p_\pm \pm \rho a_f \, \Delta u_\pm = \Omega \Delta t_\pm - \rho u \frac{1}{A} \frac{\Delta A}{\Delta x} a_f^2 \Delta t_\pm \tag{4.28b}$$

where

$$\Omega = \sum_{i=1}^{n} (\gamma_f R_i T - (\gamma_f - 1) h_i) \sigma_i \tag{4.29}$$

Discretization of the chemical rate Eqs. (4.23) and (4.24) is not provided, as they are integrated using `ode15s` as detailed later.

The overall solution methodology for an interior point module is illustrated in Fig. 4.1a. Note that the origins of the C_+, C_- and C_o characteristics are denoted as x_+, x_- and x_o respectively. Provided with an initial value line 1–3, this module calculates various flow properties at grid point 4 (x_4). As the grid size is user determined, the values of Δx and Δt are known; thus, the location of x_4 is known. Further, in an unsteady, continuous quasi-one-dimensional flow, all three characteristics (Eqs. 4.22a

and 4.22b) must pass through every point in the space–time continuum [49]. Thus, the flow properties at x_4 can be calculated once the characteristics that intersect at this grid point are identified.

The algorithm begins with the integration of gasdynamic Eqns. (4.27a)–(4.28b) assuming thermochemically frozen properties on the characteristics. For the predictor step of a subsonic flow, consider the procedure for a C_o characteristic. An initial estimate for the origin of this characteristic, x_o, can be obtained by using the flow properties at grid point 2 to calculate the slope of C_o followed by projecting it backward in time to the line 1–2 from x_4. With the new location of x_o, flow properties at the origin of C_o are recalculated using linear interpolation between the encompassing points 1 and 2. Using the new properties obtained at x_o, C_o is reconstructed and the procedure is repeated to obtain better approximations for the slope of C_o. The iterations are finally terminated on convergence of the value of x_o. Note that for this case, only gasdynamic properties need to be interpolated since Eq. (4.27a) only requires values of u and a. At the final step, all the flow properties at the origin of C_o characteristic will be obtained. The same procedure is carried out for the C_+ and C_- characteristics, with the initial guesses for x_+ and x_- being grid points 1 and 3 for a subsonic flow. For a supersonic flow in the positive direction, the origin of the C_- characteristic shifts to the region between grid points 1 and 2, thus changing the initial guess and interpolating points. But the remaining characteristics and the overall calculation procedure remain the same as subsonic flow.

Once the locations and thereby the flow properties at the origins of all three characteristics have been determined, Eqs. (4.28a) and (4.28b) are utilized to solve for the flow properties at x_4, as these equations represent the variation of properties along the characteristics. In this case, however, interpolation of the chemical source terms in the compatibility equations is required. Quan et al. [57] report that the variation

of the source term Ω is generally not drastic even for rocket nozzles; thus, to solve Eqs. (4.28a) and (4.28b), the value of Ω is simply linearly interpolated based on data from adjacent grid points. This step would mark completion of the predictor step for an inert interior point module, as the gas dynamic properties at x_4 are obtained after solving the compatibility equations. For MoC of a chemically reacting mixture of gases, further integration of the chemical rate equation is necessary to obtain the species composition at x_4.

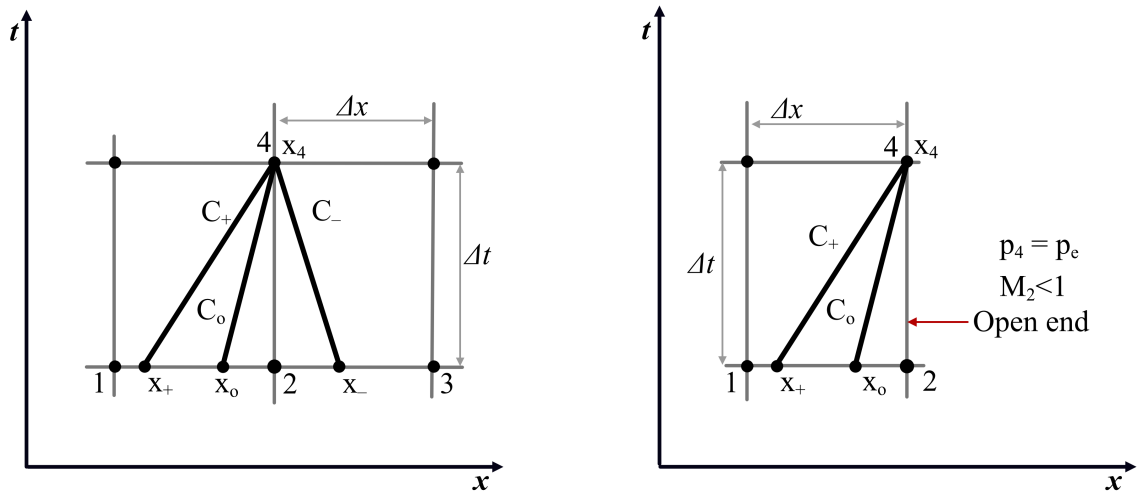

(a) Interior point module.

(b) Open-end point module.

Figure 4.1: MoC solution algorithm.

Once the thermochemically frozen gasdynamic evolution of the fluid parcel has been calculated, initial information on the evolution of properties along the pathline are obtained. This information is necessary for solving the chemical rate equations, as will be apparent further. The compatibility equations representing chemical and gasdynamic evolution of a fluid parcel are Eqs. (4.23) and (4.24), which are $n+1$ in number. However, to fix the state of a fluid, two state properties are necessary, in addition to the gas composition, thus totaling $n+2$ variables. To close the number

equations required to solve the problem, we can either use the density variation or static pressure variation calculated on the pathline from the frozen calculations. Since static pressure generally would be the least affected parameter in high temperature flows, the variation of pressure calculated from gasdynamic evolution is chosen over density variation. Essentially, we assume that the variation of pressure is linear over the time step, as we only know the values at the initial and end points. The initial values of mass fractions on the pathline to be integrated are obtained again by linear interpolation. Once the material derivative of static pressure and initial mass fractions on the pathline are fixed, Eqs. (4.23) and (4.24) can be integrated using `ode15s` to obtain the updated gas state properties at x_4.

The state properties of the gas mixture were evaluated using the Chemistry Subroutine described in Appendix B, both during integration of chemical rate equations and to obtain Ω at grid points 1, 2 and 3 for thermochemically frozen gasdynamic calculations. This procedure completes the predictor step for the finite–rate chemistry interior point solver. Subsequently, the corrector step involves repeating the same procedure as the predictor step, but using average flow properties for the coefficients of the exact/total derivatives in the compatibility equations and for the slopes of the characteristic curves. Repetitive application of the modified Euler predictor–corrector method along with the integration of chemical rate equations result in the convergence of required flow properties at x_4.

4.2.2 Open end point module

The open end point module, as the name suggests, deals with flow at the boundary of the domain being modeled. For simplicity, only the outflow condition is considered here. The characteristic curves for this module with a subsonic outflow are illustrated in Fig. 4.1b, from which it is seen that the C_- characteristic does not lie

within the flow domain. This complicates the solution procedure since the flowfield surrounding the outlet is necessary to close the number of required compatibility equations. This could be solved, however, if the flow at the exit is assumed to adjust itself immediately to the static pressure imposed by the surroundings, that is, $p_4 = p_{exit}$. With the value of p_4 known, the relations for C_+ and C_o characteristics can be used as detailed in the interior point module to calculate the density, velocity and mass fractions at the exit. For a supersonic flow on the other hand, all three characteristics originate within the domain and so the exit conditions do not influence the solution at x_4. Thus, the interior point solver could simply be used to solve such a scenario.

4.3 Validation studies

Validation of the modules discussed in Section 4.2 was carried out by modeling three different cases and comparing the results to existing methods in the literature. As the primary aim for developing these modules is to aid in parametric analyses of shock tubes and tunnels, only reduced chemical mechanism files were used since these require significantly fewer Jacobian evaluations during integration of the chemical rate equations. All the mechanism files use modified Arrhenius rate expressions to represent the rate constants for various elementary reactions. Thermodynamic properties for individual elements in these mechanism files were modeled based on NASA Glenn curvefits developed by McBride et al. [104]. With the equations in §4.1, the NASA Glenn curvefits were used to calculate equilibrium reaction constants, when the forward reaction rates alone were known in a chemical mechanism.

Though the modules could solve both steady and unsteady flows, current studies were limited to cases of finite-rate chemistry in steady flows, due to the ready availability of data and methods for validation of steady-state scenarios. Thus, the

final solutions were obtained by setting up a domain with initial values followed by marching forward in time until a specific convergence criteria were met. For the first two cases described in this section which are one-dimensional, the flowfield was said to have converged when all the axial static pressure values varied by less than 1 Pa for two consecutive steps. For the nozzle simulations, flowfield convergence criterion was said to be achieved when all the mass fractions in the domain converged to within 10^{-5} over successive time steps and the associated temperatures converged to within 0.1 percent (absolute error was less than 1.5 K). Experience showed that this was more stringent than the static pressure convergence criterion used in the previous cases.

4.3.1 One-dimensional supersonic combustor

The first flowfield that was resolved using the new MoC subroutines represented the simple scenario of supersonic combustion in a one-dimensional duct. The inlet conditions were specifically chosen to ensure that the gas velocities remained supersonic when the reactions go to completion. As the simulated flowfield of interest spans across the region undergoing chemically reactions, the supersonic flow condition simplified the development of the MoC combustor model as detailed later. A fully premixed, stoichiometric hydrogen–air mixture was assumed to be continuously injected at the inlet. This gaseous mixture was also set to a static temperature significantly above the autoignition temperature of hydrogen. With high inlet velocities and mixture temperatures, the chemical reactions occurring the gaseous mixture can be studied in the flowfield, as the gas flows through the computational domain. Specific details about the boundary conditions and the domain are provided in Table 4.1. A reduced mechanism for H_2–O_2–N_2 combustion based on Shang et al. [106] was used. This mechanism contains six reacting species and one inert species with a seven-step

reaction kinetics. The rate data for all the reactions considered in this mechanism are provided in Appendix A.

Table 4.1: Boundary conditions for supersonic combustor simulation

Case	M_{inlet}	P_1 [Pa]	T_1 [K]	u_1 [m/s]	P_e [Pa]	L [m]	Gas
1c	2.25	101 325	1 500	1 996	N/A	0.1	$2H_2 + O_2 + 3.76N_2$
2c	3	101 325	1 500	2 661	N/A	0.2	$2H_2 + O_2 + 3.76N_2$

Since the flow through the entire combustor is expected to remain supersonic, the exit conditions do not influence the flowfield inside the combustor and so this case could be entirely modeled using the interior point module. Thus, to simulate the reaction zone, the length of the domain was fixed at 99 percent of the length required to reach equilibrium temperature. Additionally, in this case, as mentioned above, information propagation happens only in the downstream direction; thus, conditions at the inlet completely define the flowfield in the domain. Therefore, the global algorithm consisted of applying interior point module repetitively from the inlet to the outlet.

The algorithm was initiated by assuming that the entire domain was in the same condition as the inlet and the solution was marched forward in time to achieve steady state. A grid study was performed for Case 1c, as the overall reaction length was shorter for this case. To fix the grid size, four different cases were run with cell sizes of 2.00, 1.00, 0.50 and 0.33 mm. The resulting temperatures were compared to the benchmark solution (discussed below). The maximum deviation in temperature over the entire domain was found to be $\sim$ 15.6, 6.3, 2.4 and 1.6 percent respectively for the cell sizes. An accuracy of 2.4 percent was deemed acceptable for the purpose of this preliminary study and a grid size of 0.5 mm was chosen to simulate both the

cases. The temperature profiles in the combustor due to various grid sizes considered are shown in Fig. 4.2.

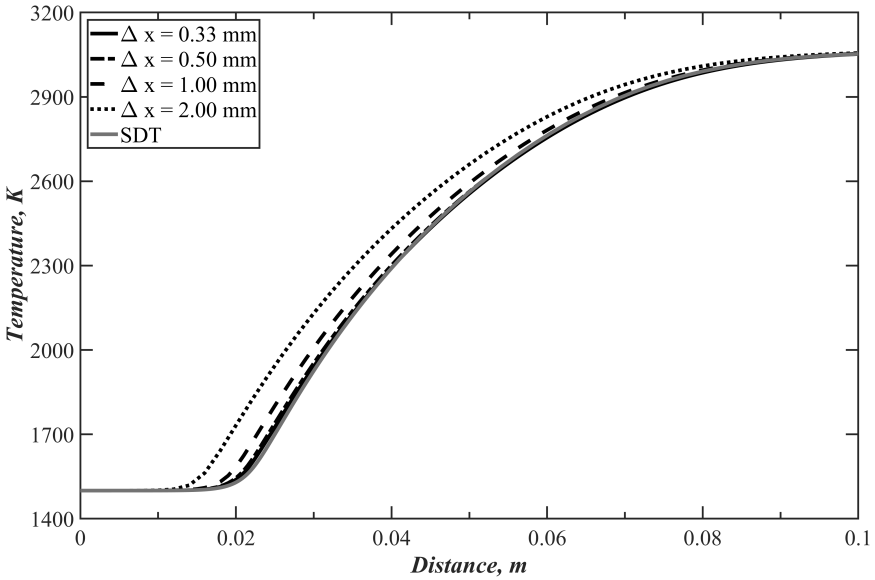

Figure 4.2: Temperature profile variation with grid size.

Finally, results obtained here were compared to the those obtained using the `zndsolve` module in the Shock and Detonation Toolbox (SDT) [107], which was equivalent to the steady-state case modeled here. A comparison of temperature and Mach number for Case 1c is given in Fig. 4.3a, with the corresponding comparison of molefractions given in Fig. 4.3b. A similar comparison for Case 2c is given in Figs. 4.4a and 4.4b, for which the maximum deviation in temperature was found to be ~ 1.5 percent. The effect of smearing of the solution could be seen as an early onset of ignition in both the cases. This also caused the plots of temperature, Mach number and mass fractions to be offset from the values calculated by SDT in the region of rapid chemical reactions. However, the final state at the exit of the combustor was still found to match within 0.1 percent of SDT results for both the cases.

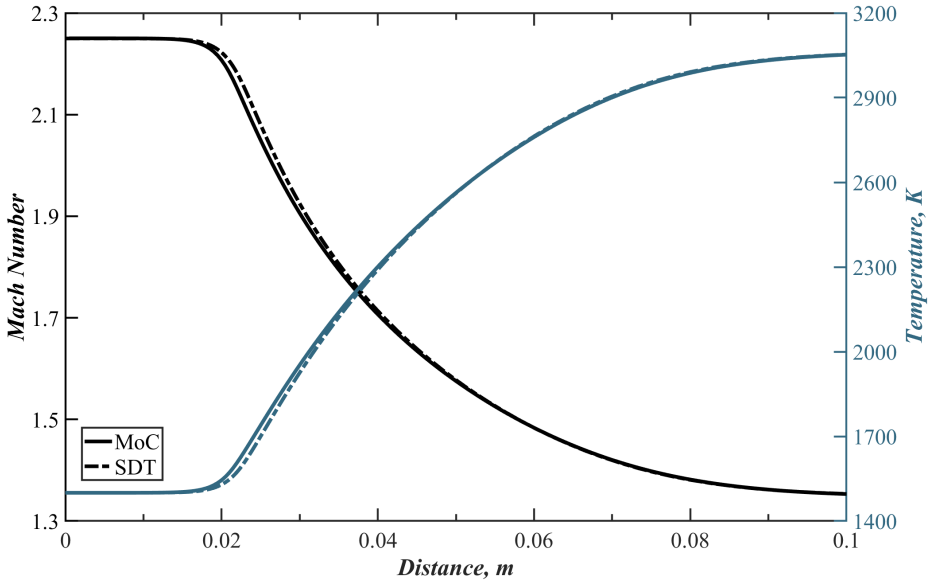

(a) Mach number and temperature

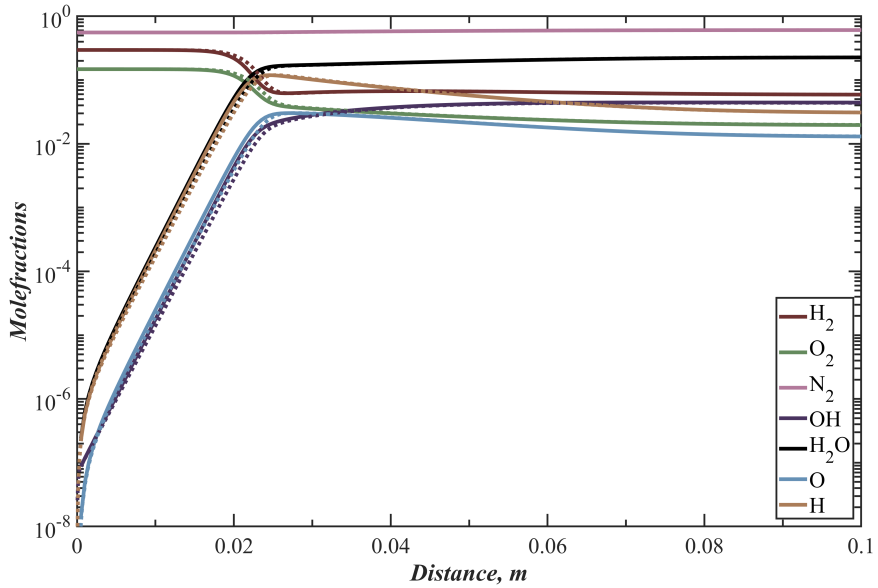

(b) Molefractions

Figure 4.3: Comparison of MoC and SDT results for supersonic combustion, Case 1c.

4.3.2 Chemical non-equilibrium behind a normal shock

This case simulated finite-rate chemistry behind a high velocity normal shock wave traveling in air. The domain simulated was essentially the same as that of the supersonic combustor, that is, a one-dimensional duct, but the solution procedure and

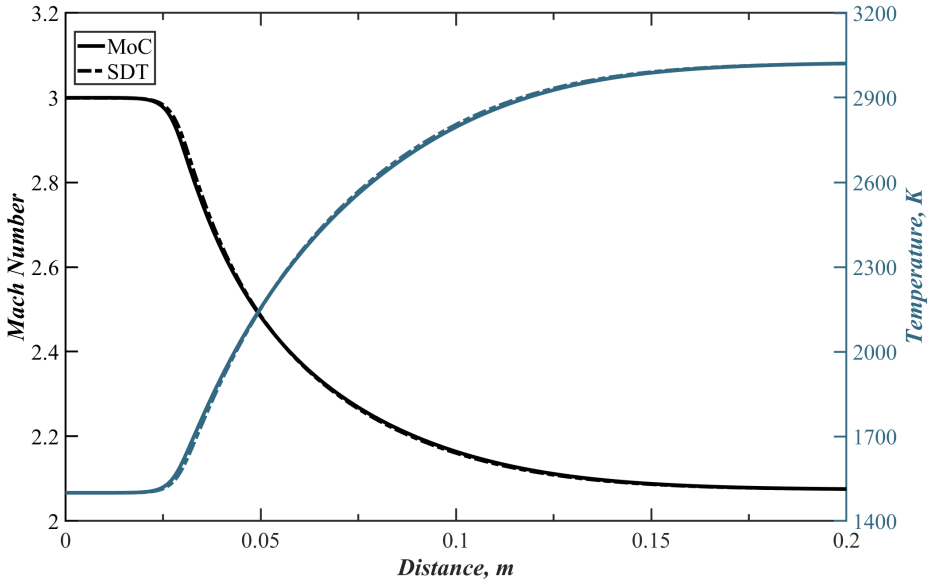

(a) Mach number and temperature

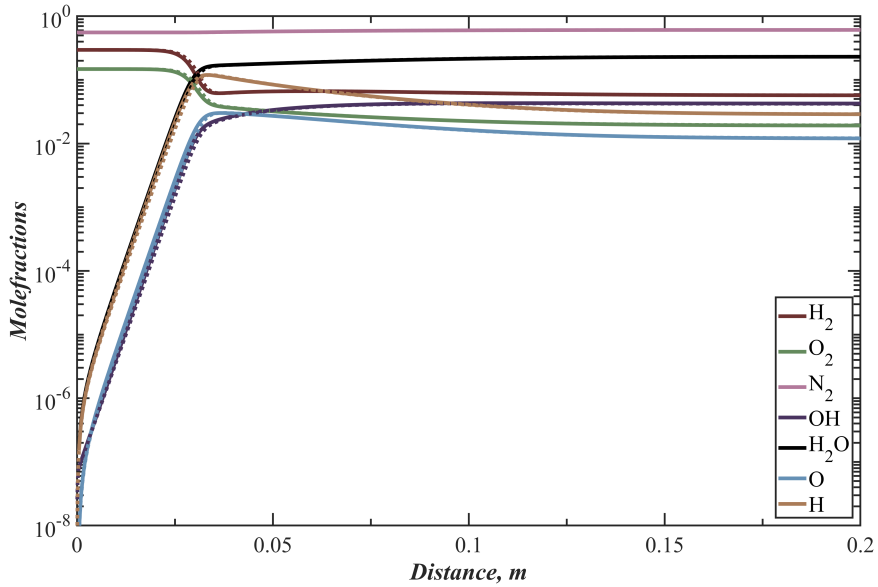

(b) Molefractions

Figure 4.4: Comparison of MoC and SDT results for supersonic combustion, Case 2c.

boundary conditions differ from the previous case as detailed further. For the ease of simulation, the flow behind a normal shock was simulated in the shock frame of reference as discussed further. Consider a constant velocity normal shock traveling in a duct as shown in Fig. 4.5a. Through Galilean transformation, this can be converted

into a steady shock wave as shown in Fig. 4.5b. In the shock frame of reference, the flow behind the shock front can be treated as one-dimensional duct flow.

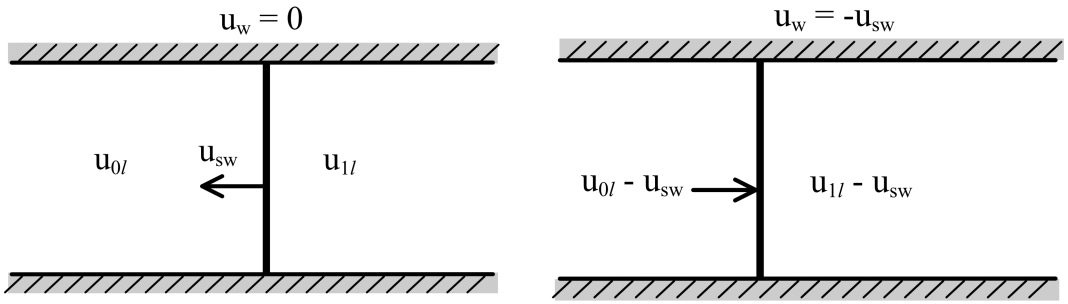

(a) Unsteady shock wave. (b) Transformed steady shock wave.

Figure 4.5: Galilean transformation of an unsteady normal shock wave.

In the transformed frame of reference, the inlet conditions to the duct are the post-shock gas properties. When the incoming gas stream is in thermochemical equilibrium, the finite-rate relaxation behind the shock wave (and thereby the duct) can be assumed to occur in two stages, that is, thermal and chemical relaxation [95]. As discussed earlier in this chapter, the flowfields considered here are always assumed to be in thermal equilibrium. Thus, all the modes of molecular internal energy such as translational, rotational and vibrational modes equilibrate instantaneously at the post-shock conditions across the shock front. Since the timescales associated this phase are negligible, the incoming gas stream can be assumed to be chemically frozen in composition across the shock front. Behind the shock front, the flow then expe-riences a relatively larger, second region where the chemical reactions proceed in a finite-rate towards equilibrium.

The process described above was used to define the boundary conditions of the computational domain shown in Fig. 4.6. Additionally, the flow behind a shock wave is subsonic in the shock frame of reference. Therefore, the entire computational

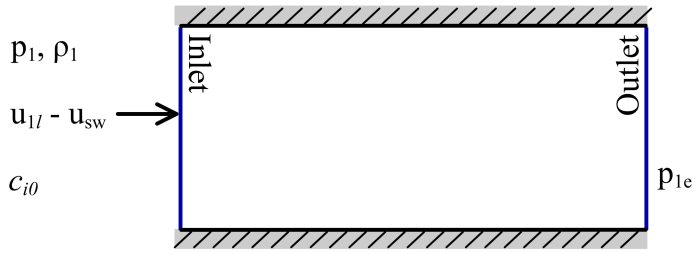

Figure 4.6: Boundary conditions for the normal shock simulation

domain is also subsonic, which results in information being propagated both upstream and downstream in the flowfield. Thus, the exit boundary condition of the "duct" will influence the entire flowfield in the domain. Though the flow at the exit could be modeled using the open-end point module, correct exit boundary conditions must be chosen, as any error in the imposed pressure at the exit plane would cause errors in the solution of the entire flowfield. It was assumed that if the duct length was chosen far away from the "inlet", where equilibrium conditions would be achieved, then the exit pressure would simply be the equilibrium post-shock pressure. This could be calculated based on the iterative procedure outlined in Vincenti and Kruger [95] for a normal shock under thermochemical equilibrium. The "inlet" conditions, on the other hand, were the thermally equilibrated, but chemically frozen post-shock conditions as described earlier. These were calculated again using the same iterative method as that for the equilibrium shock, but the chemical composition was frozen at the pre-shock state, while seeking convergence of static enthalpy.

Table 4.2: Boundary conditions for stationary normal shock

u_{sl} [m/s]	P_0 [Pa]	T_0 [K]	P_1 [kPa]	T_1 [K]	$u_{1,sw}$ [m/s]	P_e [kPa]	L [m]	Gas Composition
3 754	1 773.19	223.9	337.85	5 688.7	500.58	350.17	0.0250	$0.22O_2 + 0.78N_2$
3 754	1 773.19	223.9	337.85	5 688.7	500.58	350.17	0.017 5	$0.22O_2 + 0.78N_2$
3 754	1 773.19	223.9	337.85	5 688.7	500.58	350.17	0.015 0	$0.22O_2 + 0.78N_2$
3 600	1 773.19	223.9	310.37	5 278.3	484.90	321.20	0.017 5	$0.22O_2 + 0.78N_2$

Two validation cases have been simulated with normal shock velocities of 3 754 m/s (Case 1s) and 3 600 m/s (Case 2s). Further information on the boundary conditions are shown in Table 4.2. The reaction mechanism used here is the five species, six-step reduced Dunn–Kang model developed by Shuen et al. [108]. The rate constants used in this chemical mechanism are provided in Appendix A.

Validation for this case was again performed against SDT, using the integration procedure included for the reaction zone behind a Zeldovich–von Neumann–Doring detonation model, which represents similar finite-rate chemistry behind a steady chemically frozen normal shock wave front. Since a different working gas was used for this case compared to the supersonic combustor case, the grid study was repeated to ensure that the final results were independent of grid size. For the grid study, a domain length of 0.027 m was chosen, as the static pressure behind the normal shock changes less than 1 Pa after this location. Again, the temperatures due to different grid sizes were compared to that simulated through SDT and are shown in Fig. 4.7a. For grid sizes of 2.00, 1.00, 0.50, 0.25 and 0.125 mm, the maximum deviation in static temperatures from SDT were $\sim$ 9.2, 5.1, 3, 1.8 and 1.0 percent respectively. Thus, further simulations discussed here used a grid size of 0.25 mm. First, the sensitivity of the numerical solution to the domain length was studied. Two additional cases with the domain lengths listed in Table 4.2 were simulated to ensure that the domain length chosen was appropriate. The results of this study are shown through the temperature profiles in Fig. 4.7b. It was seen that all three cases exhibited temperatures that were within 0.01 percent of each other. Thus, the original domain length of 0.027 m was deemed appropriate for these simulations.

As opposed to the supersonic combustor case where thermal ignition occurred after an ignition delay, the flow behind a normal shock wave contains an immediate region of rapid relaxation. Even under these conditions, MoC results for all the

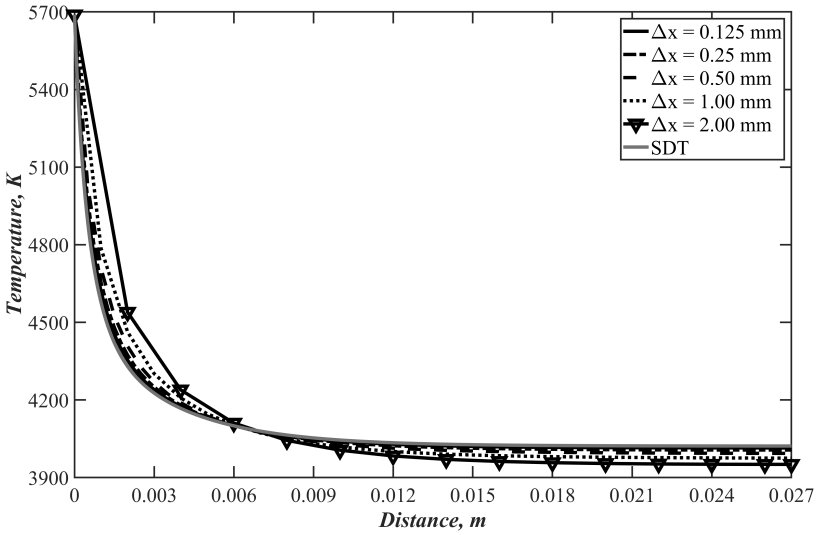

(a) Effect of grid size on temperature profile.

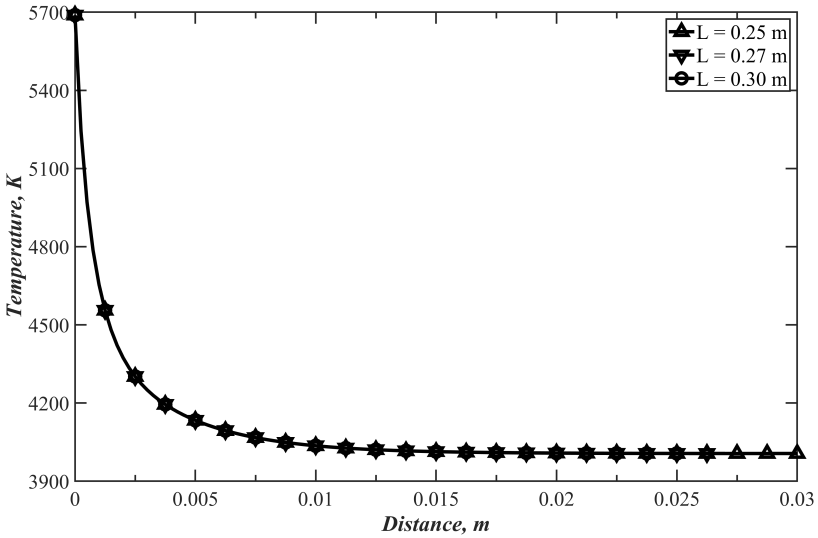

(b) Effect of domain length on temperature profile.

Figure 4.7: Preliminary studies for determining grid size and domain length: normal shock wave case.

state properties differ from SDT results by a maximum of 1.8 percent for Case 1s. Additionally, for Case 1s, it is observed that all the state properties at exit differ by less than one percent from SDT predictions, with the molefractions for molecular and atomic oxygen differing by about three and two percent respectively. Comparison of

MoC results against SDT results for case 1s is shown in Fig. 4.8, while that for case 2s is shown in Fig. 4.9.

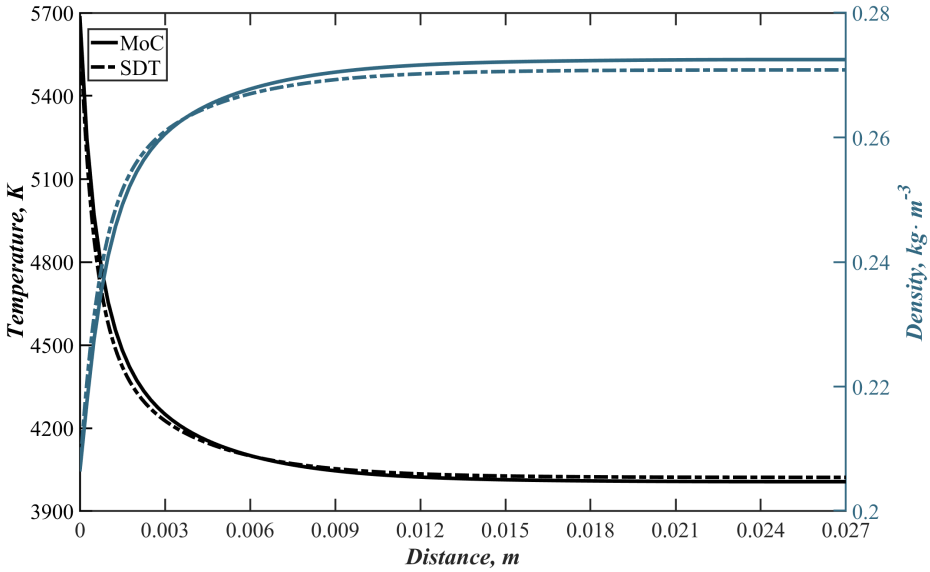

(a) Temperature and density.

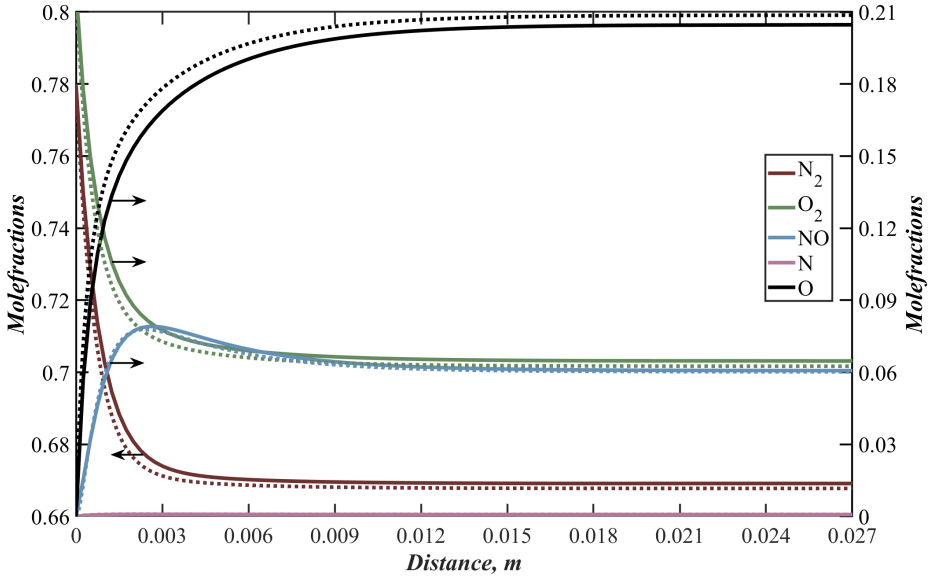

(b) Molefractions.

Figure 4.8: Comparison of results from MoC and SDT for normal shock wave in air, Case 1s.

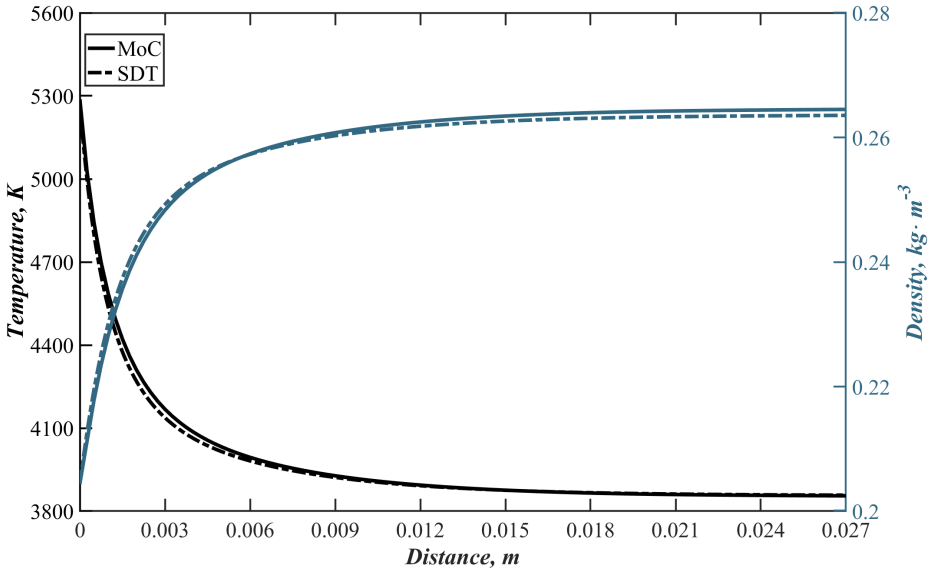

(a) Temperature and density

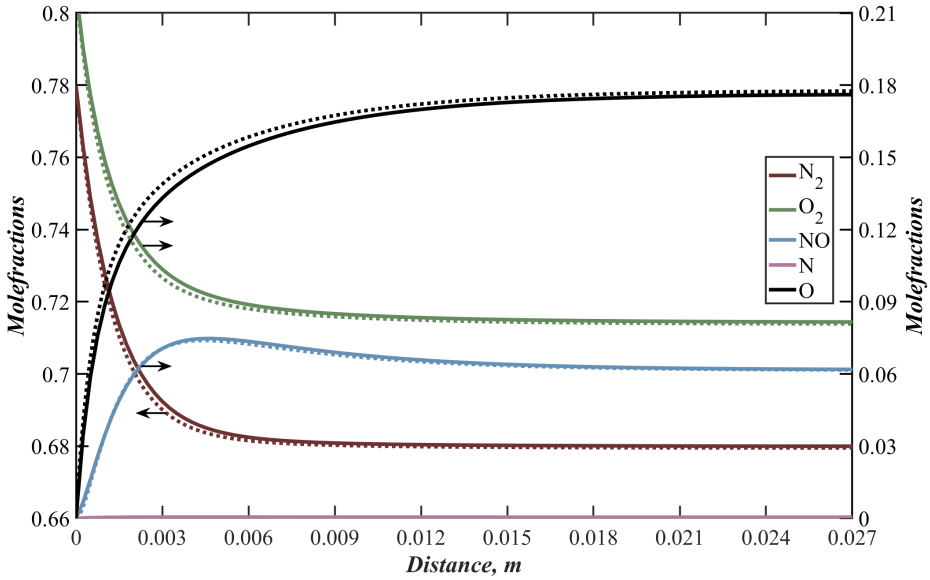

(b) Mass fractions

Figure 4.9: Comparison of results from MoC and SDT for normal shock wave in air, Case 2s.

The mole fractions of all reacting species have been plotted in Figs. 4.8b and 4.9b. It is seen that the model captured the continuous dissociation of molecular oxygen into atomic oxygen, which is expected since the temperature was significantly above 2 000 K (and the static pressure was still comparable to 1 atm). In the case

of nitrogen, from Fig. 4.8b, it can be seen that dissociation occurred until the temperature dropped to ∼4 300 K, after which the concentration of molecular nitrogen began to approach equilibrium around ∼4 000 K. For Case 2s, maximum deviation of all state properties and molefractions were less than about one percent from SDT results. Since the post-shock temperature was significantly lesser than Case 1s, relaxation occurred less rapidly compared to Case 1s, which resulted in a better match against SDT results, as seen in Fig. 4.9.

4.3.3 Chemical non-equilibrium flow in a nozzle

The cases simulated above were constant area duct flows with small pressure ratios across the inlet to exit, as the effect of finite-rate chemistry was the primary phenomenon of interest. Additionally, in both the cases, the gas state approached equilibrium values at the exit of the domain and the MoC modules were able to capture that phenomenon accurately. This case in contrast models the gasdynamic expansion of the reservoir gas in a hypervelocity nozzle, where the chemical composition may not always reach equilibrium state. The nozzle geometry utilized here is based on the nominal geometry reported in Gu et al. [109]. The converging section of the nozzle is conical with a 10°half angle. The inlet has an area-ratio of 21.78, with the throat radius being 15 mm. The diverging section of the nozzle is also conical, but with a smaller half angle of 6°. The region near the throat joins smoothly with the converging and diverging sections with a radius of curvature twice the throat radius. The reservoir conditions also mirror those used by Gu et al. [109], which will later be compared here with the thermochemical nonequilibrium simulations. The test gas is air, represented by a mixture of 78 percent molecular nitrogen and 22 percent molecular oxygen by volume. The reservoir condition assumes the test gas to be in thermochemical equilibrium at 1 MPa and 4 000 K. The chemical mechanism

file used to capture finite-rate chemistry is again the five species, eleven reaction, Reduced Dunn–Kang mechanism (see Appendix A).

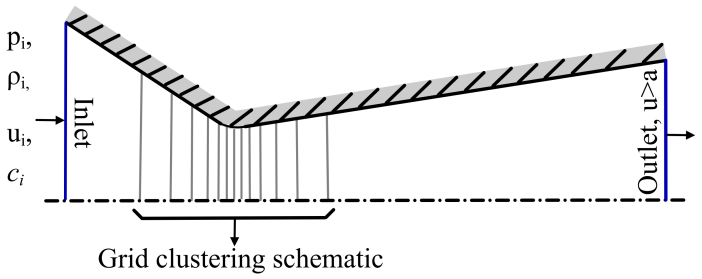

Figure 4.10: Schematic of the nozzle boundary conditions and mesh.

A schematic of the computational domain is shown in Fig. 4.10. At design operation where the nozzle exit flow is supersonic, the entire nozzle flowfield can still be simulated using the interior point module, as the compatibility equations were written for a quasi-one-dimensional domain. Thus, overall nozzle algorithm is similar to that of supersonic combustor. The flowfield however differs, as the nozzle consists of a combination of subsonic and supersonic regions. Since the outflow is still supersonic, the surrounding atmosphere and the backpressure do not influence the nozzle flowfield and once again, the interior point solver can be used as before. For the ease of simulation, the entire flowfield is initiated to the calorically perfect gas solution, after which the interior point algorithm marches in time over the computational domain to achieve steady state. The boundary conditions for this simulation are shown schematically in Fig. 4.10. Since the converging section of the nozzle experiences near equilibrium flow, the inlet properties are calculated from typical equilibrium nozzle relations [49, 103, 95] based on the reservoir gas state and inlet geometry. In addition to the MoC simulation, an ODE solver was developed to resolve the finite-rate chemistry occurring in a quasi-one-dimensional (Q1D) flow. The results from

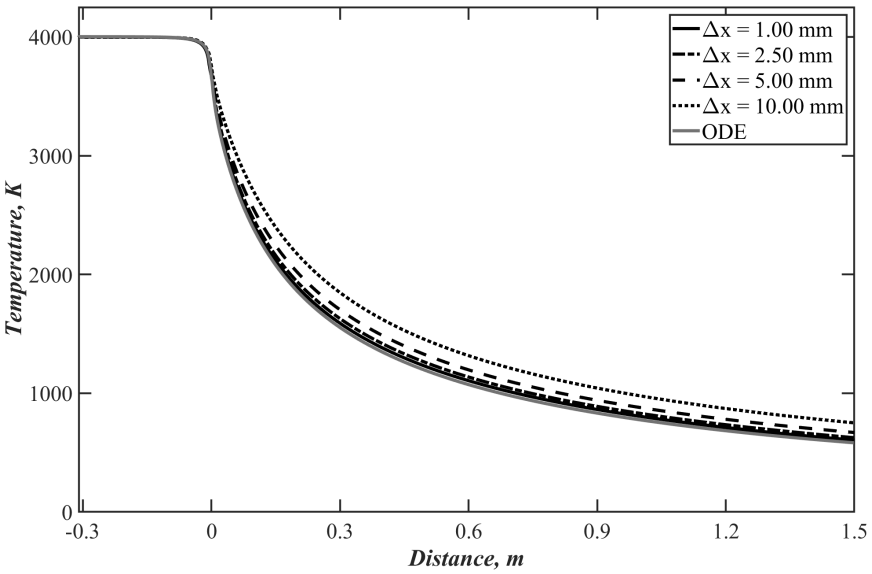

Figure 4.11: Nozzle temperature profile variation with grid size.

these calculations were used to validate the Q1D time-marching MoC solution. For a description of the ODE solver, see Appendix C.

First, a grid study was carried out to ensure grid convergence in the computational domain. As the steady nozzle flowfield turns supersonic near the throat, in addition to drastic variation of flow properties, careful discretization of the domain is necessary to avoid numerical instabilities. Thus, the grid structure in this simulation, as shown schematically in Fig. 4.10 was non-uniform, as opposed to the previous cases. The throat was taken to be the origin of discretization in all the cases discussed here. From the initial point at the throat, a growth factor of 1.005 was used to create the grid along either direction in the nozzle. Thus, if the dimension of the initial spatial grid is fixed, then the entire nozzle can be discretized (along one spatial dimension) based on the growth factor and the converging-diverging section axial dimensions. This initial grid size, shown in Fig. 4.11 as Δx was varied from 10.00 mm to 1.00 mm. As the grid size was reduced, the difference between the MoC and ODE solutions reduced from $\sim$ 28.9 through 14.9, 7.35 to 4.0 percent finally. Given that the

1.00 mm grid size was already computationally intensive and the MoC temperatures seem to approach the ODE solution, the 1.00 mm grid size was deemed acceptable for this preliminary study. Thus, further comparisons with the ODE solutions employ the results from 1.00 mm case.

Figure 4.12 shows the comparison of various gasdynamic properties in the nozzle due to MoC and the ODE solver. Quantitatively, the molefractions and velocities calculated by MoC are within one percent of the ODE solution. The maximum difference in densities and temperatures throughout the nozzle due to the MoC and ODE solvers are within 4 percent. The static pressure on the other hand varies by about 8 percent at the nozzle exit between these models. Note that the gasdynamic expansion results in a static pressure drop of $\sim \mathcal{O}(10^{-4})$ throughout the nozzle. Thus, the actual difference in static pressures at the exit is $\sim$ 20 Pa. Given the drastic variation of gasdynamic properties throughout the nozzle and the interior point algorithm linearly interpolating the gasdynamic properties between two grid points, the accuracies obtained here are satisfactory. Qualitatively, it can be seen that all the properties vary gradually in the converging section, followed by steep gradients near the throat. The molefractions of molecular nitrogen and oxygen increase from their reservoir state due to chemical recombination until a location slightly downstream of the nozzle throat. In the same region, the molefraction of atomic oxygen can be seen to decline correspondingly. As is known generally, the chemical composition of the test gas freezes slightly downstream of the nozzle throat due to falling reaction rates and higher test gas velocities [110].

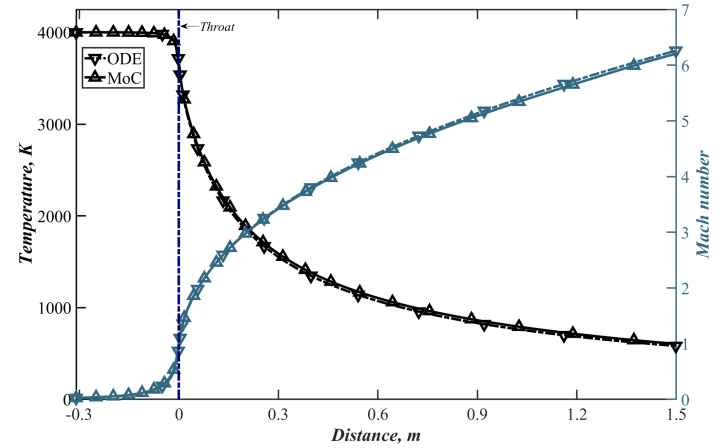

(a) Mach number and temperature.

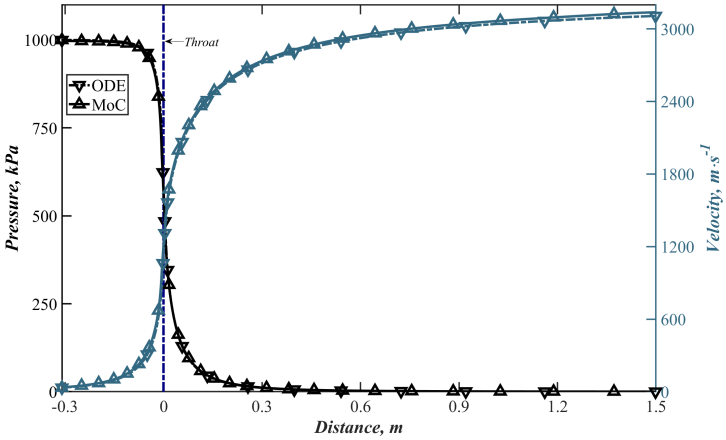

(b) Velocity and static pressure.

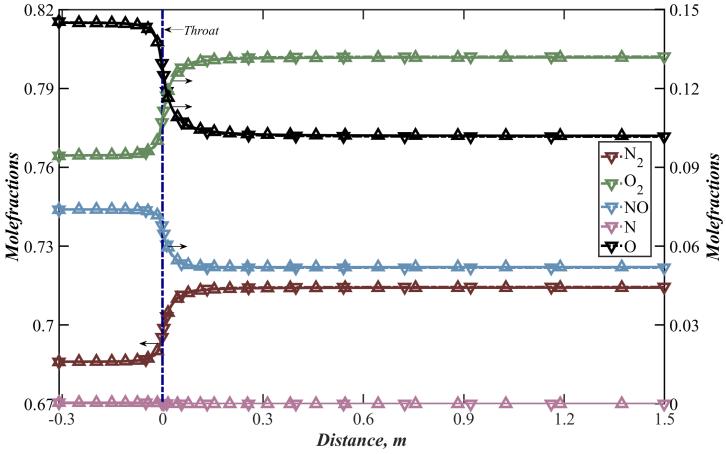

(c) Species Molefractions.

Figure 4.12: Comparison of nozzle flow properties between MoC and ODE Solver, see Appendix C

CHAPTER 5

VECTORIZATION OF INVERSE METHOD-OF-CHARACTERISTICS ALGORITHMS [1]

It is evident from the previous chapter that IMoC can resolve nonequilibrium flowfields. However, it is also evident that flowfields with steep gradients were not reproduced with great accuracy and that a large numerical grid would be required to reproduce solutions in such flowfields. This can be attributed to two primary aspects discussed further.

The original IMoC algorithm as described in the previous chapters integrates all the characteristics from an initial value line to a pre-determined grid point. This procedure requires that the characteristics of interest be identified first, which in turn requires that the gasdynamic properties be known everywhere on the initial value line. Since this is impossible to construct, the gasdynamic properties are only logged on at the pre-determined grid points. These locations can then be used for interpolation of various properties at intermediate locations. Additionally, the original IMoC algorithms were developed for calorically perfect gas flows where gasdynamic properties could be reasonably interpolated linearly between these grid points. In the case of flows with finite rate processes with steep gradients in thermochemical state, the accuracy of the solution may degrade under linear interpolation as seen earlier.

[1]This material was presented at the 34^{th} International Symposium on Shock Waves Symposium as a paper entitled 'Vectorization of Inverse Method-of-Characteristics Algorithms for Quasi-One-Dimensional Unsteady Flows' by A. Jayamani, and F. K. Lu.

Secondly, the overall algorithm performance is limited by the MoC subroutines, as every grid point must be individually solved by repetitively invoking the interior point algorithm. A reduced-order model employing these MoC subroutines incurs a rapidly increasing computational cost as the number of grids employed in a domain increases. Thus, for the overall reduced-order models to improve in efficiency, the MoC algorithm itself needs optimization. On further scrutiny of the inverse marching algorithms discussed so far, it is seen that the hyperbolic nature of the governing equations along with the numerical integration carried over a known $x - -t$ grid, decouples the flowfield evaluation for all the grid points at a given time step. Since the solution algorithm for a continuous region remains the same, these repetitive calculations can be optimized through vectorization. With modern programming tools and increased computational power, such an optimization of the MoC algorithms could vastly improve their computational efficiency and thereby help in building efficient reduced-order models.

To solely focus on revising and optimizing the original IMoC algorithms, the complexity of accounting for finite-rate processes is forsaken for the time-being. Instead of utilizing the calorically perfect model discussed in Chapter 3, a thermally perfect gas model is chosen. This model provides some relevance to the finite-rate algorithms in terms of evaluating various thermochemical properties, as will be seen throughout the remainder of this work. Thus, this chapter discusses the extension of original calorically perfect IMoC approach to thermally perfect gases, in addition to their optimization through vectorization.

5.1 Governing equations

Similar to the approach in Section 3.1, the governing equations for a quasi-one-dimensional unsteady flow of a thermally perfect gas can be written as

$$\frac{\partial \rho}{\partial t} + u\frac{\partial \rho}{\partial x} + \rho\frac{\partial u}{\partial x} + \rho u\frac{1}{A}\frac{dA}{dx} = 0 \tag{5.1a}$$

$$\rho\left(\frac{\partial u}{\partial t} + u\frac{\partial u}{\partial x}\right) + \frac{\partial p}{\partial x} = \frac{\delta F_{\mathsf{f}}}{V} \equiv \beta \tag{5.1b}$$

$$\frac{\partial p}{\partial t} + u\frac{\partial p}{\partial x} - a^2\left(\frac{\partial \rho}{\partial t} + u\frac{\partial \rho}{\partial x}\right) = (\gamma - 1)\left[\frac{\delta \dot{q}}{V} - u\beta\right] \equiv \psi \tag{5.1c}$$

As the above equations apply for a thermally perfect gas flow, $\gamma = f(c_p) = f(T)$. In the momentum (5.1b) and energy (5.1c) equations, the volumetric sink terms represent momentum and heat losses respectively. While these terms have been retained in all the equations and in the MoC subroutines, the effect of losses are not considered here for brevity. Thus, in the MoC models discussed here, these sink terms have been set to zero ($\psi = 0$, $\beta = 0$).

The MoC is used to reduce Eqs. (5.1a–5.1c) to ordinary differential equations called compatibility equations as given by

$$\left[\frac{dp}{dx}\right]_o - a^2\left[\frac{d\rho}{dx}\right]_o = \frac{\psi}{u} \tag{5.2a}$$

$$\left[\frac{dp}{dt}\right]_\pm \pm \rho a\left[\frac{du}{dt}\right]_\pm = \psi \pm a\beta - \rho u a^2\frac{1}{A}\frac{dA}{dx} \tag{5.2b}$$

The subscripts added to the above equations as before denote the characteristic curves along which these compatibility equations are valid. These characteristic curves themselves are given by

$$\left[\frac{dt}{dx}\right]_o = \lambda_o = \frac{1}{u} \tag{5.3a}$$

$$\left[\frac{dt}{dx}\right]_\pm = \lambda_\pm = \frac{1}{u \pm a} \tag{5.3b}$$

The characteristic curve given by Eq. (5.3a) represents the trajectory of a fluid parcel and is the pathline. The characteristics given by Eq. (5.3b) represent acoustic waves which carry the information about perturbations in a given flowfield. Thus, these are the unsteady Mach lines that propagate on either side of a fluid parcel. Together, the characteristic and compatibility equations describe a given continuum flowfield evolution and therefore are again the basis of the numerical procedure to determine a given flowfield.

Typical numerical methods employed to solve the characteristic and compatibility equations fall under two categories—direct marching and inverse marching methods. Since the problem is hyperbolic, both these methods require that all the gasdynamic and thermochemical properties be known along an initial value line. Thereon, direct marching methods, as the name implies project multiple characteristics forward in time to identify their intersecting point. Depending on the nature of the problem, another characteristic may be projected back from the intersection to the initial value line. Since the properties at the intersecting location are not known initially, the slopes of the characteristics are guessed at first, which results in an iterative procedure to determine the intersecting point and thereby the properties at that location. When this procedure is repeated for a sufficient number of characteristics, a 'characteristic net' is produced where the flowfield properties are known at the intersection points. The inverse marching method in contrast, resolves the flowfield on a predefined space-time grid where the flowfield properties are sought. With the initial value line and a defined solution point in space-time co-ordinates, this method firstly guesses the required properties at the solution point and then iteratively projects all the characteristics back to the initial value line. As the iterations progress, the estimated characteristics better approximate the actual characteristics and so the gasdynamic and thermodynamic properties converge at the solution point. In this

study, the numerical approach utilizes inverse marching algorithm, which has lent itself to vectorization readily. When equilibrium or non-equilibrium calculations are performed, vectorized algorithms provide significant improvement in computational efficiency, which is desirable for reduced-order models.

5.2 MoC unit processes

In the quasi-one-dimensional, unsteady flowfield considered here, the expected gasdynamic waves are shock waves, contact surfaces, weak compression and rarefaction waves. Each of these waves can be resolved by utilizing the characteristic and compatibility equations developed in the previous section directly or with the aid of supplementary conditions. These individual MoC algorithms representing specific gasdynamic waves are called unit processes. When the wave mechanics of a given gasdynamic flowfield are known, representative unit processes can be assembled to build a reduced-order model and resolve the overall flowfield. Typically, discontinuities such as shock waves and contact surfaces represent a negligible portion of a given flowfield. Almost the entirety of the flowfield is thus made up of continuous waves, which are primarily weak compression and rarefaction waves. The unit process associated with these continuous waves, the interior point solver naturally becomes the prime candidate for vectorization. For better comparison, the original interior point solver is briefly discussed again, followed by a description of the new vectorized approach.

A schematic for the interior point solver algorithm is shown in Fig. 5.1. As this MoC scheme uses the inverse marching method, calculations are carried out over a pre-defined space–time (x–t) grid. Figure 5.1, for instance will be a small region in the overall flowfield and the coordinates of grid points 1–4 will be known. Additionally, all the flow properties will be known at locations 1, 2 and 3, which is the initial value

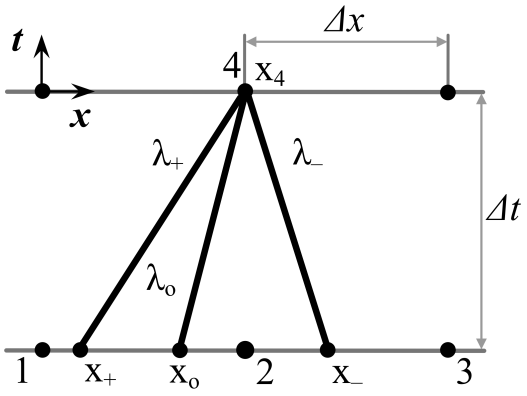

Figure 5.1: Interior point algorithm.

line. For obtaining flow properties in between these points linear interpolation is used. The solution procedure to calculate all flow properties at location 4 is based on the Euler predictor–corrector method utilizing discretized forms of Eqs. (5.2a–5.3b) shown below,

$$(x_4 - x_o) = u\Delta t \tag{5.4a}$$

$$(x_4 - x_\pm) = (u \pm a)\Delta t \tag{5.4b}$$

$$(p_4 - p_o) - a^2(\rho_4 - \rho_o) = \frac{\psi}{u}(x_4 - x_o) \tag{5.4c}$$

$$(p_4 - p_\pm) \pm \rho a\,(u_4 - u_\pm) = (\psi \pm a\beta - \rho u a^2 \frac{1}{A}\frac{dA}{dx})\,\Delta t \tag{5.4d}$$

The first step in this procedure identifies all the characteristics that pass through location 4. Assuming that the CFL condition is satisfied [49], all these characteristics must originate in between locations 1 and 3. Thus, the flowfield data along the initial value line and Eqs. (5.4a)–(5.4b) can be utilized to identify all the characteristics arriving at location 4. Since the MoC algorithm to identify these characteristics is similar, the general procedure can be illustrated through that for the λ_+ characteristic. For the initial calculation, the values of various properties at location 4 are not known.

Thus, the initial guess for these properties is taken to be those at location 1. Using these flow properties and the coordinates of location 4, Eq. (5.4b) can be solved to identify x_+ on the initial value line. Then, all the flow properties at x_+ are evaluated through linear interpolation utilizing the known flow properties at locations 1 and 2. Now, the slope of the λ_+ characteristic can be updated based on the average flow properties at locations x_+ and x_4, and the process repeated until the value of x_+ converges. Thereafter, the remaining characteristics must be identified using a similar procedure, but depending on the expected locations of x_- and x_o, the initial guesses and interpolation data differ.

Care was exercised when choosing the initial guesses and locations for interpolation, as the origin of all of the characteristics can differ between supersonic and subsonic flows moving in the positive and negative directions. Depending on the specific problem, an aphysical initial guess in a supersonic flowfield may lead to instabilities. Consider a supersonic flow spanning across locations 1, 2 and 3. The λ_- now will originate from the region between locations 1 and 2. If an initial guess is chosen between locations 2 and 3, the solution may become unstable. The situation is even worse if the interpolation for λ_- is carried out between locations $2-3$ instead of $1-2$.

Once all the characteristics have been identified, Eqs. (5.4c) and (5.4d) are simultaneously solved to identify the properties at location 4. In the finite difference equations (5.4a–5.4d), properties without a subscript represent average values on the characteristic. Finally, the entire process described above is repeated with the newly calculated values for location 4 and iterations are carried out until the flow properties at location 4 converge.

An implementation of the above-described interior point solver in a hypothetical flowfield is shown in the first row of Fig. 5.2. When grid points I–IV are solved by this

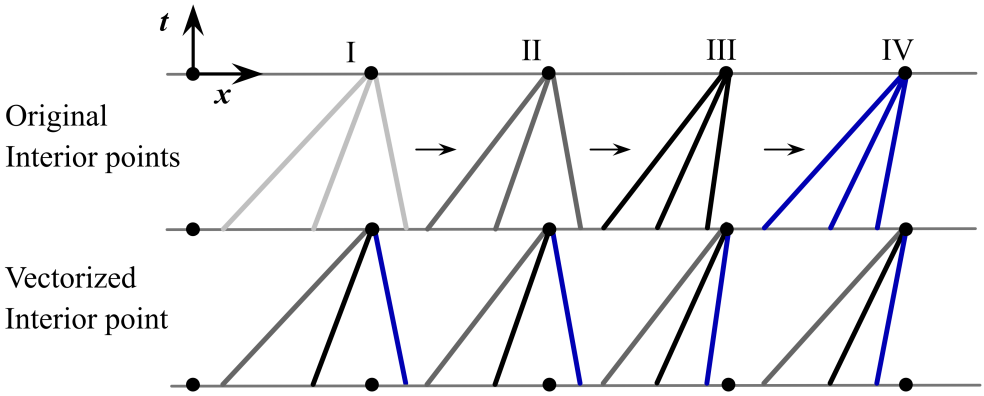

Figure 5.2: Implementation of vectorized interior point solver.

method, the same process is repeated for every location, which is computationally inefficient. Given that the characteristics passing through all the grid points in a continuous region (locations I–IV in this case) can be determined independently, Eqs. (5.4c) and (5.4d) can be efficiently solved using vectorization as described below.

Similar to the original algorithm, the characteristics passing through all the grid points are identified first. To identify the λ_+ characteristics passing through every desired grid point, Eq. (5.4b) is again used. In this case, the initial guesses for the solution points I–IV are taken to be the values at the same physical location, but at the previous time step. For instance, if Fig. 5.1 represents a specific grid point in the vectorized algorithm, the initial guesses for various flow proerties at x_4 are those at x_2. For simplicity, these values are also used as the initial guesses to calculate the slopes of all the other characteristics in the Euler predictor step. Additionally, piecewise cubic curvefits are provided for the distribution of all the required properties along the initial value line to circumvent interpolation issues. In a global algorithm, these curvefits can be created for the entire continuous region I–IV at a given time-step for better accuracy and efficiency. With these modifications, Eq. (5.4b) can be simultaneously solved for locations I–IV, similar to the original interior

point algorithm. Such a vectorized integration procedure is schematically shown in the second row of Fig. 5.2. As depicted in Fig. 5.2, with this approach every iteration of Eq. (5.4b) provides the x_+ values for all the λ_+ characteristics. When all the x_+ values and thus the λ_+ characteristics converge, the same approach is repeated for the remaining characteristics, but with appropriate characteristic equations. Finally, the compatibility relations, Eqs. (5.4c) and (5.4d) are also simultaneously solved for all the locations at once. This procedure is then repeated until all the flow properties converge at all the desired solution points. Using this approach, an entire continuous region in a flowfield can be simultaneously evaluated with a single function call to the interior point algorithm.

The description above provides a generic vectorized algorithm for the interior point solver. Clearly, the calculations for a thermally perfect gas must accommodate the variation of specific heats and their ratio γ with respect to static temperature. In the MoC algorithm reported in this chapter, curvefits of these properties were created during every simulation. For a given initial gas composition, the NASA Glenn thermodynamic data library [104] was imported into Cantera [85] to calculate chemically frozen mixture properties at a temperature range of interest. These data were then utilized to create piecewise cubic curvefits in MATLAB® as a function of temperature. Note that the overall simulation run times reported in §5.3 include that required to construct these curvefits. Though the characteristic and compatibility equations shown here and Chapter 3 look identical, the key difference lies in the calculation of sonic velocity (within the scope of this chapter). For a thermally perfect gas, the static pressure and density calculations are similar to that of a calorically perfect MoC algorithm. Thereafter, instead of using a constant γ, the thermally perfect algorithm uses the local static temperature to determine γ using the thermodynamic curvefits, which in turn is used to calculate the local sonic velocity.

In addition to the interior point solver, the calorically perfect MoC algorithms for shock waves, contact surfaces and wall points [49] were also extended to accommodate a thermally perfect gas. But these algorithms were not vectorized and are only discussed briefly here. The thermally perfect contact surface algorithm shown schematically in Fig. 5.3a closely resembles the calorically perfect algorithm from Chapter 3. This may be seen from both Fig. 5.3a and the discretized characteristic and compatibility equations for the contact surface algorithm, Eqs. (5.5a)–(5.5e). The only practical difference between these two algorithms is the use of curvefits in sonic velocity calculations and in the interpolation procedure to evaluate the dependent variables along the initial value line.

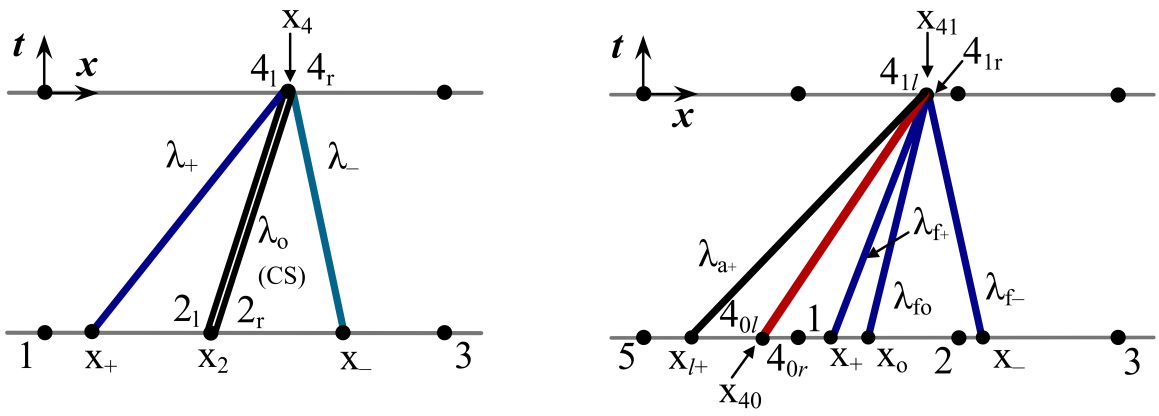

(a) Contact surface.

(b) Shock wave.

Figure 5.3: Algorithms for discontinuous waves.

The contact surface algorithm differs from the interior point algorithm, as the location the contact surface at the end of the time-step, x_4, is not known *a priori* and must be determined as a part of the solution. Thus, for the initial step of the

algorithm x_4 is approximated by projecting the contact surface over the current time-step using its velocity at x_2 and Eq. 5.5a.

$$(x_4 - x_2) = u\Delta t \tag{5.5a}$$

$$(x_4 - x_\pm) = (u \pm a)\Delta t \tag{5.5b}$$

$$(p_4 - p_2) - a_l^2(\rho_{4l} - \rho_{2l}) = \frac{\psi_l}{u}(x_4 - x_2) \tag{5.5c}$$

$$(p_4 - p_2) - a_r^2(\rho_{4r} - \rho_{2r}) = \frac{\psi_r}{u}(x_4 - x_2) \tag{5.5d}$$

$$(p_4 - p_\pm) \pm \rho a\,(u_4 - u_\pm) = (\psi \pm a\beta)\,\Delta t \tag{5.5e}$$

Based on the value of x_4 and Eq. 5.5b, both λ_+ and λ_- characteristics can be resolved using the typical IMoC algorithm. For the thermally perfect case, the modified IMoC algorithm requires curvefits for thermally perfect gas properties and initial value curvefits for all the dependent variables on either side of the contact surface. Thus, in Fig. 5.3a, the grid points 1 and 3 are merely placeholders for the initial value line. The available curvefits and therefore the known initial value line would typically span between 2_l, or 22_r and another boundary which may be a discontinuity or the domain wall. Thus, the initial value curvefits supplied to the contact surface algorithm encompass more information than necessary, as the time-step calculated based on the CFL criterion ensures that $x_2 - x_+ < \Delta x$. But, these curvefits have still been used to retain consistent interpolation accuracy between all the MoC algorithms and for simplicity in the expansion tube algorithm. Also, given the possibility that the gas on either side of the contact surface may be different, appropriate thermodynamic curvefits must be used in evaluating γ on the left and right sides of the contact surface. Once all the characteristics have been identified, the compatibility equations, Eqs. (5.5c)–(5.5e) can be solved similar to Chapter 3 to identify all the properties on both the sides of the contact surface, which completes the predictor step. Now, the

corrector step can be carried out for Eqs. (5.5a)–(5.5e), as all the flowfield values at x_4 are known from the predictor step. Subsequently, the corrector step is iteratively applied until the location x_4 and all the dependent variables at x_4 converge.

The thermally perfect shock wave algorithm, shown in Fig. 5.3b incorporates concepts from both the contact surface and interior point algorithms. The overall approach again treats the flowfield ahead and aft of the shock wave separately. The shock speed is simultaneously varied so that the post-shock properties match those across the trailing characteristic that overtakes the shock wave. Similar to the above contact surface algorithm, initial value curvefits on either side of the shock wave are supplied to the algorithm. The shock wave is projected over the current time-step to identify x_{41}. Using this location and the initial value curvefits, the interior point solver is invoked to identify the flowfield properties ahead of the shock wave. With the pre-shock gas state known, thermally perfect shock wave relations are utilized to calculate post-shock properties denoted 4_{1l} in Fig. 5.3b. Then, the trailing characteristic λ_{a_+} can be identified based on x_{41} and u_{41} using Eq. (5.4b). Finally, the compatibility relation, Eq. (5.4d) is used to obtain the static pressure, p_{41} across the trailing characteristic. Comparing the value of p_{41} between the λ_{a_+} characteristic and the post-shock properties, the shock speed is adjusted for the next iteration. The above procedure is repeated until the post-shock properties match those across the trailing characteristic.

5.3 Expansion tube model

The expansion tube is a high-enthalpy impulse facility which can generate test gas flows with negligible dissociation. As shown in the schematic of Fig. 5.4, the facility essentially consists of three sections isolated by diaphragms and filled with

different gases. The driver section is filled with a light gas at a high pressure. In some cases, this section may be heated to achieve higher driver performance. The driven section contains the test gas. The acceleration section or simply the accelerator is nearly at vacuum regardless of the fill gas. The test section, not shown in the schematic, may follow the accelerator immediately or after a non-reflected nozzle.

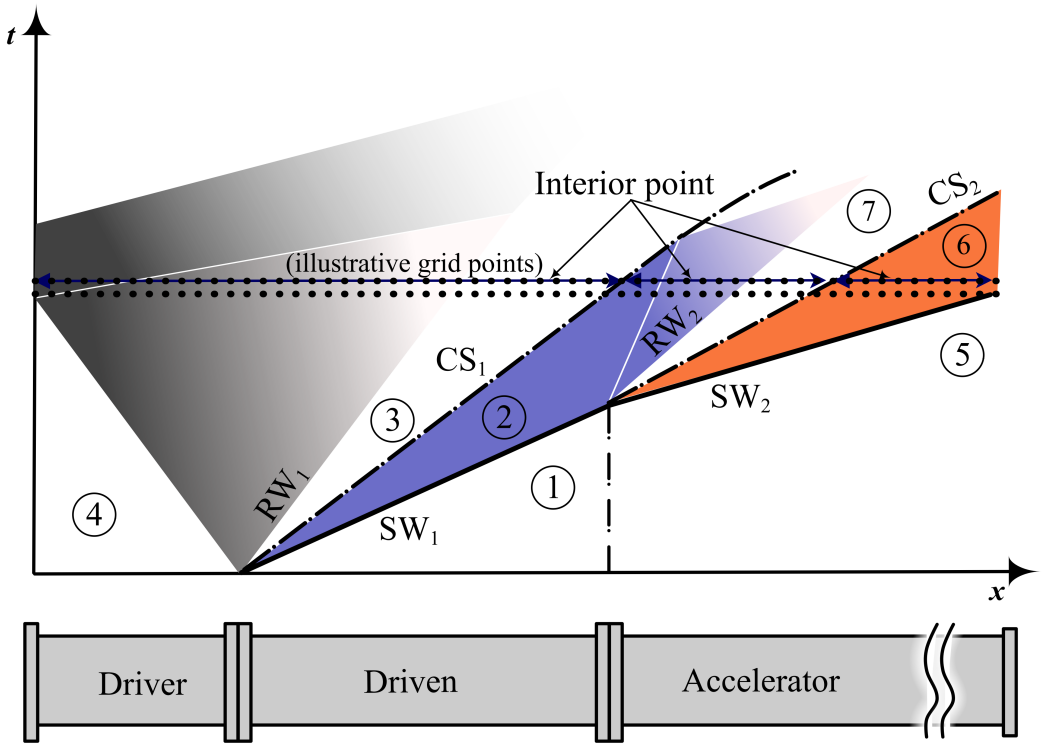

Figure 5.4: Expansion tube operation and algorithm (nomenclature in the text)

An idealized wave diagram depicting typical expansion tube gasdynamics is also shown in Fig. 5.4. The facility operation begins when the diaphragm separating the driver and driven sections is ruptured. The high-pressure driver gas then expands into the driven section creating a shock wave instantaneously. This process is idealized as a centered rarefaction wave (RW_1) in the driver and as the shock wave (SW_1) in the driven section. The interface between the driver and driven gases is idealized

as impermeable and massless membrane, the contact surface (CS_1), which travels at the local fluid velocity and thus is also a pathline. By design, the fill pressure ratio between the driver and driven sections is limited to prevent dissociation in the test gas behind (SW_1). As the driven shock wave (SW_1) reaches the end of the test gas slug, the diaphragm separating the driven and acceleration sections is assumed to disappear instantaneously. Thus, the shock processed test gas between the driven shock wave (SW_1) and the contact surface (CS_1) now expands into the acceleration section through a rarefaction wave (RW_2) resulting in a shock wave (SW_2) in the accelerant gas. Thus, wave system across the driven and accelerant gases resembles that across the driver and driven gases. From Fig. 5.4, it also seen that the leading characteristic of the test gas rarefaction wave (RW_2) has a positive slope, which is caused by the supersonic gas velocity of the driven gas in region ②. This is in contrast to the negative slope of the leading characteristic in (RW_1), due to the quiescent driver gas. As discussed in Chapter 2, the driven gas which has been finally accelerated to state ⑦ forms the test gas. Therefore, if a test article placed at the end of the acceleration section, the test time would begin with the arrival of contact surface (CS_2) and end with either the trailing or reflected characteristic of the rarefaction wave (RW_2).

Each of the wave processes in the expansion tube operation shown in Fig. 5.4 can be resolved using MoC algorithms similar to the detonation tube algorithm in Chapter 3. The expansion tube algorithm similarly requires that the facility geometry and initial fill conditions be known. Then, the unsteady facility flowfield can be solved over an x–t grid, which is shown partially in Fig. 5.4. The actual grid would spatially span across the entire facility and temporally span from the instant of primary diaphragm rupture to some user-specified time. The overall expansion algorithm can be briefly summarized as follows.

From the facility fill conditions, the initial values for the driven shock wave (SW_1) and contact surface (CS_1) can be found using the pressure-velocity diagram described in Chapter 3. These values along with the CFL criterion provide the constraints for constructing the x–t grid on which the facility flowfield will be resolved, see Fig. 5.4. Thereon for every timestep different MoC algorithms are called to resolve the flowfield evolution. Discontinuities are appropriately resolved by the shock wave or contact surface MoC algorithms. The flowfield at the left wall is solved by the wall point algorithm. The interior point solver is then called twice to resolve the continuous regions—first, for the region between the wall and (CS_1) and then for that between (CS_1) and (SW_1). Typical of IMoC algorithms, the grid points near discontinuities are populated by interpolation. In this case, the interpolation data is obtained from piecewise cubic curvefits created for the vectorized interior point solver. As observed earlier in Chapter 3, there should be negligible difference in the results due to interpolation and a dedicated MoC algorithm that resolves near-discontinuity grid points. During the initial few steps of the expansion tube algorithm, the analytical solution is used (instead of the interior point solver) for resolving (RW_1) to avoid interpolation errors. Clearly, a centered rarefaction wave spanning two grid-points at the most cannot be used to construct a piecewise cubic curvefit solely based on the gasdynamic properties at those grid points. Thus, resorting to the use of analytical solution for describing the properties of (RW_1) results in fewer numerical problems caused by IMoC smearing and therefore higher accuracy. This procedure for a single time-step is then repeated until (SW_1) reaches the secondary diaphragm at the end of driven section.

Based on the wave diagram discussion above, the secondary diaphragm is assumed to instantaneously disappear once the driven shock wave (SW_1) reaches its location. Subsequently, the transmission of (SW_1) into the acceleration section can

solved by the pressure-velocity diagram, but now the "driver" gas is also traveling at supersonic velocities. Since the pressure-velocity diagram can take into account non-zero driver gas conditions, this can be easily accounted for. Typically, the driven shock wave (SW_1) crosses the secondary diaphragm in between a time-step. In this case, the trajectory of the accelerant (SW_2) as it arrives at the end of the time-step can be determined based on the time of diaphragm rupture. Similar to the driver-driven wave system, the properties across (RW_2) for the initial few steps after secondary diaphragm rupture are based on the analytical Riemann solution. At this point in the algorithm, the expansion tube wave system contains four discontinuities separating the flowfield into three continuous regions spanning from the driver endwall to the accelerator exit. Still, the time-marching procedure described for the driver-driven wave system can be used to resolve the entire expansion tube flowfield, but the procedure now includes more subroutine calls to account for the increased number of discontinuities and continuous regions.

Table 5.1: Expansion tube simulation parameters (based on LENS-X[50])

	Driver	Driven	Acceleration
Length, m	6.2	14.8	26.45
Gas	He	Air	Air
Composition, % mole	He:1	N_2:0.79, O_2:0.21	N_2:0.79, O_2:0.21
Pressure, kPa	8271.429	20.679	0.331
Temperature, K	427	298	298

The expansion tube solver described above was used to solve the equilibrium expansion tube case from LENS-X [51, 50]. The facility geometry and initial fill conditions are provided in Table 5.1. For this test-run, the LENS-X driver was filled with heated helium, while the driven and accelerant gases were air. The composition

of air shown for this case is slightly different than the simulations in Chapter 4, so that in a later part of this work, comparisons can be made to existing results using the above composition.

A grid study carried out with 962, 1603 and 1924 spatial nodes showed that the velocities of shock waves SW_1 and SW_2 converged to within one percent between these cases. Fig. 5.5 shows the results from the expansion tube algorithm along with the analytical solution at two different instants in the driver-driven and driven-accelerator wave systems. It is seen that the MoC algorithm accurately resolves all the gasdynamic properties in both the instants. Quantitatively, all these properties are within one percent of the analytical solution. The MoC algorithm, compiled on a tablet having Intel i5-4300U processor with 8 gigabyte memory, takes less than 50 seconds to construct the entire flowfield even for the 1924 nodes case.

Further, Fig. 5.5 shows that the driven gas temperatures behind SW_1 is below 2000 K, at nearly half an atmosphere. This is in line with the comments made earlier regarding the limitation on SW_1 velocity to prevent dissociation of air. Thus, the thermally perfect algorithm maybe selectively employed in the driven section of expansion tubes. In this simulation, as reported in Table 5.1, heated helium driver was used. Thus, a thermally perfect simulation is unnecessary. However, given that the computational cost of these thermally perfect MoC algorithms is almost negligible, thermally perfect MoC can still be used for expansion tube drivers at all times. This would also be beneficial in situations where heated molecular driver gases are used, which may be better approximated by a thermally perfect rarefaction wave.

In the case of the driven-accelerator wave system shown in Fig. 5.6, the temperature of the shock compressed accelerant gas (air) exceeds the limits of thermally perfect gas assumption. While it is clear that the MoC algorithm reproduces the analytical solution, the considered thermochemical model in itself is unreliable. Thus,

this simulation will be re-visited in subsequent chapters to model this case more accurately from a thermochemical viewpoint. Also seen in Fig. 5.6 is the fact that an expansion tube may pose problems for numerical simulations due to the extreme variation in various state properties. For instance, the fill pressures between the driver and the accelerator vary by $\sim \mathcal{O}(10^4)$. This reasoning was a catalyst in the use of analytical solution to resolve the initial flowfield across the centered rarefaction wave systems after shock transmission. Figs. 5.5 and 5.6 show that the MoC model accurately resolves the strong rarefaction waves in the expansion tube and replicates the analytical solution in both the driver-driven and driven-accelerator wave systems even when the flowfield properties vary drastically during the facility operation.

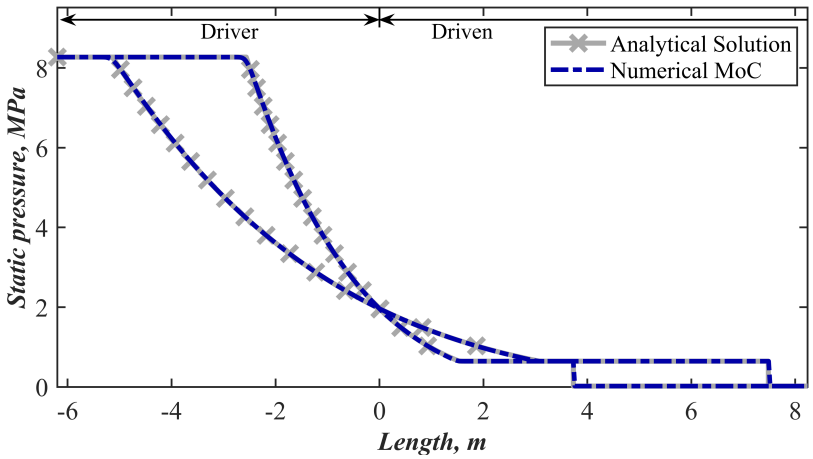

(a) Static pressure distribution

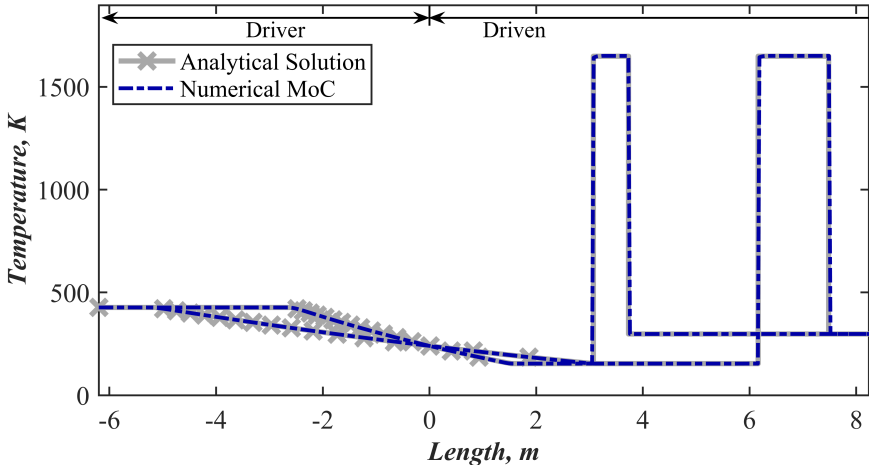

(b) Static temperature distribution

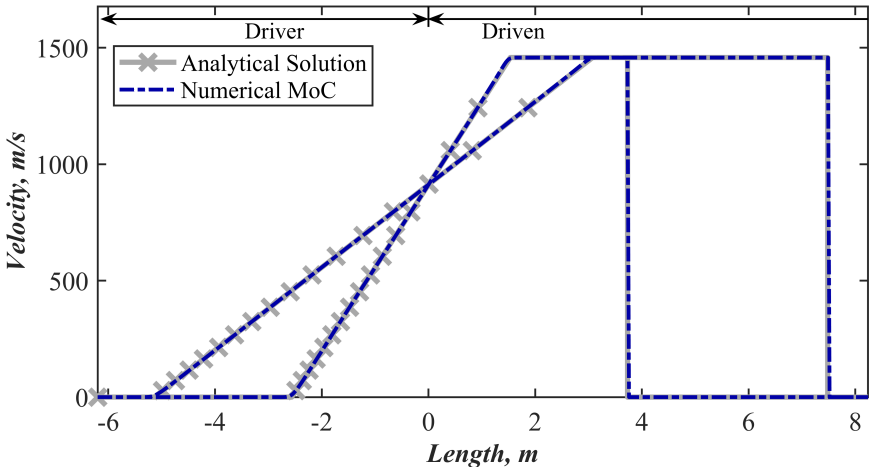

(c) Velocity distribution

Figure 5.5: Comparison of driver-driven wave system due to MoC model and analytical solution

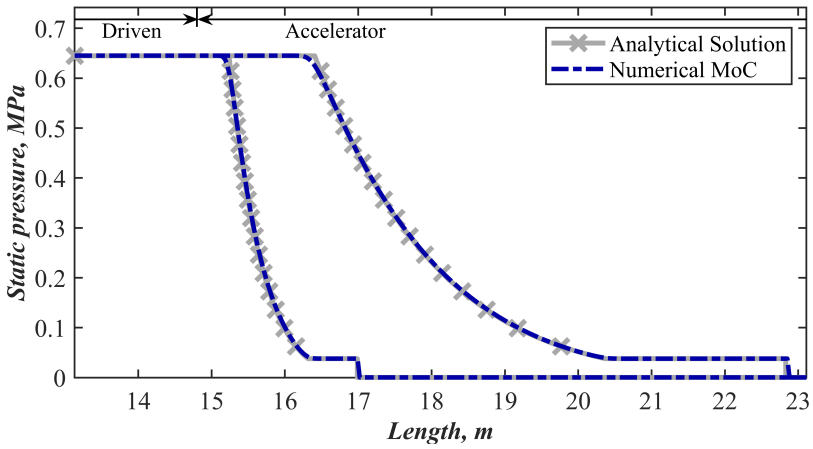

(a) Static pressure distribution

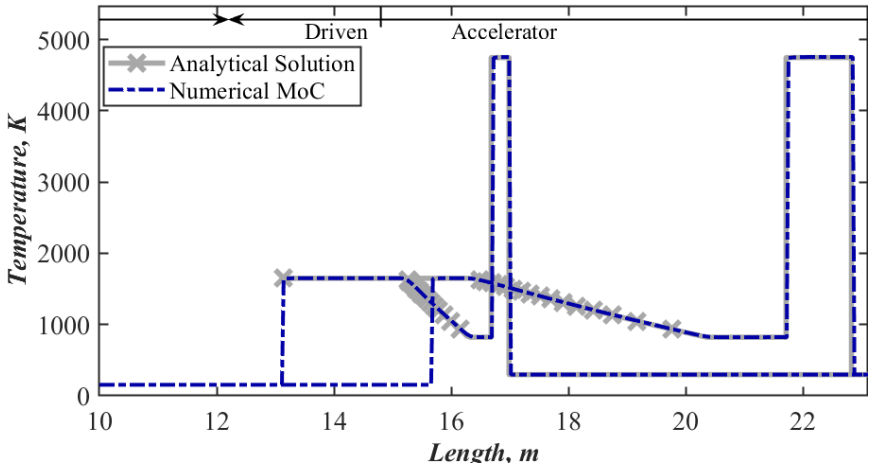

(b) Static temperature distribution

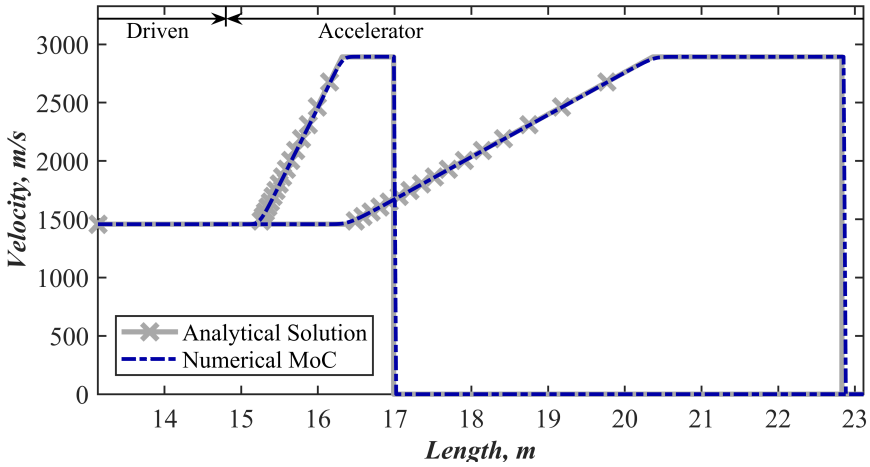

(c) Velocity distribution

Figure 5.6: Comparison of driven-accelerator wave system due to MoC model and analytical solution

CHAPTER 6

INVERSE METHOD-OF-CHARACTERISTICS ALGORITHMS FOR FLOWS IN THERMOCHEMICAL EQUILIBRIUM[1]

The thermally perfect MoC algorithms developed in Chapter 5 were intended to provide the baseline approach for vectorization of MoC algorithms. The effectiveness of vectorizing MoC algorithms will be truly noticeable when flows experiencing high temperature effects such as chemical reactions are modeled using MoC. For numerical simulations, the simplest model that accounts for chemical reactions is the thermochemical equilibrium model. The primary reason for its simplification is owed to the fact that the gas state at thermochemical equilibrium is determined if two thermodynamic state variables are known. In comparison, a thermally perfect gas (and thereby the MoC algorithm) only requires the static temperature to account for high temperature effects, as the chemical composition is fixed. Because of this similarity, extending the vectorized thermally perfect MoC algorithms to account for equilibrium thermochemistry is also relatively straightforward. Despite the ease of such an implementation, equilibrium algorithms are far more useful practically in hypervelocity models than thermally perfect algorithms.

Some high enthalpy facilities can be entirely modeled using equilibrium algorithms, while some other facilities others will selectively employ equilibrium algorithms in specific regions of their overall flowfields. An inspection of representative

[1]This material was presented at the 25th International Space Planes and Hypersonic Systems and Technologies Conference as a paper entitled 'Inverse Method-of-Characteristics Algorithms for Unsteady Gas Flows with Shifting Thermochemical Equilibrium' by A. Jayamani, and F. K. Lu.

hypervelocity flowfields such as expansion tubes and hypervelocity nozzles leads to the observation that if at all thermochemical non-equilibrium occurs in a facility, it often spans a rather narrow region in the entire flowfield. Thus, it would be more efficient to selectively employ non-equilibrium subroutines in reduced-order models, perhaps based on a comparison of the relevant local time scales in a flowfield. But such an approach assumes the availability of other simplified MoC subroutines for thermally perfect and thermochemical equilibrium regimes. Having already developed thermally perfect gas MoC subroutines in Chapter 5, this chapter develops thermochemical equilibrium MoC subroutines. Similar in approach to the earlier chapters, IMoC subroutines were developed for shock waves, contact surfaces and rarefaction waves occurring in flows under shifting thermochemical equilibrium, hereafter referred to simply as thermochemical equilibrium flows. The vectorized MoC approach developed earlier is further extended to include simplified sink terms representing the effect of momentum and heat losses. This will aid in developing useful reduced-order models which can replicate flowfields of typical impulse facilities with large length-to-diameter ratios. Also demonstrated in this chapter are two practical reduced-order models developed using these MoC subroutines to resolve the flowfields in high enthalpy expansion and detonation tubes.

6.1 Governing equations

In view of the flow phenomena of interest here, consider the unsteady flow of a gaseous mixture in a quasi-one-dimensional duct. The governing equations for such a gaseous flow are the continuity, momentum and energy equations. Further, the gaseous system to be modeled is expected to be a closed system with no mass addition, or removal. Thus the mass continuity equation contains no sink terms. However, as the effect of losses on the gaseous mixture is to be considered, the momentum

and energy equations contain appropriate sink terms to accommodate for frictional and heat transfer effects. With all these considerations, the differential form of the gasdynamic governing equations for an unsteady quasi-one-dimensional flowfield can be written as

$$\frac{\partial \rho}{\partial t} + u\frac{\partial \rho}{\partial x} + \rho\frac{\partial u}{\partial x} + \rho u \frac{1}{A}\frac{dA}{dx} = 0 \tag{6.1a}$$

$$\rho\left(\frac{\partial u}{\partial t} + u\frac{\partial u}{\partial x}\right) + \frac{\partial p}{\partial x} = \frac{\delta F_{\mathsf{f}}}{V} \equiv \beta \tag{6.1b}$$

$$\rho\left(\frac{\partial h}{\partial t} + u\frac{\partial h}{\partial x}\right) - \left(\frac{\partial p}{\partial t} + u\frac{\partial p}{\partial x}\right) = \frac{\delta \dot{q}}{V} - u\beta \equiv \Psi \tag{6.1c}$$

In the momentum equation above (6.1b), the volumetric sink term can be rewritten using the definition of skin friction coefficient as

$$\beta = -\frac{1}{2}\rho u|u|\frac{4C_{\mathsf{f}}}{D} \tag{6.2}$$

While there are empirical methods available to estimate the value of C_{f} based on pipe flow correlations (see Chapter 3), this chapter assumes that the skin friction coefficient can be approximated as a constant throughout the control volume. It may also be worthwhile to recall the approach from Chapter 3, where the value of C_{f} was estimated using pipe flow correlations for a calorically perfect detonation tube model. This variable C_{f} approach has not been attempted here for simplicity.

In the energy equation (6.1c), the volumetric heat flux term can be modeled using modified Newton's law of cooling. Since the gaseous mixture is assumed to be in thermochemical equilibrium, it is desirable to evaluate the heat flux based on enthalpy difference. Assuming a heat transfer coefficient C_h, the volumetric heat flux term can be written as

$$\frac{\delta \dot{q}}{V} = \frac{4C_h}{D}\rho|u|(h_w - h_0) \tag{6.3}$$

The heat transfer coefficient can again be modeled using different empirical methods. In this chapter, Reynolds analogy is chosen for its simplicity, which results in the following relation connecting friction and heat transfer coefficients

$$C_h = \frac{C_\mathrm{f}}{2} \tag{6.4}$$

The wall enthalpy term in (6.3) can be evaluated at the facility's cold wall temperature using thermodynamic curvefits as will be discussed shortly. With the use of Reynolds analogy, the recovery factor term becomes unity and the local stagnation enthalpy is evaluated based on the core flow properties as

$$h_0 = h + \frac{1}{2}u^2 \tag{6.5}$$

The gasdynamic governing equations above (6.1a-6.1c) will have to be supplemented by equations describing the constituent gas thermochemistry. To this end, consider a gaseous mixture of n thermally perfect species with the massfraction of species i in the gaseous mixture given by $c_i = \rho_i/\rho$. (As before, any thermodynamic property with the subscript i represents the individual gas species and those without a subscript denote global mixture properties.) Under thermochemical equilibrium, the internal energy composition of all the species in the gaseous mixture can be defined using a single value of static temperature. For such a mixture, the arguments made in Chapter 4 about the behavior of an individual species in a mixture still hold. Thus, each species i in the mixture can be individually expected to satisfy its own perfect gas law given by

$$p_i = \rho_i R_i T \qquad (i = 1, 2, \ldots, n) \tag{6.6}$$

Similarly, a gaseous mixture in thermochemical equilibrium also obeys Dalton's law of partial pressures. Therefore, the mixture static pressure is simply the sum of the individual species partial pressures p_i.

$$p = \sum_{i=1}^{n} p_i \tag{6.7}$$

Then, Eqs. (6.6) and (6.7) can be combined to write a global equation of state for the entire gaseous mixture as

$$p = \rho \sum_{i=1}^{n} c_i R_i T \tag{6.8}$$

Further, under thermochemical equilibrium, the state of a given gaseous mixture is uniquely defined if two thermodynamic properties are fixed. For instance, given an initial mixture of various gaseous species, the mass fractions of its constituent species are readily determined if two state properties of the gaseous mixture are known, viz., $c_i = f(p, \rho)$. Thus, it is beneficial to reformulate the governing equations (6.1a)–(6.1c) so that the dependent variables are p, ρ and u, similar to the other MoC models developed before. This can be achieved by utilizing the global equation of state (Eq. 6.8) and the definition of global enthalpy, $h = \sum_{i=1}^{n} c_i h_i$, to re-write the energy equation (Eq. 6.1c) as

$$\frac{\partial p}{\partial t} + u\frac{\partial p}{\partial x} - a^2\left(\frac{\partial \rho}{\partial t} + u\frac{\partial \rho}{\partial x}\right) = (\gamma - 1)\Psi \equiv \psi \tag{6.9}$$

It emphasized that the thermodynamic properties in the above equations are evaluated under equilibrium thermochemistry. Thus, the sonic velocity for instance is $a = a_{eq}$ and the ratio of specific heats is $\gamma = \gamma_{eq}$. This emphasis is added, as the above equation is identical to the calorically perfect energy equation, for instance, by notation. Clearly the underlying thermochemistry differs between these two scenarios. When the gas is in thermochemical equilibrium, its chemical and internal (vibrational) energy composition can change throughout a flowfield, while for a calorically perfect

gas, they are frozen at their initial values. Thus, the method of calculating various thermodynamic properties clearly differs between these models.

In this work, equilibrium thermochemistry is primarily incorporated into the reduced-order models using curvefits. To construct these curvefits for a given species mixture, a desired range of temperatures and pressures is selected and equilibrium calculations are initially carried out using the open-source toolkit Cantera [85]. The necessary thermodynamic properties are then extracted from these calculations and curve-fits are created in terms of the state variables p and ρ, which form a part of the dependent variables in the MoC algorithms. As will be described in the subsequent sections, the use of curvefits is also advantageous, as they are readily amenable to vectorization. The working gases used in this chapter are helium, oxyhydrogen mixtures and air. Thus, the constituents used to create various gaseous mixtures are He, N_2, O_2, N, O, NO, H_2, H, OH, and H_2O. The thermodynamic data for these species were obtained from the NASA Glenn thermodynamic properties library [104].

6.2 MoC formulation and algorithms

The governing equations (Eqs. 6.1a,6.1b,6.9) introduced in the previous section are similar to those derived for a perfect gas, and thus are quasilinear hyperbolic partial differential equations. Therefore, the MoC procedure can be used to reduce these partial differential equations to ordinary differential equations. The validity of these ordinary differential equations is limited to certain curves called characteristic curves, which in this case will turn out to be three in number. Following the procedure of Zucrow and Hoffman [49], the characteristic curves for a quasi-one-dimensional, unsteady flow of a gaseous mixture in thermochemical equilibrium are given by

$$\left[\frac{dt}{dx}\right]_o = \lambda_o = \frac{1}{u} \tag{6.10a}$$

$$\left[\frac{dt}{dx}\right]_\pm = \lambda_\pm = \frac{1}{u \pm a} \tag{6.10b}$$

The first of these characteristic curves given by Eq. (6.10a) denotes a particle pathline. The subsequent equation, Eq. (6.10b) represents acoustic disturbances that travel along and opposed to the local continuum fluid velocity and thus are the Mach lines of unsteady flow. As mentioned earlier, the sonic velocity in Eq. (6.10b) represents equilibrium sound speed. All three of these characteristic curves pervade the entire flowfield and are the waves which "communicate" any changes in the gasdynamic properties occurring in the flowfield. The variation of properties themselves are governed by the reduced governing equations given by

$$\left[\frac{dp}{dx}\right]_o - a^2\left[\frac{d\rho}{dx}\right]_o = \frac{\psi}{u} \tag{6.11a}$$

$$\left[\frac{dp}{dt}\right]_\pm \pm \rho a\left[\frac{du}{dt}\right]_\pm = \psi \pm a\beta - \rho u a^2\frac{dA}{dx} \tag{6.11b}$$

These reduced equations called compatibility equations are associated with the characteristics denoted in their subscripts. Thus, together the characteristic and compatibility equations (6.10a)–(6.11b) determine the unsteady flowfield evolution in any given continuous domain. Where discontinuities are encountered, it will be seen that with the aid of supplementary conditions these equations can be applied to either side of the discontinuity. Finally, these simplified equations can be numerically integrated using the vectorized inverse marching approach developed in Chapter 5 as described in the following paragraphs.

As has been mentioned earlier, four different MoC subroutines representing various fundamental gasdynamic phenomena were developed in this study. Two of

these subroutines resolve gasdynamics of continuous regions, while the remainder resolve discontinuities. The salient features of all these algorithms are contained in the subroutine which resolves weak compression and rarefaction waves. Named the interior point solver, this algorithm is discussed first aptly. The solution procedure for the interior point solver is depicted in Fig. 6.1a through the characteristics involved. The grid points 1-2-3 represent the initial value line while grid point 4 is the location where the flow properties are to be calculated. In the original Zucrow and Hoffman [49] algorithms, the known flowfield variables at the grid points 1, 2 and 3 were used to create linearly varying curves of the dependent properties. In the current study, the initial value line is assumed to be provided in the form of a polynomial curvefit, which in this case was a piecewise-cubic function. Thus, similar to Chapter 5, the grid points 1, 2 and 3 are simplified representation of the true initial value line.

The characteristic and compatibility equations above are integrated using the Euler predictor-corrector algorithm. Firstly, (Eqs. 6.10a–6.11b) are discretized as follows

$$(x_4 - x_o) = \frac{1}{\lambda_o}\,\Delta t \tag{6.12a}$$

$$(x_4 - x_\pm) = \frac{1}{\lambda_\pm}\,\Delta t \tag{6.12b}$$

$$(p_4 - p_o) - a^2(\rho_4 - \rho_o) = \frac{\psi}{u}(x_4 - x_o) \tag{6.12c}$$

$$(p_4 - p_\pm) \pm \rho a\,(u_4 - u_\pm) = (\psi \pm a\beta - \rho u a^2 \frac{dA}{dx})\,\Delta t \tag{6.12d}$$

As an illustration, consider the procedure to identify the λ_+ characteristic shown in Fig. 6.1a. To identify this characteristic using the inverse marching method, various gasdynamic properties at grid point 4 are initially assumed to be the same as that at grid point 2. Using these properties and the location of x_4 the characteristic equation (Eq. 6.12b) is solved to identify the origin of λ_+ characteristic, x_+. With

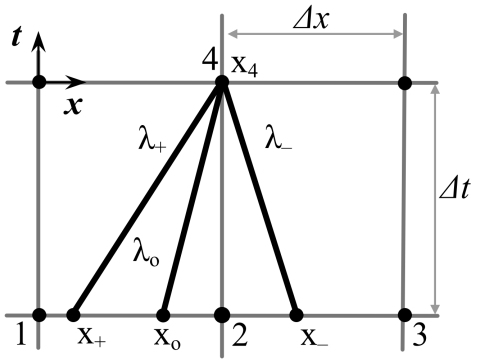

(a) Interior point.

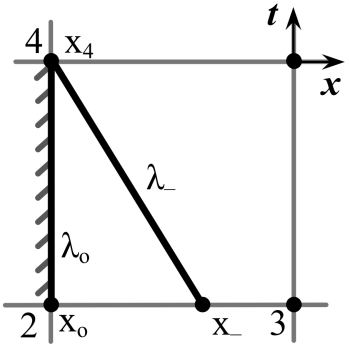

(b) Wall point.

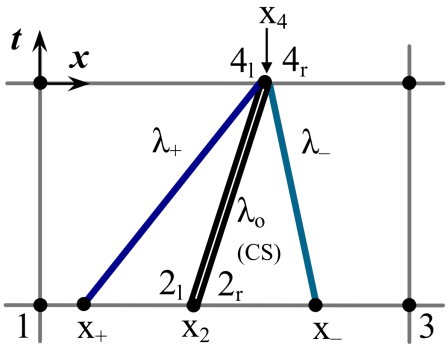

(c) Contact surface.

Figure 6.1: Schematics for MoC algorithms.

the newly identified characteristic origin, better estimates for λ_+ can be made, which in turn results in better estimates for the origin x_+. This iterative procedure is continued until the value of x_+ converges to a specified tolerance. With the vectorized MoC and a polynomial curvefit spanning the entire continuous region, all the λ_+ characteristics that reach various grid points in the continuous region can be identified at once. Therefore, the use of grid point 4 alone, as shown in Fig. 6.1a is merely for illustration (see Chapter 5). This procedure is similarly repeated for the pathline and the remaining Mach line. Once the origins of all three characteristics are identified, the compatibility equations (Eqs. 6.12c-6.12d) can be solved to identify the dependent variables p, ρ and u at location 4. This constitutes the predictor step. The corrector

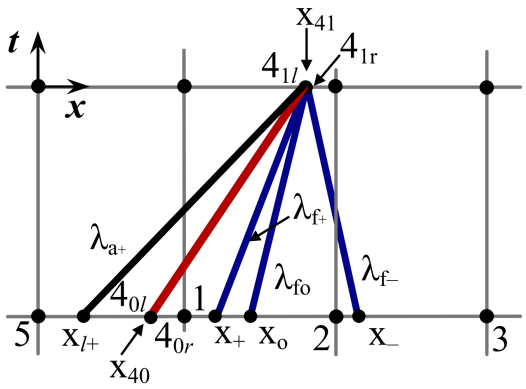

Figure 6.2: MoC algorithm for a shock wave.

step is similar to the predictor, but with the difference that all the coefficients in the characteristic and compatibility equations utilize average properties between the origin of the characteristic and location 4. Further, the corrector step is repeated until all the dependent properties converge at location 4. Once this occurs, the massfractions at location 4 can be estimated using the equilibrium curvefits supplied to the algorithm.

Next, the wall point algorithm shown in Fig. 6.1b is briefly discussed. This case represents the left-bounding wall point in a given domain. Based on symmetry arguments, this procedure can be adapted to the right-bounding wall point as well. From Fig. 6.1b, it can be seen that the pathline on the wall point remains stationary on the wall. Thus, the number of unknown variables reduces by one. Further, the λ_- characteristic disappears, as there is no fluid domain to the left of the wall. Thus, the integration procedure described for the interior point algorithm can be modified based on the above discussion to evaluate various properties at location 4.

The algorithms representing discontinuities can also be obtained through modifying the interior point solver. The discontinuities such as shock waves and contact surfaces represent boundaries of a continuum domain. But, the conditions governing their existence can be used in tandem with the methods developed for the interior

point solver to connect various flow properties on either sides of the discontinuity. For instance, consider the algorithm for contact surface shown in Fig. 6.1c. By definition, the static pressure and fluid velocity are continuous across the contact surface. Thus, $u_{2_l} = u_{2_r}$ and $p_{2_l} = p_{2_r}$. Therefore the contact surface itself is a pathline. However, since the contact surface represents the boundary between two different fluid states, the density and/or species composition may not be the same on either sides of the contact surface. Thus, the compatibility equation (Eq. 6.12c) for the pathline is individually written for either sides of the contact surface, despite the pathline being represented by the same characteristic curve. Clearly, the λ_+ and λ_- characteristics represent waves in two different fluid media and must be solved appropriately using the fluid thermochemical properties on the relevant side of the contact surface. While the integration procedure for the λ_+ and λ_- characteristics utilizes inverse marching, the contact surface is always projected forward in time, as the contact surface is individually tracked and its initial conditions are always known. Finally, due to the pressure and velocity continuity condition, the compatibility equations (Eq. 6.12d) can be solved readily to find the p and u at location 4. The predictor-corrector algorithm is again utilized iteratively to ensure convergence of all the gasdynamic properties at location 4 on either sides of the contact surface.

Finally, the algorithm for a right-running shock wave is shown in Fig. 6.2. A propagating shock wave always overtakes all the characteristics ahead of it and is overtaken by the characteristic that travels in the same direction as the shock wave. Thus, with an estimated shock location x_{4l}, the values of various flow properties immediately before the shock wave can be identified using the interior point algorithm as shown in Fig. 6.2. Across the shock wave, the discontinuity in various state properties are governed by the equilibrium Rankine-Hugoniot conditions. But, as the shock wave is itself overtaken by the trailing λ_{a_+}, the fluid state properties at

the aft of the shock wave computed through the Rankine-Hugoniot conditions must match with those computed through the compatibility equations for the overtaking λ_{a_+}. To achieve this, the shock velocity in location 4 is varied until the post-shock conditions match between the Rankine-Hugoniot and compatibility relations. In the case of a left running shock wave, the trailing characteristic becomes λ_{a_-}, while the other procedures remain the same.

6.3 Application of equilibrium MoC to unsteady problems

The MoC algorithms developed in the previous section are utilized to develop reduced order models for two pertinent high enthalpy impulse facilities, viz., an expansion tube and a detonation-driven shock tube. Eventhough an expansion tube may be expected to have a lesser degree of thermochemical excitation in its operation, the algorithm was primarily developed to address an anomaly previously observed in a thermochemical non-equilibrium MoC solver [111]. Thus, the expansion tube discussions here do not account for momentum and heat losses. The detonation-driven shock tube on the other hand, is a relevant problem in terms of both thermochemistry and losses. The former is more pronounced due to the recombination that may occur as the burnt driver gas is expanded to very low pressures, while the latter is noticeable due to the large L/D ratios employed in these facilities. There are two general modes of operation for a detonation-driven shock tube, or simply a detonation tube. Based on the relative propagation of the detonation wave in the driver compared to the test gas, these are classified as upstream or downstream modes. This chapter models an upstream mode detonation tube and compares the estimated pressure loads in the damping section to experimental results.

6.3.1 Expansion tube flowfield

Expansion tubes were introduced to alleviate the problem of test gas dissociation, which occurs when large energies are added to the gas primarily through a shock wave. A simplified operation of an expansion tube is shown in the form of a wave diagram in Fig. 6.3. From the illustration, it can be seen that an expansion tube is similar in construction to the classical shock tube, but it contains an additional section variously called the acceleration, or expansion section. The design philosophy is that the energy is added to a test gas in two stages - firstly through a shock wave and then followed by an expansion wave. As the goal is to circumvent dissociation in the test gas, the initial shock wave strength is limited by the onset of dissociation in the driven gas.

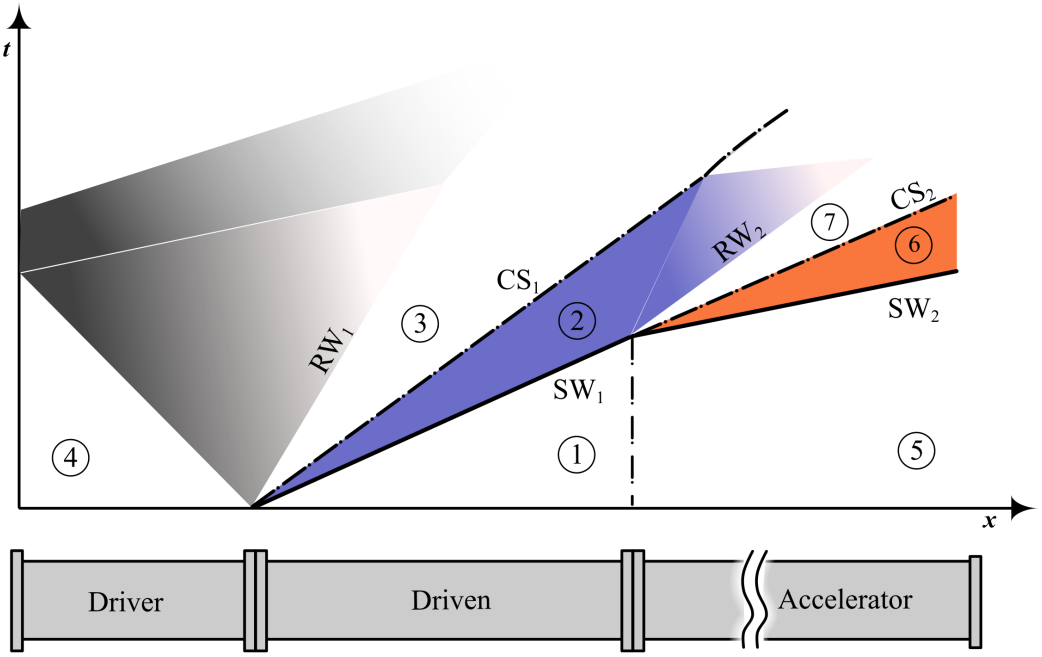

Figure 6.3: Schematic and wave diagram of an expansion tube operation (RW_1 - primary rarefaction, CS_1 - primary contact surface, SW_1 - primary shock wave, RW_2 - secondary rarefaction, CS_2 - secondary contact surface, SW_2 - secondary shock wave).

The operation of an expansion tube can be further explained through the wave processes in Fig. 6.3 (also see Fig. 6.4). The expansion tube consists of three sections named driver, driven and acceleration sections, which are initially isolated from each other using breakable diaphragms. The driven section contains the test gas, while the driver and acceleration sections contain high pressure and low pressure gases which add energy to the test gas in two different ways. From Fig. 6.3, it can be inferred that various quasi-steady regions, identified by circled numbers, exist throughout the expansion tube flowfield. Since the driver and driven sections are identical to the classical shock tube, their section nomenclature is likewise similar. At the beginning of the expansion tube operation, the driver, driven and acceleration gases are at rest in regions denoted ④, ① and ⑤ respectively. The facility operation begins as the diaphragm between the driver and driven sections rupture, idealized here as an instantaneous disappearance. This causes the high pressure driver gas to expand into the lower pressure driven gas, which is idealized as a centered rarefaction wave (RW_1). Due to the large pressure difference, the centered rarefaction wave instantaneously causes a shock wave (SW_1) to form in the driven gas. The shock compressed test gas occupies the quasi-steady region ②, while the expanded driver gas occupies another quasi-steady region ③.

Since there are two wave systems in an expansion tube operation, the waves associated with the driver-driven system are denoted primary waves, for instance the primary shock wave, as identified in Fig. 6.3. Now, as the primary shock wave reaches the end of the driven section, the diaphragm separating the driven and acceleration sections is assumed to disappear. This in turn causes the quasi-steady driven gas to expand into the acceleration section. Similar to the driver-driven wave system, the driven gas is assumed to expand through a centered rarefaction wave, which causes an instantaneous shock wave in the acceleration section. All the corresponding waves

in this system are denoted secondary waves, as shown in Fig. 6.3. The useable test gas slug is the expanded driven gas in region ⑦. Ideally, this region is bounded by the secondary contact surface at the front and either the trailing characteristic, or the leading reflected characteristic from the secondary rarefaction wave.

The above discussion of an expansion tube flowfield forms the basis of the MoC model developed in this study. As such, Fig. 6.3 also serves as a diagrammatic representation of the algorithm behind the MoC model. The required inputs for the algorithm which form the domain geometry and initial conditions are detailed in Table 6.1. In addition to these, curvefits for equilibrium properties of individual gas slugs are also a necessary input. Once all the inputs are provided, the overall expansion tube algorithm proceeds in the following manner. From the inputs file provided, the initial gas states at regions ④, ① and ⑤ are known. Since the integration scheme utilizes inverse marching approach a space-time grid needs to be constructed first. Then, various subroutines developed in the previous section can be employed over this is x-t grid to calculate the unsteady flow evolution. As the stability of underlying inverse marching method depends on the Courant–Friedrichs–Levy condition, that is, $\Delta t(u \pm a)_{max} < \Delta x$, the algorithm must first obtain the maximum possible wave speeds in the driver-driven wave system. This is evaluated based on the analytical equilibrium shock tube solution, which assumes that centered rarefaction wave in thermochemical equilibrium is formed in the driver gas and subsequently drives a thermochemical equilibrium normal shock wave in the driven section. As opposed to the calorically perfect shock tube, which permits an analytical solution, the equilibrium shock tube solution must be iteratively solved where the static pressure and velocity after the equilibrium driver expansion is matched to that behind an equilibrium normal shock in the driven section. The solution so obtained also forms the initial conditions for the primary wave system in this algorithm. With known maximum wave speeds,

Table 6.1: Expansion tube simulation parameters (based on LENS-X[50], repeated from Chapter 5)

	Driver	Driven	Acceleration
Length, m	6.2	14.8	26.45
Gas	He	Air	Air
Composition, % mole	He:1	N_2:0.79, O_2:0.21	N_2:0.79, O_2:0.21
Pressure, kPa	8271.429	20.679	0.331
Temperature, K	427	298	298

an x-t grid is constructed for the entire domain length and up to a user-specified time. Then, the solution procedure marches forward in time by resolving the flow properties for every subsequent time-step. As almost the entirety of the flowfield is made up of regions with continuous waves, which in this case is either expansion waves, or quasi-steady regions, vectorized interior point algorithm is simultaneously applied over all the grid points in a given continuous region. For instance, when the driver-driven wave system is resolved, the entire region between the wall and the primary contact surface is resolved at once. Then, region ② is resolved at once. Finally, the wall point, contact surface and shock wave solvers are individually called to advance over a given time-step. With the inverse marching method, the grid points nearby discontinuities need a special procedure for flowfield evaluation (see Chapter 3). In this case, the dependent variable polynomial fits created at every time-step for the MoC initial value line provide enough accuracy to evaluate the flowfield at these points by interpolation. This entire procedure is repeated for every time-step until the primary shock wave reaches the end of the driven section, when the diaphragm separating the driven and accelerator gases is assumed to disappear. The equilibrium shock tube solution is again employed to calculate the initial waves in the driven-accelerator wave system. Finally, the same algorithm detailed above is repeated over

the entire expansion tube domain to resolve the continuous regions and discontinuities at every subsequent time-step, until the specified final time.

With the above algorithm, a sample case for an expansion tube flowfield was resolved. With the new equilibrium expansion tube algorithm, the LENS-X simulation carried out in Chapter 5 was revisited here. The initial and boundary conditions for this case are again provided in Table 6.1. At first, a grid study was carried out to ensure convergence. Three cases were studied with the number of spatial grid points selected to be 962, 1603 and 1924. Though not shown here, this study showed that both the primary and secondary shock speeds differed by less than 1 percent between these three cases. Since these shock waves essentially determine (and are also influenced by) the quasi-steady state properties in various regions in the expansion tube, a convergence in shock speeds indicates that the overall has indeed converged. Thus, the results shown here correspond to the case with 1603 spatial grid points.

The overall unsteady flowfield evolution as resolved by the expansion tube algorithm is shown in Fig. 6.4. As the plot shows pressure contours, the trajectories of primary and secondary contact surfaces have been explicitly overlaid here for illustration. It can be seen that the resolved wave system is similar to the ideal wave system depicted in Fig. 6.3. Further evaluation of the results can be carried out by inspecting various flowfield property variation in the entire domain at arbitrary times. A simple way of validation is to compare the quasi-steady state properties that are resolved by the expansion tube algorithm against analytical Riemann invariants. This can be done individually for the driver-driven and driven-accelerator waves systems. Fig. 6.5 provides the spatial distributions of pressure, velocity, temperature and species composition in the driver and driven sections. At regions ② and ③, all these values are within 1 percent of the analytical Riemann solution. Of specific interest is Fig. 6.5b, which shows a static temperature distribution in regions ② and ③ that is nearly

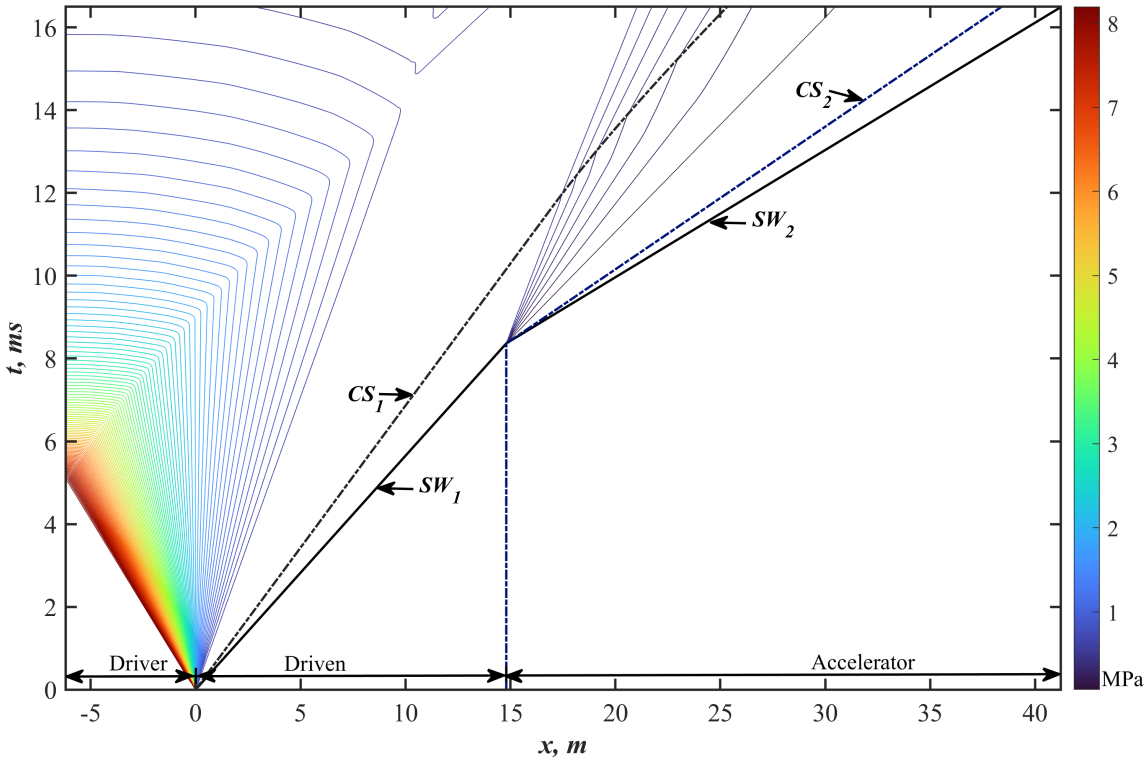

Figure 6.4: MoC generated ideal expansion tube flowfield (see Fig. 6.3 for nomenclature).

the same as the analytical solution and is devoid of any unrealistic overshoots as seen in an earlier work [111]. From the same plot, species distribution in the shock compressed test gas in region ② can also be seen to show negligible dissociation. Now, a similar instantaneous spatial distribution of various flow properties can be obtained after the establishment of the driven-accelerator wave system, as shown in Fig. 6.6. With a stronger secondary shock wave in the accelerator gas, the true capability the equilibrium solver is displayed, where the dissociation occurring in the accelerator air is clearly seen in the oxygen and nitrogen species fractions. Comparing Figs. 6.6a and 6.6b the test gas can still be seen to retain its near original composition as intended. Again, all the flow properties in regions ⑥ and ⑦ as resolved by the expansion tube

algorithm are within 1 percent of the analytical Riemann solution, which validates the expansion tube algorithm.

6.3.2 Damping Section Loading in a Detonation-driven Shock Tube

Detonation-driven shock tubes were developed in an effort to increase the enthalpy simulation capabilities of the classical shock tube [64, 12]. These facilities replace the high pressure inert driver gas in a classical shock tube with a reactive mixture and explosively release the energy in the driver gas using a detonation wave. The burnt gas, which is at high pressures and temperatures is then expanded unsteadily to drive a shock wave in the test gas. This chapter focuses on a specific mode of detonation tube operation, the upstream mode. The operation of this facility is illustrated in Fig. 6.7 using an idealized wave diagram. Similar to the expansion tube, the detonation tube also consists of three different gaseous slugs initially at rest and isolated from each other using diaphragms. Accordingly, Fig. 6.7 shows three different sections named damper, detonation driver and the driven section. The driven section contains the test gas as earlier. The detonation driver, as the name implies contains the chemically reacting mixture which will be ignited. In this mode of operation, the igniter is installed near the diaphragm between detonation driver and driven sections. Finally, the damping section, or the damper contains an inert gas at very low pressures for reasons to be explained later.

The operation of the detonation tube begins when a sufficiently high amount of energy is deposited into the detonation driver using an igniter. This causes a detonation wave to form in the driver gas, which can be approximated as an instantaneous detonation wave formation (experimentally, this limit is approached under conditions known as direct initiation). Simultaneously, the driver-driven diaphragm ruptures due to the high pressure and temperature gas behind the detonation wave. Due to

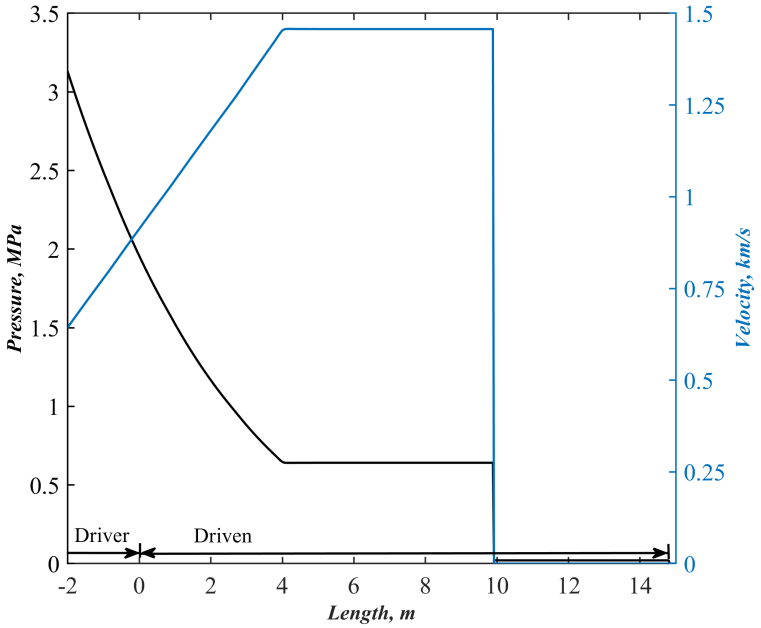

(a) Pressure and velocity distribution.

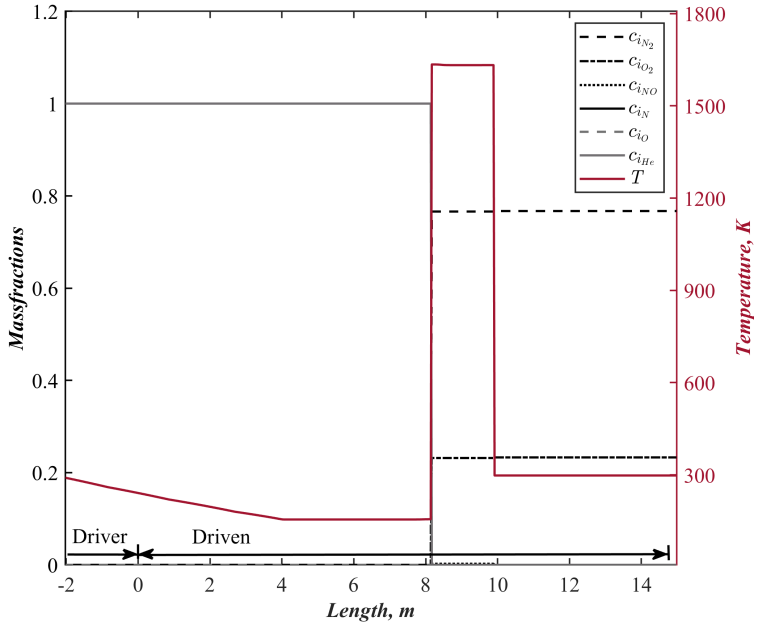

(b) Temperature and species distribution.

Figure 6.5: Instantaneous spatial properties in the driver-driven wave system (Regions ① - ③).

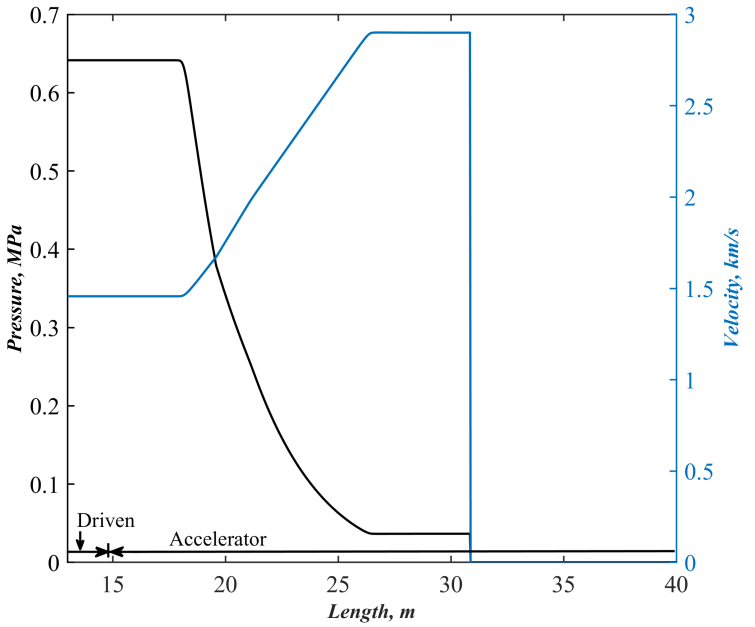

(a) Pressure and velocity distribution.

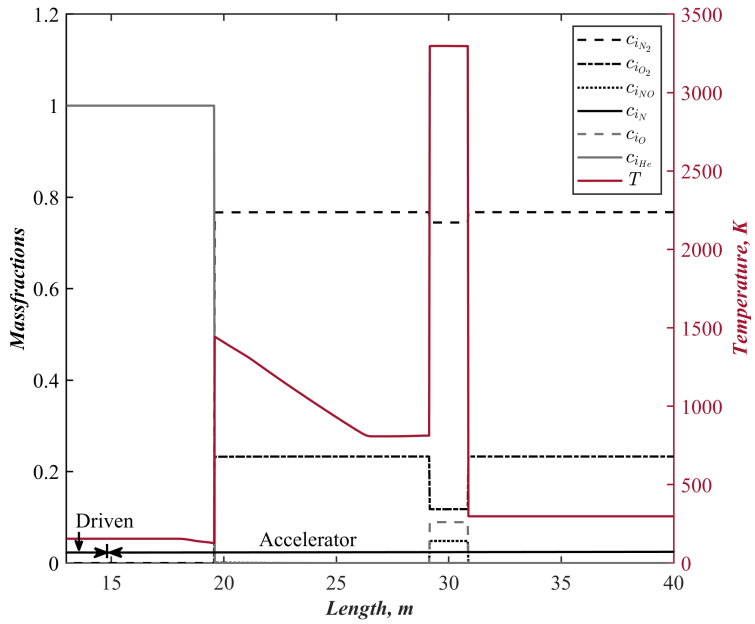

(b) Temperature and species distribution.

Figure 6.6: Instantaneous spatial properties in the driven-accelerator wave system (Regions ⑤ - ⑦ and ②).

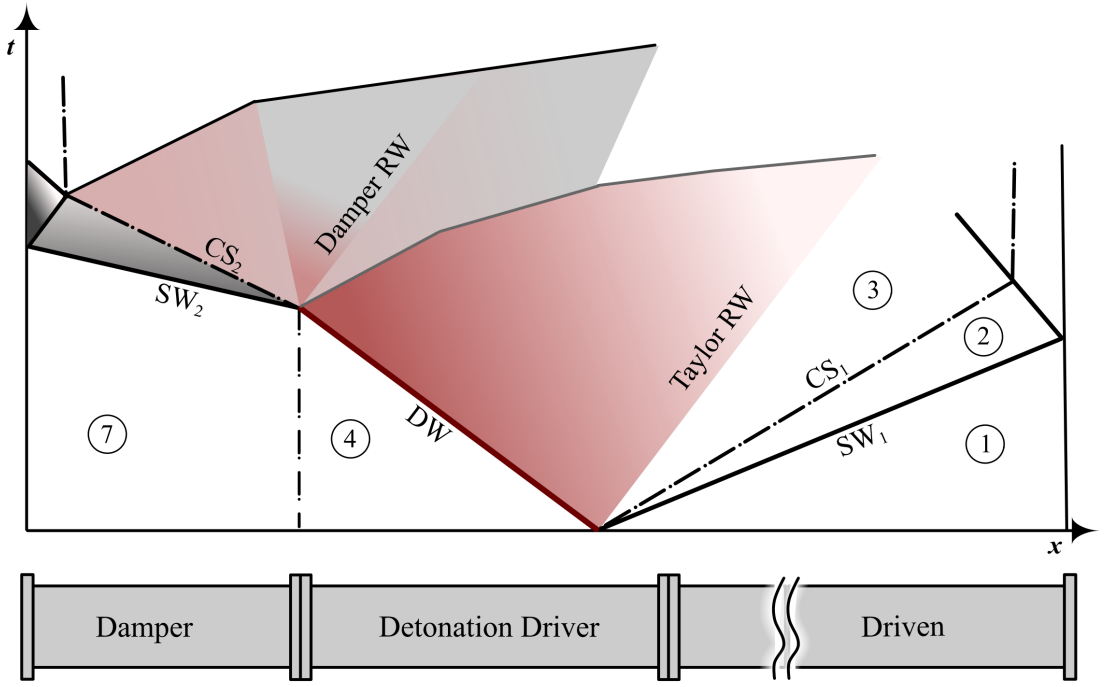

Figure 6.7: Schematic and wave diagram of a detonation tube operation (DW - detonation wave, RW - rarefaction wave, CS_1 - primary contact surface, SW_1 - primary shock wave, CS_2 - secondary contact surface, SW_2 - secondary shock wave).

the lower pressure test gas in the driven section, the burnt driver gas expands into the driven section, in turn driving a shock wave into the test gas.

In a classical shock tube, the leading wave propagating into the driver after diaphragm rupture is at local acoustic velocity, which merely initiates the acceleration of the driver gas into the driven section through the driver rarefaction. In the case of an upstream detonation tube, the leading wave that processes the driver gas is the detonation wave, traveling into the unburnt driver gas. When a freely propagating detonation wave, such as the one shown in Fig. 6.7, is achieved, the end-state of the burnt gas known as the Chapman-Jouguet (CJ) state is a unique property of the initial state of the gaseous mixture. Thus, every pathline in the driver gas is excited to a constant state, resulting in quasi-steady driver condition. This in turn

ensures that the primary shock wave (SW_1), see Fig. 6.7, is of constant strength under ideal conditions. Now, as the detonation wave reaches the end of the driver section, it transitions into a shock wave (SW_2) in the inert damping section. If this section were to be replaced by an endwall, the reflection of the detonation wave imposes a tremendous load on the endwall, which may damage the facility [12]. To avert this situation, a damping section is added and is usually maintained at near-vacuum conditions. Still, due to the high fill pressures in the detonation driver, the transmitted shock strength in the damping section is quite high. Thus, as the transmitted shock wave travels upstream and reflects off the damping section endwall, the pressure loads imposed on the facility are still quite high, which require careful consideration during the design phase. Therefore, this section primarily focuses on modeling this endwall loading using the MoC subroutines developed earlier in this chapter.

The detonation tube algorithm is similar to the expansion tube algorithm described earlier, but is adapted to the ideal detonation tube wave processes shown in Fig. 6.7 (also see Fig. 6.8). For simplicity, the detonation wave was resolved using the Shock and Detonation Toolbox (SDT) [84] and was merely propagated with the same properties over every time-step. Thus, the effect of losses on the detonation wave itself was not considered. Similar to the initial calculations for driven-acceleration wave system in the expansion tube, the secondary shock wave in the damping section is calculated using the equilibrium shock tube solution, with the CJ state as the driver state. While the driven section endwall conditions were not considered here, the damping section endwall was modeled for shock wave reflection and its subsequent interaction with the trailing secondary contact surface. Practically, the enormous temperatures experienced by the damper gas near the endwall in turn cause, at most, a weak shock wave reflection at the interface, as the reflected secondary shock wave

encounters the oncoming secondary contact surface. Therefore, the current algorithm only tracks the transmitted shock wave at the contact surface-shock wave interaction in the damping section, as the interior point solver can resolve weak shock waves. The interaction between the shock wave and contact surface is modeled using an approach similar to the shock tube solution discussed earlier. The type of interaction can be identified based on the acoustic impedance approach implemented earlier for calorically perfect gases in Chapter 3.

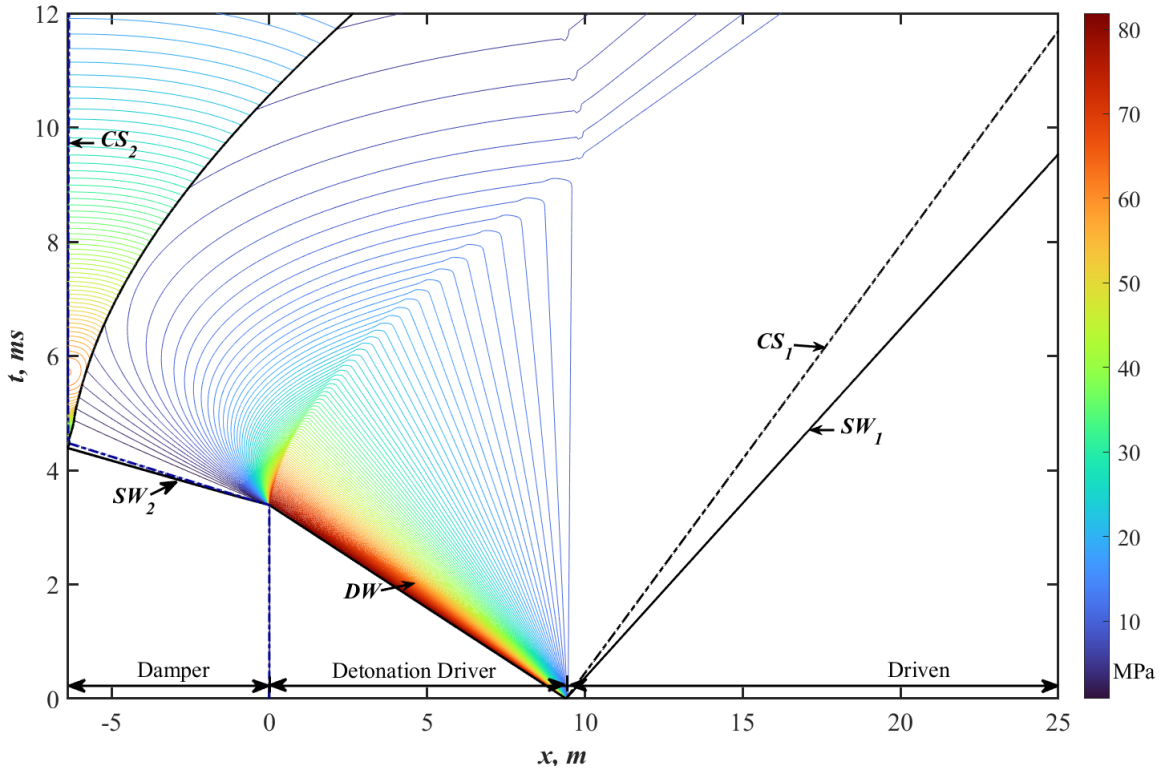

Figure 6.8: MoC generated ideal flowfield evolution for TH2-D (see Fig. 6.7 for nomenclature).

The detonation tube algorithm was used to model the static pressure history in the damping section of TH2-D in the Shock Wave Laboratory (SWL) in RWTH Aachen University reported in Olivier et al. [112]. The initial and boundary condi-

tions for the simulation are shown in Table 6.2 below. Note that the driven section length and fill conditions were chosen so that the driven section endwall phenomena did not require modeling. Also, to ascertain that such a simplified approach is appropriate, the monitored locations in the damping section were confirmed to be outside the domain of influence of the driven section endwall phenomena. This can also be inferred from the MoC results in Fig. 6.8 based on the facility geometry provided in Table 6.2. Additionally, various fill conditions in TH2-D show that the [12] detonation driver gas always expands to supersonic velocities and, the waves from driven section endwall do not reach even the end of detonation driver at least for about 10 ms into the detonation tube operation. Thus the simplified MoC model provides meaningful endwall loading results to be compared with the experimental pressure traces.

Table 6.2: TH2-D simulation parameters (based on Fig. 11 in Olivier et al. [112])

	Damper	Detonation Driver	Driven
Length, m	6.4	9.4	18.6
Diameter, m	0.140	0.140	0.140
Gas	Nitrogen	Oxy-hydrogen mixture	Air
Composition, % mole	N_2:1	H_2:0.6, O_2:0.4	N_2:0.79, O_2:0.21
Pressure, kPa	3	4000	366
Temperature, K	298	298	298

For the described fill conditions, the ideal flowfield evolution in TH2-D without the effect of losses as estimated by the MoC algorithm is shown in Fig. 6.8. As it can be inferred, the driven section endwall phenomena have not been modeled here, but the driven section conditions do not influence the damping section endwall phenomena in the time-frame considered. As the facility operation begins, the MoC generated x-t diagram shows an upstream running detonation (DW) propagating in the driver

section. The high pressure burnt gas behind the detonation wave expands into the driven section to drive the primary shock wave (SW_1). The expanded driver gas and the compressed driven gas are separated by the primary contact surface (CS_1). At a later time, the detonation wave reaches the driver endwall and transmits into the damping section as the secondary shock wave (SW_2). The extremely high strength of the secondary shock wave can be observed in the x-t diagram in the form of a closely trailing secondary contact surface (CS_2) in the damping section. Subsequently, the secondary shock wave travels to the end of the damping section and reflects off the endwall (SW_2) at ~ 4.5 ms. After this time, it can be seen that the secondary contact surface (CS_2) remains almost coincident with the damping section endwall due to the high pressure and momentum of the expanding driver gas. Closer inspection also reveals that the right-traveling reflected shock wave is pushed upstream after the shock-wave contact surface interaction, due to the relatively high momentum and acoustic impedance of the burnt driver gas.

Finally, the damping section results from MoC are compared against numerical simulation results from KASIMIR and experimental results from TH2-D, both from Shock Wave Laboratory (SWL) in Aachen, see Fig. 6.9. All these results represent pressure traces recorded at a distance of 2 m from the damping section endwall. Two simulations from the MoC model are shown here, one without the effect of losses and one accounting for losses using a constant C_f of 0.01. Note that the time of initial pressure raise from the lossless MoC was adjusted to be coincident with that from KASIMIR and the same Δt was then applied to the MoC result with losses shown in Fig. 6.9. It is seen that the lossless MoC results are similar to the results from KASIMIR, which models the detonation tube using equilibrium thermochemistry with no losses. When the effect of frictional and heat losses is considered in the MoC model, the plateau pressure, peak loading and the pressure decay behind the

transmitted secondary shock wave in the driver gas are comparable to experiments.

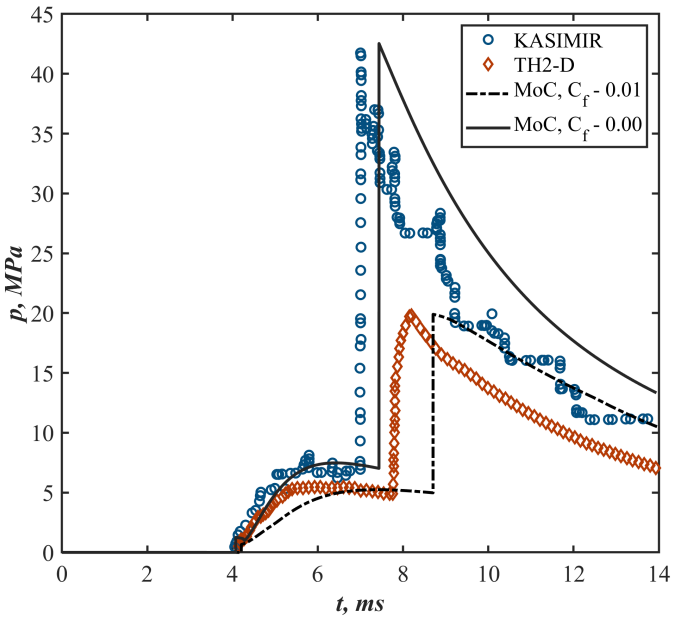

Figure 6.9: Comparison of wall static pressure estimates in the damping section (SWL Aachen data digitized from [112] using WebPlotDigitizer [113]).

CHAPTER 7

METHOD-OF-CHARACTERISTICS MODELS FOR FLOWS IN THERMOCHEMICAL NONEQUILIBRIUM [1]

The final chapter of this work discusses the MoC algorithms developed to resolve gas flows under thermochemical nonequilibrium. As mentioned throughout this work, thermochemical nonequilibrium models are imperative in modeling hypervelocity facility flowfields. When these facilities are used to simulate high-enthalpy flows, the associated high velocities in the test gas induce and also vibrational freezing. Thus, merely utilizing chemical nonequilibrium models to numerically simulate these facilities' operation may not provide an accurate estimate of all the test gas state properties. But, any effort to model thermochemical nonequilibrium occurring in a hypervelocity facility adds significant complexity in terms of computational modeling, and invites a marked increase in computational cost. The latter can be addressed through the use of reduced-order models, similar to the ones shown later in this chapter. This may also have been observed already in the vectorized MoC algorithms discussed in Chapter 6, for instance. Unfortunately, the complexities associated with modeling a thermochemical nonequilibrium gas state are unavoidable. Thus, this chapter builds on the work reported in Chapters 4, 5 and 6 to introduce MoC algorithms for thermochemical nonequilibrium flows.

First, the applicability of thermal nonequilibrium considered in this chapter is limited to diatomic molecules, for the ease of modeling. But, instead of the simplest

[1] Contains excerpts from the AIAA paper entitled 'Method of Characteristics Modeling of Nonequilibrium Flow in an Impulse Facility' by Jayamani, A., and Lu, F. K., AIAA Paper 2023-2088

Landau-Teller model, where only vibration–translation exchanges are considered, this chapter also considers the vibration–vibration exchange in diatomic molecules for better accuracy. The standalone chemistry solver used in Chapter 4 was improved to accommodate for thermal nonequilibrium and utilized here. Finally, the MoC subroutines developed in this chapter are based on the vectorized IMoC algorithms introduced in Chapter 5 and 6. Thus, the MoC subroutines developed in this chapter incorporate methods from all the previous chapters in this work, which were carried out to eventually build the thermochemical nonequilibrium algorithm reported here. Then, these MoC algorithms were used to simulate the flowfields in hypervelocity nozzles and expansion tubes in an effort to validate the newly developed algorithms.

7.1 Theory

The gasdynamic laws governing a generic flow are conservation of mass, momentum and energy. For brevity, the discussions below start directly from their respective differential formulations. Consider an adiabatic unsteady gas flow through a one-dimensional conduit of differentially varying area. Additionally assume that the effects of friction and heat transfer can be neglected and that the control volume has neither mass addition nor removal. Under such assumptions, the gasdynamic laws for area averaged properties across the cross-section of the conduit simplify to

$$\frac{\partial \rho}{\partial t} + u\frac{\partial \rho}{\partial x} + \rho\frac{\partial u}{\partial x} + \rho u\frac{1}{A}\frac{dA}{dx} = 0 \tag{7.1a}$$

$$\rho\frac{\partial u}{\partial t} + \rho u\frac{\partial u}{\partial x} + \frac{\partial p}{\partial x} = 0 \tag{7.1b}$$

$$\rho\frac{\partial h}{\partial t} + \rho u\frac{\partial h}{\partial x} - \frac{\partial p}{\partial t} - u\frac{\partial p}{\partial x} = 0 \tag{7.1c}$$

The above equations need information about the thermochemical gas state for closure. In the simplest case of a homogeneous monoatomic gas flow where the atoms remain

intact, the composition of the gas remains constant and the entirety of its sensible internal energy is stored in the random translational motion of the atoms. This model is classically known as the calorically perfect gas (scope limited to atoms here), where the specific heats and chemical composition of a gas are constants. In the calorically perfect gas models used in classical gasdynamics, it is also assumed that the thermal state of the gas adjusts instantaneously to any changes in bulk properties brought about by the gasdynamic evolution. In other words, it is assumed that the internal energy is rapidly redistributed within the gas as the flow evolves. However, in the case of flows of interest in this chapter—diatomic molecules under high temperatures and high flow velocities—neither the chemical composition nor the specific heats remain constant. To complicate matters, the evolution of this thermochemical state happens in tandem with the flow evolution at a finite-rate, a situation known as thermochemical nonequilibrium. Thus, the following subsections contain the methodology used to account for thermal and chemical nonequilibrium in the gas state.

7.1.1 Thermal nonequilibrium

In contrast to atoms, the internal energy of a diatomic molecule can be stored in multiple modes other than its random translational motion, which will be discussed shortly. From the quantum state description, it transpires that these internal energy modes are permitted to exist only at certain discrete states or energy levels. As the internal energy of a molecule varies, its transition to a different energy state happens only through successive transitions between adjacent energy levels. It is further assumed that this variation of internal energy occurs as a result of direct collisions between different constituent molecules and atoms, an assumption which is generally valid up to 8000 K [95].

For simplicity, ignoring the contribution due to the internal structure of the atoms, that is, electronic excitation and the contributions due to the nucleus, the specific internal energy of a diatomic molecule can be simplified to

$$e_{int} = e_{tran} + e_{rot} + e_{vib} \tag{7.2}$$

where e_{tran} is the energy associated with the translational motion of the molecules, e_{rot} is the component due to molecular rotation and e_{vib} is the component due to the structure and dynamics of the molecular bond. Assuming that a Boltzmann distribution of the energy states exists in all the categories, each of the above terms will have an associated temperature, that is, T_{tran}, T_{rot} and T_{vib}. However, if all the energy modes are in equilibrium with each other, a single temperature defines the internal energy of all the groups.

The internal energy corresponding to the rotational and translational modes can be evaluated by assuming the molecules to be rigid dumbbells which possess independent translational velocity and constants moment of inertia. Evaluating the appropriate molecular partition functions yield [95]

$$e_{tran} = \frac{3}{2} R T_{tran} \tag{7.3a}$$

$$e_{rot} = R T_{rot} \tag{7.3b}$$

The vibrational energy of diatomic molecule can be evaluated based on a harmonic oscillator model of its constituent atoms, which leads

$$e_{vib} = \frac{R\Theta_v}{e^{\Theta_v / T_{vib}} - 1} \tag{7.4}$$

So far, the internal energy of a pure diatomic species has been considered. In the case of a gaseous mixture consisting of n number of monoatomic and diatomic species, with individual mass fractions given by c_i, the total specific internal energy is

simply provided by $e_{mix} = \sum_{i=1}^{n} c_i e_i$. Obviously, when the gaseous mixture consists of atoms, the only active component of internal energy in Eq. (7.2) is the translational mode.

In developing Eqs. (7.3a)–(7.4) it was assumed that none of the energy groups are in equilibrium with each other. However, even for the high-enthalpy air flows considered here, translational and rotational energies can be considered to be in equilibrium with each other. Thus, T_{tran} and T_{rot} can be replaced by a single temperature, T_{rt}. This is based on the observation that the number of molecular collisions required for translational and rotational energies to reach equilibrium is less than 10 [114, 95, 115], a number which is achieved in a nanosecond in air, even at standard atmospheric conditions. Thus, the only source of thermal nonequilibrium considered here is due to the variation of vibrational energy.

In modeling the vibrational relaxation/excitation of a harmonic oscillator, the simplest applicable theory is that of Landau and Teller [95]. The theory considers the vibrational excitation of a harmonic oscillator through energy exchange with the translational–rotational modes which themselves are assumed to be in equilibrium throughout the process. The Landau–Teller model assumes that the rate of vibrational energy excitation is linearly proportional to the deviation of the instantaneous vibrational energy from its local equilibrium value. Though this theory has been shown to replicate vibrational excitation behind normal shock waves, Landau–Teller results for relaxing flows in nozzles have not been able to replicate the population distribution in lower vibrational levels. While original experiments led to a conclusion that the observed relaxation rates were faster by about a factor of 1 000, it is believed that the true multiplication factor may not be greater than 5 [116, 117]. (For a discussion on the systematic errors that may lead to such faster relaxation, refer to [117]). Reasons attributed to the true relaxation rate discrepancy include

the anharmonic nature of interatomic forces between molecules, multiple quantum jump transitions, non-resonant energy transfer between colliding partners and non-Boltzmann distributions during relaxation processes.

To reconcile these differences, Bray [118, 116] studied the relaxation of homogeneous anharmonic Morse-type oscillators under isothermal and non-isothermal conditions. Bray concluded that qualitatively, when vibrational excitation occurs in an isothermal heat bath, the effects of anharmonicity are expected to be minor. Therefore, the Landau–Teller model seems appropriate behind shock waves, as is known. For vibrational relaxation in a non-isothermal heat bath, multiple factors including anharmonicity, vibration–vibration (VV) energy exchange and rate of change of the heat bath's translational temperature seem to influence the relaxation behavior. Collectively, it was shown that these effects indeed cause a faster relaxation rate than the Landau–Teller model and may lead to non-Boltzmann distribution of the vibrational population. As the current paper aims to model vibrational relaxation through unsteady expansion fans and nozzles, a simple Landau–Teller relaxation will not adequately represent the underlying physical phenomena. While it is desirable to employ an anharmonic oscillator model, uncertainty in their VV transition rate data and computational complexities associated with state-to-state models point towards a simpler model for vibrational relaxation.

With the intent of capturing the dominant VV exchange and yet retaining a simplistic model for a quasi-one-dimensional analysis, the vibrational relaxation model described by Taylor et al. [119] is used here. Though the current work uses this model to represent vibrational relaxation of a chemically reacting diatomic gaseous mixture, Palmer and Hanson [58], for instance, have used this model to calculate vibrational relaxation of a steady, two-dimensional chemically frozen polyatomic gaseous mixture.

For a gaseous mixture containing a total of n species amongst which m are vibrationally active, the rate of change of specific vibrational energy of species i is given by

$$-\frac{DE_{v,i}}{Dt} = \sum_{i'=1}^{n} \frac{\mathcal{N}_{i'}}{\tau_{i-i'}^{VT}} E_{v,i} + \sum_{\substack{i'=1,\\ i'\neq i}}^{m} \frac{\mathcal{N}_{i'}}{\tau_{i-i'}^{VV}} \left[E_{v,i}(1-E_{v,i'}) \frac{1-e^{-\Theta_{v,i}/T}}{1-e^{-\Theta_{v,i'}/T}} - E_{v,i'}(1-E_{v,i}) \right] \tag{7.5}$$

where

$$E_v = \frac{e^* - e_{vib}}{e^*}$$

and where e_{vib} represents the local specific vibrational energy of the species in consideration and e^* represents the specific vibrational energy of a harmonic oscillator in equilibrium with the local transational-rotational temperature. Thus, this model again considers vibrational relaxation of a harmonic oscillator through VV energy exchange with other harmonic oscillators in addition to VT energy exchange with self and all the other species. In the simplest of the cases, which is self relaxation of a pure diatomic species, Eq. (7.5) simplifies to the Landau–Teller model.

The rate constants for appropriate VV and VT processes are required for solving Eq. (7.5). Since air is the primary medium of interest here, VT relaxation times are calculated based on Millikan–White's formula

$$p\tau_{VT} = \exp\left[a\left(T_{rt}^{-1/3} - b \right) - 18.42 \right] \ \text{atm} \cdot \text{s} \tag{7.6}$$

The values of a and b are taken from Park [120]. It is noted that the relaxation times used here do not contain the high-temperature correction term detailed in Park [120] since the maximum temperatures of interest here is around the 5 000 K limit [121] which, when far exceeded, results in the Millikan–White formula predicting faster relaxation times. For VV, the rate constants can be obtained from Taylor et al. [119] using the probabilities of collision between various diatomic molecules reported

therein. Based on digitization of the plots in [119], the probabilities of collision between N_2 and O_2 and N_2 and NO are approximated to be

$$P(\underset{01}{\overset{10}{N_2, O_2}}) = 3.5(T_{rt}/1000)^{3.1716} \times 10^{-6}$$

$$P(\underset{01}{\overset{10}{N_2, NO}}) = 7.35(T_{rt}/1000)^{2.4371} \times 10^{-5}$$

The relaxation times for the reverse processes mentioned above are obtained using the principle of detailed balancing [95, 119]. For completeness, the VV exchange between O_2 and NO is assumed to have the same probability as N_2 and NO collisions, similar to the approach of Park and Lee [122]. This assumption was not made on physical reasoning, but merely because of the uncertainty in possibly obtaining experimental VV rate data between molecular oxygen and nitric oxide.

7.1.2 Chemical nonequilibrium

Consider a chemically reacting gaseous mixture with a total of n species. If the flow process considered is indeed in chemical nonequilibrium at the given point in time, there would be a net change in the species population from the previous instant of time. This section details the procedure used in this work to calculate the chemical species production term. Noting that a chemically reacting gaseous mixture in thermal nonequilibrium can still be considered to be a mixture of perfect gases [95], individual species can be expected to obey the perfect gas law. Thus,

$$p_i = \rho_i R_i T_{rt} \qquad (i = 1, 2, \ldots, n) \quad (7.7)$$

The static temperature used in the above equation is the translational–rotational temperature. From the discussions in Chapter 4, the static pressure of a perfect gas is a function of its molecular momentum. When finite-rate vibrational excitation/relaxation of these molecules are taken into account through the harmonic oscillator

model, it is assumed that the constituent atoms are oscillating about an equilibrium point. Thus, the effect of molecular vibration does not contribute to the bulk momentum of the molecules [95] and the use of T_{rt} in Eq. (7.7) is justified. Therefore, similar to that of a gaseous mixture in chemical nonequilibrium (see Chapter 4), the global static pressure of a gaseous mixture in thermochemical nonequilibrium can also be obtained using Dalton's law of partial pressures. Defining mass fractions of various species as $c_i = \rho_i/\rho$, the global gas law becomes

$$p = \rho \sum_{i=1}^{n} c_i R_i T_{rt} \qquad (i = 1, 2, \ldots, n) \qquad (7.8)$$

where the global properties contain no subscripts. Thus, all the species in the gaseous mixture are assumed to have the same translational–rotational temperature, as the translational and rotational modes are always expected to be in equilibrium based on the arguments made in the last subsection.

If there exist l elementary reactions which represent the underlying chemical processes of all the reacting species,

$$\sum_{i=1}^{n} \nu'_{ij} \mathbb{A}_i \underset{k_{bj}}{\overset{k_{fj}}{\rightleftharpoons}} \sum_{i=1}^{n} \nu''_{ij} \mathbb{A}_i \qquad (j = 1, 2, \ldots, l) \qquad (7.9)$$

then, under chemical nonequilibrium, a net production or depletion of various species occurs over time. Similar to Chapter 4, this rate change in molar species concentration, accounted by the species source function for a unit volume is given by

$$\overline{\sigma}_i = \sum_{j=1}^{l} (\nu''_{ij} - \nu'_{ij}) \left[k_{fj} \prod_{i=1}^{n} \left(\frac{\rho c_i}{\mathbb{M}_i} \right)^{\nu'_{ij}} - k_{bj} \prod_{i=1}^{n} \left(\frac{\rho c_i}{\mathbb{M}_i} \right)^{\nu''_{ij}} \right] \qquad (7.10)$$

As was mentioned before, for every elementary reaction j, the forward and backward reaction rates can be related through their respective equilibrium gas constant k_p via

$$\frac{k_{fj}}{k_{bj}} = k_{pj} (\mathcal{R}T)^{(\nu'_{ij} - \nu''_{ij})} \qquad (j = 1, 2, \ldots, l) \quad (7.11)$$

For flows in chemical nonequilibrium, but thermal equilibrium, the temperature used to evaluate the reaction rates in Eqs. (7.10) and (7.11) does not pose a dilemma, as a single temperature defines all the internal energy modes. However, for flows under thermochemical nonequilibrium, as the temperature can be multi-valued, the reaction rate calculation can either use T_{rt}, or, a combination of T_{rt} and T_v. Given the influence of vibrational energy on dissociation, Park [123] proposed a semi-empirical, two-temperature model, where the rate constants for dissociation reactions employ a geometric average of T_{rt} and T_v of the respective species. The recombination rates however, are calculated using T_{rt} alone, as this process is merely dependent on the molecular kinetic energy of the colliding particles. Thus, for an elementary dissociation-recombination reaction j, the temperature at which the forward reaction rates, that is, the dissociation rates are evaluated is defined as

$$T_{av,j} = \sqrt{T_{rt} T_{v,i}} \tag{7.12}$$

where the dissociating species is 'i'. Subsequently, the Arrhenius rate equation discussed in Chapter 4 becomes,

$$k_{f,j} = B T_{av}^{\alpha} e^{(-E_a/\mathcal{R}T_{av})} \tag{7.13}$$

As the backward reactions represent recombination kinetics, $k_{b,j}$ retains the same form as before in the Arrhenius equation. However, if the calculations involve finding $k_{b,j}$ as a function of $k_{f,j}$, then

$$k_{b,j} = \frac{k_{f,j}(T_{rt})}{K_{pj}(T_{rt})} \tag{7.14}$$

To evaluate the chemical rate constants in Eq. (7.10) taking into account two-temperature model, the chemistry subroutine developed in Appendix B was modified. The modified chemistry subroutine can calculate rate constants when both the forward and backward rate constant data are available, or, if only the dissociation rate contants

are available. See Appendix D for specific details on the formulation utilized in this chapter to evaluate reaction rate constants.

Finally, similar to Vincenti and Kruger [95], the species continuity equation accounting for the rate change of mass fractions of a chemically reacting gas flow can be written as

$$\rho\left(\frac{\partial c_i}{\partial t}+u\frac{\partial c_i}{\partial x}\right)=\mathbb{M}_i\overline{\sigma}_i=\sigma_i \quad (i=1,2,\ldots,n) \tag{7.15}$$

Again, since the only reacting species of concern here is air, the only chemical reaction mechanism used here is the reduced Dunn–Kang mechanism introduced by Shuen et al. [108]. This mechanism considers air to be made up of five constituent species—N_2, O_2, NO, N and O—with six elementary reactions and was used previously in Chapter 4 to model chemical nonequilibrium behind a normal shock wave and dissociating air flow through a nozzle. Further information on the chemical kinetics mechanism used in the MoC calculations here are given in Appendix D.

7.2 MoC formulation and numerical implementation

The governing equations discussed in the previous section represent a set of quasi-linear hyperbolic partial differential equations. MoC provides a way to reduce these equations to ordinary differential equations so that they can be solved with ease. Before the MoC procedure is carried out, all the governing equations have to be expressed in terms of the primary dependent variables of interest — p, ρ, u, c_i and e_v. Thus, the energy equation (7.1c) is rewritten using the definition of global enthalpy $h=\sum_{i=1}^{n}c_i(e_i+R_iT_{rt})$ as

$$\frac{\partial p}{\partial t}+u\frac{\partial p}{\partial x}-a_f^2\left(\frac{\partial \rho}{\partial t}+u\frac{\partial \rho}{\partial x}\right)=\sum_{i=1}^{n}(\gamma_f R_iT_{rt}-(\gamma_f-1)h_{i,f})\sigma_i-\rho(\gamma_f-1)\sum_{i=1}^{m}c_i\zeta_i \tag{7.16}$$

where ζ_i represents the thermal source function, obtained from Eq. (7.5) but rewritten as

$$\frac{De_{v,i}}{Dt} = \frac{\partial e_{v,i}}{\partial t} + u\frac{\partial e_{v,i}}{\partial x} = \zeta_i \tag{7.17}$$

Note that the sonic velocity in Eq. (7.16) is the thermochemically frozen value which arises naturally during the derivation. Additionally, if the flow is assumed to be in thermal equilibrium, then thermal rate equation vanishes, which results in Eq. (7.16) simplifying to that of a chemically reacting flow, reported previously in Chapter 4. Finally, for a thermochemically frozen flow, all the source terms in Eq. (7.16) vanish, resulting in the energy equation for a perfect gas flow reported in Chapter 3.

Thus, the complete set of governing equations for an inviscid, quasi-one-dimensional thermochemically relaxing gas flow comprises of Eqs. (7.1a),(7.1b), (7.16), (7.15) and (7.17). These partial differential equations are converted to ordinary differential equations on certain curves called characteristic curves. While the resulting ordinary differential equations provide the variation of the dependent variables in the flowfield, the characteristic curves themselves represent the propagation of disturbances in the flowfield. Close observation will reveal that the equations representing species continuity (7.15) and variation of vibrational energy (7.17) are already in the characteristic form, with the fluid velocity representing both their characteristic curves. Utilizing the MoC procedure detailed in Zucrow and Hoffman [49], the characteristic curves for the system of governing equations become

$$\left(\frac{dt}{dx}\right)_o = \lambda_o = \frac{1}{u} \tag{7.18a}$$

$$\left(\frac{dt}{dx}\right)_\pm = \lambda_\pm = \frac{1}{u \pm a_f} \tag{7.18b}$$

In the above equations, the characteristic curve λ_o represents the pathline, while the curves $\lambda_\pm$ represent the sonic disturbances that propagate along and against the

flow direction. It is seen that the characteristic equations are in the same form as that obtained for a calorically perfect gas in Chapter 3 and that for a chemically reacting mixture of gases in Chapter 4. However, the definition of "frozen" sonic velocity differs between these three models. Overlooking the trivial case of a calorically perfect gas flow, the sonic velocity calculation for a chemically reacting flow assumes that the species composition is frozen at the local values, but the internal energy is always in equilibrium. However, for a thermochemical nonequilibrium flow, the sonic velocity calculation utilizes the species composition and internal energy at locally frozen values.

The compatibility equations that are valid on the characteristic curves represented by Eqs. (7.18a) and (7.18b) are

$$dp_o - a_f^2 d\rho_o = \sum_{i=1}^{n} (\gamma_f R_i T_{rt} - (\gamma_f - 1)h_i)\sigma_i dt_o - \rho(\gamma_f - 1)\sum_{i=1}^{m} c_i \zeta_i dt_o \tag{7.19a}$$

$$(dc_i)_o = \frac{\sigma_i}{\rho} dt_o \qquad (i = 1, 2, \ldots, n) \tag{7.19b}$$

$$(de_{v,i})_o = \zeta_i dt_o \qquad (i = 1, 2, \ldots, m) \tag{7.19c}$$

$$dp_\pm \pm \rho a_f du_\pm = \sum_{i=1}^{n} (\gamma_f R_i T_{rt} - (\gamma_f - 1)h_i)\sigma_i dt_\pm - \rho(\gamma_f - 1)\sum_{i=1}^{m} c_i \zeta_i dt_\pm - \rho u \frac{1}{A}\frac{dA}{dx} a_f^2 dt_\pm \tag{7.19d}$$

where the subscripts of the total derivatives in the compatibility equations denote the appropriate characteristic curves on which they are are valid. Equations (7.18a)–(7.19d) provide the fundamental set of equations which can be manipulated based on a specific flow scenario to solve for the unknowns, which are the dependent variables here. The current work has resulted in the development of three subroutines which are capable of resolving a thermochemically relaxing flowfield comprising compression and/or expansion waves, contact surfaces and shock waves. All three subroutines

employ the inverse marching method employed previously in Chapters 4 and 5 with modifications as will be discussed.

The inverse marching method can be explained as follows. Every point in the continuum x–t space contains three intersecting characteristic curves, to be called characteristics hereafter. Associated with these characteristics are the compatibility equations that describe the flow properties variation in the flowfield. Since the problem is hyperbolic, flow perturbations originating on an initial value line will propagate along these characteristics, thereby allowing the flow properties at the intersection to be determined. Based on an initial guess for the unknown properties at the location of interest, all three characteristics are projected back to the initial value line, followed by integration of the compatibility equations to obtain improved estimates of the flow properties at the point of interest. This procedure is repeated until all the calculated flow properties converge to a specified error tolerance.

The subroutine which resolves continuous regions of compression or expansion waves is now discussed, as it utilizes all the characteristic and compatibility equations described above. Similar to the nomenclature used in all the chapters so far, this subroutine is called the interior point module. The algorithm for the interior point module utilizes a predefined grid in the x–t plane, as shown in Fig. 7.1a. The initial value line is again schematically represented by the region between grid points 1 and 3, with grid point 4 representing the location at which unknown flowfield variables are to be calculated. Also shown in Fig. 7.1a are the characteristics that intersect at grid point 4, with the same nomenclature as Eqs. (7.18a) and (7.18b).

The solution procedure is carried out in two steps, with the gasdynamic and thermochemical integration procedures carried out separately. During the first step which is the gasdynamic integration, Eqs. (7.18a–7.19a) and (7.19d) are solved using the vectorized Euler predictor–corrector method as described in Chapter 5. Here, the

themochemical state of the gas is assumed to be frozen at its initial value. To solve the compatibility equations along the characteristics, values of all the dependent variables at the origin of the characteristics need to be evaluated. The current method utilizes piecewise cubic interpolation to determine these properties, as opposed to linear interpolation used by Zucrow and Hoffman [49]. Further, in the case of a calorically perfect gas flow, the source terms, for instance, the friction and heat loss terms are evaluated based on the local state properties at the origin of the characteristics. In the current case however, similar to Chapter 4, the thermochemical source terms during the gasdynamic integration are also obtained through interpolation, as evaluation of these terms based on local state properties significantly increases the computational time.

Once the gasdynamic integration is complete the pathline of the particle that passes through grid point 4 at the current time is known. Thus, all the required state properties of the particle is known at the initial value line. Additionally, because of the gasdynamic integration, the frozen state properties are now known at grid point 4. Assuming a linear variation of the static pressure on the pathline, the thermochemical state equations (7.19b and (7.19c) are evaluated using `ode15s`. As noted previously, the chemical-state source terms are evaluated using Cantera [124], while the thermal-state properties are directly evaluated based on the equations developed in Section 7.1.1. With the completion of thermochemical integration, all the state properties of the fluid are obtained at grid point 4, which completes the first iteration. This alternating integration procedure to account for gasdynamic and thermochemical state variation is carried out until various flow properties at grid point 4 converge to a specified tolerance. The interior point module can be repeated over an array of predefined grid points to obtain a complete description of the flowfield of interest.

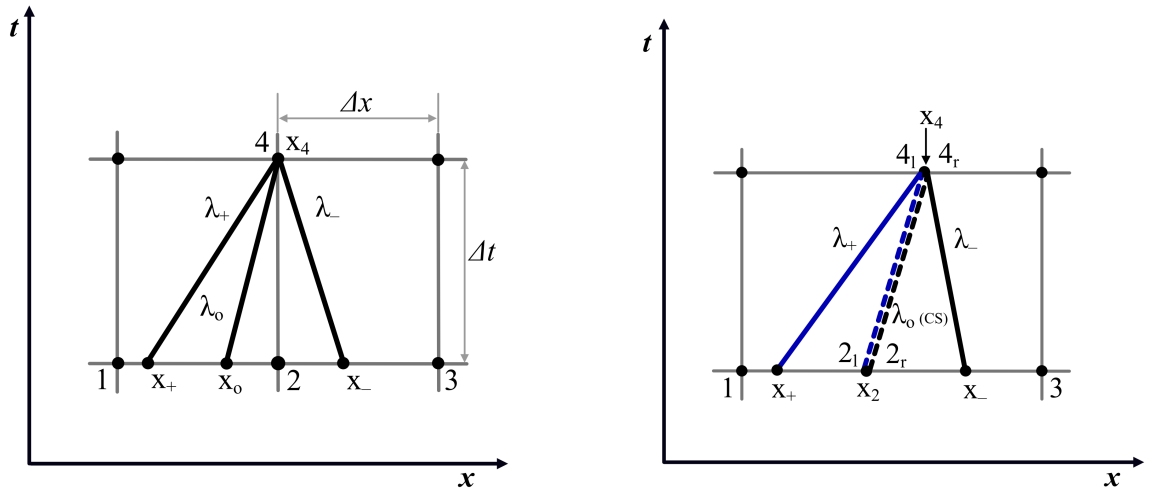

(a) Interior point module.

(b) Contact surface module.

Figure 7.1: MoC sub-routine algorithms.

The next subroutine to be discussed represents the gasdynamics of a contact surface. By definition, the contact surface is an impermeable, massless membrane separating two fluids in an inviscid flow. Then, mass continuity and momentum balance equations necessitate that the fluid velocity and static pressure be continuous across a contact surface [47], but other state properties such density, temperature and species composition may be discontinuous. The contact surface is hence a discontinuity and the differential equations developed above cannot be directly applied. However, the conditions imposed by its definition show that the contact surface itself represents a pathline. Thus, the characteristic and compatibility equations can be separately applied to either side of the contact surface. With the additional condition of continuity of pressure and velocity, the total derivatives of pressure and velocity are the same for species representing either side of the contact surface. Utilizing these observations along with the characteristic and compatibility equations developed above, the relaxation process of a contact surface can be solved. A representation of the algorithm for a contact surface is given in Fig. 7.1b, with different fluids represented by different

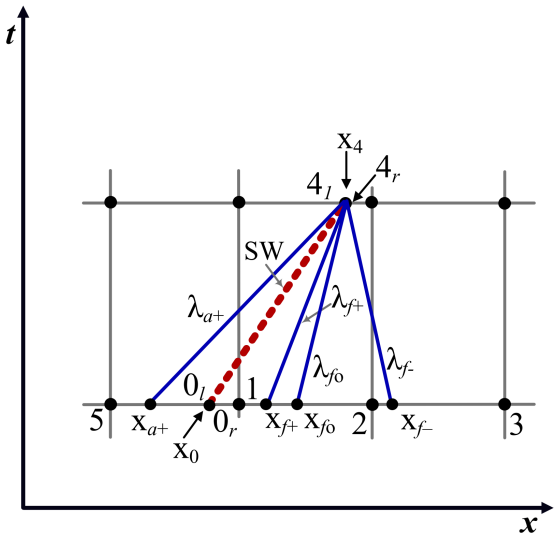

Figure 7.2: Shock wave (SW) module.

colors. The properties on the left and right sides of the contact surface are denoted by subscripts l and r, respectively. In contrast to the interior point solver, the location of a contact surface at the end of the current time-step is not known in advance and must be solved as a part of the integration procedure as detailed in Chapters 5 and 6. The overall integration procedure is again similar to the interior point solver with gasdynamic and thermochemical integration steps carried out separately until convergence of various dependent variables. Since either side of the contact surface represents a different fluid parcel, the integration to account for their thermochemical relaxation is carried out separately for each side. Also, as the relaxation of a contact surface is solved at every time-step, the initial values for thermochemical state evolution are always known, and therefore interpolation for the initial gas state is circumvented.

The final subroutine discussed here represents another discontinuity, a shock wave. Similar to the contact surface, the algorithm for resolving a shock wave evaluates the regions ahead and aft of the shock wave separately as all the gasdynamic

properties are discontinuous across a shock wave. A general representation of the algorithm for a right running shock wave is shown in Fig. 7.2. The properties ahead and aft of the shock wave are subscripted as f and a respectively. It is seen that the shock wave overtakes all characteristics ahead of it, and is overtaken by the characteristic that travels in the direction of the shock wave. The overtaking characteristic brings in information about the flowfield aft of the shock wave, which in this case is the thermochemical relaxation of the shock processed gas. As the shock wave is a discontinuity, it is assumed that the thermochemical state of the gas has not had the time to adjust to the change brought about by the impulsive compression. Though the static pressure, density, velocity and translational–rotational temperature are discontinuous across the shock wave, the vibrational energy of various species and the chemical composition of the gas processed by the shock wave remain at their respective initial values.

Note that the description of a shock wave as a discontinuity is from the continuum perspective. The true structure of a shock wave is a few mean free paths thick [5], which based on the discussions previously in §7.1.1) represents the order of collisions required for the translational–rotational temperature to reach equilibrium. Thus, it is appropriate to consider the translational–rotational temperature to be in equilibrium immediately behind the shock wave from a continuum perspective. Since the thermochemical state of the shock wave is fixed at its initial value, by definition, the shock wave is calorically perfect. Thus, the appropriate jump conditions that describe the gasdynamic process are given by the Rankine–Hugoniot equations [69, 49, 47]. The solution algorithm for the shock wave module essentially probes for a shock wave velocity where the post shock conditions due to Rankine-Hugoniot equations match the gasdynamic conditions obtained by solving the compatibility equation on the overtaking λ_+ characteristic. The iterative variation of the shock

wave velocity is terminated once the static pressure and velocity behind the shock wave and those calculated on the λ_+ characteristic converge to a specified tolerance.

7.3 Validation

The algorithms described in the previous section were validated against existing experimental and numerical results. As a salient part of all the algorithms is obtained through modification of the interior point module, initial validation efforts were directed towards verifying the interior point solver. Additionally, since the algorithm for chemical nonequilibrium was already validated in Chapter 4, the ability of the new algorithm to account for thermal nonequilibrium was investigated initially. For ease of modeling, steady, quasi-one-dimensional nozzle flows were considered first.

The first section of the validation studies reports two cases of steady, hypervelocity nozzle flows representing a self relaxing nitrogen flow and that of dissociating air flowing through a hypervelocity nozzle. With satisfactory results obtained for both these cases, final validation studies for unsteady one-dimensional flows were conducted. The unsteady case considered here is that of LENS-X simulated previously in Chapters 5 and 6, which requires the use of all the subroutines described above. Two operating conditions of the facility representing thermochemical equilibrium and nonequilibrium flows were solved and the validation results are presented. All the comparison data plotted were extracted using Webplot digitizer software [113] from the plots in the sources quoted appropriately.

7.3.1 Hypervelocity nozzle flows

The first set of validation cases, as mentioned previously, involve thermochemically relaxing nozzle flows. Such flows lend themselves to easy modeling, as the flow through the entire domain can be modeled solely using the interior point algorithm.

This simplification is applicable to a hypervelocity nozzle operating in its design condition, where the flow properties through the entire nozzle vary smoothly, that is, no discontinuities are present. Further, the exit velocity in these scenarios is supersonic; thus, the surrounding ambient conditions at the nozzle exit do not affect the flow inside. The solver algorithm used for both these cases employs predefined grid points in the x–t space with the time-step limited by the Courant–Friedrichs–Levy condition, for a given spatial grid size. The steady-state solution is obtained as the asymptotic limiting solution of a time-marching scheme. In this scheme, the initial guess for the variation of flow properties throughout the nozzle is taken to be the thermochemical equilibrium solution, which is readily calculated as the nozzle geometry and reservoir conditions are known. Then, the axial variation of flow properties at the next time-step can be obtained by using the interior point module across all the grid points at that time-step. This procedure is repeated for successive time-steps until the axial distribution of vibrational temperatures of all the molecular species vary by less than 0.01 percent between two steps. A grid independence study with three different spatial discretization, namely, 250, 350 and 600 nodes was conducted for the thermal nonequilibrium simulation. A comparison of the vibrational temperature distribution showed that the maximum difference in the temperature profiles between 350 and 600 grid size cases was less than 0.01 percent. Thus, the results provided below were obtained using 350 spatial nodes.

7.3.1.1 Self-Relaxing Nitrogen

This section details the preliminary validation case, which approximates a self-relaxing nitrogen flow. Under such an approximation, the only relaxation effect to occur is thermal. Additionally, for a self-relaxing diatomic harmonic oscillator, the only thermal relaxation process will be VT exchange with same species. Appropri-

ately, the thermal relaxation model used here simplifies to the classic Landau–Teller model representing VT relaxation. The reference benchmark article considered here is by Sharma et al. [125], where an expanding nitrogen flow in a hypervelocity nozzle was studied numerically and experimentally. The experimental studies were carried out in the Electric Arc Shock Tube (EAST) facility at NASA Ames Research Center. To simulate a hypervelocity nozzle flow, a two-dimensional nozzle plug insert with optical access windows was installed near the end of the driven section. The hyperbolic nozzle with a smaller inlet area compared to the driven section inner diameter resembled a reflected shock tunnel operation. Vibrational temperatures shown in Fig. 7.3 were obtained through spontaneous Raman scattering (SRS) measurements at seven locations along the nozzle. Note that the Raman measurements at different locations were obtained over a series of runs and the variation in reservoir conditions were taken into account in the measurements reported. For further information about the methodology and the setup, the interested reader is referred to [125], as only the key information about the experiment is discussed here. The driven section of the shock tube was filled with prepurified grade nitrogen at 150 Torr. Once the shock tube was fired and the driven diaphragm ruptured, a shock wave of 2 600 m/s velocity was sent into the driven section, which reflected on the face of the nozzle insert to produce a stagnant reservoir condition of approximately 100 atm and 5 600 K. This condition is used as the steady-state reservoir condition in the nozzle flow modeled here and the stagnant gas is assumed to be in thermochemical equilibrium. Thermochemical equilibrium calculations at the conditions mentioned above show that the reservoir gas consists of 99.46 % molecular nitrogen by mass, with the remainder being atomic nitrogen. The reason for describing this validation study as an approximation to a self-relaxing nitrogen flow may be apparent from the calculated reservoir gas composition.

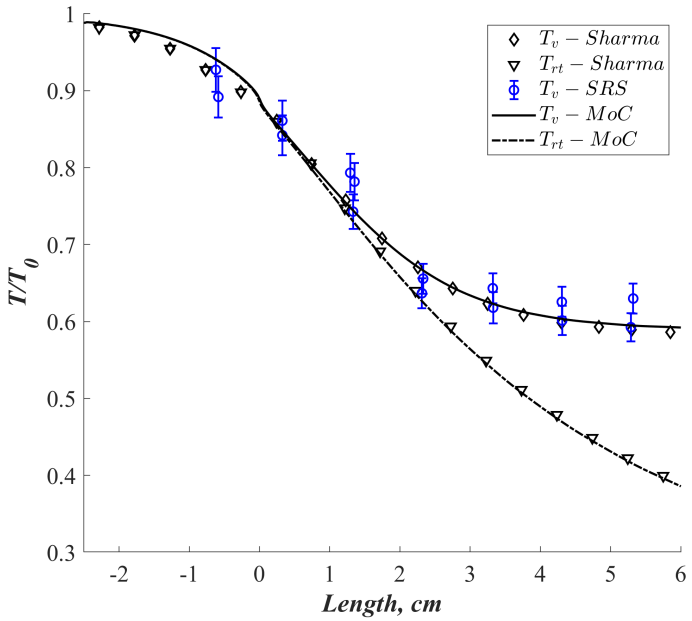

Figure 7.3: Thermal relaxation of nitrogen: comparison of equivalent MoC results with computations and experiments.

Sharma et al. [125] also performed numerical analysis to supplement the experiments. Two models were considered, with the first one being a Navier–Stokes model considering finite-rate chemistry with vibrational relaxation in accordance with the Landau–Teller model. An equivalent inviscid nozzle geometry was obtained from the Navier–Stokes solution which was then used in a quasi-one-dimensional analysis utilizing a state-to-state vibrational relaxation model. The current work utilizes this equivalent inviscid nozzle profile and the results obtained through the MoC model are compared to the Navier–Stokes results as well as the experiments reported by Sharma et al., see Fig. 7.3. It is seen that the MoC model closely agrees with the experimental and numerical results. Thus, for a self-relaxing diatomic gas flow, MoC captures the essential vibrational energy freezing occurring in the nozzle as the gas expands to low densities. The phenomenon of vibrational freezing in turn can be attributed to the dwindling energy exchange process due to the gasdynamic expansion. From a molec-

ular view, the continuously reducing density results in fewer particle collisions as the gas expands, which directly reduces the energy transfer from the vibrational mode to the translational mode. Once the gas density has fell significantly, this energy exchange ceases, as there are insufficient number of efficient collisions between the molecules. This causes the vibrational energy of the expanding gas to freeze during the expansion, seen in the form of a nearly constant vibrational temperature towards the exit of the nozzle in Fig. 7.3.

7.3.1.2 Dissociating air

With the successful validation of self-relaxing nitrogen flow, a test case for coupled thermochemical relaxation was studied next. Practical flows of this nature are prevalent in hypervelocity nozzle operation where typical modeling interest leans towards nonequilibrium effects occurring in air as it expands through the nozzle. In this regard, existing literature for computational models of hypervelocity nozzles was reviewed and reflected shock tunnel nozzle computations from Gu et al. [109] were used for validation of the dissociating air MoC model. This was also the geometry and reservoir conditions used in Chapter 4. Gu et al. [109] modeled the steady-state quasi-one-dimensional flow through a hypothetical reflected shock tunnel nozzle to study the nonequilibrium aspects associated with the converging section of hypervelocity facility nozzles. A state-to-state approach was used to model the evolution of vibrational energies of various species based on forced harmonic oscillators and QCT assumption. Similar to the approach in this work, Gu et al. also considered air to be a gaseous mixture with five possible species and an initial composition of 78 percent nitrogen and 22 percent oxygen by volume. For the purpose of validation studies, two cases simulated by Gu et al., with 1 MPa stagnation pressure and 4 000 K/7 000 K stagnation temperatures were replicated here. A comparison of the pertinent mass

fractions and T_{rt} due to MoC and state-to-state results from Gu et al. [109] is shown below in Fig. 7.4,

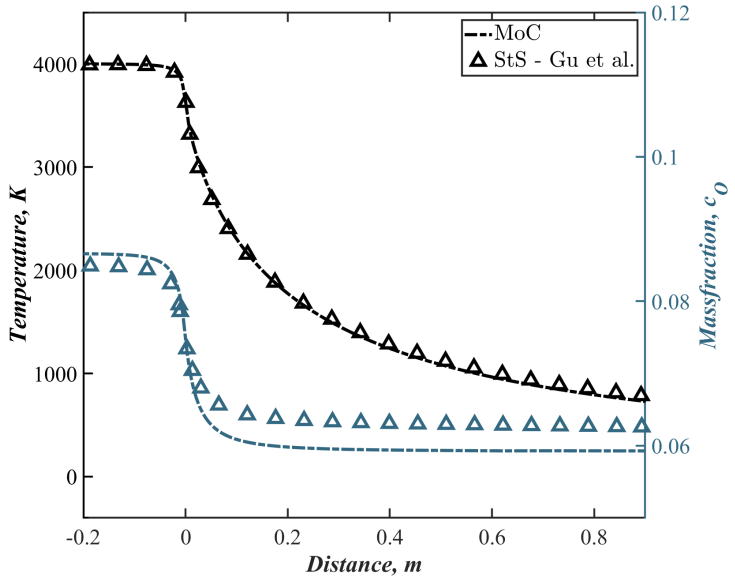

(a) Mass fractions.

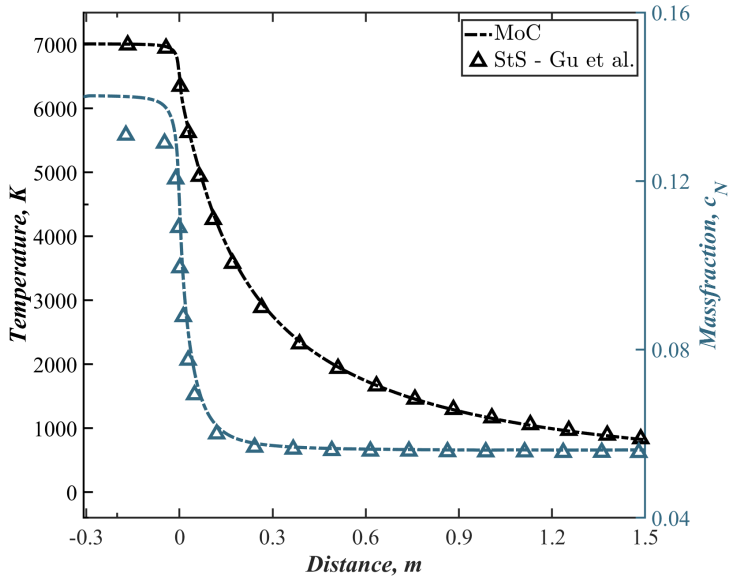

(b) Temperatures.

Figure 7.4: Dissociating air flow: comparison of MoC results (lines) with Gu et al. [109].

It is seen that the static temperatures T_{rt} from the MoC results throughout the nozzle agree well with that of the state-to-state model for both the 4 000 K and 7 000 K cases. However, the mass fraction distributions of atomic oxygen and nitrogen in the nozzle due to MoC seems to differ noticeably from that of the state-to-state model. This can be attributed primarily to the thermochemical equilibrium calculations used in the MoC model for the reservoir, as opposed to the state-to-state calculations by Gu et al. Considering the differences in the considered chemical kinetics and the vibrational relaxation models, a difference in mass fractions of $\sim$ 0.01 seems acceptable for validation of the MoC algorithm developed here.

Now, the above results from thermochemical nonequilibrium MoC are compared with that from the chemically reacting nozzle ODE solver developed in Appendix C. The results for various state properties are interest are shown in Fig. 7.5 for the 4 000 K case and in Fig. 7.6 for the 7 000 K case. It is seen that the static temperature distribution due to the chemical nonequilibrium model lies slightly above the thermochemical nonequilibrium results. This is due to the thermal equilibrium assumption in the former, which results in the release of additional energy from the vibrational modes, as the gas expands.

The thermochemical nonequilibrium plots in Figs. 7.6a, 7.6b, Figs. 7.5a and 7.5b warrant further scrutiny. In both the cases, it is seen that the chemical composition freezes earlier than vibrational energy during the expansion. This may be expected, as the time scales associated with chemical reactions are larger than that required for vibrational relaxation. Thus, as the gas expands and accelerates the finite-rate process with larger time scale freezes first. Additionally, both chemical recombination and vibrational relaxation are dependent on molecular collisions, which are in turn dependent upon the gas density.

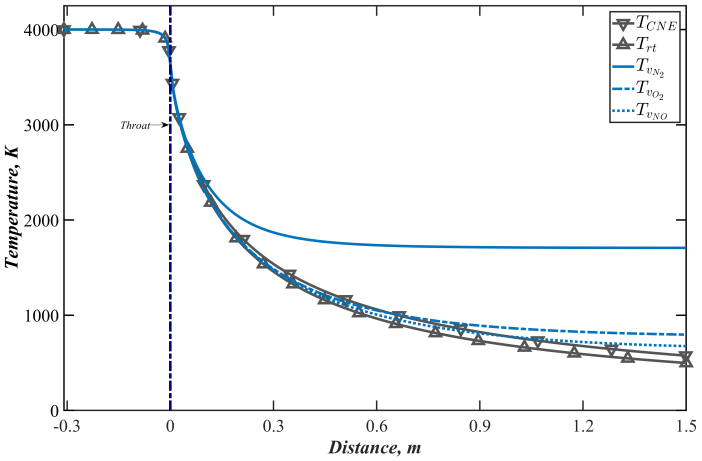

(a) Temperatures.

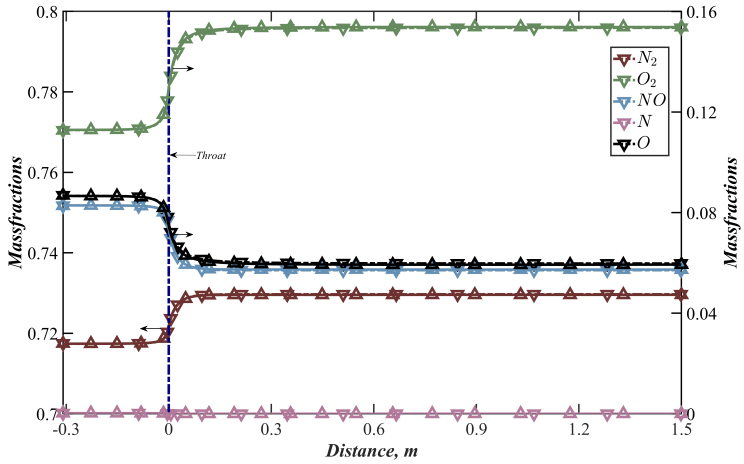

(b) Mass fractions.

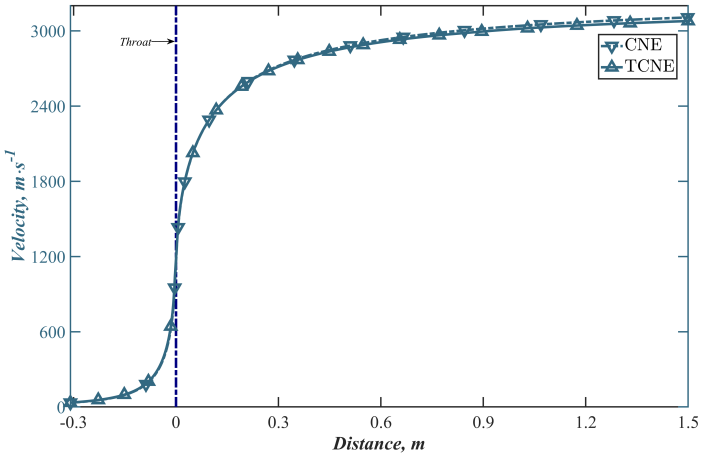

(c) Velocities.

Figure 7.5: Comparison of chemical and thermochemical nonequilibrium (TCNE) results for $T_0 = 4\,000$K (upfacing triangles are TCNE).

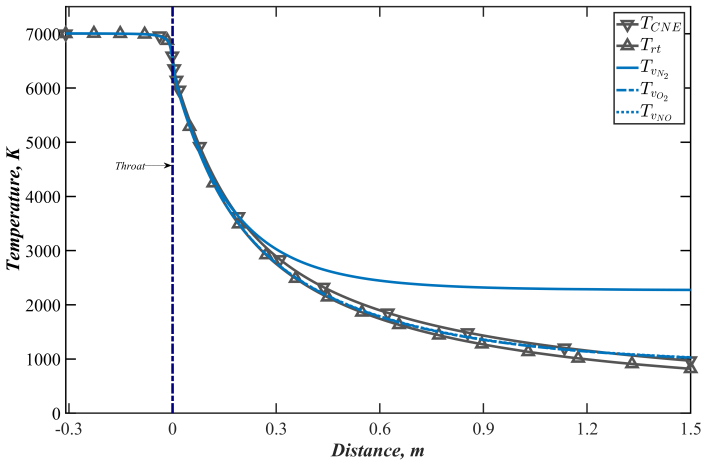

(a) Temperatures.

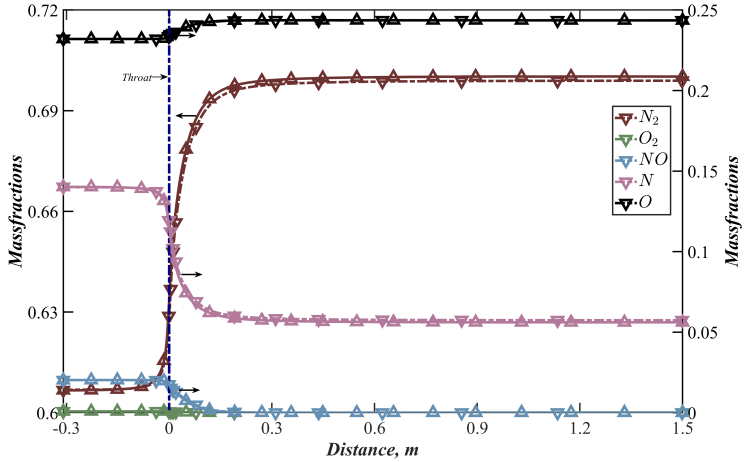

(b) Massfractions.

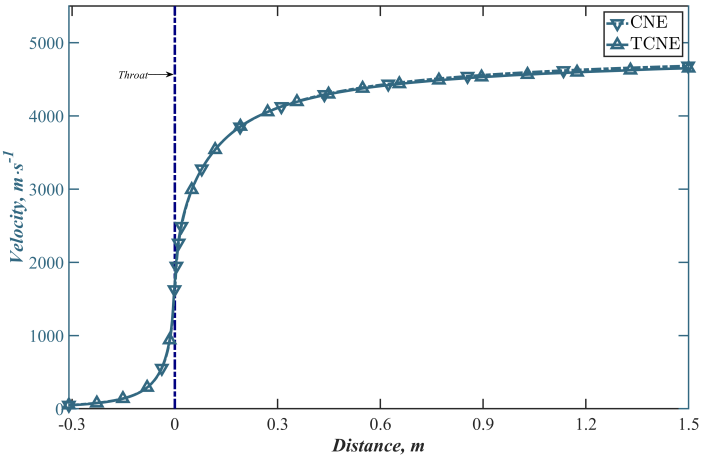

(c) Velocities.

Figure 7.6: Comparison of chemical and thermochemical nonequilibrium (TCNE) results for $T_0 = 7\,000$K (upfacing triangles are TCNE).

Vibrational relaxation is a two-body mechanism while chemical recombination is a three-body mechanism. Thus the reduction in gas density due to its expansion affects chemical recombination significantly more than vibrational relaxation and induces chemical freezing earlier in the nozzle compared to vibrational freezing. A remarkable practical implication due this effect is that the test gas chemical composition calculated by chemical and thermochemical nonequilibrium models should provide very similar results, as is seen in Fig. 7.5b and 7.6b. Subsequently, it is also seen that the exit velocities calculated by these two models closely match. Therefore, a chemical nonequilibrium model offers a significantly easier way to accurately calculate test gas velocity and composition at the exit of a hypervelocity nozzle.

7.3.2 Expansion tube

The final validation study explores the effectiveness of all the subroutines developed in this chapter (shock wave, contact surface and interior point modules) in evaluating the unsteady flowfield of an expansion tube. The overall flowfield for an expansion tube operation is shown schematically in Fig. 7.7 in the form of expected ideal wave processes. These wave processes were used to develop the nonequilibrium expansion tube model, similar to the approach in Chapters 5 and 6. The starting solution for this algorithm was based on the analytical solution from the classical Riemann equation. Based on this initial solution, the spatial grid and CFL condition, the time-step for the x–t grid was calculated. Thereafter, for every subsequent time-step different MoC modules were called to solve for the flowfield evolution in entire axial length of the facility, as was done in Chapters 5 and 6.

To increase the efficiency of the expansion tube model, different gas slugs in the expansion tube were modeled using different MoC algorithms as shown in Fig. 7.7. The high-pressure driver gas expands to lower temperatures and pressures. Therefore,

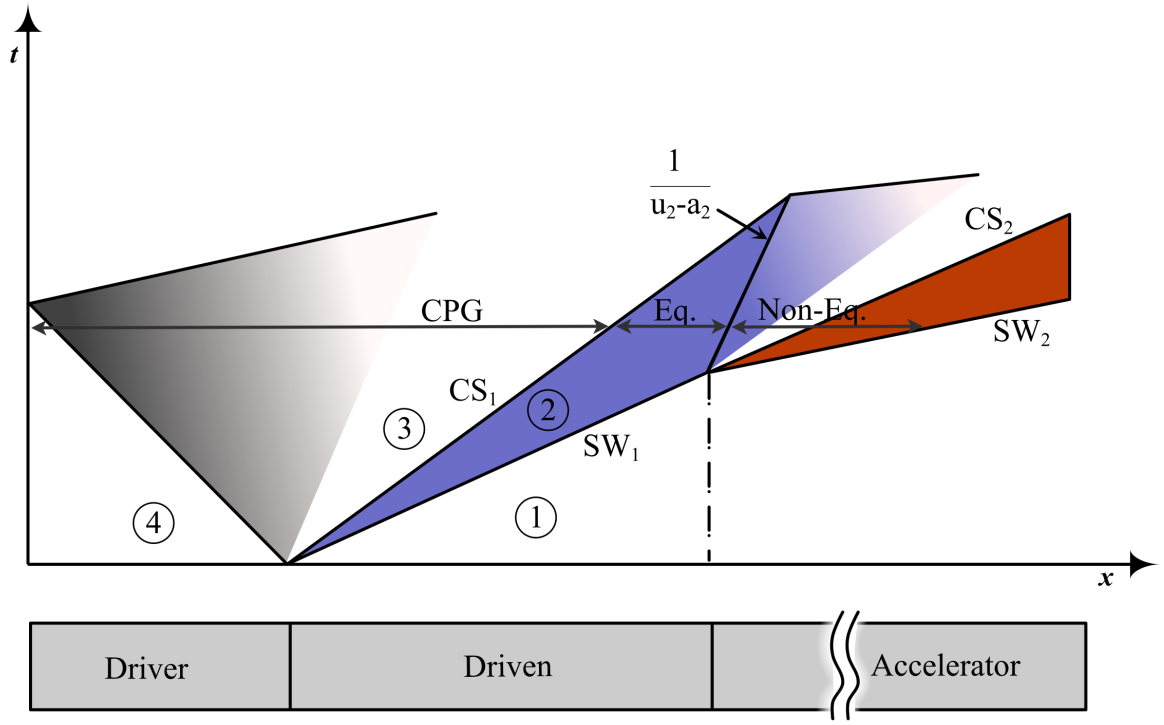

Figure 7.7: Expansion tube model.

this expansion can be represented by a calorically perfect interior point module. In this case, the thermally perfect model reported in Chapter 5 was used to model the driver gas, for computational efficiency and ease of implementation. However, to simulate the calorically perfect expansion of helium, the specific heat (and thereby γ) was held constant in the curvefits supplied to the thermally perfect interior point solver. The compressed test gas, that is, the region between the primary contact surface CS_1 and the primary shock wave SW_1 is more appropriately modeled using a thermochemical equilibrium solution. Since the governing equations neglect frictional and heat losses, it can be expected that the test gas in region ② will be the same as the analytical solution calculated earlier. Thus, for simplicity the growth of region ② was merely obtained by convecting the Riemann solution over subsequent time steps. Once the primary shock wave SW_1 reaches and ruptures the secondary diaphragm,

the calorically perfect p–u solution developed previously in Chapter 3 was used to calculate the shock transmission into the acceleration section.

With the rupture of the secondary diaphragm, the nonequilibrium calculations begin. Since the nonequilibrium expansion of the test gas begins with the leading characteristic of the secondary rarefaction wave (see Fig. 7.7), the nonequilibrium interior point module was initiated from this location at every subsequent time-step. The regions behind this leading characteristic were treated in the same way prior to secondary diaphragm rupture. Ahead of this leading characteristic, the nonequilibrium interior point module was used to resolve the regions between the secondary contact surface CS_2 and the secondary shock wave SW_2, and the region between the leading characteristic and the secondary contact surface CS_2. The advancement of shock wave and contact surface modules were treated appropriately by their MoC modules. Similar to the thermally perfect and thermochemical equilibrium models discussed in Chapters 5 and 6, the grid points surrounding these discontinuities were obtained through piecewise cubic interpolation.

The benchmark cases for the expansion tube model were based on two operational conditions reported by the LENS-X facility [50, 51]. In the current case, the MoC results are compared to CFD results due to Nompelis et al. [51]. Fill conditions for both these runs are provided in Table 7.1 below. In both these simulations, similar to Nompelis et al. [51], air was assumed to be composed of 74.03 percent nitrogen and 25.97 percent oxygen by mass.

Case A in Table 7.1 corresponds to a lower enthalpy simulation of 5 MJ/kg, which was previously simulated in Chapters 5 and 6. MoC results associated with the driven-accelerator wave system of this simulation are shown in Fig. 7.9. In the subsequent discussions in this chapter, only the results for the driven-accelerator wave systems are shown, as the nonequilibrium phenomena occur only here.

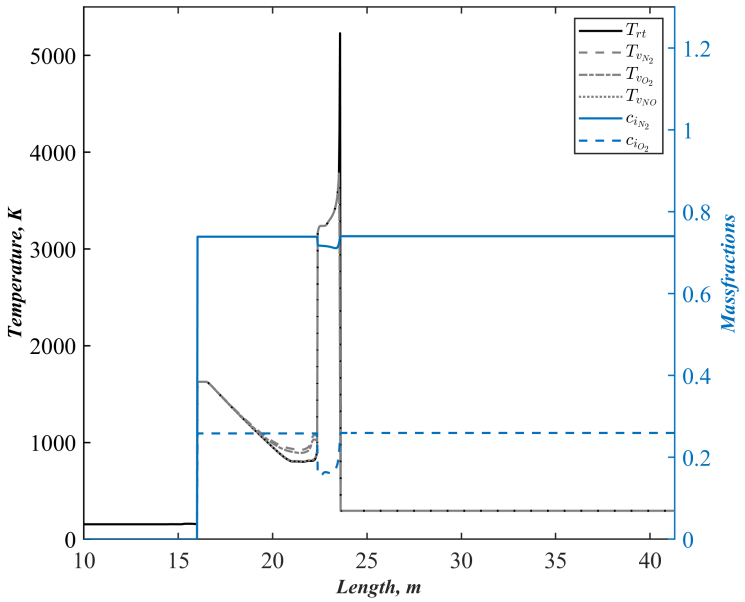

(a) Initial nonequilibrium phase.

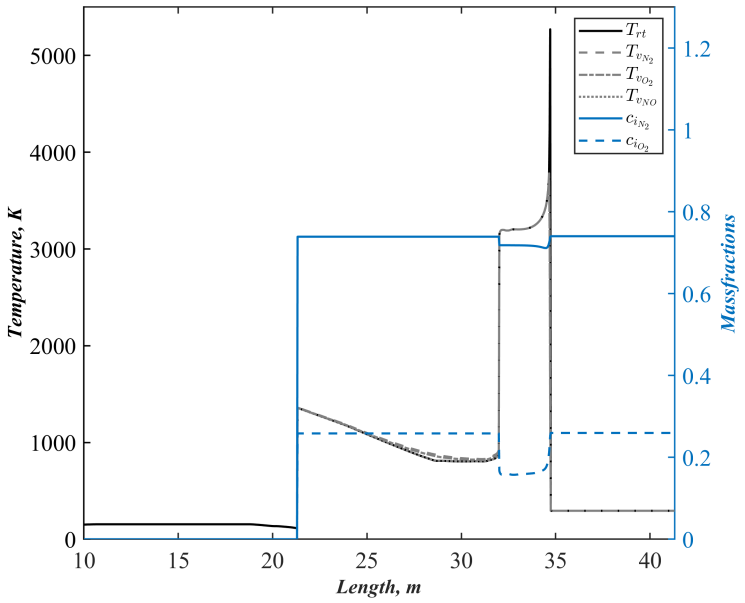

(b) Near equilibrium phase.

Figure 7.8: Evolution of thermochemical and gasdynamic properties for Case A. feqlens1)

Table 7.1: Expansion tube fill conditions reported for LENS-X [51].

Section	Gas	Case A		Case B	
		T, °R	p, psi	T, °R	p, psi
Driver	He	770.0	1 200	630.0	2 000
Driven	Air	529.3	3.000	630.0	1.4700
Acceleration	Air	529.3	0.048	630.0	0.0059

The evolution of internal energy in the test gas as it expands and travels the acceleration section is evident from Figs. 7.8a and 7.8b. Figure 7.8a, which represents an earlier time in the driven-accelerator wave system shows that the gaseous mixture's translational–rotational temperature is about 110 K lower than the vibrational temperatures of nitrogen and oxygen. But, the vibrational temperature of nitric oxide is almost coincident with the gas translational–rotational temperature. Figure 7.8b representing a later time in the expansion tube operation shows in contrast that the test gas immediately trailing the secondary contact surface is almost in thermal equilibrium. Thus, in this case, gasdynamic expansion accommodates sufficient molecular collisions in the test gas to drive the vibrational energy distributions to thermal equilibrium. From the species composition shown in this plot, it is also obvious that the composition of air remains intact in the test gas slug, while the accelerant slug undergoes significant dissociation. Further, the temperatures observed in the accelerant gas slug show rapid relaxation. Thus, it may be computationally efficient to simulate this region through an equilibrium MoC model. The final temperatures obtained through MoC shown for Case A are within two percent of those reported in Nompelis et al. [51].

Figure 7.9 shows all the species considered in the MoC model corresponding to the time shown in Fig. 7.8b. The mass fractions show significant amounts of atomic

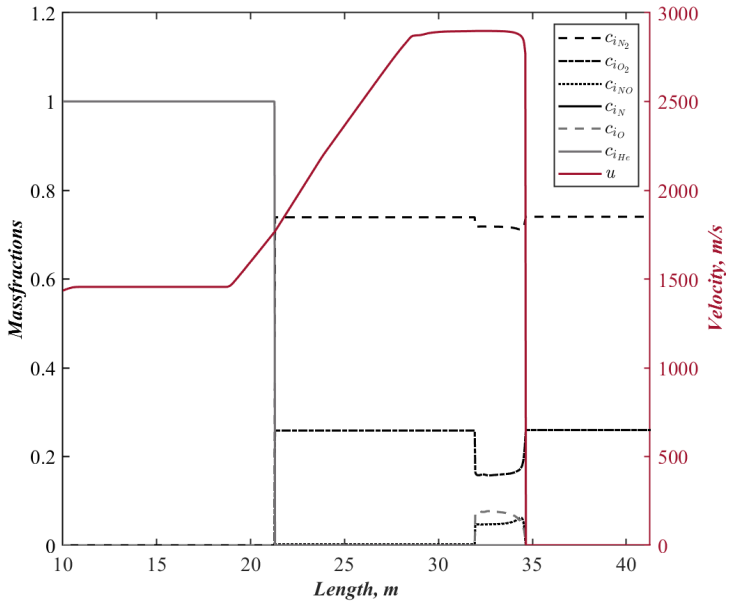

Figure 7.9: Test gas composition and velocity near equilibrium for Case A.

oxygen and nitric oxide in the accelerant gas, as may be expected. Combining the velocity and mass fractions plot, the locations of various discontinuities are inferred, namely, secondary shock wave at ≈ 35 m, secondary contact surface at ≈ 32 m and primary contact surface at ≈ 21 m. The driver gas, which is helium, can be seen immediately behind the secondary contact surface in Fig. 7.9. Nompelis et al. [51] report a test gas velocity of $\approx 2\,918$ m/s, whereas MoC results show a test gas velocity of $\approx 2\,887$ m/s which is about one percent lower.

The results from the MoC simulation of Case B in Table 7.1 are shown in Figs. 7.10 and 7.11 in a format similar to that of Case A. This simulation corresponds to a high enthalpy test gas at 10 MJ/kg and thus the test gas velocities can be expected to be significantly higher than Case A. Given that the primary shock wave velocity is limited in an expansion tube, higher enthalpy simulations are only possible by adding more energy to the test gas through the secondary rarefaction wave. This in turn

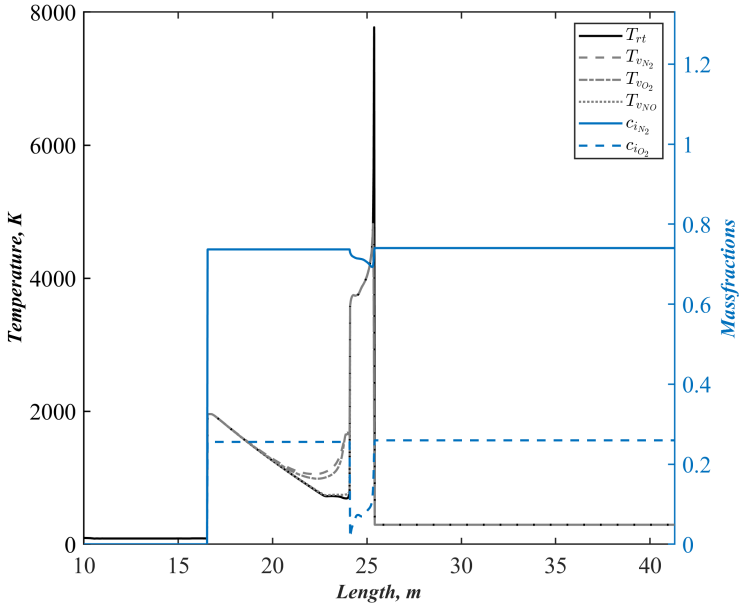

(a) Initial nonequilibrium phase.

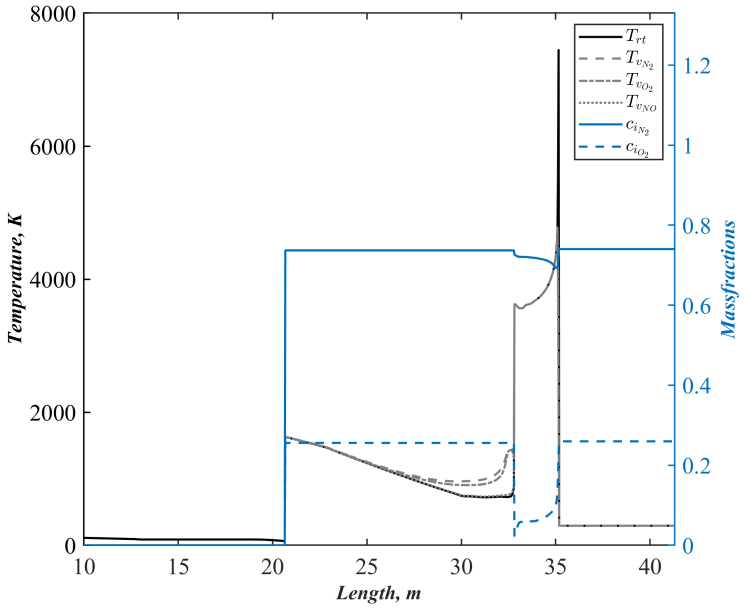

(b) Final frozen phase.

Figure 7.10: Evolution of thermochemical and gasdynamic properties for Case B.

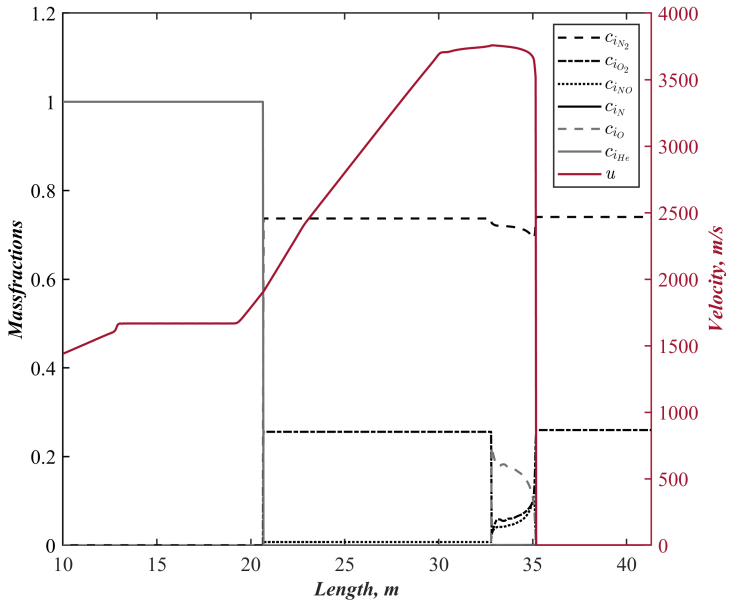

Figure 7.11: Eventual test gas composition and velocity for Case B.

causes vibrational energy freezing in the test gas, as the gasdynamic time scales become increasingly shorter. This is seen in Fig. 7.10, where the evolution of vibrational and translational–rotational temperatures are shown. In this case, Fig. 7.10a which depicts the driven-acceleration wave system at an earlier time shows that the temperature difference between the vibrational and translational–rotational temperatures is about 300 K. As the test gas slug travels further into the acceleration section, the vibrational energies freeze due to high test gas velocities and lower densities, with the temperature difference still being about 150 K, as seen in Fig. 7.10b. Nompelis et al. also report a similar thermal nonequilibrium for this case, with the translational–rotational temperature of the test gas being $\approx$ 770 K at the acceleration section exit. Corresponding MoC arrived temperature of the test gas at the same location during secondary contact surface exit is $\approx$ 740 K.

Figure 7.11 shows the species composition and fluid velocity corresponding to Fig. 7.10b. Due to stronger shock velocity, significant atomic oxygen is present in the accelerant gas. However, the test gas still remains predominantly intact in terms of the gaseous composition. The test gas velocity reported by Nompelis et al. [51] for this case was $\approx 3\,777$ m/s, while current MoC shows $\approx 3\,750$ m/s.

CHAPTER 8

CONCLUSIONS AND FUTURE WORK

Overall this work has extended the classical inverse MoC algorithms to flows in thermochemical nonequilibrium. The conclusions from various phases of this work are below,

8.1 Phase 1

The unsteady flowfield evolution in a downstream-mode detonation tube was resolved using an algorithm based on MoC subroutines. These subroutines directly resolved the evolution of continuous and discontinuous waves. The interaction between discontinuities, namely, detonation/shock waves and contact surfaces was locally treated by classical wave polar analysis. Validation experiments for the MoC model were carried out in a downstream-mode detonation tube facility with $L/D \approx 100$. The experiments used nitrogen and helium as the driven gas to tailor the shock wave–contact surface interaction in the driven section. It was shown that the setup wall roughness to estimate friction factor in arbitrary gases could be determined using a simple experiment. Comparison of non-isentropic MoC results with experiments showed that the MoC model resonably replicates the detonation driver plateau pressure even in the under-driven mode. The trajectory of the decelerating incident shock wave in the driven section is captured well for different driven gases. Similarly, the driven endwall pressure history immediately after incident shock wave reflection matches well between the MoC model and experiments. The MoC model also reliably determines the transmitted and reflected waves due to shock wave–contact surface in-

teraction in the driven section. Experimental results indicate that downstream-mode detonation tubes with strong Taylor rarefaction may experience non-ideal effects in the detonation driver, resulting in deviations from the MoC model results at prolonged times.

The effect of recessed transducers in time-of-flight measurements could be reliably accommodated using geometric shock dynamics. The shock wave in the main flow path can be assumed to be transmitted into the recess cavity and the transmitted shock wave can be approximated using geometric shock dynamics. Simple kinematic calculations using such a method show that for moderately decaying inert shock waves, the effect of transducer recess is negligible if they are of the same height. For time-of-flight measurements across two transducers with different recess cavity heights, the geometric shock dynamics based calculations show good agreements with theoretical estimates. The agreement is poor for detonation waves, which is expected due to the chemical reactions trailing the detonation wave.

8.2 Phase 2

An inverse marching, MoC-based numerical method was developed for modeling inviscid quasi-one-dimensional flows under chemical nonequilibrium. Additionally, a stand-alone chemistry solver was developed to be incorporated into the MoC subroutines. Two MoC algorithms were developed to resolve exit outflow and weak compression/rarefaction waves in a quasi-one-dimensional continuum flowfield. Further, validation of the subroutines was carried out by modeling three different steady-state cases, namely, one-dimensional supersonic combustion, flow behind a normal shock wave and a hypervelocity nozzle flow. Additionally, an ODE solver was developed to validate the hypervelocity nozzle flow results obtained from the MoC analyses. These cases employed two different working gas mixtures with their chemical kinetics

represented by two different reduced mechanisms. Comparison of MoC results with the ODE results from the Shock and Detonation Toolbox and with nozzle ODE solver showed that the developed MoC model is capable of predicting inviscid, quasi-one-dimensional steady nonequilibrium flows with good accuracy.

8.3 Phase 3

Calorically perfect MoC algorithms were extended to accommodate thermally perfect gases and the interior point solver was vectorized. Using these MoC algorithms a computationally efficient expansion tube model was developed. Results from this model have been successfully validated against analytical solutions. Additionally, equilibrium MoC algorithms were developed for quasi-one dimensional unsteady gas-dynamics, considering the effect of momentum and heat losses. Calculations pertaining to thermochemistry evolution were incorporated into the solver using equilibrium chemistry curvefits. Individual MoC subroutines were developed for predominant unsteady waves such as weak compression/rarefaction waves, shock waves and contact surfaces. Utilizing these subroutines, two different reduced-order models were developed to resolve equilibrium flowfields in an expansion and a detonation tube. The expansion tube algorithm was validated against equilibrium Riemann solution. Detonation tube results primarily focused on unsteady wave dynamics in the damping section. To account for the effect of losses, experimental results were used to calibrate the MoC model and thereby reliably estimate the peak loads observed in the detonation tube damping section.

8.4 Phase 4

MoC algorithms capable of resolving a thermochemically relaxing flowfield were developed. These algorithms individually resolve some of the predominant unsteady flow phenomena namely shock waves, contact surfaces and compression and rarefaction waves. Thermal relaxation phenomena considered in these algorithms account for both VT and VV transfer occurring in diatomic molecules. The coupling between chemical and vibrational nonequilibrium was modeled using a Park's two-temperature model. To ensure that the newly developed algorithms provide acceptable results, validation studies were carried out for different nonequilibrium flow scenarios. Simplest of the validation cases studied the ability of the MoC algorithms to resolve steady-state quasi-one-dimensional nozzle flows. Results showed that the developed algorithm was capable of replicating the existing results for thermal relaxation of nitrogen and thermochemical relaxation of air through hypervelocity nozzles. Finally, as a practical application of the algorithms developed, a high enthalpy expansion tube flowfield was resolved and the results again showed that the MoC algorithms reliably reproduce a set of validated computational fluid dynamics simulations of the impulse facility.

8.5 Future Work

The IMoC algorithms developed in this work can be further improved with the following suggestions,

- The IMoC approach discussed in this work predominantly uses a structured grid. It was seen in Chapter 4 that the use of adaptive grid in the steady state nozzle simulation increased the accuracy and computational efficiency of the overall algorithm. Thus, the use of adaptive grids in the unsteady IMoC approach may similarly improve the computational efficiency and accuracy of the algorithm. This may be very beneficial in flows under severe thermochemical nonequilibrium, where regions of rapid relaxation may employ a finer mesh compared to quasi-steady regions.
- The chemistry subroutine developed in this work can also be modified to account for thermochemical equilibrium calculations. Thus, the use of curvefits in thermochemical equilibrium MoC model can be circumvented. It may be known that obtaining accurate curvefits for equilibrium properties of a gaseous mixture accommodating a large range of pressures and temperatures is laborious. Thus, equilibrium chemistry calculations will render the MoC subroutines more robust and versatile.
- The thermochemical nonequilibrium algorithms developed here are limited to quasi-one-dimensional unsteady flows. The same approach can be easily modified to resolve steady two-dimensional flows, enabling better resolution of nozzle flows, for instance.
- The chemical nonequilibrium algorithm developed here can be used to fully model a detoantion-driven shock tube, thereby directly resolving the detonation wave propagation.

- The thermochemical nonequilibrium algorithm developed here can be extended to account for polyatomic molecules, similar to the approach of Palmer and Hanson [58].

APPENDIX A

RATE DATA FOR FINITE RATE CHEMISTRY

This Appendix provides the finite-rate chemistry data used in Chapter 4. The nomenclature here follows the Arrhenius rate equation detailed in Section 4.1. The first mechanism provided in Table A.1 below represents a simplified kinetic model for combustion of hydrogen in air. The mechanism consists of six reacting species, H_2, O_2, H_2O, OH, H and O. The inert species is N_2. In total, the combustion of hydrogen is modeled to proceed in 7 steps, with reactions 6 through 8 and 9 through 11 each representing a single reaction with different collision partners. This is a simplified mechanism introduced by Shang et al. [106] based on the original mechanism of Drummond et al. [126]. The units for various parameters below are in kg, m^3, kmol, J and K.

Table A.1: Drummond mechanism

No.	**Reaction**	**Forward Rate Constant**			**Third Body** M
		A_f	B_f	$E_f/\mathcal{R} \times 10^3$	
1	$H_2 + O_2 \rightleftharpoons OH + OH$	1.700×10^{10}	0.0	24.233	
2	$H + O_2 \rightleftharpoons OH + O$	1.420×10^{11}	0.0	8.254	
3	$OH + H_2 \rightleftharpoons H + H_2O$	3.160×10^{4}	1.8	1.525	
4	$O + H_2 \rightleftharpoons H + OH$	2.070×10^{11}	0.0	6.920	
5	$OH + OH \rightleftharpoons H_2O + O$	5.500×10^{10}	0.0	3.523	
6	$OH + H + H_2 \rightleftharpoons H_2O + H_2$	8.840×10^{16}	-2.0	0.000	
7	$OH + H + M \rightleftharpoons H_2O + M$	3.315×10^{16}	-2.0	0.000	N_2, O_2
8	$OH + H + H_2O \rightleftharpoons H_2O + H_2O$	2.652×10^{17}	-2.0	0.000	
9	$H + H + H_2 \rightleftharpoons H_2 + H_2$	2.612×10^{12}	-1.0	0.000	
10	$H + H + M \rightleftharpoons H_2 + M$	1.306×10^{12}	-1.0	0.000	N_2, O_2
11	$H + H + H_2O \rightleftharpoons H_2 + H_2O$	6.530×10^{12}	-1.0	0.000	

The second mechanism shown in Table A.2 is a simplified chemistry model for high temperature air consisting of 5 reacting species N_2, O_2, NO, N and O. This is a reduced form of the Dunn–Kang mechanism [127] introduced by Shuen et al. [108] with eleven elementary reactions. In Table A.2, Reactions 4 and 5 represent the shuffle reactions involving NO, while the remaining reactions represent neutral dissociation–recombination reactions. The units for various parameters below are again in kg, m^3, kmol, J and K.

Table A.2: Reduced Dunn–Kang mechanism

No.	**Reaction**	**Forward Rate Constant**			**Backward Rate Constant**			**Third Body** M
		A_f	B_f	$E_f/\mathcal{R} \times 10^4$	A_b	B_b	$E_b/\mathcal{R} \times 10^3$	
1	$O_2 + M \rightleftharpoons 2O + M$	3.600×10^{15}	-1.0	5.95	3.00×10^{9}	-0.5	0.00	N, NO
2	$N_2 + M \rightleftharpoons 2N + M$	1.900×10^{14}	-0.5	11.30	1.10×10^{10}	-0.5	0.00	O, NO, O_2
3	$NO + M \rightleftharpoons N + O + M$	3.900×10^{17}	-1.5	7.55	1.00×10^{14}	-1.5	0.00	O_2, N_2
4	$O + NO \rightleftharpoons N + O_2$	3.200×10^{6}	1.00	1.97	1.30×10^{7}	1.0	3.58	
5	$O + N_2 \rightleftharpoons N + NO$	7.000×10^{10}	0.00	3.80	1.56×10^{10}	0.0	0.00	
6	$N + N_2 \rightleftharpoons 2N + N$	4.085×10^{19}	-1.5	11.30	2.27×10^{15}	-1.5	0.00	
7	$O_2 + O \rightleftharpoons 2O + O$	9.000×10^{16}	-1.0	5.95	7.50×10^{10}	-0.5	0.00	
8	$O_2 + O_2 \rightleftharpoons 2O + O_2$	3.240×10^{16}	-1.0	5.95	2.70×10^{10}	-0.5	0.00	
9	$O_2 + N_2 \rightleftharpoons 2O + N_2$	7.200×10^{15}	-1.0	5.95	6.00×10^{9}	-0.5	0.00	
10	$N_2 + N_2 \rightleftharpoons 2N + N_2$	4.700×10^{14}	-0.5	11.30	2.72×10^{10}	-0.5	0.00	
11	$NO + M \rightleftharpoons N + O + M$	7.800×10^{17}	-1.5	7.55	2.00×10^{14}	-1.5	0.00	O, N, NO

APPENDIX B

VALIDATION OF CHEMISTRY SOLVER

To improve the performance of MoC subroutines, a standalone chemistry subroutine (CS) was developed. Currently, Arrhenius-type reaction rates can be evaluated using CS. In this type of rate calculations, almost always, the forward reaction rate constants are known. The backward rate constants are either explicitly known or must be calculated using the appropriate reaction equilibrium constants as described in §4.1. Examples for both these cases can be seen in Appendix A, where the reaction mechanism for high temperature air, i.e., the reduced Dunn–Kang mechanism (Table A.2) has rate data for both forward and backward reactions, while the Drummond mechanism for hydrogen–air combustion (Table A.1) only provides the data for forward reactions. Both of these calculations can be carried out in CS as necessary. Additionally, from Chapter 4 and Appendix C, it can be seen that supplementary chemical source terms need to be calculated. These terms are also evaluated using CS. A flowchart of this calculation procedure is shown in Fig. B.1. Note that the procedure also assumes that the molecular weights of all the constituent species are known.

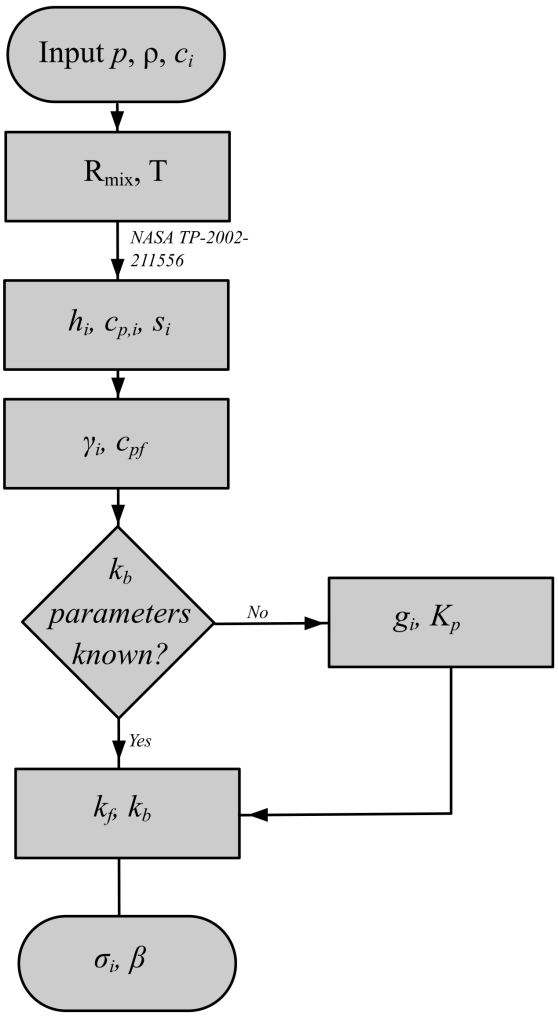

Figure B.1: Flowchart of Chemistry Subroutine (CS).

The rate constants as evaluated by the Chemistry Subroutine with known Arrhenius parameters are shown in this section. Validation of supplementary chemical source terms is shown in Appendix C. Figures B.2–B.5 only show the forward reaction rates for two-body reactions as evaluated by CS, with the results compared against those from Cantera [124].

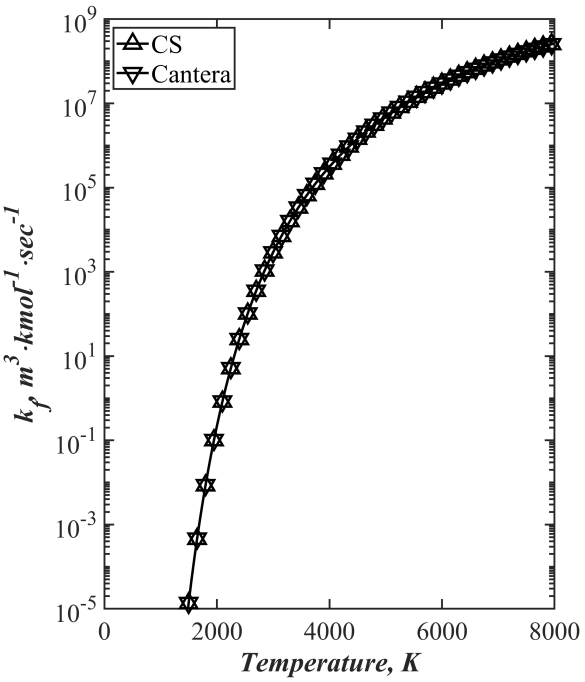

Figure B.2: k_f comparison between Cantera and CS, Reaction: $O_2 + M \rightleftharpoons 2O + M$.

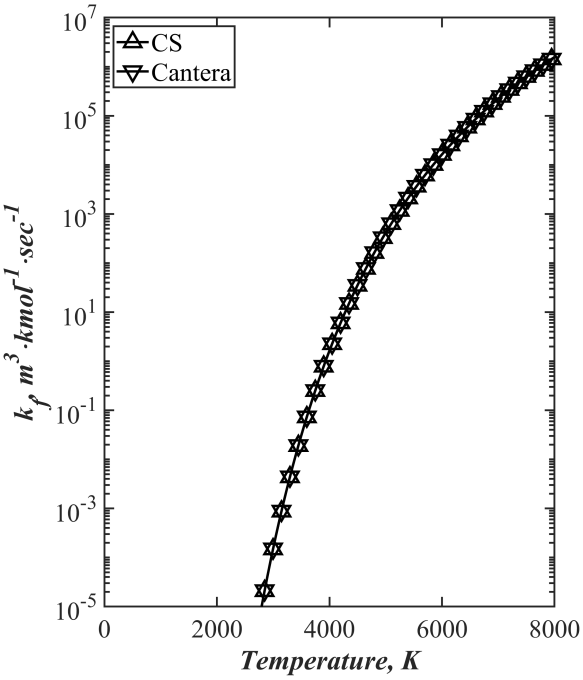

Figure B.3: k_f comparison between Cantera and CS, Reaction: $N_2 + M \rightleftharpoons 2N + M$.

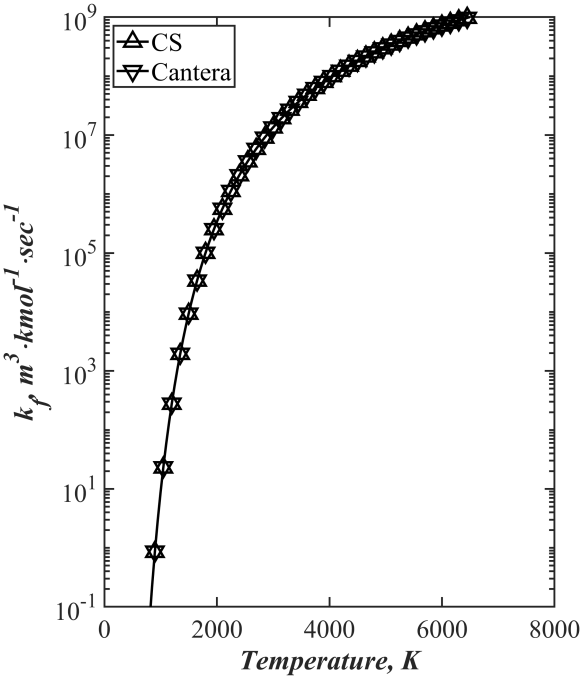

Figure B.4: k_f comparison between Cantera and CS, Reaction: $O + NO \rightleftharpoons N + O_2$.

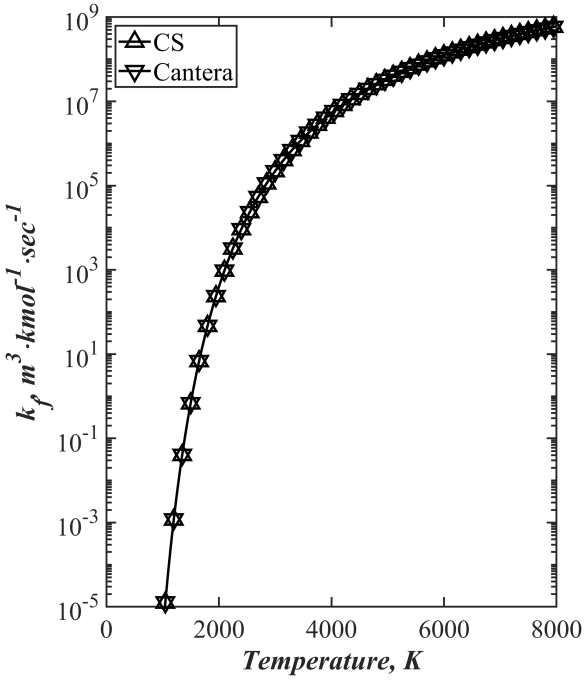

Figure B.5: k_f comparison between Cantera and CS, Reaction: $O + N_2 \rightleftharpoons N + NO$.

Figures B.6–B.9 validate CS calculations when backward rate constants are evaluated based on equilibrium constants and forward reaction rates. In this case, Gibbs free energy is evaluated based on the NASA Glenn polynomial curvefits as discussed in Chapter 4. For comparison of the evaluated results due to CS, both forward and backward rates are shown in the plots. Figsures B.6 and B.7 show reaction rates for two-body reactions, while Figs. B.8 and B.9 show three body reactions. In both these scenarios, CS provides results nearly identical to Cantera.

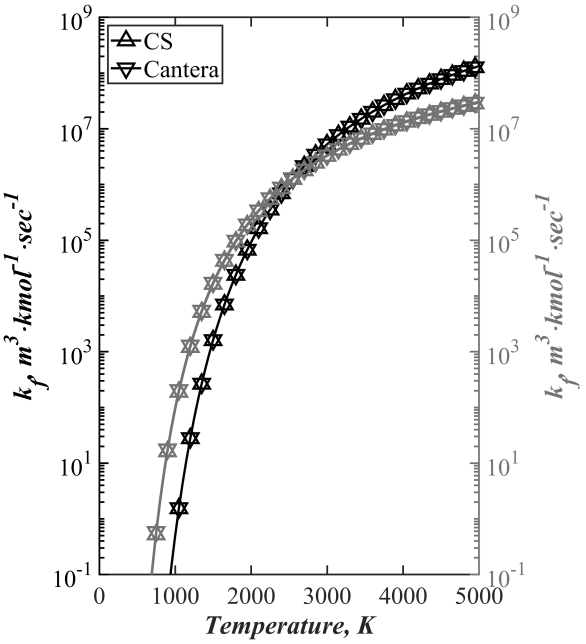

Figure B.6: k_f, k_b comparison between Cantera and CS, Reaction: $H_2 + O_2 \rightleftharpoons OH + OH$.

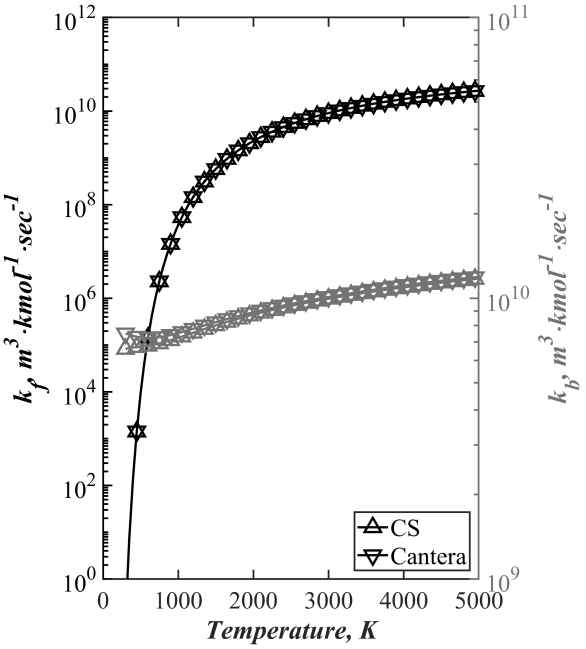

Figure B.7: k_f, k_b comparison between Cantera and CS, Reaction: $H + O_2 \rightleftharpoons OH + O$.

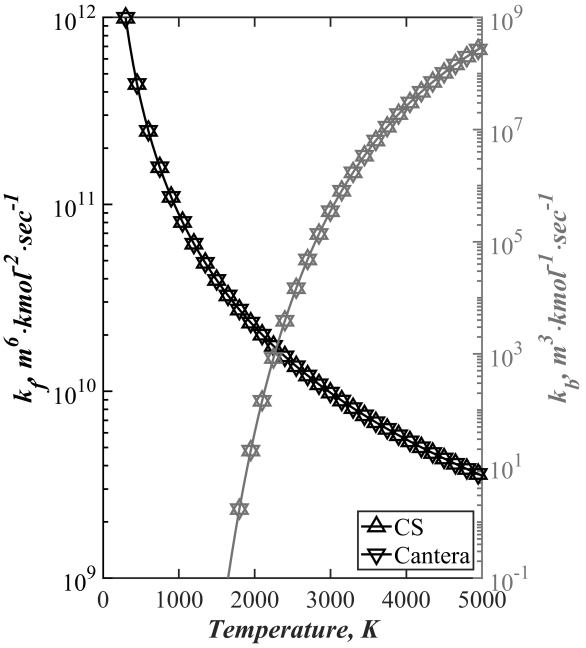

Figure B.8: k_f, k_b comparison between Cantera and CS, Reaction: $OH + H + H_2 \rightleftharpoons H_2O + H_2$.

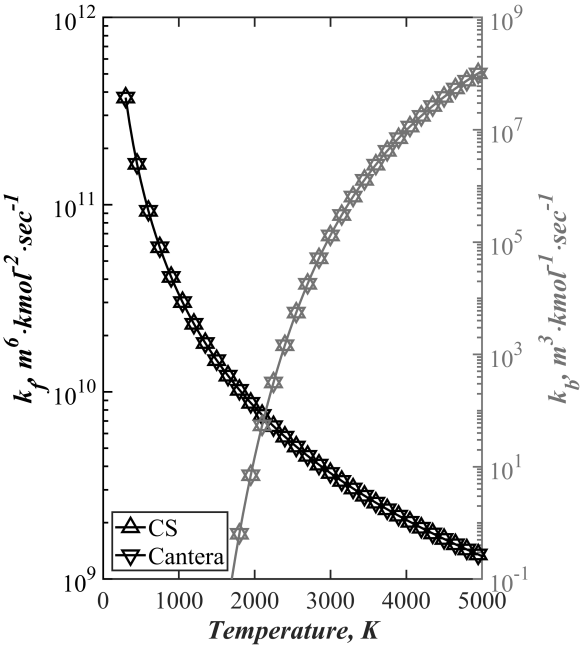

Figure B.9: k_f, k_b comparison between Cantera and CS, Reaction: $OH + H + O_2 \rightleftharpoons H_2O + O_2$.

APPENDIX C

ODE SOLVER FOR CHEMICAL NON-EQUILIBRIUM IN A QUASI-ONE-DIMENSIONAL NOZZLE

This section describes an ODE solver for an adiabatic, inviscid, chemically reacting nozzle flow field in a steady-state scenario. The results obtained in this section were used to validate the MoC results for the quasi-one-dimensional (Q1D) chemically reacting nozzle flow case discussed in Chapter 4. The approach detailed here is that of Zucrow and Hoffman [49] and thus a brief overview of the constitutive equations and the integration method is provided below.

The governing equations for a Q1D unsteady chemically reacting flowfield already derived in Chapter 4 can be simplified to obtain those for a steady flow scenario (for a different approach to arrive at these equations, see Zucrow and Hoffman [49]). Dropping the temporal derivative and manipulating the global continuity equation, Eq. (4.18a) results in,

$$\frac{1}{\rho}\frac{\partial \rho}{\partial x} + \frac{1}{u}\frac{\partial u}{\partial x} + \frac{1}{A}\frac{dA}{dx} = 0 \tag{C.1}$$

Since the gasdynamic properties only vary in the spatial direction, the above equation becomes,

$$\frac{1}{\rho}\frac{d\rho}{dx} + \frac{1}{u}\frac{du}{dx} + \frac{1}{A}\frac{dA}{dx} = 0 \tag{C.2}$$

The momentum equation, Eq. (4.18b) similarly re-written for the steady state case becomes,

$$\rho u\frac{du}{dx} + \frac{dp}{dx} = 0 \tag{C.3}$$

Finally, the steady-state, combined energy and momentum equation is given by,

$$\frac{dp}{dx} - a_f^2\frac{d\rho}{dx} = \frac{1}{u}\sum_{i=1}^{n}(\gamma_f R_i T - (\gamma_f - 1)h_i)\sigma_i \tag{C.4}$$

where γ_f in the above equation is calculated assuming that the gaseous mixture is chemically frozen, but thermally in equilibrium. For a steady-state Q1D nozzle flow,

the flowfield is essentially represented by a single traversing streamline, which is the steady pathline. Thus, the species continuity equation is similar to Eq. (4.23),

$$\rho u \frac{dc_i}{dx} = \sigma_i \qquad (i = 1, 2, \ldots, n) \tag{C.5}$$

In addition to the above equations, the equation of state for a mixture of perfect gases can be re-written to obtain an expression for static temperature as,

$$\frac{dT}{dx} = \frac{T}{p}\frac{dp}{dx} - \frac{T}{\rho}\frac{d\rho}{dx} - \frac{T}{R_{mix}}\sum_{i=1}^{n} R_i \frac{dc_i}{dx} \tag{C.6}$$

Given the boundary condition at the inlet to a Q1D nozzle and the nozzle area distribution, the above equations re-written as follows can be integrated using ode15s in MATLAB.

$$\frac{1}{u}\frac{du}{dx} = \frac{1}{M_f^2 - 1}\left[\frac{1}{A}\frac{dA}{dx} - \frac{\beta}{\rho u a_f^2}\right] \tag{C.7}$$

$$\frac{1}{\rho}\frac{d\rho}{dx} = -\frac{M_f^2}{M_f^2 - 1}\left[\frac{1}{A}\frac{dA}{dx} - \frac{\beta}{\rho u a_f^2}\right] + \frac{\beta}{\rho u a_f^2} \tag{C.8}$$

$$\frac{1}{T}\frac{dT}{dx} = -\frac{(\gamma_f - 1)M_f^2}{M_f^2 - 1}\left[\frac{1}{A}\frac{dA}{dx} - \frac{\beta}{\rho u a_f^2}\right] + \frac{(\gamma_f - 1)}{\gamma_f p u}\sum_{i=1}^{n} h_i \sigma_i \tag{C.9}$$

$$\frac{dc_i}{dx} = \frac{\sigma_i}{\rho u} \qquad (i = 1, 2, \ldots, n) \tag{C.10}$$

If the nozzle is a choked de Laval nozzle, integration of Eqs. (C.8)–(C.10) around the transonic region results in numerical instabilities, as the above equations exhibit a singularity at the throat. Thus, instead of using the nozzle's area variation as an

integration parameter, the governing equations can be rewritten in terms of a known pressure distribution as follows,

$$\frac{du}{dx} = -\frac{1}{\rho u}\frac{dp}{dx} \tag{C.11}$$

$$\frac{d\rho}{dx} = \frac{1}{a_f^2}\left[\frac{dp}{dx} - \frac{\beta}{u}\right] \tag{C.12}$$

$$\frac{dT}{dx} = \frac{(\gamma_f - 1)T}{\gamma_f p}\left[\frac{dp}{dx} - \frac{1}{u}\sum_{i=1}^{n} h_i \sigma_i\right] \tag{C.13}$$

$$\frac{dc_i}{dx} = \frac{\sigma_i}{\rho u} \qquad (i = 1, 2, \ldots, n) \tag{C.14}$$

The above equations are indeed of use in simulating a chemically reacting nozzle flow, as the expanding gas in the converging section of the de Laval nozzle is nearly in thermochemical equilibrium. Thus, the entire nozzle flowfield is first solved assuming thermochemical equilibrium using Q1D nozzle relations [49, 103]. Then, the pressure distribution from these equilibrium calculations are used to integrate Eqs. (C.11–C.14) from the inlet to a location slightly downstream of the throat. Thereafter, integrating Eqs. (C.7–C.10) solves the remainder of the flowfield. This procedure was used to solve the nozzle flowfield described in Chapter 4.

Additionally, to validate the chemistry subroutine described in Appendix B, the above equations were also integrated with Cantera [124] evaluated chemical source terms. A comparison of the results due to the use of Cantera and chemistry subroutine is shown in Fig. C.1. As seen again, the results due to chemistry subroutine and Cantera calculations are nearly identical, which validates the former.

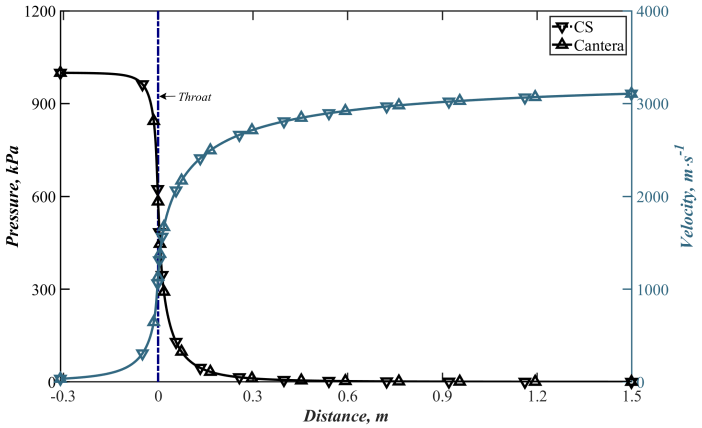

(a) Static pressure and velocity

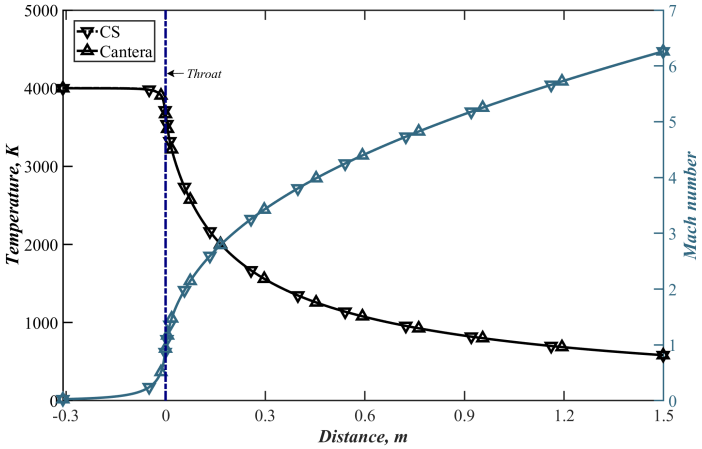

(b) Temperature and Mach number

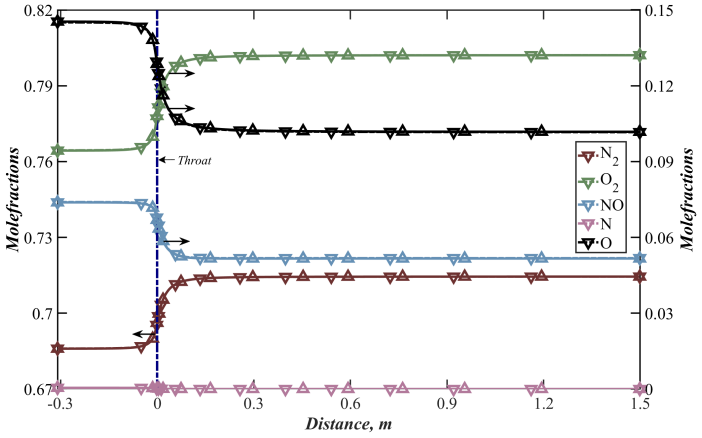

(c) Molefractions

Figure C.1: Comparison of Nozzle ODE Solver employing Chemistry Subroutine and Cantera

APPENDIX D

RATE DATA FOR FINITE RATE THERMOCHEMISTRY

This section provides the rate data used in Chapter 7. Firstly, the parameters used in Millikan–White's formula for VT rate calculations are provided. As mentioned earlier, these data were reported by Park [128].

Table D.1: VT Rate Data for Millikan–White Formula

Species	Collision Partner	a	b
N_2	N_2	221	0.0290
	O_2	229	0.0295
	NO	225	0.0293
	N	180	0.0262
	O	72.4	0.0150
O_2	N_2	134	0.0295
	O_2	138	0.300
	NO	136	0.0298
	N	72.4	0.015
	O	47.7	0.059
NO	N_2	49.5	0.042
	O_2	49.5	0.042
	NO	49.5	0.042
	N	49.5	0.042
	O	49.5	0.042

The second mechanism shown in Table D.2 is a modified form of Dunn–Kang mechanism [127] from Appendix A. In Table D.2, all the dissociation reactions consider preferential dissociation through the use of Park's two-temperature approximation. As seen in the reaction mechanism, the dissociation reaction temperatures now include the vibrational temperature in the rate constant calculations. The units for various parameters below are again in kg, m^3, kmol, J and K.

Table D.2: Reduced Dunn–Kang Mechanism, two-temperature

No.	**Reaction**	**Forward Rate Constant**				**Backward Rate Constant**				**Third Body** M
		A_f	B_f	$E_f/\mathcal{R} \times 10^4$	T	A_b	B_b	$E_b/\mathcal{R} \times 10^3$	T	
1	$O_2 + M \rightleftharpoons 2O + M$	3.600×10^{15}	-1.0	5.95	$\sqrt{T_{v_{O_2}} T_{RT}}$	3.00×10^9	-0.5	0.00	T_{RT}	N, NO
2	$N_2 + M \rightleftharpoons 2N + M$	1.900×10^{14}	-0.5	11.30	$\sqrt{T_{v_{N_2}} T_{RT}}$	1.10×10^{10}	-0.5	0.00	T_{RT}	O, NO, O_2
3	$NO + M \rightleftharpoons N + O + M$	3.900×10^{17}	-1.5	7.55	$\sqrt{T_{v_{NO}} T_{RT}}$	1.00×10^{14}	-1.5	0.00	T_{RT}	O_2, N_2
4	$O + NO \rightleftharpoons N + O_2$	3.200×10^6	1.00	1.97	T_{RT}	1.30×10^7	1.0	3.58	T_{RT}	
5	$O + N_2 \rightleftharpoons N + NO$	7.000×10^{10}	0.00	3.80	T_{RT}	1.56×10^{10}	0.0	0.00	T_{RT}	
6	$N + N_2 \rightleftharpoons 2N + N$	4.085×10^{19}	-1.5	11.30	$\sqrt{T_{v_{N_2}} T_{RT}}$	2.27×10^{15}	-1.5	0.00	T_{RT}	
7	$O_2 + O \rightleftharpoons 2O + O$	9.000×10^{16}	-1.0	5.95	$\sqrt{T_{v_{O_2}} T_{RT}}$	7.50×10^{10}	-0.5	0.00	T_{RT}	
8	$O_2 + O_2 \rightleftharpoons 2O + O_2$	3.240×10^{16}	-1.0	5.95	$\sqrt{T_{v_{O_2}} T_{RT}}$	2.70×10^{10}	-0.5	0.00	T_{RT}	
9	$O_2 + N_2 \rightleftharpoons 2O + N_2$	7.200×10^{15}	-1.0	5.95	$\sqrt{T_{v_{O_2}} T_{RT}}$	6.00×10^9	-0.5	0.00	T_{RT}	
10	$N_2 + N_2 \rightleftharpoons 2N + N_2$	4.700×10^{14}	-0.5	11.30	$\sqrt{T_{v_{N_2}} T_{RT}}$	2.72×10^{10}	-0.5	0.00	T_{RT}	
11	$NO + M \rightleftharpoons N + O + M$	7.800×10^{17}	-1.5	7.55	$\sqrt{T_{v_{NO}} T_{RT}}$	2.00×10^{14}	-1.5	0.00	T_{RT}	O, N, NO

REFERENCES

[1] H. H. Hornung, "Ground Testing for Hypervelocity Flow, Capabilities and Limitations," EN-AVT-186-01, 2010.

[2] S. Gu and H. Olivier, "Capabilities and Limitations of Existing Hypersonic Facilities," *Progress in Aerospace Sciences*, vol. 113, p. 100607, 2020. [Online]. Available: https://www.sciencedirect.com/science/article/pii/S0376042120300191

[3] P. Vieille, "Sur les discontinuités produites par la détente brusque de gas comprimés," *Comptes Rendus de l'Académie des Sciences de Paris*, vol. 129, pp. 1228–1230, 1899.

[4] A. G. Gaydon and I. R. Hurle, *The Shock Tube in High Temperature Chemical Physics*. Reinhold Publishing Corporation, New York, 1963.

[5] H. W. Liepmann and A. Roshko, *Elements of Gasdynamics*. Wiley, New York, 1957.

[6] W. Bleakney, D. K. Weimer, and C. H. Fletcher, "The shock tube: A facility for investigations in fluid dynamics," *Review of Scientific Instruments*, vol. 20, no. 11, pp. 807–815, 1949. [Online]. Available: https://doi.org/10.1063/1.1741395

[7] G. Rudinger, "Note on the Use of the Shock Tube as an Intermittent Supersonic Wind Tunnel," *Physical Review*, vol. 75, pp. 1948–1949, 1949. [Online]. Available: https://link.aps.org/doi/10.1103/PhysRev.75.1948

[8] I. I. Glass and J. G. Hall, "Handbook of Supersonic Aerodynamics, Vol. 6, Section 18 – Shock Tubes," John Hopkins University Applied Physics Laboratory," NAVORD Report 1488, 1959.

[9] N. Fomin, "110 Years of Experiments on Shock Tubes," *Journal of Engineering Physics and Thermophysics*, vol. 83, pp. 1118–1135, 2010. [Online]. Available: https://doi.org/10.1007/s10891-010-0437-9

[10] B. D. Henshall, "On Some Aspects of the Use of Shock Tubes in Aerodynamic Research," British Aeronautical Research Council R. & M. No. 3044, 1957.

[11] H. Olivier, "The Aachen Shock Tunnel TH2 with Dual Driver Mode Operation," in *Experimental Methods of Shock Wave Research*, O. Igra and F. Seiler, Eds. Springer, 2016, pp. 111–129. [Online]. Available: https://doi.org/10.1007/978-3-319-23745-9

[12] F. K. Lu and D. Marren, *Advanced Hypersonic Test Facilities*. American Institute of Aeronautics and Astronautics, Virginia, 2002, vol. 198, ch. 3, 4, 6 and 7. [Online]. Available: https://doi.org/10.2514/4.866678

[13] B. A. Cruden and D. W. Bogdanoff, "Shock Radiation Tests for Saturn and Uranus Entry Probes," *Journal of Spacecraft and Rockets*, vol. 54, no. 6, pp. 1246–1257, 2017. [Online]. Available: https://doi.org/10.2514/1.A33891

[14] R. J. Stalker, "A Study of the Free-Piston Shock Tunnel," *AIAA Journal*, vol. 5, no. 12, pp. 2160–2165, 1967. [Online]. Available: https://doi.org/10.2514/3.4402

[15] H. G. Hornung, "Performance Data of the New Free-piston Shock Tunnel at GALCIT," 28th Joint Propulsion Conference and Exhibit, Nashville, TN, AIAA Paper 92-3943, 1992. [Online]. Available: https://doi.org/10.2514/6.1992-3943

[16] G. Eitelberg, T. J. McIntyre, and W. H. Beck, "The High Enthalpy Shock Tunnel at Göttingen," 28th Joint Propulsion Conference and

Exhibit, Nashville, TN, AIAA Paper 92-3942, 1992. [Online]. Available: https://doi.org/10.2514/3.62711

[17] A. Hertzberg and W. E. Smith, "A Method for Generating Strong Shock Waves," *Journal of Applied Physics*, vol. 25, no. 1, pp. 130–131, 1954. [Online]. Available: https://doi.org/10.1063/1.1721501

[18] G. A. Bird, "A Note on Combustion Driven Shock Tubes," AGARD Report 146, 1957.

[19] W. J. Loubsky, R. S. Hiers, and D. Stewart, "Performance of a Combustion Driven Shock Tunnel with Application to the Tailored- Interface Operating Conditions," NASA Ames Research Center, California," NASA-TM-X-54960, 1964.

[20] P. B. Coates and A. G. Gaydon, "A Simple Shock Tube with Detonating Driver Gas," *Proceedings of the Royal Society of London. Series A. Mathematical and Physical Sciences*, vol. 283, no. 1392, pp. 18–32, 1965. [Online]. Available: https://royalsocietypublishing.org/doi/abs/10.1098/rspa.1965.0004

[21] R. L. Trimpi, "A Preliminary Theoretical Study of the Expansion Tube, a New Device for Producing High-Enthalpy Short Duration Hypersonic Gas Flows," NASA Langley Research Center, Virginia, Tech. Rep. NASA Technical Report R-133, 1962.

[22] J. I. Erdos, R. J. Bakos, A. Castrogiovanni, and R. C. Rogers, "Dual Mode Shock-expansion/reflected-shock Tunnel," 35th AIAA Aerospace Sciences Meeting and Exhibit, Reno, NV, AIAA Paper 97-0560, 1997. [Online]. Available: https://doi.org/10.2514/6.1997-560

[23] H. Grönig, H. Olivier, and M. Habermann, "Development of a detonation driver for a shock tunnel," *The Review of High Pressure Science*

and Technology, vol. 7, pp. 879–884, 1998. [Online]. Available: https://doi.org/10.4131/jshpreview.7.879

[24] C.-Y. Tsai and R. J. Bakos, "Mach 7-21 Flight Simulation in the HYPULSE Shock Tunnel," Proceedings of the 23rd ISSW, pp. 345–355, 2002.

[25] C. K. Yuan and Z. L. Jiang, "Experimental Investigation of Hypersonic Flight-Duplicated Shock Tunnel Characteristics," *Acta Mechanica Sinica*, vol. 37, no. 3, pp. 422–433, 2021. [Online]. Available: https://doi.org/10.1007/s10409-020-01036-0

[26] B. H. Fetz, "Analysis of the Optimum Performance of Buffered Shock Tubes," Aerospace Research Laboratories, Wright-Patterson AFB, Ohio, Tech. Rep. ARL 64-41, 1964.

[27] B. H. K. Lee, "Detonation-driven Shocks in a Shock Tube," *AIAA Journal*, vol. 5, no. 4, pp. 791–792, 1967. [Online]. Available: https://doi.org/10.2514/3.4065

[28] H. R. Yu, "Shock Tunnel and its Application to Aeroheating Experiments (in Chinese)," Doctoral Dissertation, Institute of Mechanics, Chinese Academy of Sciences, Beijing, 1963.

[29] Y. Hongru, "Oxyhydrogen Combustion and Detonation Driven Shock Tube," *Acta Mechanica Sinica*, vol. 15, no. 2, pp. 97–107, 1999. [Online]. Available: https://doi.org/10.1007/BF02485874

[30] H. R. Yu, B. Esser, M. Lenartz, and H. Grönig, "Gaseous Detonation Driver for a Shock Tunnel," *Shock Waves*, vol. 2, no. 4, pp. 245–254, 1992. [Online]. Available: https://doi.org/10.1007/BF01414760

[31] R. J. Bakos, J. Calleja, J. I. Erdos, M. A. Sussman, and G. Wilson, "An Experimental and Computational Study Leading to New Test Capabilities for the HYPULSE Facility with a Detonation Driver," 19th AIAA Advanced

Measurement and Ground Testing Technology Conference, New Orleans, LA, AIAA 96-2193, 1996. [Online]. Available: https://doi.org/10.2514/6.1996-2193

[32] W. S. Stuessy, H.-C. Liu, F. K. Lu, and D. R. Wilson, "Initial Operation of a High-Pressure Detonation-Driven Shock Tube Facility," 35th Aerospace Sciences Meeting and Exhibit, Reno, NV, AIAA 97-0665, 1997. [Online]. Available: https://doi.org/10.2514/6.1997-665

[33] F. K. Lu and D. R. Wilson, "Detonation Driver for Enhancing Shock Tube Performance," *Shock Waves*, vol. 12, no. 6, pp. 457–468, Apr 2003. [Online]. Available: https://doi.org/10.1007/s00193-003-0186-1

[34] J. J. Jones and J. A. Moore, "Exploratory Study of Performance of the Langley Pilot Model Expansion Tube with a Hydrogen Driver," NASA Langley Research Center, Virginia," NASA TN D-3421, 1966.

[35] C. G. Miller, "Operational Experience in the Langley Expansion Tube with Various Test Gases," NASA Langley Research Center, Virginia," NASA TM 78637, 1977.

[36] A. Paull and R. J. Stalker, "Test Flow Disturbances in an Expansion Tube," *Journal of Fluid Mechanics*, vol. 245, p. 493–521, 1992. [Online]. Available: https://doi.org/10.1017/S0022112092000569

[37] A. Dufrene, M. MacLean, R. Parker, and M. Holden, "Experimental Characterization of the LENS Expansion Tunnel Facility Including Blunt Body Surface Heating," 49th AIAA Aerospace Sciences Meeting including the New Horizons Forum and Aerospace Exposition, Orlando, FL, AIAA Paper 2011-626, 2011. [Online]. Available: https://doi.org/10.2514/6.2011-626

[38] T. Dean, T. R. Blair, M. Roberts, C. Limbach, and R. D. Bowersox, "On the Initial Characterization of a Large-Scale Hypervelocity Expansion Tunnel,"

AIAA SciTech 2022 Forum, San Diego CA & Virtual, AIAA Paper 2022-1602, 2022. [Online]. Available: https://doi.org/10.2514/6.2022-1602

[39] A. Dufrene, M. Sharma, and J. M. Austin, "Design and Characterization of a Hypervelocity Expansion Tube Facility," *Journal of Propulsion and Power*, vol. 23, no. 6, pp. 1185–1193, 2007. [Online]. Available: https://doi.org/10.2514/1.30349

[40] Y. M. Abul-Huda and M. Gamba, "Flow Characterization of a Hypersonic Expansion Tube Facility for Supersonic Combustion Studies," *Journal of Propulsion and Power*, vol. 33, no. 6, pp. 1504–1519, 2017.

[41] B. Esser, "Die Zustandsgrößen im Stoßwellenkanal als Ergebnisse eines exakten Riemannlösers," Doctoral Dissertation, Rheinisch-Westfälischen Technischen Hochschule Aachen, 1992.

[42] A. Yamanaka, Y. Ariga, T. Obara, P. Cai, and S. Ohyagi, "Study on Performance of Detonation-Driven Shock Tube," *JSME International Journal Series B Fluids and Thermal Engineering*, vol. 45, no. 2, pp. 425–431, 2002. [Online]. Available: https://doi.org/10.1299/jsmeb.45.425

[43] Z. Jiang and H. Yu, "Development and Calibration of Detonation-Driven High-Enthalpy and Hypersonic Test Facilities," in *Experimental Methods of Shock Wave Research*, O. Igra and F. Seiler, Eds. Springer International Publishing, 2016, pp. 285–313. [Online]. Available: https://doi.org/10.1007/978-3-319-23745-9_9

[44] K. Luo, Q. Wang, J. Li, J. Li, and W. Zhao, "Numerical Modeling of a High-enthalpy Shock Tunnel Driven by Gaseous Detonation," *Aerospace Science and Technology*, vol. 104, p. 105958, 2020. [Online]. Available: https://www.sciencedirect.com/science/article/pii/S1270963820306404

[45] J. W. Li, W. Qiu, W. Zhao, P. Lu, and Y. Tan, "Performance of a Detonation Driven Shock Tunnel," 21st AIAA International Space Planes and Hypersonics Technologies Conference, Xiamen, China, AIAA Paper 2017–2306, 2017. [Online]. Available: https://doi.org/10.2514/6.2017-2306

[46] M. S. Priyadarshini, A. Munafò, A. M. Brandis, B. A. Cruden, and M. Panesi, "One-dimensional Modeling Methodology for Shock Tubes: Application to the EAST Facility," 2018 Joint Thermophysics and Heat Transfer Conference, Atlanta, GA, AIAA Paper 2018-4181. [Online]. Available: https://arc.aiaa.org/doi/abs/10.2514/6.2018-4181

[47] R. Courant and K. O. Friedrichs, *Supersonic Flow and Shock Waves*. Interscience, New York, 1948.

[48] G. Rudinger, *Wave Diagrams for Nonsteady Flow in Ducts*. Van Nostrand, New York, 1955.

[49] M. Zucrow and J. Hoffman, *Gas Dynamics: Volume 2, Multidimensional Flow*. Wiley, New York, 1977.

[50] M. MacLean, A. Dufrene, T. Wadhams, and M. Holden, "Numerical and Experimental Characterization of High Enthalpy Flow in an Expansion Tunnel Facility," 48th AIAA Aerospace Sciences Meeting Including the New Horizons Forum and Aerospace Exposition, Orlando, FL, AIAA Paper 2010-1562, 2010. [Online]. Available: https://doi.org/10.2514/6.2010-1562

[51] I. Nompelis, G. Candler, M. Holden, and T. Wadhams, "Numerical Simulation of High-Enthalpy Experiments in the LENS-X Expansion Tube Facility," 42nd AIAA Aerospace Sciences Meeting and Exhibit, Reno, NV, AIAA Paper 2004-1000, 2004. [Online]. Available: https://doi.org/10.2514/6.2004-1000

[52] J. H. Skinner, Jr., "Plane-flame Simulation of the Wake Behind an Internally Propelled Vehicle," Rensselaer Polytechnic Institute, New York," RPI-TR-AE-6701, 1967.

[53] M. Radulescu and R. Hanson, "Effect of Heat Loss on Pulse-Detonation-Engine Flow Fields and Performance," *Journal of Propulsion and Power*, vol. 21, no. 2, pp. 274–285, 2005. [Online]. Available: https://doi.org/10.2514/1.10286

[54] K. Kawane, S. Shimada, J. Kasahara, and A. Matsuo, "The Influence of Heat Transfer and Friction on the Impulse of a Detonation Tube," *Combustion and Flame*, vol. 158, no. 10, pp. 2023–2036, 2011. [Online]. Available: https://www.sciencedirect.com/science/article/pii/S001021801100071X

[55] C. Morris, "Simplified Analysis of Pulse Detonation Rocket Engine Blowdown Gasdynamics and Performance," 38$^{\text{th}}$ Joint Propulsion Conference and Exhibit, Indianapolis, IN, AIAA Paper 2002-3715, 2002. [Online]. Available: https://arc.aiaa.org/doi/abs/10.2514/6.2002-3715

[56] J. T. Peace and F. K. Lu, "Performance Modeling of Pulse Detonation Engines Using the Method of Characteristics," *Aerospace Science and Technology*, vol. 88, pp. 51–64, 2019. [Online]. Available: http://www.sciencedirect.com/science/article/pii/S1270963818327020

[57] V. Quan, J. E. Melde, J. R. Kliegel, G. R. Nickerson, and H. M. Frey, "Kinetic Performance of Barrier-Cooled Rocket Nozzles," *Journal of Spacecraft and Rockets*, vol. 5, no. 10, pp. 1137–1142, 1968. [Online]. Available: https://doi.org/10.2514/3.29438

[58] J. L. Palmer and R. K. Hanson, "Application of Method of Characteristics to Underexpanded, Freejet Flows with Vibrational Nonequilibrium," *AIAA Journal*, vol. 36, no. 2, pp. 193–200, 1998. [Online]. Available: https://doi.org/10.2514/2.7501

[59] L. N. Connor, Jr., "Calculation of the Centered One-dimensional Unsteady Expansion of a Reacting Gas Mixture Subject to Vibrational and Chemical Nonequilibrium," NASA Langley Research Center, Virginia," NASA TN D-3851, 1967.

[60] R. Sedney, "The Method of Characteristics," in *Nonequilibrium Flows, Part II*, P. P. Wegener, Ed. Marcel Dekker, New York, 1970.

[61] E. L. Petersen and R. K. Hanson, "Improved Turbulent Boundary-Layer Model for Shock Tubes," *AIAA Journal*, vol. 41, no. 7, pp. 1314–1322, 2003. [Online]. Available: https://doi.org/10.2514/2.2076

[62] W. S. Liu, I. I. Glass, and A. D. Young, "Laminar boundary layers behind detonation waves," *Proceedings of the Royal Society of London. A. Mathematical and Physical Sciences*, vol. 387, no. 1793, pp. 331–349, 1983. [Online]. Available: https://doi.org/10.1098/rspa.1983.0063

[63] A. Jayamani and F. K. Lu, "A Study of Detonation Driven Shock Tube Using the Method of Characteristics," 23rd AIAA International Space Planes and Hypersonic Systems and Technologies Conference, Montreal, Quebec, Canada, AIAA Paper 2020–2454, 2020. [Online]. Available: https://arc.aiaa.org/doi/abs/10.2514/6.2020-2454

[64] F. K. Lu, D. R. Wilson, R. J. Bakos, and J. I. Erdos, "Recent Advances in Detonation Techniques for High-Enthalpy Facilities," *AIAA Journal*, vol. 38, no. 9, pp. 1676–1684, 2000. [Online]. Available: https://doi.org/10.2514/2.1153

[65] D. L. Chapman, "VI. On the Rate of Explosion in Gases," *The London, Edinburgh, and Dublin Philosophical Magazine and Journal of Science*, vol. 47, no. 284, pp. 90–104, 1899. [Online]. Available: https://doi.org/10.1080/14786449908621243

[66] R. J. Bakos and J. I. Erdos, "Optimizing Pressure Recovery in a Detonation Driven Reflected Shock Tunnel," Proceedings of the 21st ISSW, 1997.

[67] G. Ben-Dor, O. Igra, and T. Elperin, *Handbook of Shock Waves: Volume 2, Shock Wave Interactions and Propagation*. Academic, California, 2001. [Online]. Available: https://www.sciencedirect.com/book/9780120864300

[68] P. A. Thompson, *Compressible-Fluid Dynamics*. McGraw-Hill, New York, 1976.

[69] M. J. Zucrow and J. D. Hoffman, *Gas Dynamics: Volume 1*. Wiley, New York, 1976.

[70] H. W. Gale, "Numerical Analysis of Unsteady Compressible Gas Dynamics of Varied Area Channels: Applied to Gas Dynamic Laser Start," PhD Dissertation, Purdue University, 1974.

[71] R. Courant and D. Hilbert, *Methods of Mathematical Physics, Volume 1*. Wiley, New York, 1989. [Online]. Available: https://doi.org/10.1002/9783527617210

[72] Q. Xiao, A. Sow, B. M. Maxwell, and M. I. Radulescu, "Effect of Boundary Layer Losses on 2D Detonation Cellular Structures," *Proceedings of the Combustion Institute*, vol. 38, no. 3, pp. 3641–3649, 2021. [Online]. Available: https://www.sciencedirect.com/science/article/pii/S1540748920305186

[73] D. R. Wilson, Y. Lee, and C. Stewart, "Transient Flow Analysis of the AEDC/HPDE MHD Generator," 21st AIAA Aerospace Sciences Meeting, Reno, NV, AIAA Paper 83-0395, 1983. [Online]. Available: https://arc.aiaa.org/doi/abs/10.2514/6.1983-395

[74] C. P. T. Groth, J. J. Gottlieb, and P. A. Sullivan, "Numerical Investigation of High-temperature Effects in the UTIAS–RPI Hypersonic Impulse Tunnel," *Canadian Journal of Physics*, vol. 69, no. 7, pp. 897–918, 1991. [Online]. Available: https://doi.org/10.1139/p91-144

[75] P. A. Jacobs, "Quasi-one-dimensional Modeling of a Free-Piston Shock Tunnel," *AIAA Journal*, vol. 32, no. 1, pp. 137–145, 1994. [Online]. Available: https://doi.org/10.2514/3.11961

[76] P. Jacobs, "Shock Tube Modelling with L1d," The University of Queensland," Research Report 13/98, Nov 1998.

[77] N.-S. Cheng, "Formulas for Friction Factor in Transitional Regimes," *Journal of Hydraulic Engineering*, vol. 134, no. 9, pp. 1357–1362, 2008. [Online]. Available: https://doi.org/10.1061/(ASCE)0733-9429(2008)134:9(1357)

[78] J. Nikuradse, "Laws of flow in rough pipes," NACA TM-1292, 1933, *Translation of "Strömungsgesetze in rauhen Rohren." VDI-Forschungsheft 361. Beilage zu "Forschung auf dem Gebiete des Ingenieurwesens" Ausgabe B Band 4, July/August 1933.*

[79] H. W. Liepmann and F. E. Goddard, "Note on the Mach Number Effect Upon the Skin Friction of Rough Surfaces," *Journal of the Aeronautical Sciences*, vol. 24, no. 10, pp. 784–784, 1957.

[80] F. E. Goddard, "Effect of Uniformly Distributed Roughness on Turbulent Skin-Friction Drag at Supersonic Speeds," *Journal of the Aerospace Sciences*, vol. 26, no. 1, pp. 1–15, 1959. [Online]. Available: https://doi.org/10.2514/8.7911

[81] J. P. Holman, *Heat Transfer*, 10th ed. McGraw-Hill, Boston, 2010.

[82] E. R. Van Driest, "The Problem of Aerodynamic Heating," *Aeronautical Engineering Review*, vol. 15, pp. 26–41, 1956.

[83] E. Eckert, "Engineering Relations for Heat Transfer and Friction in High-Velocity Laminar and Turbulent Boundary-layer Flow Over Surfaces with Constant Pressure and Temperature," *Transactions of the ASME*, vol. 78, no. 6, pp. 1273–1283, 1956. [Online]. Available: https://doi.org/10.1115/1.4014011

[84] S. Browne, J. Ziegler, and J. E. Shepherd, "Numerical Solution Methods for Shock and Detonation Jump Conditions," California Institute of Technology," GALCIT Report FM2006.006, 2008.

[85] D. G. Goodwin, R. L. Speth, H. K. Moffat, and B. W. Weber, "Cantera: An Object-Oriented Software Toolkit for Chemical Kinetics, Thermodynamics, and Transport Processes (2.5.1)," 2021. [Online]. Available: https://doi.org/10.5281/zenodo.4527812

[86] B. McBride and S. Gordon, "Computer Program for Calculation of Complex Chemical Equilibrium Compositions and Applications: Part I," NASA Lewis Research Center," NASA RP-1311-1, 1994.

[87] B. J. McBride and S. Gordon, "Computer Program for Calculation of Complex Chemical Equilibrium Compositions and Applications: Part II," NASA Lewis Research Center," NASA RP-1311-2, 1996.

[88] I. I. Glass and G. N. Patterson, "A Theoretical and Experimental Study of Shock-Tube Flows," *Journal of the Aeronautical Sciences*, vol. 22, no. 2, pp. 73–100, 1955. [Online]. Available: https://doi.org/10.2514/8.3282

[89] T. Ikui and K. Matsuo, "Investigations of the Aerodynamic Characteristics of the Shock Tubes: Part 1, The Effects of Tube Diameter on the Tube Performance," *Bulletin of JSME*, vol. 12, no. 52, pp. 774–782, 1969. [Online]. Available: https://doi.org/10.1299/jsme1958.12.774

[90] T. Furukawa, T. Aochi, and A. Sasoh, "Expansion Tube Operation with Thin Secondary Diaphragm," *AIAA Journal*, vol. 45, no. 1, pp. 214–217, 2007. [Online]. Available: https://doi.org/10.2514/1.23846

[91] I. I. Glass and J. P. Sislian, *Nonstationary Flows and Shock Waves*. Clarendon, Oxford, 1994. [Online]. Available: https://doi.org/10.1093/oso/9780198593881.001.0001

[92] J. H. S. Lee, *The Detonation Phenomenon*. Cambridge, New York, 2008. [Online]. Available: https://doi.org/10.1017/CBO9780511754708

[93] R. J. Bakos and J. I. Erdos, "Options for Enhancement of the Performance of Shock-Expansion Tubes and Tunnels," 33rd AIAA Aerospace Sciences Meeting and Exhibit, Reno, NV, AIAA Paper 95-0799, 1995. [Online]. Available: https://doi.org/10.2514/6.1995-799

[94] A. Jayamani and F. K. Lu, "A Method of Characteristics Solver for Unsteady Quasi-One-Dimensional Chemically Reacting Gas Flows," AIAA Scitech 2021 Forum, Virtual Event, AIAA Paper 2021-0315, 2021. [Online]. Available: https://arc.aiaa.org/doi/abs/10.2514/6.2021-0315

[95] W. G. Vincenti. and C. H. Kruger, *Introduction to Physical Gas Dynamics*. Wiley, New York, 1965.

[96] S. Gai, "Free Piston Shock Tunnels: Developments and Capabilities," *Progress in Aerospace Sciences*, vol. 29, no. 1, pp. 1–41, 1992. [Online]. Available: https://www.sciencedirect.com/science/article/pii/037604219290002Y

[97] H. R. Wallingford and D. I. H. Barr, *Appendix 1 : Recommended roughness values*, 8th ed. ICE Publishing, 2006, vol. 1, pp. 40–41. [Online]. Available: https://www.icevirtuallibrary.com/doi/abs/10.1680/tfthdopsac.33559.bm03

[98] G. B. Whitham, *Linear and Nonlinear Waves*. Wiley, New York, 1974. [Online]. Available: https://doi.org/10.1002/9781118032954

[99] B. W. Skews, "The Shape of a Diffracting Shock Wave," *Journal of Fluid Mechanics*, vol. 29, no. 2, p. 297–304, 1967. [Online]. Available: https://doi.org/10.1017/S0022112067000825

[100] M. I. Radulescu, R. Mével, Q. Xiao, and S. Gallier, "On the Self-Similarity of Diffracting Gaseous Detonations and the Critical Channel Width Problem,"

Physics of Fluids, vol. 33, no. 6, p. 066106, 2021. [Online]. Available: https://doi.org/10.1063/5.0054219

[101] R. S. Figliola and D. E. Beasley, *Theory and Design for Mechanical Measurements*. Wiley, New York, 2000.

[102] D. S. Bynum, R. L. Ledford, and W. E. Smotherman, "Wind Tunnel Pressure Measuring Techniques," NATO-AGARD Fluid Dynamics Panel," AGARDograph No. 145, 1970.

[103] J. D. Anderson, *Hypersonic and High-Temperature Gas Dynamics*. American Institute of Aeronautics and Astronautics, Virginia, 2006. [Online]. Available: https://doi.org/10.2514/4.861956

[104] B. J. McBride, M. J. Zehe, and S. Gordon, "NASA Glenn Coefficients for Calculating Thermodynamic Properties of Individual Species," NASA Glenn Research Center," NASA/TP-2002-211556, 2002.

[105] L. F. Shampine and M. W. Reichelt, "The MATLAB ODE Suite," *SIAM Journal on Scientific Computing*, vol. 18, no. 1, pp. 1–22, 1997. [Online]. Available: https://doi.org/10.1137/S1064827594276424

[106] H. Shang, Y. Chen, P. Liaw, C. Chen, and T. Wang, "Investigation of Chemical Kinetics Integration Algorithms for Reacting Flows," 33rd AIAA Aerospace Sciences Meeting and Exhibit, Reno, NV, AIAA Paper 95-0806, 1995. [Online]. Available: https://doi.org/10.2514/6.1995-806

[107] Kao, S. and Ziegler, J. and Bitter, N. and Schmidt, N. and Lawson, J. and Shepherd, J. E., "Numerical Tools for Shock and Detonation Wave Modeling," California Institute of Technology," GALCIT Report FM2018.001, 2023.

[108] J.-S. Shuen, M.-S. Liou, and B. Van Leer, "Inviscid Flux-Splitting Algorithms for Real Gases with Non-Equilibrium Chemistry," *Journal of*

Computational Physics, vol. 90, no. 2, pp. 371–395, 1990. [Online]. Available: https://doi.org/10.1016/0021-9991(90)90172-W

[109] S. Gu, J. Hao, and C.-y. Wen, "Air Thermochemistry in the Converging Section of de Laval Nozzles on Hypersonic Wind Tunnels," *AIP Advances*, vol. 12, no. 8, p. 085320, 08 2022. [Online]. Available: https://doi.org/10.1063/5.0106554

[110] K. N. C. Bray, "Atomic Recombination in a Hypersonic Wind-tunnel Nozzle," *Journal of Fluid Mechanics*, vol. 6, no. 1, p. 1–32, 1959. [Online]. Available: https://doi.org/10.1017/S0022112059000477

[111] A. Jayamani and F. K. Lu, "Method of Characteristics Modeling of Nonequilibrium Flow in an Impulse Facility," AIAA Scitech 2023 Forum, National Harbor, MD, AIAA Paper 2023-2088, 2023. [Online]. Available: https://do.org/10.2514/6.2021-0315

[112] H. Olivier, J. Zonglin, H. R. Yu, and F. K. Lu, *Detonation-Driven Shock Tubes and Tunnels*. American Institute of Aeronautics and Astronautics, Virginia, 2002, vol. 198, ch. 6. [Online]. Available: https://doi.org/10.2514/5.9781600866678.0135.0203

[113] A. Rohatgi, "Webplotdigitizer: Version 4.4," 2020. [Online]. Available: https://automeris.io/WebPlotDigitizer

[114] Y. V. Stupochenko, S. A. Losev, and A. I. Osipov, *Relaxation in Shock Waves*. Springer, 1967. [Online]. Available: https://doi.org/10.1007/978-3-642-48246-5

[115] Y. B. Zeldovich and Y. P. Raizer, *Physics of Shock Waves and High-Temperature Hydrodynamic Phenomena*. Academic, New York, 1966, vol. 1.

[116] K. Bray, "Vibrational Relaxation of Anharmonic Oscillator Molecules: II. Non-Isothermal Conditions," *Journal of Physics B: Atomic and Molecular Physics*, vol. 3, no. 11, p. 1515, 1970. [Online]. Available: https://doi.org/10.1088/0022-3700/3/11/013

[117] S. M. Ruffin, "Vibrational Energy Transfer of Diatomic Gases in Hypersonic Expanding Flows," Doctoral Dissertation, Stanford University, 1993.

[118] K. N. C. Bray, "Vibrational Relaxation of Anharmonic Oscillator Molecules: Relaxation Under Isothermal Conditions," *Journal of Physics B: Atomic and Molecular Physics*, vol. 1, no. 4, pp. 705–717, 1968. [Online]. Available: https://doi.org/10.1088/0022-3700/1/4/322

[119] R. L. Taylor, M. Camac, and R. Feinberg, "Measurements of Vibration-Vibration Coupling in Gas Mixtures," *Symposium (International) on Combustion*, vol. 11, no. 1, pp. 49–65, 1967. [Online]. Available: https://doi.org/10.1016/S0082-0784(67)80133-4

[120] C. Park, "Review of Chemical-Kinetic Problems of Future NASA Missions. I-Earth Entries," *Journal of Thermophysics and Heat transfer*, vol. 7, no. 3, pp. 385–398, 1993. [Online]. Available: https://doi.org/10.2514/3.431

[121] C. Park, "Problems of Rate Chemistry in the Flight Regimes of Aeroassisted Orbital Transfer Vehicles," 19$^{\text{th}}$ Thermophysics Conference, Snowmass, CO, AIAA Paper 84-1730. [Online]. Available: https://doi.org/10.2514/6.1984-1730

[122] C. Park and S.-H. Lee, "Validation of Multitemperature Nozzle Flow Code," *Journal of Thermophysics and Heat Transfer*, vol. 9, no. 1, pp. 9–16, 1995. [Online]. Available: https://doi.org/10.2514/3.622

[123] C. Park, "Assessment of a Two-Temperature Kinetic Model for Dissociating and Weakly Ionizing Nitrogen," *Journal of Thermophysics and Heat Transfer*, vol. 2, no. 1, pp. 8–16, 1988. [Online]. Available: https://doi.org/10.2514/3.55

[124] D. G. Goodwin, H. K. Moffat, I. Schoegl, R. L. Speth, and B. W. Weber, "Cantera: An Object-oriented Software Toolkit for Chemical Kinetics, Thermodynamics, and Transport Processes," https://www.cantera.org, 2023, version 3.0.0. [Online]. Available: https://doi.org/10.5281/zenodo.8137090

[125] S. P. Sharma, S. M. Ruffin, W. D. Gillespie, and S. A. Meyer, "Vibrational Relaxation Measurements in an Expanding Flow Using Spontaneous Raman Scattering," *Journal of Thermophysics and Heat Transfer*, vol. 7, no. 4, pp. 697–703, 1993. [Online]. Available: https://doi.org/10.2514/3.479

[126] J. P. Drummond, R. C. Rogers, and M. Y. Hussaini, "A Detailed Numerical Model of a Supersonic Reacting Mixing Layer," 22$^{\text{nd}}$ Joint Propulsion Conference, Huntsville, AL, AIAA Paper 86-1427, 1986. [Online]. Available: https://doi.org/10.2514/6.1986-1427

[127] M. G. Dunn and S.-W. Kang, "Theoretical and Experimental Studies of Reentry Plasmas," NASA Langley Research Center," NASA-CR-2232, 1973.

[128] C. Park, "Thermochemical Relaxation in Shock Tunnels," *Journal of Thermophysics and Heat Transfer*, vol. 20, no. 4, pp. 689–698, 2006. [Online]. Available: https://doi.org/10.2514/1.22719

BIOGRAPHICAL STATEMENT

Ananth Jayamani was born in Tamil Nadu, India in 1990. He holds a bachelor's degree in Aeronautical Engineering awarded (2012) by Anna University, Chennai. After working in the aerospace industry briefly, he enrolled as a graduate student in UT Arlington during the Fall of 2016. He joined Prof. Lu's group at the Aerodynamics Research Center in Summer 2017 to work on high speed aerodynamics.

L.H.S. = R.H.S.

Hence proved.